千葉大学 IceCube グループ論文集

ハドロン宇宙国際研究センター ニュートリノ天文学部門

2014年2月

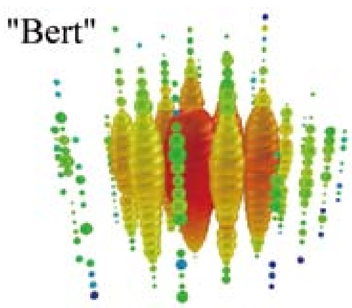

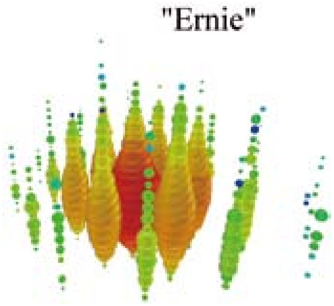

The Papers Collection from the IceCube Group at Chiba University, Japan.

Division of Neutrino Astronomy, International Center for Hadron Astrophysics

February 2014

IceCube 論文集出版にあたって

IceCube 国際共同実験グループが発足して 12 年が経ちました。私達千葉大学グループは超高エネルギー宇宙ニュートリノの探索を通じて最高エネルギー宇宙線の起源を理解することを旗印に活動を行ってきました。高エネルギー宇宙ニュートリノが実在する初の実験的証拠を掴み、最高エネルギー宇宙線由来の GZK ニュートリノ捕捉を射程内に捉える感度を実現する、という重要な研究成果の達成に私達は大きく貢献することができたと自負しています。この機会に、これまでに出版された論文を一つに纏め、得られた研究成果を多くの皆さんと共有し、次のステップへの糧にしたいと考え、この論文集を作ることにしました。

IceCube 実験は数多くの論文を出版していますが、その中で日本グループが大きく貢献したものをこの論文集では選び出しています。グループメンバーが個人として出版した関連論文も含めました。ニュートリノがいかにして超高エネルギー宇宙の実像に迫りうるのか、その大きなポテンシャルをこれらの論文から汲み取っていただければ私としては大きな喜びです。

ここに収められた成果の全てはチームの力に依っています。もし私に運というものがあるとすれば、それは自分のグループに優秀なメンバーが集まったことです。チームの一員としても、また独立した研究者としても素晴らしい人材に恵まれたことが、これらの成果を産み出す源泉となりました。また言うまでもないことですが、日本だけではなく世界中の IceCube 実験グループとのポジティブな協力が全ての基盤です。IceCube 国際共同実験グループはとても働きやすい「職場」です。多くの国の個性豊かな研究者との共同研究はとても楽しい経験でした。

IceCube 実験に代表される基礎科学プロジェクトは成果が出るまでに時間がかかります。私達も論文が一編も書けない苦しい年月を経験してきました。その苦しい時期に私達を励まし、いつか出るであろう成果に賭けて応援していただいた多くの皆さん、どうもありがとうございました。私自身は、いままでの成果には納得はしていますが満足はしていません。まだまだやるべきことがあります。さらに新しい知見を得るべく、これからも邁進していくつもりです。ご期待ください。

2014年 2月 3日

吉田滋

It has been a dozen of years since the IceCube international collaboration was organized. We, the IceCube group from Chiba University, have been engaged in searches of ultra-high energy neutrinos, our flagship mission, which leads to understanding of the origin of the highest energy cosmic rays. Our group has been deeply committed the first observational evidence of existence of a high energy astrophysical neutrino flux, and the consequent achievement of sensitivity good enough to make a detection of ”cosmogenic” neutrinos a reality. On this occasion, we would like to share the obtained scientific knowledges with you by publishing this collection of papers.

The IceCube collaboration has published numerous papers. This collection picked up the ones the Japan’s group has greatly contributed to. The papers published with authors of an individual member from the group are also included among them. It is my pleasure if this series of papers presents to you how neutrinos can probe the ultra-high energy Universe and their great potential to finally resolve the long-standing mystery of the ultra-high energy comic-ray origin.

An every each of the achievements collected here has relied on a power of team work. It is very fortunate that my team is filled with so talented associates. They are really amazing, not just as a member of the team, but also as an independent scientist. None of the papers listed here could have been published without them. And moreover, collaborations with IceCube colleagues from all over the world are indispensable foundations to all the achievements my group has fortunately made. It has been really a fun to work on IceCube with my collaborators in many countries.

A basic science mission like the IceCube project requires a lengthy and time-consuming process to get ready for producing scientific results. We have had to survive a long difficult time when there was no chance to write any single science paper. I really appreciated all of you who have encouraged us during this ”predawn” period, trusting our capability to produce something important to particle astrophysics in near future. Our journey still goes on. I have no doubt that even more amazing discoveries are following. Stay tuned!

Shigeru Yoshida

Shigeru Yoshida
Chiba City, Japan
Feburuary 3, 2014.

目　　次

CONTENTS

"Probing the origin of cosmic rays with extremely high energy neutrinos using the IceCube Observatory"

(IceCube collaboration) ·· 1

PeV ニュートリノ事象を発見した超高エネルギー宇宙ニュートリノ探索解析の詳細報告。解析から得られた 100PeV 以上の超高エネルギー領域での宇宙ニュートリノ流量の最も厳しい上限値から、超高エネルギー宇宙線源の性質に重要な制限を与えた。ニュートリノ観測結果から超高エネルギー宇宙線起源に関する天体物理学的に有意義な知見を初めて与えた成果である。2013 年出版。

The detailed report on the extremely-high energy cosmic neutrino searches leading to the discovery of the two PeV-Energy neutrinos. The analysis placed the strong limit on the neutrino fluxes in the energy range above 100 PeV. The limit constrains the important region of the parameter space concerning the characteristics of the highest energy cosmic-ray sources. This paper represents the first achievement that neutrino observations have indeed provided astrophysically important implications on the origin of ultra-high energy cosmic rays. Published in 2013.

"First Observation of PeV-Energy Neutrinos with IceCube"

(IceCube collaboration) ·· 16

千葉大グループが推進してきた超高エネルギー宇宙ニュートリノ探索によって発見された PeV のエネルギーを持つニュートリノ事象発見の報告。このエネルギーは観測史上最高エネルギーであり、高エネルギー宇宙ニュートリノが存在することを最初に実験的に示唆した記念碑的論文。2013 年出版。

The report on the observation of PeV-Energy neutrinos discovered by the ultra-high energy cosmic neutrino search, the program the Chiba IceCube group has been promoting since its beginning. Their energies are the highest observed so far. It is the monumental paper to describe the very first experimental indication of the existence of an astrophysical neutrino flux. Published in 2013.

"Constraints on the origin of the ultrahigh energy cosmic rays using cosmic diffuse neutrino flux limits: An analytical approach"

(Shigeru Yoshida and Aya Ishihara) ································ 23

宇宙背景輻射との衝突で生じるニュートリノ流量を解析的に算出する手法を導出し、ニュートリノ流量上限値を超高エネルギー宇宙線源の性質の制限に変換する処方を示した。近い将来この方法によって IceCube 実験は超高エネルギー宇宙線源に関する有意義な知見をもたらすことを論じた。2012 年出版。

Presented the semi-analytic formula to calculate fluxes of cosmogenic neutrinos produced by the collisions with the CMB. It provides the recipe to extract bounds on the characteristics of the ultra-high energy cosmic-ray sources from the limits on the neutrino fluxes. It was discussed that the future limits from the IceCube detector is able to fruitfully constrain the ultra-high energy cosmic ray sources. Published in 2012.

"Constraints on the extremely-high energy cosmic neutrino flux with the IceCube 2008-2009 data"

(IceCube collaboration) ·· 32

超高エネルギ領域(PeV-EeV)で世界で最も厳しい宇宙ニュートリノ流量上限値を出した解析結果。約半分の検出器が埋設・運転された 2008-2009 年のデータによる。IceCube 実験が EeV 領域で世界一の感度を持つことを示した節目の論文。超高エネルギー宇宙線の素粒子物理的起源説に極めて厳しい制限を与えている。2011 年出版。

The analysis placing the most stringent bound on the cosmic neutrino flux in ultra-high energy region (PeV-EeV). Based on the data taken with the half-constructed IceCube detector collected between April 2008 and May 2009. It is the milestone paper demonstrating that IceCube provides the world No.1 sensitivity in EeV range. It places the strong constraints on the particle physics-oriented scenarios on the origin of high energy cosmic rays. Published in 2011.

"Constraints on neutrino-nucleon interactions at energies of 1 EeV with the IceCube Neutrino Observatory"

(Shigeru Yoshida) ··· 41

超高エネルギー領域における IceCube 実験の data はニュートリノ・核子相互作用断面積の上限値を決めることによって標準理論を超える素粒子物理の枠組みに制限を加え得ることを示した。2010 年出版。

It demonstrated that the data in ultra-high energy region from the IceCube is capable of constraining new particle physics that enhances the neutrino-nucleon interaction cross section. A bound in the parameter space of the black hole creation as a possible consequence of low-scale gravity was obtained. Published in 2010.

"First search for extremely high energy cosmogenic neutrinos with the IceCube Neutrino Observatory"

(IceCube Collaboration) ··· 47

IceCube 実験で可能な最も高エネルギー領域における宇宙ニュートリノ探索をターゲットに掲げている千葉大学グループによる最初の物理論文。全検出器の約 1/4 が埋設され稼働していた。2007 年時のデータによる。IceCube 実験がメインエネルギー領域である TeV だけではなく PeV-EeV 領域でも競争力があることを示した。2010 年出版。

The first physics analysis paper written by the Chiba group who has been targeting searches of the cosmic neutrinos at the highest energies beyond PeV for a primary physics program. Based on the data taken by the partially (approximately a quater) constructed IceCube in 2007. It demonstrated that IceCube is competitive not only in TeV regime, the main energy range of the project, but also in PeV-EeV regime where the GZK cosmogenic neutrinos are expected to exist. Published in 2010.

"Calibration and characterization of the IceCube photomultiplier tube"

(IceCube Collaboration) ··· 58

IceCube 実験の基幹デバイスである光電子増倍管の応答測定及びキャレーブレーション結果。このデバイスの測定に責任を持っていた千葉大学グループの実験建設時における主要な寄与であった。IceCube 実験の全ての物理解析の基礎を与える論文の一つ。2010 年出版。

The laboratory characterization and calibration of the PMTs, the key device, in the IceCube experiment. This paper represents the major contributions of the Chiba group who had been in charge of the PMT measurements during the detector construction phase. This is one of the papers which provide foundations for all physics analyses with the IceCube detector. Published in 2010.

宇宙ニュートリノ初公表時のスライド

The presentation slide of the 1st annoucement on the detection of the cosmic neutrino event candidates. ················ 72

写真集

A collection of photographs ··· 73

PHYSICAL REVIEW D **88,** 112008 (2013)

Probing the origin of cosmic rays with extremely high energy neutrinos using the IceCube Observatory

M. G. Aartsen,[2] R. Abbasi,[29] M. Ackermann,[45] J. Adams,[15] J. A. Aguilar,[23] M. Ahlers,[29] D. Altmann,[22] C. Arguelles,[29] J. Auffenberg,[29] X. Bai,[33,*] M. Baker,[29] S. W. Barwick,[25] V. Baum,[30] R. Bay,[7] J. J. Beatty,[17,18] J. Becker Tjus,[10] K.-H. Becker,[44] S. BenZvi,[29] P. Berghaus,[45] D. Berley,[16] E. Bernardini,[45] A. Bernhard,[32] D. Z. Besson,[27] G. Binder,[8,7] D. Bindig,[44] M. Bissok,[1] E. Blaufuss,[16] J. Blumenthal,[1] D. J. Boersma,[43] C. Bohm,[36] D. Bose,[38] S. Böser,[11] O. Botner,[43] L. Brayeur,[13] H. -P. Bretz,[45] A. M. Brown,[15] R. Bruijn,[26] J. Casey,[5] M. Casier,[13] D. Chirkin,[29] A. Christov,[23] B. Christy,[16] K. Clark,[39] F. Clevermann,[20] S. Coenders,[1] S. Cohen,[26] D. F. Cowen,[42,41] A. H. Cruz Silva,[45] M. Danninger,[36] J. Daughhetee,[5] J. C. Davis,[17] M. Day,[29] C. De Clercq,[13] S. De Ridder,[24] P. Desiati,[29] K. D. de Vries,[13] M. de With,[9] T. DeYoung,[42] J. C. Díaz-Vélez,[29] M. Dunkman,[42] R. Eagan,[42] B. Eberhardt,[30] J. Eisch,[29] S. Euler,[1] P. A. Evenson,[33] O. Fadiran,[29] A. R. Fazely,[6] A. Fedynitch,[10] J. Feintzeig,[29] T. Feusels,[24] K. Filimonov,[7] C. Finley,[36] T. Fischer-Wasels,[44] S. Flis,[36] A. Franckowiak,[11] K. Frantzen,[20] T. Fuchs,[20] T. K. Gaisser,[33] J. Gallagher,[28] L. Gerhardt,[8,7] L. Gladstone,[29] T. Glüsenkamp,[45] A. Goldschmidt,[8] G. Golup,[13] J. G. Gonzalez,[33] J. A. Goodman,[16] D. Góra,[22] D. T. Grandmont,[21] D. Grant,[21] P. Gretskov,[1] J. C. Groh,[42] A. Groß,[32] C. Ha,[8,7] A. Haj Ismail,[24] P. Hallen,[1] A. Hallgren,[43] F. Halzen,[29] K. Hanson,[12] D. Heereman,[12] D. Heinen,[1] K. Helbing,[44] R. Hellauer,[16] S. Hickford,[15] G. C. Hill,[2] K. D. Hoffman,[16] R. Hoffmann,[44] A. Homeier,[11] K. Hoshina,[29] W. Huelsnitz,[16] P. O. Hulth,[36] K. Hultqvist,[36] S. Hussain,[33] A. Ishihara,[14,†] E. Jacobi,[45] J. Jacobsen,[29] K. Jagielski,[1] G. S. Japaridze,[4] K. Jero,[29] O. Jlelati,[24] B. Kaminsky,[45] A. Kappes,[22] T. Karg,[45] A. Karle,[29] M. Kauer,[29] J. L. Kelley,[29] J. Kiryluk,[37] J. Kläs,[44] S. R. Klein,[8,7] J.-H. Köhne,[20] G. Kohnen,[31] H. Kolanoski,[9] L. Köpke,[30] C. Kopper,[29] S. Kopper,[44] D. J. Koskinen,[19] M. Kowalski,[11] M. Krasberg,[29] A. Kriesten,[1] K. Krings,[1] G. Kroll,[30] J. Kunnen,[13] N. Kurahashi,[29] T. Kuwabara,[33] M. Labare,[24] H. Landsman,[29] M. J. Larson,[40] M. Lesiak-Bzdak,[37] M. Leuermann,[1] J. Leute,[32] J. Lünemann,[30] O. Macías,[15] J. Madsen,[35] G. Maggi,[13] R. Maruyama,[29] K. Mase,[14,‡] H. S. Matis,[8] F. McNally,[29] K. Meagher,[16] M. Merck,[29] T. Meures,[12] S. Miarecki,[8,7] E. Middell,[45] N. Milke,[20] J. Miller,[13] L. Mohrmann,[45] T. Montaruli,[23,§] R. Morse,[29] R. Nahnhauer,[45] U. Naumann,[44] H. Niederhausen,[37] S. C. Nowicki,[21] D. R. Nygren,[8] A. Obertacke,[44] S. Odrowski,[21] A. Olivas,[16] A. Omairat,[44] A. O'Murchadha,[12] L. Paul,[1] J. A. Pepper,[40] C. Pérez de los Heros,[43] C. Pfendner,[17] D. Pieloth,[20] E. Pinat,[12] J. Posselt,[44] P. B. Price,[7] G. T. Przybylski,[8] L. Rädel,[1] M. Rameez,[23] K. Rawlins,[3] P. Redl,[16] R. Reimann,[1] E. Resconi,[32] W. Rhode,[20] M. Ribordy,[26] M. Richman,[16] B. Riedel,[29] J. P. Rodrigues,[29] C. Rott,[38] T. Ruhe,[20] B. Ruzybayev,[33] D. Ryckbosch,[24] S. M. Saba,[10] H. -G. Sander,[30] M. Santander,[29] S. Sarkar,[34] K. Schatto,[30] F. Scheriau,[20] T. Schmidt,[16] M. Schmitz,[20] S. Schoenen,[1] S. Schöneberg,[10] A. Schönwald,[45] A. Schukraft,[1] L. Schulte,[11] O. Schulz,[32] D. Seckel,[33] Y. Sestayo,[32] S. Seunarine,[35] R. Shanidze,[45] C. Sheremata,[21] M. W. E. Smith,[42] D. Soldin,[44] G. M. Spiczak,[35] C. Spiering,[45] M. Stamatikos,[17,∥] T. Stanev,[33] N. A. Stanisha,[42] A. Stasik,[11] T. Stezelberger,[8] R. G. Stokstad,[8] A. Stößl,[45] E. A. Strahler,[13] R. Ström,[43] G. W. Sullivan,[16] H. Taavola,[43] I. Taboada,[5] A. Tamburro,[33] A. Tepe,[44] S. Ter-Antonyan,[6] G. Tešić,[42] S. Tilav,[33] P. A. Toale,[40] M. N. Tobin,[29] S. Toscano,[29] E. Unger,[10] M. Usner,[11] S. Vallecorsa,[23] N. van Eijndhoven,[13] A. Van Overloop,[24] J. van Santen,[29] M. Vehring,[1] M. Voge,[11] M. Vraeghe,[24] C. Walck,[36] T. Waldenmaier,[9] M. Wallraff,[1] Ch. Weaver,[29] M. Wellons,[29] C. Wendt,[29] S. Westerhoff,[29] N. Whitehorn,[29] K. Wiebe,[30] C. H. Wiebusch,[1] D. R. Williams,[40] H. Wissing,[16] M. Wolf,[36] T. R. Wood,[21] K. Woschnagg,[7] D. L. Xu,[40] X. W. Xu,[6] J. P. Yanez,[45] G. Yodh,[25] S. Yoshida,[14,¶] P. Zarzhitsky,[40] J. Ziemann,[20] S. Zierke,[1] and M. Zoll[36]

(IceCube Collaboration)

[1]*III. Physikalisches Institut, RWTH Aachen University, D-52056 Aachen, Germany*
[2]*School of Chemistry & Physics, University of Adelaide, Adelaide, South Australia 5005, Australia*
[3]*Department of Physics and Astronomy, University of Alaska Anchorage, 3211 Providence Drive, Anchorage, AK 99508, USA*
[4]*CTSPS, Clark-Atlanta University, Atlanta, Georgia 30314, USA*
[5]*School of Physics and Center for Relativistic Astrophysics, Georgia Institute of Technology, Atlanta, Georgia 30332, USA*
[6]*Department of Physics, Southern University, Baton Rouge, Louisiana 70813, USA*
[7]*Department of Physics, University of California, Berkeley, California 94720, USA*
[8]*Lawrence Berkeley National Laboratory, Berkeley, California 94720, USA*
[9]*Institut für Physik, Humboldt-Universität zu Berlin, D-12489 Berlin, Germany*
[10]*Fakultät für Physik & Astronomie, Ruhr-Universität Bochum, D-44780 Bochum, Germany*
[11]*Physikalisches Institut, Universität Bonn, Nussallee 12, D-53115 Bonn, Germany*
[12]*Université Libre de Bruxelles, Science Faculty CP230, B-1050 Brussels, Belgium*
[13]*Vrije Universiteit Brussel, Dienst ELEM, B-1050 Brussels, Belgium*

[14]*Department of Physics, Chiba University, Chiba 263-8522, Japan*
[15]*Department of Physics and Astronomy, University of Canterbury, Private Bag 4800, Christchurch, New Zealand*
[16]*Department of Physics, University of Maryland, College Park, Maryland 20742, USA*
[17]*Department of Physics and Center for Cosmology and Astro-Particle Physics, Ohio State University, Columbus, Ohio 43210, USA*
[18]*Department of Astronomy, Ohio State University, Columbus, Ohio 43210, USA*
[19]*Niels Bohr Institute, University of Copenhagen, DK-2100 Copenhagen, Denmark*
[20]*Department of Physics, TU Dortmund University, D-44221 Dortmund, Germany*
[21]*Department of Physics, University of Alberta, Edmonton, Alberta, Canada T6G 2E1*
[22]*Erlangen Centre for Astroparticle Physics, Friedrich-Alexander-Universität Erlangen-Nürnberg, D-91058 Erlangen, Germany*
[23]*Département de physique nucléaire et corpusculaire, Université de Genève, CH-1211 Genève, Switzerland*
[24]*Department of Physics and Astronomy, University of Gent, B-9000 Gent, Belgium*
[25]*Department of Physics and Astronomy, University of California, Irvine, California 92697, USA*
[26]*Laboratory for High Energy Physics, École Polytechnique Fédérale, CH-1015 Lausanne, Switzerland*
[27]*Department of Physics and Astronomy, University of Kansas, Lawrence, Kansas 66045, USA*
[28]*Department of Astronomy, University of Wisconsin, Madison, Wisconsin 53706, USA*
[29]*Department of Physics and Wisconsin IceCube Particle Astrophysics Center, University of Wisconsin, Madison, Wisconsin 53706, USA*
[30]*Institute of Physics, University of Mainz, Staudinger Weg 7, D-55099 Mainz, Germany*
[31]*Université de Mons, 7000 Mons, Belgium*
[32]*T.U. Munich, D-85748 Garching, Germany*
[33]*Bartol Research Institute and Department of Physics and Astronomy, University of Delaware, Newark, Delaware 19716, USA*
[34]*Department of Physics, University of Oxford, 1 Keble Road, Oxford OX1 3NP, United Kingdom*
[35]*Department of Physics, University of Wisconsin, River Falls, Wisconsin 54022, USA*
[36]*Oskar Klein Centre and Department of Physics, Stockholm University, SE-10691 Stockholm, Sweden*
[37]*Department of Physics and Astronomy, Stony Brook University, Stony Brook, New York 11794-3800, USA*
[38]*Department of Physics, Sungkyunkwan University, Suwon 440-746, Korea*
[39]*Department of Physics, University of Toronto, Toronto, Ontario, Canada, M5S 1A7*
[40]*Department of Physics and Astronomy, University of Alabama, Tuscaloosa, Alabama 35487, USA*
[41]*Department of Astronomy and Astrophysics, Pennsylvania State University, University Park, Pennsylvania 16802, USA*
[42]*Department of Physics, Pennsylvania State University, University Park, Pennsylvania 16802, USA*
[43]*Department of Physics and Astronomy, Uppsala University, Box 516, S-75120 Uppsala, Sweden*
[44]*Department of Physics, University of Wuppertal, D-42119 Wuppertal, Germany*
[45]*DESY, D-15735 Zeuthen, Germany*

(Received 20 October 2013; published 16 December 2013)

We have searched for extremely high energy neutrinos using data taken with the IceCube detector between May 2010 and May 2012. Two neutrino-induced particle shower events with energies around 1 PeV were observed, as reported previously. In this work, we investigate whether these events could originate from cosmogenic neutrinos produced in the interactions of ultrahigh energy cosmic rays with ambient photons while propagating through intergalactic space. Exploiting IceCube's large exposure for extremely high energy neutrinos and the lack of observed events above 100 PeV, we can rule out the corresponding models at more than 90% confidence level. The model-independent quasidifferential 90% C.L. upper limit, which amounts to $E^2\phi_{\nu_e+\nu_\mu+\nu_\tau} = 1.2 \times 10^{-7}$ GeV cm^{-2} s^{-1} sr^{-1} at 1 EeV, provides the most stringent constraint in the energy range from 10 PeV to 10 EeV. Our observation disfavors strong cosmological evolution of the highest energy cosmic-ray sources such as the Fanaroff-Riley type II class of radio galaxies.

DOI: 10.1103/PhysRevD.88.112008 PACS numbers: 98.70.Sa, 95.85.Ry, 95.55.Vj

I. INTRODUCTION

Cosmic neutrinos are expected to be produced in the interactions of high energy hadronic particles from cosmic accelerators with surrounding photons and matter. At PeV energies or greater, neutrinos are a unique tool for the direct survey of the ultrahigh energy universe, because photons at these energies are highly attenuated by the cosmic microwave background (CMB). In addition to neutrinos directly produced in cosmic-ray sources, secondary neutrinos produced in the propagation of ultrahigh energy cosmic rays (UHECRs) with energies reaching about

[*]Also at Physics Department, South Dakota School of Mines and Technology, Rapid City, SD 57701, USA.
[†]Corresponding author.
aya@hepburn.s.chiba-u.ac.jp
[‡]Corresponding author.
mase@hepburn.s.chiba-u.ac.jp
[§]Also at Sezione INFN, Dipartimento di Fisica, I-70126, Bari, Italy.
[∥]Also at NASA Goddard Space Flight Center, Greenbelt, MD 20771, USA.
[¶]Corresponding author.
syoshida@hepburn.s.chiba-u.ac.jp

100 EeV are expected. These "cosmogenic" neutrinos are produced by the Greisen-Zatsepin-Kuzmin (GZK) mechanism via interactions of UHECRs with the CMB and extragalactic background light (infrared, optical, and ultraviolet) [1–3]. A measurement of cosmogenic (or GZK) neutrinos probes the origin of the UHECRs because the spectral shapes and flux levels are sensitive to the redshift dependence of UHECR source distributions and cosmic-ray primary compositions [4,5]. Neutrinos are ideal particles to investigate the origin of UHECRs since neutrinos propagate to the Earth essentially without deflection and absorption. The main energy range of the cosmogenic neutrinos is predicted to be around 100 PeV–10 EeV [6,7]. In this extremely high energy (EHE) region, cosmogenic production is considered the main source of cosmic neutrinos.

A measurement of these EHE neutrinos requires a detection volume on the order of at least 1 km^3 as their fluxes are expected to be very low, yielding approximately one event per year in such a volume [8,9]. The IceCube Neutrino Observatory [10] at the geographical South Pole is the first cubic-kilometer scale neutrino detector. Its large instrumented volume as well as its omnidirectional neutrino detection capability have increased the sensitivity for EHE cosmogenic neutrinos significantly. Previous EHE neutrino searches performed with IceCube [9,11] showed that IceCube has become the most sensitive neutrino detector in the energy range of 1 PeV–10 EeV compared to experiments using other techniques [12–16]. The sensitivity of the complete IceCube detector reaches to the modestly high flux cosmogenic models which assume a pure proton composition of cosmic rays. The flux for a heavier composition such as iron is at least 2–3 times lower, although the decrease depends on the source evolution [17] and strongly on the maximal injection energy of the sources [18]. In order to test the heavier composition model predictions, longer exposure or other detection techniques such as the radio detection are needed.

The EHE neutrino search presented here uses data obtained from May 2010 to May 2012. The analysis is sensitive to all three neutrino flavors. The basic search strategies are similar to previous searches [9,11]. The main improvement comes from the enlargement of the detector and the statistical enhancement of the data as well as improved modeling of optical properties of the deep glacial ice [19] in the Monte Carlo simulations. The improvements allow a refined geometrical reconstruction of background events and thus a better background rejection. Two neutrino-induced PeV-energy particle shower events were discovered by this EHE neutrino analysis as reported in Ref. [20]. In this paper, we describe the details of the analysis. Then, we investigate whether the two observed events are consistent with cosmogenic neutrinos. Afterwards, cosmogenic neutrino models are tested for compatibility with our observation in order to constrain the UHECR origin.

The paper is structured as follows: In Secs. II and III, the IceCube detector and the data samples are described. The improved analysis methods and the associated systematic uncertainties are discussed in Secs. IV and V. In Sec. VI, results from the analysis are presented. Implications of the observational results on the UHECR origin are discussed in Sec. VII by testing several cosmogenic neutrino models. The model-independent upper limit of the EHE neutrino flux is shown in Sec. VIII. Finally, the results are summarized in Sec. IX.

II. THE IceCube DETECTOR

The IceCube detector observes the Cherenkov light from the relativistic charged particles produced by high energy neutrino interactions using an array of digital optical modules (DOMs). Each DOM comprises a 10" R7081-02 photomultiplier tube (PMT) [21] in a transparent pressure sphere along with a high voltage system, a digital readout board [22], and a LED flasher board for optical calibration in ice. These DOMs are deployed along electrical cable bundles that carry power and information between the DOMs and the surface electronics. The cable assemblies called strings were lowered into holes drilled to a depth of 2450 m with a horizontal spacing of approximately 125 m (Fig. 1). The DOMs sit where the glacial ice is transparent at depths from 1450 to 2450 m at intervals of 17 m. PMT waveforms are recorded when the signal in a DOM crosses a threshold and the nearest or next-to-nearest DOM observes a photon within 1 μs (hard local coincidence, HLC). An event is triggered if eight DOMs record a HLC within 5 μs. The lower, inner part of the detector called DeepCore [23] is filled with DOMs with a smaller vertical and horizontal spacing of 7 and 72 m, respectively. The DeepCore array is mainly responsible for the enhancement of the performance below 100 GeV, the threshold energy of IceCube. Additional DOMs frozen into tanks

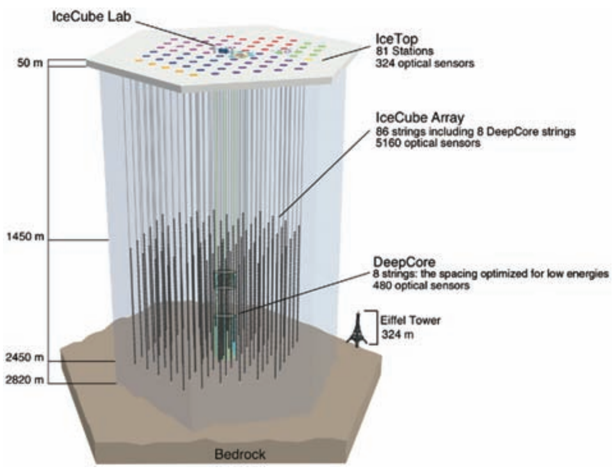

FIG. 1 (color online). A schematic view of the IceCube detector.

located at the surface near the top of each hole constitute an air shower array called IceTop [24]. IceTop allows for the study of cosmic-ray physics and provides the capability to study the atmospheric muon background. The whole detector system comprises 5160 DOMs on 86 strings out of which eight strings correspond to DeepCore, and an additional 324 DOMs in the surface array. The configurations of the IceCube detectors are displayed in Fig. 1.

III. DATA AND SIMULATION

The IceCube detector construction was completed in December, 2010. During the construction phase, from May 31, 2010 to May 12, 2011, 79 strings (IC79), approximately 90% of the full detector, were operational. The IC79 run was immediately followed by the first year of data taking with the full detector (IC86) which lasted from May 13, 2011 to May 15, 2012. The data from these periods were used in this analysis. The corresponding live time for the IC79 and IC86 runs were 319.2 days and 350.9 days respectively, excluding periods of detector calibration and unstable operation. Approximately 10% of the sample (33.4 days of IC79 and 20.8 days of IC86 running) was used as a statistically independent test sample for verification. The final analysis was performed in a blind way where the test sample was not used for the signal search.

There are two classes of background events: atmospheric muon bundle events and events induced by atmospheric neutrinos. Muon bundles consist of a large number of high energy muons produced by cosmic-ray interactions in the atmosphere. Regardless of their high muon multiplicities, they are observed as a single track since their lateral separations of about 10 m is shorter than the minimum DOM separation of 17 m except for DeepCore. Since the detector is large and the data recording time window is also long (10 μs), there is a non-negligible chance that two or more muon bundles arrive at the same time. These events called ''coincident events'' complicate geometrical reconstruction. Special treatment is required to reduce this background. Atmospheric muon bundles were simulated with the CORSIKA air shower simulation [25] with the SIBYLL 2.1 hadronic interaction model [26]. Muons from the showers were propagated from the Earth's surface to IceCube depths with the Muon Monte Carlo package [27]. These were the same programs as in previous studies [9] except that we have improved our description of the optical properties of the glacier ice [19] used in the simulation of the photon propagation from the particles to the DOMs.

For the atmospheric neutrinos, the All Neutrino Interaction Simulation package [28] was used to simulate each neutrino flavor separately between 50 GeV and 1 EeV. The neutrino events were simulated following an E_ν^{-1} spectrum on the surface of the Earth with appropriate flux weights to represent the spectrum resulting from decays of cosmic-ray-induced pions and kaons in the atmosphere (''conventional'' atmospheric neutrinos). We use the cosmic-ray spectrum modeled in Ref. [29] to take into account the spectral bend at the cosmic-ray knee. The neutrino multiplicity employed in this calculation was derived from a modified Elbert formula [30,31]. At PeV energies and above, ''prompt'' atmospheric neutrinos from decays of charmed mesons are expected to dominate over the conventional atmospheric neutrinos. We consider the default value of the prompt neutrino flux from Enberg et al. [32] modified to incorporate the cosmic-ray spectrum model in Ref. [29].

In order to efficiently simulate high energy events with energies exceeding 100 TeV at IceCube depths, the JULIeT package was used in which the propagation of neutrinos was efficiently obtained by solving numerical transport equations as described in Ref. [8].

Figure 2 shows examples of simulated signal and background events observed in the IceCube detector. The sizes and colors of the spheres indicate the number and the timing of photoelectrons (p.e.) observed in each DOM. A signal muon event produces a number of stochastic energy losses along the path. Tau events with energies greater than 10 PeV resemble muon tracks, except that they exhibit less energy loss due to their heavier masses. They may also generate characteristic ''double bang events'' at energies between 1 and 10 PeV due to neutrino interactions and successive tau decays inside the detector volume. Particle showers are induced by neutral current interactions of neutrinos of any flavor or by charged current interactions

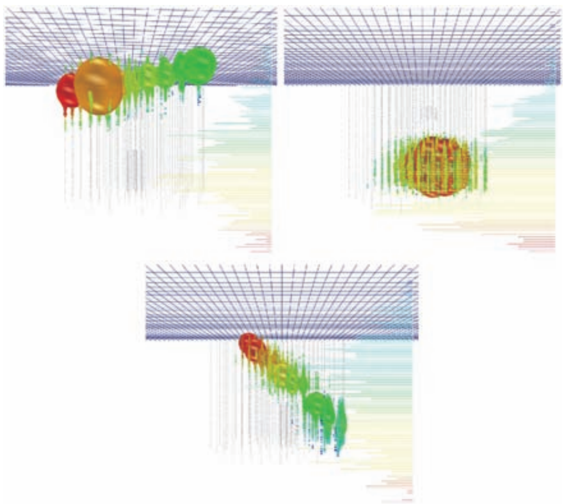

FIG. 2 (color online). Event displays of simulated events. Each sphere represents a DOM. Colors indicate the arrival time of the photon (red indicates the earliest and blue the latest). The size of the sphere and the length of the horizontal lines at the right border indicate the measured amount of photoelectrons in each DOM. Upper left: An upgoing muon entering into the detector array with energy of 20 PeV induced by a neutrino of 500 PeV. Upper right: A 300 PeV ν_e induced cascade event. Lower panel: A typical background atmospheric muon bundle event in the current analysis induced by primary cosmic-ray energy of 1 EeV.

of electron neutrinos. These events called cascade events generate spherical hit patterns in the detector. A background muon bundle event in the current study typically contains about 100 to 1000 muons with lateral separations of about 10 m which results in a smoother energy loss profile compared to one from a single muon or tau event.

IV. EVENT SELECTIONS

The energy spectrum of atmospheric muons and neutrinos falls steeply with energy. The cosmogenic neutrino fluxes with their harder spectra are expected to dominate over this background at high energies. Because the amount of deposited energy, i.e. the observable energy, is correlated with the energy of the incoming particles, the signal events stand out against the background events at high energy. Therefore, this analysis is targeted towards the selection of these high energy events.

The initial event filter selects events containing more than 1,000 p.e. This filtering eliminates a large number of low energy atmospheric muon-induced events, typically with less than a few TeV energy. The filtering process is performed at the South Pole and the resulting EHE sample is sent to the data warehouse at the northern hemisphere via satellite. The samples contained a total of 4.0×10^7 and 6.0×10^7 events for IC79 and IC86, respectively.

The EHE sample transferred to the northern hemisphere is subjected to off-line hit cleaning in order to remove coincident atmospheric muons and PMT noise. A hit represents a reconstructed pulse of photons from a waveform recorded by a DOM and is characterized by its time and charge. The initial hit cleaning is a time window cut on the hits outside the time interval between -4.4 and $+6.4$ μs relative to the time of the first hit on the DOM with the highest charge. Then a secondary hit cleaning based on distances and hit time intervals between DOMs is applied. Hits from the DeepCore strings are discarded at this stage and not used for higher selection levels to keep the DOM separation uniform across the detector volume. After these hit cleanings, the analysis level sample is selected by requesting at least 300 hits and 3200 p.e. in the whole detector except DeepCore. This sample contains a total of 4.5×10^5 and 5.9×10^5 observed events for IC79 and IC86, respectively. The distribution of the total number of p.e.'s (NPEs) versus the true energy of the incoming particle for IC86 simulations of neutrino-induced muons and cascades is shown in Fig. 3. The energies are sampled when the incoming particle is at 880 m from the IceCube center. A clear correlation between NPE and the energy of the muons is observed. By selecting events with a NPE above an appropriate threshold, low energy events dominated by atmospheric backgrounds are filtered out. The correlation also holds for cascade events although uncontained events with vertex positions outside the instrumentation volume weaken the correlation thereby reducing the selection efficiency for this type of event.

The left panels in Fig. 4 show the NPE distributions at analysis level for data and simulations for IC79 and IC86, respectively. The signal cosmogenic neutrino distributions dominate over the atmospheric μ and ν background distributions in the high NPE region. Three cosmogenic neutrino models are shown in the figure: Yoshida and Teshima [6] for an UHECR source distribution in the form of $(1+z)^m$ with the evolution parameter $m = 4$ and the maximum redshift of the UHECR source distribution $z_{\max} = 4$, Ahlers *et al.* [33] (the best fit model with $m = 4.6$ and $z_{\max} = 2.0$), and Kotera *et al.* [17] [Fanaroff-Riley type II (FR-II)]. Atmospheric muon bundles are the dominant contribution at this level. Due to the yet unknown chemical composition of UHECRs, the background rates are estimated by the extreme assumptions of pure proton and iron. The pure iron is employed in this analysis as our baseline model for the atmospheric muons since it yields more muons compared to the pure proton case and hence gives us a conservative background estimate. For the pure iron case the predicted rate is about a factor of 2 higher than the rate observed in IceCube. The data are bracketed by the two compositions as shown in Fig. 4 by the shaded area, demonstrating a reasonable agreement between the experimental data and the atmospheric muon background simulations.

The directional information is also used to further discriminate signal from background. Since the background of atmospheric muons is overwhelmingly large compared to our signals above the horizon, a robust directional reconstruction is crucial for the discrimination. For this purpose, a track hypothesis is assumed to reconstruct atmospheric muons. We utilize different zenith angle reconstruction algorithms for IC79 and IC86. A so-called single photoelectron (SPE) log-likelihood (LLH) fitting based on a track hypothesis using the probability distribution of the arrival time of the first photon in each DOM [34] is

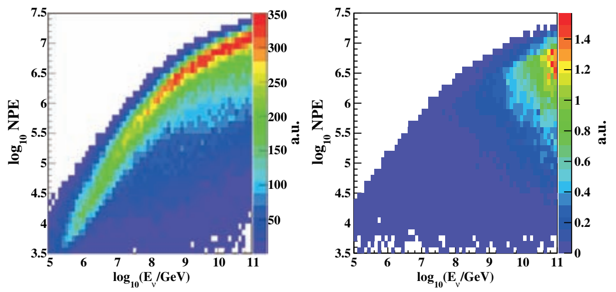

FIG. 3 (color online). Distributions of NPE versus the energies of neutrino-induced muons (left) and neutrinos which induce cascades (right) obtained at the analysis level with the IC86 signal Monte Carlo simulations. For illustrative purposes, an E^{-1} energy spectrum of the particles is assumed in these plots. The muon and neutrino energies are given when the particle enters a radius of 880 m around the IceCube center. Cascade events include all flavor neutral current and ν_e charged current interactions.

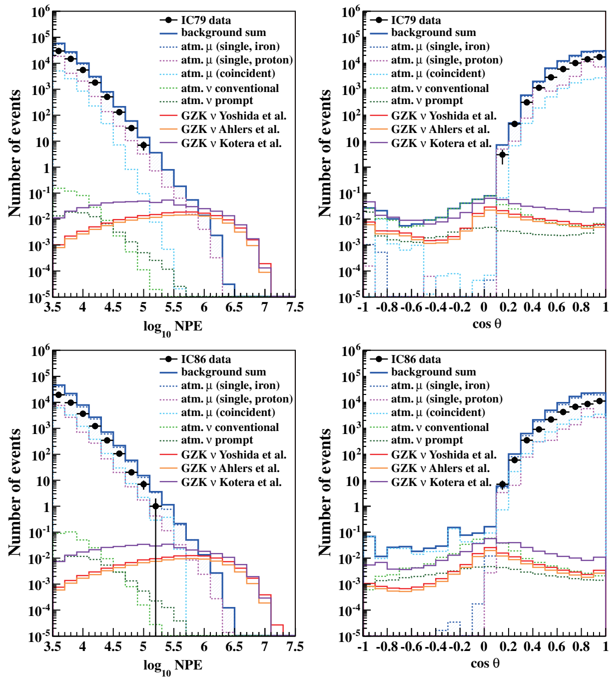

FIG. 4 (color online). Distributions of NPE (left panels) and reconstructed zenith angle (right panels) are shown for the experimental test samples of IC79 (upper panels) and IC86 (lower panels). The data are compared with expected background contributions from atmospheric muons and neutrinos, and signals from various cosmogenic (GZK) neutrino models [6,17,33]. The event numbers presented here are for the live times of the test samples of the experimental data, 33.4 days for IC79 and 20.8 days for IC86. The signal distributions are the sum of all three neutrino flavors. The background sum includes all atmospheric muons and neutrinos. The single atmospheric muons (pure iron) dominate the background so that the line is nearly identical to the line for the background sum. See text for more detail.

performed for the IC79 sample. Then a cut on the reduced log-likelihood (rLLH) parameter is applied to ensure good fit quality. The parameter rLLH is the log-likelihood value of the reconstructed track divided by the number of degrees of freedom of the fit. This rLLH cut removes coincident atmospheric muons. For the IC86 sample, photon hits that have a significantly different timing compared to the one from the main bulk of photon signals are masked using the robust regression technique [35]. Then the particle directions are reconstructed by applying the LineFit algorithm [11] to the remaining unmasked hits. The LineFit algorithm is based on a track hypothesis and uses a simple minimization of $\chi^2 = \Sigma_i \mathrm{NPE}_i(\vec{r}_i - \vec{r}_{\mathrm{COG}} - t_i\vec{v})^2$, where t_i and NPE_i represent the time of the first photoelectron and the number of photoelectrons recorded by the ith DOM at the position $\vec{r}_i$, respectively. The quantity $\vec{r}_{\mathrm{COG}} \equiv (\frac{\Sigma_i \mathrm{NPE}_i x_i}{\Sigma_i \mathrm{NPE}_i}, \frac{\Sigma_i \mathrm{NPE}_i y_i}{\Sigma_i \mathrm{NPE}_i}, \frac{\Sigma_i \mathrm{NPE}_i z_i}{\Sigma_i \mathrm{NPE}_i})$ is the position of the NPE-weighted center of gravity of the hits. The fit ignores the geometry of the Cherenkov cone and the optical properties of the medium and assumes light traveling with a velocity $\vec{v}$ along a one-dimensional path through the detector, passing through the center of gravity. The inclusion of the robust regression technique significantly improves the performance of the LineFit used in the previous study [9], allowing for simpler background rejection. The zenith angle resolution of SPE LLH for background muon events is about 0.5° for the IC79 EHE analysis level sample. The zenith angle resolution from the LineFit with the robust regression for background muons for the IC86 analysis level sample is about 1°. These performances are sufficient to remove atmospheric muon bundle background events in the current analysis.

The performance of the reconstruction on the signal neutrinos highly depends on the shape of the events (Fig. 2). Since most of the signal neutrino events ($> 80\%$) are expected to be muon or tau tracks, the reconstruction of zenith angles based upon track hypotheses as described above gives sufficiently good signal selection efficiency. The reconstructed directions of neutrino-induced cascades, however, are only poorly correlated with the true neutrino direction and exhibit systematic directional shifts. The SPE LLH reconstruction tends to shift the zenith angles towards the vertical while the LineFit shifts them to the horizontal. The behavior of the shifts also changes when their vertex positions are close to or outside the boundary of the instrumentation volume. The resulting systematic uncertainty is discussed in Sec. V.

The right panels in Fig. 4 show the event distributions at analysis level as a function of the cosine of the reconstructed zenith angle. These distributions are compared to the background and signal simulations. Atmospheric muon bundles dominate in the downward-going region and atmospheric neutrinos dominate in the upward-going region.

The signal selection criteria were optimized based on simulations of background and signal after the simulation was verified using the test sample. A cosmogenic neutrino model [6] (with $m = 4$ and $z_{\max} = 4$) is used for the optimization. The selection criteria do not severely depend on the particular choice of the cosmogenic model since the expected energy spectrum is similar. Selection criteria are obtained by optimizing the NPE threshold values in the IC79 and IC86 samples separately such that the model discovery factor [9,36] is minimized in each sample. Figure 5 presents the event distributions in the plane of NPE versus the cosine of the reconstructed zenith angle ($\cos\theta$) for the test sample and simulations. The distributions of the signal simulation are the sum of all three neutrino flavors. The solid lines in Fig. 5 indicate the final selection criteria for each sample. The events above the lines are considered to be signal event candidates. The essential point of this analysis is to select high NPE events against backgrounds regardless of the event shape. A zenith-angle-dependent high NPE threshold is required to eliminate the

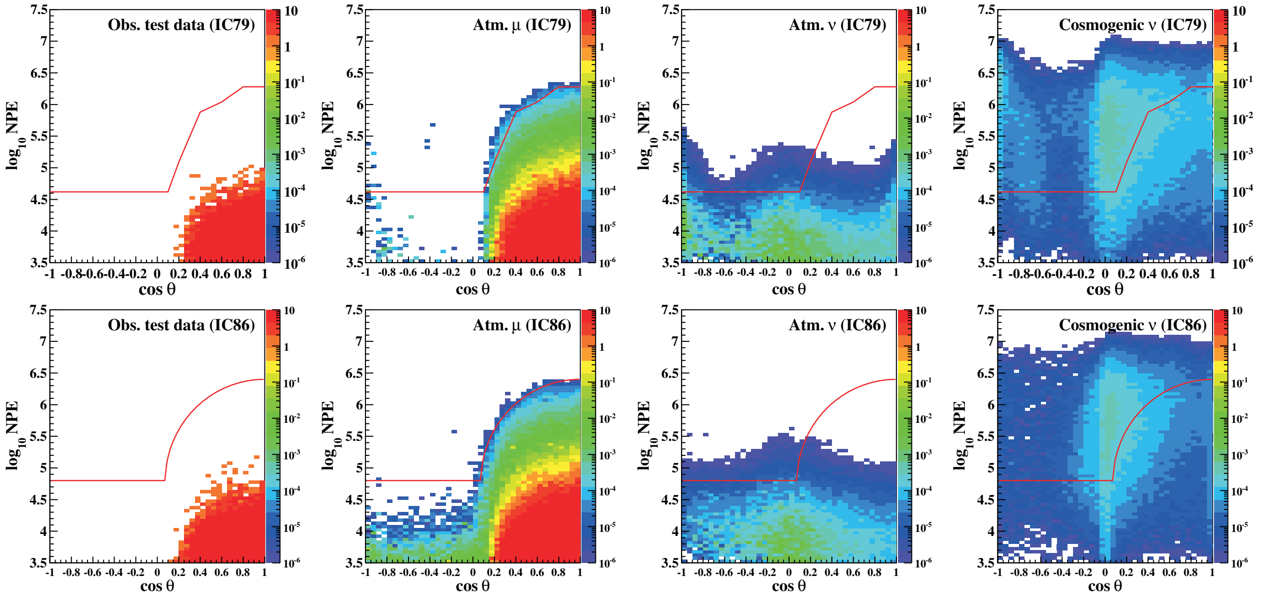

FIG. 5 (color online). Event number distributions on the plane of NPE and cosine of reconstructed zenith angle ($\cos\theta$) for the IC79 run (upper panels) and the IC86 run (lower panels). The experimental test samples are shown in left panels. The background simulations of atmospheric muon (middle-left panels), and the conventional atmospheric neutrino and prompt atmospheric neutrino [32] (middle-right panels), and simulation of signal cosmogenic neutrino model [6] (right panels) are also shown. The colors indicate event numbers per live time of 33.4 days and 20.8 days for the IC79 and IC86 test samples, respectively. The signal distributions are the sum of all three neutrino flavors. The solid lines in each panel indicate the final selection criteria.

atmospheric muon background for the downward-going region, while a constant threshold value is placed in the zenith region of $\cos\theta \lesssim 0.1$, where no atmospheric muon background is expected. The predicted number of signal and background events passing the final selection criteria are presented in Table I along with the observed number of events in the two experimental samples.

The effective neutrino detection areas at final selection criteria for the different IceCube detector configurations are shown in Fig. 6. The effective areas are given for each neutrino flavor, averaged over 4π solid angle for IC79 and IC86. The areas are averaged over equal fluxes of neutrinos and antineutrinos. Below 5 PeV, the effective area for electron neutrinos exceeds that of muon or tau neutrinos. For particle cascades induced by charged current interactions of electron neutrinos, their energies are deposited completely inside the detector if their interaction vertex lies sufficiently inside the instrumented volume. Contrarily muons (taus) from muon (tau) neutrino interactions only partially deposit their energies in the detector volume. Therefore, even though tracks have a longer path in the detector, they satisfy the NPE criteria less frequently (Fig. 5). At higher energies the effective area for tracks is larger because they can be generated in an increasingly larger volume and still reach the detector. Above 100 PeV cascades contribute less than 20% to the observable events from cosmogenic neutrino fluxes. The right panel in Fig. 6 shows the effective area summed over all three neutrino flavors for IC79 and IC86 together with that for IC40 from the previous analysis [9]. The current analysis has

TABLE I. Number of events passing cuts at on-line filtering, off-line analysis, and final level with 285.8 days of effective live time for IC79 and 330.1 days for IC86 (excluding test sample data). One cosmogenic neutrino model [6] (with $m = 4$ and $z_{\max} = 4$) is taken to evaluate the benchmark signal rates. The background rates include atmospheric muons assuming a pure iron primary composition, conventional atmospheric neutrinos, and prompt atmospheric neutrinos. Analysis sample requests the number of hit DOMs ≥ 300, $\log_{10}(\mathrm{NPE}) \geq 3.5$ for IC79 and IC86, and an additional requirement of rLLH < 8 for IC79. Systematic uncertainties in the expected event rates at the final selection level are given as asymmetric error intervals after the statistical errors.

	Experimental		Background MC		Benchmark signal MC [6]	
Contributions samples	IC79	IC86	IC79	IC86	IC79	IC86
EHE filter level	4.0×10^7	6.0×10^7	4.4×10^7	8.9×10^7	2.1	2.4
Analysis level	4.5×10^5	5.9×10^5	8.5×10^5	1.3×10^6	1.5	1.8
Final level	0	2	$0.056 \pm 0.002^{+0.028}_{-0.041}$	$0.026 \pm 0.003^{+0.015}_{-0.017}$	$0.876 \pm 0.004^{+0.119}_{-0.105}$	$1.043 \pm 0.006^{+0.142}_{-0.134}$

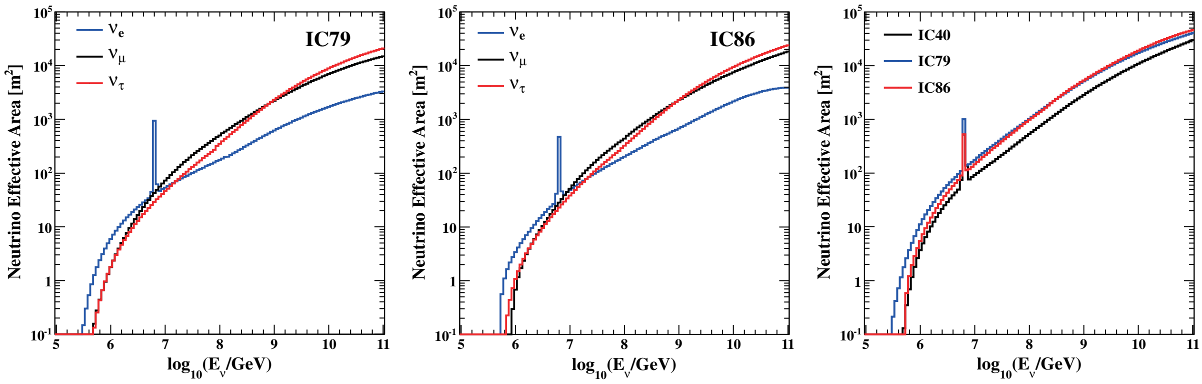

FIG. 6 (color online). The IceCube neutrino effective area at final selection criteria with different string configurations, IC79 (left panel) and IC86 (middle panel) for each neutrino flavor, averaged over 4π solid angle. The areas are averaged over equal amounts of neutrinos and antineutrinos. Three flavor sums of the effective areas are shown in the right panel. The effective area from the previous search [9] with 40 string configuration of IceCube (IC40) is also shown for comparison. Exposure of the sample used in this analysis is obtained by multiplying the effective area with the effective live time without test samples (333.5 days, 285.8 days, and 330.1 days for IC40, IC79, and IC86 , respectively) and 4π solid angle. The sharp peaked structure at 6.3 PeV for electron neutrinos is due to the Glashow resonance [37].

approximately a factor of 2 larger effective area compared to IC40. The difference between the effective areas for IC79 and IC86 below 30 PeV originates from the different NPE thresholds. The slight difference above 3×10^3 PeV is due to the rLLH cut in IC79.

V. SYSTEMATIC UNCERTAINTIES

Table II summarizes the statistical and systematic errors for signal, atmospheric muon and neutrino, prompt atmospheric neutrino, and the total background.

TABLE II. List of the statistical and systematic errors on the signal, atmospheric muon and neutrino, prompt neutrino, and the total background rate. The uncertainties in the signal rate are estimated for the cosmogenic flux of Yoshida and Teshima [6] for $(m, z_{\max}) = (4, 4)$. The uncertainties in the background rates are evaluated against the baseline estimation by CORSIKA-SIBYLL [25,26] with a pure iron composition hypothesis for atmospheric muons and the Gaisser-H3a model [29] for atmospheric neutrinos. The uncertainties in the prompt neutrino rate are estimated using the prediction by Ref. [32]. The systematic and statistical errors listed here are relative to the event rates for each signal and background source.

Sources	Cosmogenic ν signal (%)	Atmospheric muon (%)	Conventional Atmospheric neutrino (%)	Prompt neutrino (%)	Total background (%)
Statistical error	± 0.4	± 9.1	± 9.8	± 1.1	± 4.5
DOM efficiency	$^{+1.5}_{-5.1}$	$^{+41.9}_{-42.7}$	$^{+73.2}_{-17.9}$	$^{+33.6}_{-9.6}$	$^{+43.1}_{-26.1}$
Ice properties/detector response	-7.2	-47.7	-44.8	-30.8	-41.7
Neutrino cross section	± 9.0	⋯	⋯	⋯	⋯
Photonuclear interaction	$+10.0$	⋯	⋯	⋯	⋯
LPM effect	± 1.0	⋯	⋯	⋯	⋯
Angular shift for cascades	-0.5	⋯	⋯	⋯	⋯
Cosmic-ray flux variation	⋯	$^{+30.0}_{-50.0}$	± 30.0	± 30.0	$^{+18.7}_{-26.3}$
Cosmic-ray composition	⋯	-79.1	⋯	⋯	-36.7
Hadronic interaction model	⋯	$+17.7$	⋯	⋯	$+8.1$
ν yield from cosmic-ray nucleon	⋯	⋯	± 15.0	⋯	± 2.2
Prompt model uncertainty	⋯	⋯	⋯	$^{+31.6}_{-40.4}$	$^{+12.6}_{-16.1}$
Total	± 0.4(stat)	± 9.1(stat)	± 9.8(stat)	± 1.1(stat)	± 4.5(stat)
	$^{+13.6}_{-12.4}$(syst)	$^{+54.5}_{-100}$(syst)	$^{+80.5}_{-58.7}$(syst)	$^{+55.0}_{-59.8}$(syst)	$^{+49.3}_{-68.7}$(syst)

One of the dominant sources of systematic uncertainties in the signal event rates is the error associated with the Cherenkov photon measurement, namely the relationship between measured NPE and the energy of the charged particles. This is due to limitations in the understanding of detector sensitivities, photon propagation in the ice, and the detector response to bright events which, for example, involves saturation effects of the DOMs. This uncertainty is estimated by calibrating the absolute sensitivity of the DOMs in the laboratory and by measuring it *in situ* using a light source codeployed with the DOMs in the ice [9,11]. The other uncertainties in the signal rates involve the relevant interactions of neutrinos and leptons produced during the propagation through the Earth. For example, the Landau-Pomeranchuk-Migdal (LPM) effect [38,39] can be important since it elongates electromagnetic showers. The elongated shower length is about 20–40 m for 1–10 EeV electrons [40], thus still being comparable to the IceCube DOM separation of 17 m, and hence negligible. Uncertainties due to other propagation effects are estimated as described in [11].

The uncertainty of the systematic shifts of reconstructed zenith angles for cascade events causes a systematic error in the estimation of the signal neutrino passing rate. The effect is NPE dependent and thus energy dependent. We artificially vary the systematic zenith angle shift by different factors to evaluate the resulting uncertainties. The complete randomization of zenith angles was found to bring the largest reduction of the cascade event selection efficiency. The reduction is 20.0% for events with energies below 10 PeV, 8.5% between 10 and 100 PeV, and 2.0% above 100 PeV. Since most of the cosmogenic neutrino signal (99.6%) is expected above 10 PeV and the present analysis is mostly sensitive to track events above 10 PeV as seen in Fig. 6, the effect on the cosmogenic neutrino signal rate is quite limited. The systematic error on the overall signal rate due to the limited performance of the cascade event reconstruction is estimated to be -0.5%.

Systematic errors in the atmospheric muon background rate arise from uncertainties in the primary cosmic-ray composition, the hadronic interaction model implemented in the air shower simulation, and the cosmic-ray flux variation at the relevant energies. The two extreme cases of the cosmic-ray compositions, pure iron and pure proton, are used. In the current analysis, the iron-only hypothesis is used for the baseline background rates. This leads to a higher, i.e. conservative, estimate of the photon yield from the muon bundles induced by primary cosmic-ray particles at a particular energy. The difference between the pure-iron and the pure-proton hypothesis then provides the size of the relevant systematic uncertainty. The uncertainty associated with the hadronic interaction model is estimated by switching the model from SIBYLL 2.1 [26] to QGSJET-II-03 [41] in the simulations. The uncertainty in the cosmic-ray flux normalization is estimated from the variance in the flux measured by several experiments [42,43] relative to the one used in this analysis [44] at 10 EeV, the peak energy of primary cosmic rays that produce atmospheric muon events passing the final selection criteria. The contribution of the cosmic-ray normalization to the uncertainty in the atmospheric neutrino rate is estimated in a similar way at energies from 1 to 100 PeV from various models [29,45]. In addition, a systematic uncertainty for the atmospheric neutrino rate arises from the uncertainty of the parametrization of the neutrino multiplicity as described in Sec. III. A comparison to the full simulation by CORSIKA [25] provides the relevant uncertainty. The systematic uncertainties for backgrounds associated with the photon detection efficiency and the optical properties of the ice are determined in the same manner as for signal events.

The atmospheric neutrino background is calculated over 4π solid angle and simulated independently of the atmospheric muon background. In reality, downward-going atmospheric neutrino events would be accompanied by atmospheric muons, which improve their geometrical reconstruction. Because correctly reconstructed downward-going events are mostly rejected due to the higher NPE threshold employed in the final event selection, the background rate obtained from the independent neutrino and muon simulations is likely overestimated.

The systematic error on the prompt neutrino flux is estimated similarly. A relatively large uncertainty arises from the parametrization in the framework of the Enberg *et al.* model [32] which we used for the calculation of the baseline rate of prompt neutrinos. A possible nonperturbative QCD contribution in charm production involves an even larger uncertainty. We have not observed clear evidence for prompt contributions in atmospheric neutrinos so far [46].

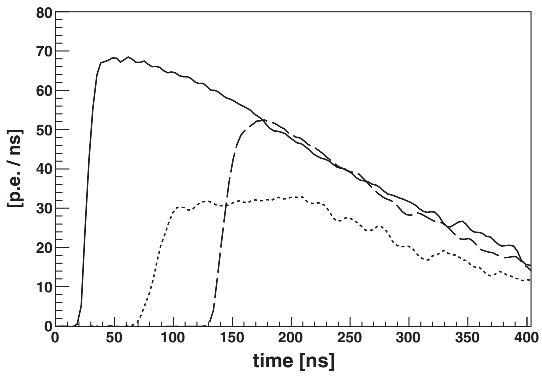

FIG. 7. Waveforms of PMT outputs captured by three DOMs in the neighborhood of the reconstructed vertex position of the event obtained in January, 2012. The waveform drawn as a solid curve is recorded in the DOM closest to the vertex (the brightest DOM). The waveform in the lower (upper) next to nearest to the brightest DOM on the same string is shown as a dashed (dotted) curve. Photons arrive earlier in the upper DOM because it is closer to the cascade vertex than the lower DOM. The signals from the upper DOM exhibit clear signatures of scattered late photons, suggesting that this cascade is a downward-going event.

VI. RESULTS

Two events passing the final selection criteria are observed [20]. The waveform profiles and the detector hit patterns of both events are consistent with that of Cherenkov photons from particle cascades induced by neutrinos well inside the IceCube instrumentation volume. There is no indication of outgoing/incoming muon or tau tracks. Several waveforms captured by the DOMs in the neighborhood of one of the reconstructed cascade vertex position are shown in Fig. 7. The total charge contained in the waveforms plays a dominant role in estimating the deposited energy of the cascade. The leading edge time mainly determines the vertex position. The relative widths of the waveforms in DOMs in the forward and rear directions of the cascade are relevant for the reconstruction of the arrival direction of neutrinos. Since photons can only reach the backward direction by scattering, the distribution of photon arrival times is much wider in the backward region of the cascades. The relations of the waveform features to the energy, direction, and vertex position are described using a single likelihood function built from a product of Poisson probabilities of the number of photons predicted to arrive in a given time bin against the number extracted from the recorded waveform. Minimizing the log-likelihood under simultaneous variation of the energy and geometry of the cascade hypothesis yields estimates of the deposited energy, direction, and interaction vertex of the cascade.

The reconstructed deposited energies of the two observed cascades are 1.04 ± 0.16 PeV and 1.14 ± 0.17 PeV, respectively. The statistical energy resolutions for these events are obtained by simulating cascades with parameters close to the reconstructed energies and cascade vertices, and are found to be 3%. The total error on the energy is dominated by systematic uncertainties. These include the absolute detection efficiency of the DOM and the optical properties of the ice, both of which are major factors when relating the number of observed photons to the cascade energy. The size of the errors is estimated by reconstructing simulated events with various models of the ice properties.

The incoming neutrino energy corresponds exactly to the deposited cascade energy if a charged current interaction of an electron neutrino induces a cascade. For neutral current reactions of neutrinos of any flavor, only a fraction of the neutrino energy is transferred to a cascade depending on the inelasticity of the collision. Because the present analysis is incapable of distinguishing between neutrino flavors, both interaction channels are included when constructing the probability density function (PDF) of the energy of the incoming neutrino. Here, the systematic uncertainties for the deposited energies are taken into account. The PDF of the neutrino energy at the surface of the Earth is built by simulating neutrino interactions over a wide energy range each time evaluating the probability that the resulting cascade energy matches the estimated energy and its uncertainty. The 90% C.L. energy ranges obtained from the PDFs for neutrino spectra with an E_ν^{-2} power law flux are summarized in Table III. The flavor ratio is assumed to be $\nu_e:\nu_\mu:\nu_\tau = 1:1:1$. Since the neutrino-nucleon interaction cross section increases with neutrino energy, the possibility that the energy of the primary neutrino is much higher than the observed cascade energy is not entirely negligible, depending on the neutrino spectrum. For example, the 90% C.L. energy range for a cosmogenic neutrino model [33] extends to about 500 PeV, which shows that the energy range heavily depends on the shape of the energy spectrum.

TABLE III. The 90% C.L. of the energy range of the primary neutrino in PeV at the Earth's surface for the two events for an energy spectrum following an E^{-2} power law.

	Energy range (90% C.L.)
Event (August, 2011)	0.81–7.6 PeV
Event (January, 2012)	0.93–8.9 PeV

VII. TESTS ON COSMOGENIC NEUTRINO MODELS

Our results are characterized by two observational facts: the detection of two neutrinos with deposited energies of about 1 PeV and the nondetection of neutrinos with higher deposited energies. First, we investigate whether a single cosmogenic neutrino model can account for these two observational facts simultaneously. Second, we constrain the UHECR origin with the present results. Because most cosmogenic neutrinos have energies above 100 PeV, tests on the event rate above this energy expected from cosmogenic neutrino models under various assumptions on the UHECR spectrum and the evolutions of the source distributions will lead to constraints on the UHECR origin. We note that the energy threshold of 100 PeV is an *a posteriori* parameter and, hence, the results are not part of the blind analysis.

The statistical significance of these tests is limited by our observational exposure. To obtain the best constraints, we combine the exposure of the previously published results obtained by the half-completed IceCube detector with its 40 string configuration (IC40) [9] with the present results hereafter. The IC40 data increase the observational exposure by about 30%, depending on the neutrino energy, as displayed in Fig. 6.

A. The full energy range test

We introduce here an energy inclusive test which checks the consistency of the energy distributions of cosmogenic neutrino models with the observed two events. A *p* value is calculated with the Kolmogorov-Smirnov test (KS test) using the energy spectrum of the neutrino models and the

TABLE IV. P values $P_{\rm E}$ in Eq. (1) are listed for several neutrino models. All the models shown here assume the cosmic-ray primaries to be protons and different spectral indices/cutoff energies at sources, IR/UV backgrounds, as well as different cosmological evolution parameters and extension in redshift for the sources. P values for E_ν^{-2} spectra with various cutoff energies are also shown for reference.

ν Model	P value
Yoshida and Teshima [6]	
$m = 4.0$, $z_{\rm max} = 4.0$	0.077
Ahlers *et al.* [33]	
$m = 4.6$, $z_{\rm max} = 2.0$ (“the best fit”)	0.075
Kotera *et al.* [17]	
GRB	0.052
Kotera *et al.* [17]	
Fanaroff-Riley type II	0.039
E_ν^{-2}	
With cutoff at 10 PeV	0.18
With cutoff at 100 PeV	0.13
With cutoff at 1 EeV	0.11

energy PDFs of the two observed events. The expected energy distributions from the neutrino models are obtained by multiplication of the neutrino effective area with the predicted neutrino energy spectrum. This allows us to analytically calculate p values without relying on extensive Monte Carlo simulations. In order to evaluate the final p value, P_E, that the two events (energies E_1 and E_2) are consistent with a cosmogenic flux model, the p value obtained in the KS test $P_{\rm KS}(E_1, E_2)$ is convoluted with the energy PDFs of the two events as follows:

$$P_{\rm E} = \int dE_1 \rho_1(E_1) \int dE_2 \rho_2(E_2) P_{\rm KS}(E_1, E_2), \quad (1)$$

where ρ_i is the energy PDF of the ith event. Note that the PDF is different for each model to be tested as described in the previous section. Table IV summarizes the resulting p values of this test: all cosmogenic neutrino models are inconsistent with the two observed events at more than 90% C.L.

The recent follow-up analysis [47] revealed the existence of neutrinos at TeV energies above the atmospheric background, in addition to the two PeV events reported in Ref. [20]. The event distribution indicated either a substantially softer spectrum than E_ν^{-2} or the presence of a break or cutoff at PeV energies, although the statistics are limited. The present analysis confirmed this picture using the KS test with an E_ν^{-2} spectrum hypothesis as Table IV lists the resultant p values with various assumptions of the spectral cutoff energies. The observed PeV events are unlikely to originate from a bulk of neutrinos with energies extending well above PeV, regardless of the characteristics of the events at TeV energies found in the follow-up analysis.

B. The *ex post facto* test above 100 PeV

Here, a prospective event rate in the energy region above 100 PeV is compared to the observational upper limit. A constraint on a given neutrino model is set by calculating the model rejection factor (MRF) [48] given by

$$R_{\rm MRF} = \frac{N_{100(1-\alpha)\%}}{\mu_\nu}, \quad (2)$$

where $N_{100(1-\alpha)\%}$ is the upper limit of number of events at $100(1-\alpha)\%$ C.L. and μ_ν is the event rate of signal neutrino events predicted by the model above 100 PeV. Any model with $R_{\rm MRF} \le 1$ is rejected at $\ge 100(1-\alpha)\%$ C.L. in this approach. For $\alpha = 0.1$, $N_{90\%} = 2.27$ in the Feldman-Cousins approach [49] for a null observation with a conventional background of a 0.16 event. The large number of background events comes mainly from the IC40 analysis contributing a 0.11 event [9]. Although the probability that the original neutrino energy of the two observed events is higher than 100 PeV is expected to be small, this is taken into account by calculating the most probable upper limit:

$$N_{100(1-\alpha)\%} = \sum_{n=0}^{2} P_n N^n_{100(1-\alpha)\%}. \quad (3)$$

Here, P_n is the probability of finding n events above 100 PeV determined by the energy PDFs of the two events, and $N^n_{100(1-\alpha)\%}$ is the upper limit for n observed events. Since the energy PDF highly depends on the shape of the energy spectrum, an appropriate shape of an energy spectrum has to be chosen. Since the two observed events were found to be inconsistent with cosmogenic neutrino models as shown in the previous subsection, the cosmogenic neutrino models are not used for the energy PDF, instead an E^{-2} power law spectrum is used. The $N_{90\%}$ is calculated for the standard cosmogenic models and found to be 2.273, which is slightly larger than for the case of a null detection. The systematic uncertainty on the background estimates is incorporated using a method outlined in [50]. The p value α for a given model is obtained by requesting $R_{\rm MRF} = 1$ in Eq. (2).

Table V summarizes the p values for several neutrino models. The maximal flux allowed by the constraints from the diffuse photon flux (labeled as “the maximal flux” in the table) is excluded at 95% C.L. It demonstrates that the present constraints from the limit on the ultrahigh energy neutrino flux are compatible with those from photon flux measurements by Fermi in the 10 GeV region [53].

In order to set constraints on characteristics of the UHECR sources in a more comprehensive manner, a parametrization often used in the literature [6] is employed, in which the spectral emission rate per comoving volume scales as $(1+z)^m$ for $z \le z_{\rm max}$. The event rate at energies above 100 PeV is calculated for a given m, and $z_{\rm max}$ using the formula in Ref. [4]. The constraints on the parameter

TABLE V. Expected numbers of events from several neutrino models and the p values for consistency with the present observation in energy range above 100 PeV.

ν Model	Event rate above 100 PeV	P value
Yoshida and Teshima [6]		
$m = 4.0$, $z_{\rm max} = 4.0$	2.0	0.14
Kalashev *et al.* [51]		
$m = 5.0$, $z_{\rm max} = 3.0$	3.1	0.045
Yoshida and Ishihara [4]		
$m = 5.0$, $z_{\rm max} = 2.0$	1.5	0.22
Ahlers *et al.* [33]		
$m = 4.6$, $z_{\rm max} = 2.0$	1.5	0.22
("the best fit")		
Ahlers *et al.* [33]		
("the maximal flux")	3.1	0.044
Kotera *et al.* [17]		
GRB	0.48	0.66
Kotera *et al.* [17]		
SFR	0.46	0.67
Kotera *et al.* [17]		
Fanaroff-Riley type II	2.9	0.052
Top-down 1 [52]		
SUSY	16	$\lesssim 0.0020$
Top-down 2 [52]		
GUT	3.9	0.021

space of m and $z_{\rm max}$ are derived by using Eq. (2), and are displayed in Fig. 8.

C. Discussion

The models listed in the top two rows of Table IV assume that the *ankle* structure which appears at 3 to 10 EeV in the UHECR spectrum is due to the transition from the galactic to the extragalactic component [54]. In this scenario, the cosmogenic neutrino generation mechanism is dominated by collisions of UHECRs with the CMB photons which results in a neutrino energy spectrum with a peak at about 1 EeV, well above the main regime of the energy range of the two observed events. This is the reason why these models are inconsistent with the two observed events as shown in Table IV. The models in the lower two rows of Table IV (Kotera *et al.* [17]) assume the "dip" transition model [55] where the ankle structure is mainly caused by pair-production energy losses of UHECRs on diffuse infrared, optical, and ultraviolet backgrounds (IR/UV backgrounds) during intergalactic propagation. The neutrino models in Kotera *et al.* use the IR/UV backgrounds as modeled by Stecker *et al.* [56] which comprises an increased far-infrared bump at large redshift (note that the IR/UV model employed in these neutrino models is now disfavored by gamma-ray observation with Fermi-LAT [57]). Compared to the standard cosmogenic models, the dip and the IR/UV backgrounds leads to an increased flux of neutrinos at PeV energies, so that these models in

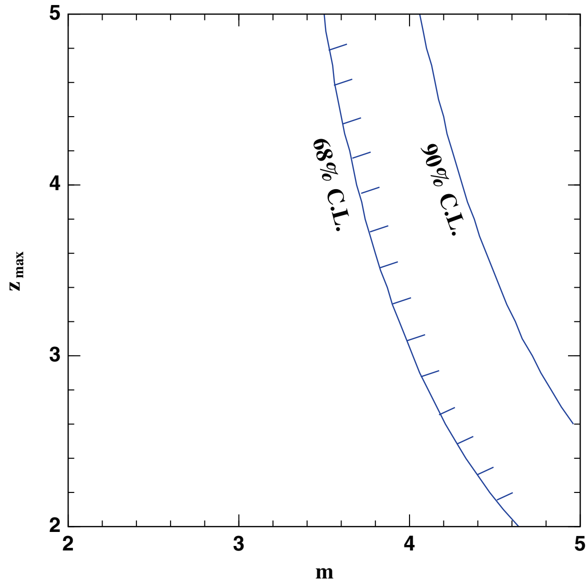

FIG. 8 (color online). Constraints on the UHECR source evolution parameters of m and $z_{\rm max}$ with the present analysis. The semianalytic formulation [4] estimates the neutrino flux for calculating the limit shown here. The area above the solid lines is excluded at the quoted confidence level.

Kotera *et al.* could be more consistent with the observation. However, even in these models, the collision of UHECRs with CMB photons produces a bulk of neutrinos with energies much higher than 100 PeV which should have been detected because of the significantly larger effective area at these energies. In addition, the substantial flux at PeV energies yields energy PDFs for the observed two events very similar to those from an E_ν^{-2} spectrum. Since the energy range for the E_ν^{-2} spectrum PDF does not extend to 10 PeV as shown in Table III, neutrinos with energy of 100 PeV or greater are less likely to be responsible for the observed PeV cascades. Because of these reasons, p values for these scenarios in Kotera *et al.* are small as shown in Table IV. In conclusion, none of the cosmogenic scenarios is consistent with the observation of the two events. This indicates that models which predict neutrino spectra extending to energies well beyond 100 PeV will not explain our measurements.

The model test based on the event rates above 100 PeV indicates that strong source evolution models ($m \gg 4$) are not responsible for the bulk of UHECRs. Among sources categorized in this class are the FR-II radio galaxies, the long-standing favorite as a candidate of the UHECR emitters [58]. Similarly a strong source evolution model for gamma-ray bursts (GRBs) [59] is also rejected by our observation since the model produces higher neutrino flux than the FR-II model. The obtained limits are highly complementary to the bound from the diffuse photon flux [53], because the cosmogenic neutrino intensity around 1 EeV, the central energy range of the presented

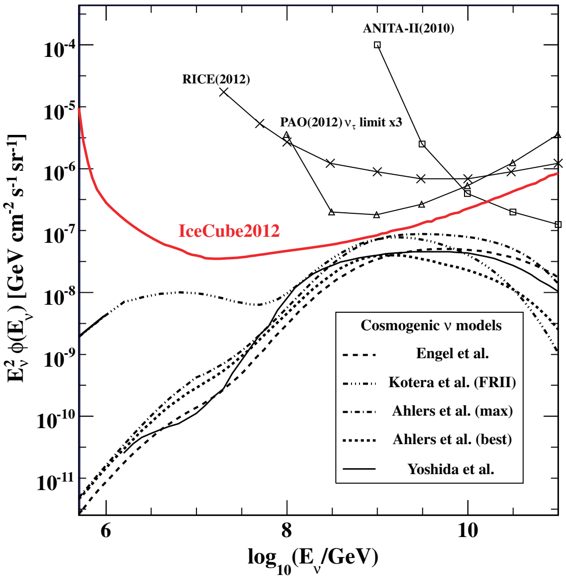

FIG. 9 (color online). All flavor neutrino flux differential 90% C.L. upper limit evaluated for each energy with a sliding window of one energy decade from the present IceCube EHE analysis including the IceCube exposure from the previously published result (IC40) [9]. All the systematic errors are included. Various model predictions (assuming primary protons) are shown for comparison; Engel *et al.* [7], Kotera *et al.* [17], Ahlers *et al.* [33], Yoshida and Teshima [6]. The model-independent differential 90% C.L. upper limits for one energy decade by other experiments are also shown for Auger (PAO) [62], RICE [63], ANITA [14,15] with appropriate normalization by taking into account the energy bin width and the neutrino flavor. The upper limit for the ν_τ flux obtained by Auger is multiplied by 3 to convert it to an all flavor neutrino flux limit (assuming an equal neutrino flavor ratio).

search with IceCube, is stable against uncertainties in the IR/UV backgrounds and the transition model between the galactic and extragalactic component of the UHECRs [4,17,60,61]. We should note, however, that the obtained bound is not valid if the mass composition of UHECRs is not dominated by proton primaries. The dominance of proton primaries is widely assumed in the models mentioned here while a dominance of heavier nuclei such as iron provides at least 2–3 times lower neutrino fluxes. The analysis is not sensitive enough to reach these fluxes yet.

VIII. THE MODEL-INDEPENDENT UPPER LIMIT

The quasidifferential, model-independent 90% C.L. upper limit on all flavor neutrino fluxes $\phi_{\nu_e+\nu_\mu+\nu_\tau}$ was evaluated for each energy with a sliding window of one energy decade. It is shown in Fig. 9 using the same method as implemented in our previous EHE neutrino searches [9,11]. An equal flavor ratio of $\nu_e{:}\nu_\mu{:}\nu_\tau = 1{:}1{:}1$ is assumed here. A difference from the calculation of the limit shown in our previous publications arises from the existence of two events in the final sample. The 90% event upper limit used in the calculation takes into account the energy PDFs of each of the observed events using Eq. (3), where P_n is a function of the neutrino energy E_ν and corresponds to the probability of having n events in the interval $[\log_{10}(E_\nu/\mathrm{GeV}) - 0.5,\ \log_{10}(E_\nu/\mathrm{GeV}) + 0.5]$. Here, the PDFs for an E_ν^{-2} spectrum are used since the two observed events are not consistent with a harder spectrum such as from cosmogenic neutrino models. The quasidifferential limit takes into account all the systematic uncertainties described in Sec. V. The effect of the uncertainty due to the angular shift of the cascade events on the upper limit is negligible above 10 PeV ($< 1\%$) as track events dominate in this energy range. Below 10 PeV, the effect weakens the upper limit by 17% because cascade events dominate. Other systematic uncertainties are implemented as in previous EHE neutrino searches [9,11]. The obtained upper limit is the strongest constraint in the EeV regime so far. In the PeV region, the constraint is weaker due to the detection of the two events. An upper limit for an E^{-2} spectrum that takes into account the two observed events was also derived and amounts to $E^2\phi_{\nu_e+\nu_\mu+\nu_\tau} = 2.5 \times 10^{-8}\ \mathrm{GeV\,cm^{-2}\,s^{-1}\,sr^{-1}}$ for an energy range of 1.6 PeV–3.5 EeV (90% event coverage).

IX. SUMMARY

We analyzed the 2010–2012 data samples collected by the 79- and 86-string IceCube detector searching for extremely high energy neutrinos with energies exceeding 1 PeV. We observed two neutrino-induced cascade events passing the final selection criteria. The energy profiles of the two events indicate that these events are cascades with deposited energies of about 1 PeV. The cosmogenic neutrino production is unlikely to be responsible for these events. An upper limit on the neutrino rate in the energy region above 100 PeV places constraints on the redshift distribution of UHECR sources. For the first time the observational constraints reach the flux region predicted for some UHECR source class candidates. The obtained upper limit is significantly stronger compared to our previous publication [9] because of the enlarged instrumented volume and the refined Monte Carlo simulations. Future data obtained with the completed detector will further enhance IceCube's sensitivity to cosmogenic neutrino models.

ACKNOWLEDGMENTS

We acknowledge the support from the following agencies: U.S. National Science Foundation - Office of Polar Programs, U.S. National Science Foundation - Physics Division, University of Wisconsin Alumni Research Foundation, the Grid Laboratory Of Wisconsin (GLOW) grid infrastructure at the University of Wisconsin - Madison, the Open Science Grid (OSG) grid infrastructure; U.S. Department of Energy, and National Energy Research

Scientific Computing Center, the Louisiana Optical Network Initiative (LONI) grid computing resources; Natural Sciences and Engineering Research Council of Canada, WestGrid and Compute/Calcul Canada; Swedish Research Council, Swedish Polar Research Secretariat, Swedish National Infrastructure for Computing (SNIC), and Knut and Alice Wallenberg Foundation, Sweden; German Ministry for Education and Research (BMBF), Deutsche Forschungsgemeinschaft (DFG), Helmholtz Alliance for Astroparticle Physics (HAP), Research Department of Plasmas with Complex Interactions (Bochum), Germany; Fund for Scientific Research (FNRS-FWO), FWO Odysseus Programme, Flanders Institute to encourage scientific and technological research in industry (IWT), Belgian Federal Science Policy Office (Belspo); University of Oxford, United Kingdom; Marsden Fund, New Zealand; Australian Research Council; Japan Society for Promotion of Science (JSPS); the Swiss National Science Foundation (SNSF), Switzerland; National Research Foundation of Korea (NRF).

[1] K. Greisen, Phys. Rev. Lett. **16**, 748 (1966).
[2] G. T. Zatsepin and V. A. Kuzmin, Pis'ma Zh. Eksp. Teor. Fiz. **4**, 114 (1966); [JETP Lett. **4**, 78 (1966)].
[3] V. Berezinsky and G. Zatsepin, Phys. Lett. **28B**, 423 (1969).
[4] S. Yoshida and A. Ishihara, Phys. Rev. D **85**, 063002 (2012).
[5] M. Ahlers, L. A. Anchordoqui, and S. Sarkar, Phys. Rev. D **79**, 083009 (2009).
[6] S. Yoshida and M. Teshima, Prog. Theor. Phys. **89**, 833 (1993).
[7] R. Engel, D. Seckel, and T. Stanev, Phys. Rev. D **64**, 093010 (2001).
[8] S. Yoshida, R. Ishibashi, and H. Miyamoto, Phys. Rev. D **69**, 103004 (2004).
[9] R. Abbasi *et al.* (IceCube Collaboration), Phys. Rev. D **83**, 092003 (2011).
[10] A. Achterberg *et al.* (IceCube Collaboration), Astropart. Phys. **26**, 155 (2006).
[11] R. Abbasi *et al.* (IceCube Collaboration), Phys. Rev. D **82**, 072003 (2010).
[12] J. Abraham *et al.* (Pierre Auger Collaboration), Phys. Rev. D **79**, 102001 (2009).
[13] P. Abreu *et al.* (Pierre Auger Collaboration), Phys. Rev. D **84**, 122005 (2011).
[14] P. W. Gorham *et al.* (ANITA Collaboration), Phys. Rev. D **82**, 022004 (2010).
[15] P. W. Gorham *et al.* (ANITA Collaboration), Phys. Rev. D **85**, 049901(E) (2012).
[16] I. Kravchenko *et al.*, Phys. Rev. D **73**, 082002 (2006).
[17] K. Kotera, D. Allard, and A. Olinto, J. Cosmol. Astropart. Phys. 10 (2010) 013.
[18] M. Ahlers and F. Halzen, Phys. Rev. D **86**, 083010 (2012).
[19] M. Aartsen *et al.* (IceCube Collaboration), Nucl. Instrum. Methods Phys. Res., Sect. A **711**, 73 (2013).
[20] M. Aartsen *et al.* (IceCube Collaboration), Phys. Rev. Lett. **111**, 021103 (2013).
[21] R. Abbasi *et al.* (IceCube Collaboration), Nucl. Instrum. Methods Phys. Res., Sect. A **618**, 139 (2010).
[22] R. Abbasi *et al.* (IceCube Collaboration), Nucl. Instrum. Methods Phys. Res., Sect. A **601**, 294 (2009).
[23] R. Abbasi *et al.* (IceCube Collaboration), Astropart. Phys. **35**, 615 (2012).
[24] R. Abbasi *et al.* (IceCube Collaboration), Nucl. Instrum. Methods Phys. Res., Sect. A **700**, 188 (2013).
[25] D. Heck *et al.*, Report No. FZKA-6019, 1998.
[26] E. J. Ahn, R. Engel, T. K. Gaisser, P. Lipari, and T. Stanev, Phys. Rev. D **80**, 094003 (2009).
[27] D. Chirkin and W. Rhode, arXiv:hep-ph/0407075v2.
[28] A. Gazizov and M. P. Kowalski, Comput. Phys. Commun. **172**, 203 (2005).
[29] T. K. Gaisser, Astropart. Phys. **35**, 801 (2012).
[30] T. K. Gaisser, *Cosmic Rays and Particle Physics* (Cambridge University Press, Cambridge, England, 1990).
[31] J. Elbert, in *Proceedings of the DUMAND Summer Workshop* (Scripps Institution of Oceanography, La Jolla, CA, 1979), Vol. 2, p. 101.
[32] R. Enberg, M. H. Reno, and I. Sarcevic, Phys. Rev. D **78**, 043005 (2008).
[33] M. Ahlers, L. A. Anchordoqui, M. C. Gonzalez-Garcia, F. Halzen, and S. Sarkar, Astropart. Phys. **34**, 106 (2010).
[34] J. Ahrens *et al.* (AMANDA Collaboration), Nucl. Instrum. Methods Phys. Res., Sect. A **524**, 169 (2004).
[35] M. G. Aartsen *et al.* (IceCube Collaboration), arXiv:1308.5501.
[36] G. C. Hill *et al.*, in *Proceedings of PHYSTAT2005, Oxford, England, 2005* (Imperial College Press, London, 2006), pp. 108–111.
[37] S. L. Glashow, Phys. Rev. **118**, 316 (1960).
[38] L. D. Landau and I. J. Pomeranchuk, Dokl. Akad. Nauk SSSR **92**, 535 (1953).
[39] A. B. Migdal, Phys. Rev. **103**, 1811 (1956).
[40] L. Gerhardt and S. R. Klein, Phys. Rev. D **82**, 074017 (2010).
[41] S. Ostapchenko, Phys. Rev. D **83**, 014018 (2011).
[42] J. Abraham *et al.* (Pierre Auger Collaboration), Phys. Lett. B **685**, 239 (2010).
[43] R. Abbasi *et al.* (HiRes Collaboration), Phys. Rev. Lett. **100**, 101101 (2008).
[44] M. Nagano and A. A. Watson, Rev. Mod. Phys. **72**, 689 (2000).
[45] V. Zatsepin and N. V. Sokolskaya, Astron. Astrophys. **458**, 1 (2006).
[46] A. Schukraft, Nucl. Phys. B, Proc. Suppl. **237–238**, 266 (2013).
[47] M. Artsen *et al.* (IceCube Collaboration), Science **342**, 1242856 (2013).
[48] G. Hill and K. Rawlins, Astropart. Phys. **19**, 393 (2003).

[49] G. J. Feldman and R. D. Cousins, Phys. Rev. D **57**, 3873 (1998).
[50] F. Tegenfeldt and J. Conrad, Nucl. Instrum. Methods Phys. Res., Sect. A **539**, 407 (2005).
[51] O. E. Kalashev, V. A. Kuzmin, D. V. Semikoz, and G. Sigl, Phys. Rev. D **66**, 063004 (2002).
[52] G. Sigl, S. Lee, P. Bhattacharjee, and S. Yoshida, Phys. Rev. D **59**, 043504 (1998).
[53] V. Berezinsky, A. Gazizov, M. Kachelriess, and S. Ostapchenko, Phys. Lett. B **695**, 13 (2011).
[54] T. Wibig and A. W. Wolfendale, J. Phys. G **31**, 255 (2005).
[55] V. S. Berezinsky, A. Gazizov, and S. Grigorieva, Phys. Rev. D **74**, 043005 (2006).
[56] F. W. Stecker, M. A. Malkan, and S. T. Scully, Astrophys. J. **648**, 774 (2006).
[57] M. Ackermann *et al.* (Fermi-LAT Collaboration), Science **338**, 1190 (2012).
[58] P. Biermann and P. Strittmatter, Astrophys. J. **322**, 643 (1987).
[59] H. Yuksel and M. D. Kistler, Phys. Rev. D **75**, 083004 (2007).
[60] H. Takami, K. Murase, S. Nagataki, and K. Sato, Astropart. Phys. **31**, 201 (2009).
[61] G. Decerprit and D. Allard, Astron. Astrophys. **535**, A66 (2011).
[62] P. Abreu *et al.* (Pierre Auger Collaboration), Astrophys. J. **755**, L4 (2012).
[63] I. Kravchenko, S. Hussain, D. Seckel, D. Besson, E. Fensholt, J. Ralston, J. Taylor, K. Ratzlaff, and R. Young, Phys. Rev. D **85**, 062004 (2012).

First Observation of PeV-Energy Neutrinos with IceCube

M. G. Aartsen,[2] R. Abbasi,[27] Y. Abdou,[22] M. Ackermann,[41] J. Adams,[15] J. A. Aguilar,[21] M. Ahlers,[27] D. Altmann,[9] J. Auffenberg,[27] X. Bai,[31,*] M. Baker,[27] S. W. Barwick,[23] V. Baum,[28] R. Bay,[7] J. J. Beatty,[17,18] S. Bechet,[12] J. Becker Tjus,[10] K.-H. Becker,[40] M. Bell,[38] M. L. Benabderrahmane,[41] S. BenZvi,[27] J. Berdermann,[41] P. Berghaus,[41] D. Berley,[16] E. Bernardini,[41] A. Bernhard,[30] D. Bertrand,[12] D. Z. Besson,[25] G. Binder,[8,7] D. Bindig,[40] M. Bissok,[1] E. Blaufuss,[16] J. Blumenthal,[1] D. J. Boersma,[39] S. Bohaichuk,[20] C. Bohm,[34] D. Bose,[13] S. Böser,[11] O. Botner,[39] L. Brayeur,[13] H.-P. Bretz,[41] A. M. Brown,[15] R. Bruijn,[24] J. Brunner,[41] M. Carson,[22] J. Casey,[5] M. Casier,[13] D. Chirkin,[27] A. Christov,[21] B. Christy,[16] K. Clark,[38] F. Clevermann,[19] S. Coenders,[1] S. Cohen,[24] D. F. Cowen,[38,37] A. H. Cruz Silva,[41] M. Danninger,[34] J. Daughhetee,[5] J. C. Davis,[17] C. De Clercq,[13] S. De Ridder,[22] P. Desiati,[27] M. de With,[9] T. DeYoung,[38] J. C. Díaz-Vélez,[27] M. Dunkman,[38] R. Eagan,[38] B. Eberhardt,[28] J. Eisch,[27] R. W. Ellsworth,[16] S. Euler,[1] P. A. Evenson,[31] O. Fadiran,[27] A. R. Fazely,[6] A. Fedynitch,[10] J. Feintzeig,[27] T. Feusels,[22] K. Filimonov,[7] C. Finley,[34] T. Fischer-Wasels,[40] S. Flis,[34] A. Franckowiak,[11] R. Franke,[41] K. Frantzen,[19] T. Fuchs,[19] T. K. Gaisser,[31] J. Gallagher,[26] L. Gerhardt,[8,7] L. Gladstone,[27] T. Glüsenkamp,[41] A. Goldschmidt,[8] G. Golup,[13] J. G. Gonzalez,[31] J. A. Goodman,[16] D. Góra,[41] D. Grant,[20] A. Groß,[30] M. Gurtner,[40] C. Ha,[8,7] A. Haj Ismail,[22] P. Hallen,[1] A. Hallgren,[39] F. Halzen,[27] K. Hanson,[12] D. Heereman,[12] D. Heinen,[1] K. Helbing,[40] R. Hellauer,[16] S. Hickford,[15] G. C. Hill,[2] K. D. Hoffman,[16] R. Hoffmann,[40] A. Homeier,[11] K. Hoshina,[27] W. Huelsnitz,[16,†] P. O. Hulth,[34] K. Hultqvist,[34] S. Hussain,[31] A. Ishihara,[14,‡] E. Jacobi,[41] J. Jacobsen,[27] K. Jagielski,[1] G. S. Japaridze,[4] K. Jero,[27] O. Jlelati,[22] B. Kaminsky,[41] A. Kappes,[9] T. Karg,[41] A. Karle,[27] J. L. Kelley,[27] J. Kiryluk,[35] F. Kislat,[41] J. Kläs,[40] S. R. Klein,[8,7] J.-H. Köhne,[19] G. Kohnen,[29] H. Kolanoski,[9] L. Köpke,[28] C. Kopper,[27] S. Kopper,[40] D. J. Koskinen,[38] M. Kowalski,[11] M. Krasberg,[27] K. Krings,[1] G. Kroll,[28] J. Kunnen,[13] N. Kurahashi,[27] T. Kuwabara,[31] M. Labare,[13] H. Landsman,[27] M. J. Larson,[36] M. Lesiak-Bzdak,[35] M. Leuermann,[1] J. Leute,[30] J. Lünemann,[28] J. Madsen,[33] R. Maruyama,[27] K. Mase,[14] H. S. Matis,[8] F. McNally,[27] K. Meagher,[16] M. Merck,[27] P. Mészáros,[37,38] T. Meures,[12] S. Miarecki,[8,7] E. Middell,[41] N. Milke,[19] J. Miller,[13] L. Mohrmann,[41] T. Montaruli,[21,§] R. Morse,[27] R. Nahnhauer,[41] U. Naumann,[40] H. Niederhausen,[35] S. C. Nowicki,[20] D. R. Nygren,[8] A. Obertacke,[40] S. Odrowski,[30] A. Olivas,[16] M. Olivo,[10] A. O'Murchadha,[12] L. Paul,[1] J. A. Pepper,[36] C. Pérez de los Heros,[39] C. Pfendner,[17] D. Pieloth,[19] E. Pinat,[12] N. Pirk,[41] J. Posselt,[40] P. B. Price,[7] G. T. Przybylski,[8] L. Rädel,[1] M. Rameez,[21] K. Rawlins,[3] P. Redl,[16] R. Reimann,[1] E. Resconi,[30] W. Rhode,[19] M. Ribordy,[24] M. Richman,[16] B. Riedel,[27] J. P. Rodrigues,[27] C. Rott,[17,∥] T. Ruhe,[19] B. Ruzybayev,[31] D. Ryckbosch,[22] S. M. Saba,[10] T. Salameh,[38] H.-G. Sander,[28] M. Santander,[27] S. Sarkar,[32] K. Schatto,[28] M. Scheel,[1] F. Scheriau,[19] T. Schmidt,[16] M. Schmitz,[19] S. Schoenen,[1] S. Schöneberg,[10] A. Schönwald,[41] A. Schukraft,[1] L. Schulte,[11] O. Schulz,[30] D. Seckel,[31] Y. Sestayo,[30] S. Seunarine,[33] C. Sheremata,[20] M. W. E. Smith,[38] M. Soiron,[1] D. Soldin,[40] G. M. Spiczak,[33] C. Spiering,[41] M. Stamatikos,[17,¶] T. Stanev,[31] A. Stasik,[11] T. Stezelberger,[8] R. G. Stokstad,[8] A. Stößl,[41] E. A. Strahler,[13] R. Ström,[39] G. W. Sullivan,[16] H. Taavola,[39] I. Taboada,[5] A. Tamburro,[31] S. Ter-Antonyan,[6] G. Tešić,[38] S. Tilav,[31] P. A. Toale,[36] S. Toscano,[27] M. Usner,[11] D. van der Drift,[8,7] N. van Eijndhoven,[13] A. Van Overloop,[22] J. van Santen,[27] M. Vehring,[1] M. Voge,[11] M. Vraeghe,[22] C. Walck,[34] T. Waldenmaier,[9] M. Wallraff,[1] R. Wasserman,[38] Ch. Weaver,[27] M. Wellons,[27] C. Wendt,[27] S. Westerhoff,[27] N. Whitehorn,[27] K. Wiebe,[28] C. H. Wiebusch,[1] D. R. Williams,[36] H. Wissing,[16] M. Wolf,[34] T. R. Wood,[20] K. Woschnagg,[7] C. Xu,[31] D. L. Xu,[36] X. W. Xu,[6] J. P. Yanez,[41] G. Yodh,[23] S. Yoshida,[14] P. Zarzhitsky,[36] J. Ziemann,[19] S. Zierke,[1] A. Zilles,[1] and M. Zoll[34]

(IceCube Collaboration)

[1]*III. Physikalisches Institut, RWTH Aachen University, D-52056 Aachen, Germany*
[2]*School of Chemistry and Physics, University of Adelaide, Adelaide South Australia 5005, Australia*
[3]*Department of Physics and Astronomy, University of Alaska Anchorage, 3211 Providence Dr., Anchorage, Alaska 99508, USA*
[4]*CTSPS, Clark-Atlanta University, Atlanta, Georgia 30314, USA*
[5]*School of Physics and Center for Relativistic Astrophysics, Georgia Institute of Technology, Atlanta, Georgia 30332, USA*
[6]*Department of Physics, Southern University, Baton Rouge, Louisiana 70813, USA*
[7]*Department of Physics, University of California, Berkeley, California 94720, USA*
[8]*Lawrence Berkeley National Laboratory, Berkeley, California 94720, USA*
[9]*Institut für Physik, Humboldt-Universität zu Berlin, D-12489 Berlin, Germany*
[10]*Fakultät für Physik und Astronomie, Ruhr-Universität Bochum, D-44780 Bochum, Germany*
[11]*Physikalisches Institut, Universität Bonn, Nussallee 12, D-53115 Bonn, Germany*

[12] *Université Libre de Bruxelles, Science Faculty CP230, B-1050 Brussels, Belgium*
[13] *Vrije Universiteit Brussel, Dienst ELEM, B-1050 Brussels, Belgium*
[14] *Department of Physics, Chiba University, Chiba 263-8522, Japan*
[15] *Department of Physics and Astronomy, University of Canterbury, Private Bag 4800, Christchurch, New Zealand*
[16] *Department of Physics, University of Maryland, College Park, Maryland 20742, USA*
[17] *Department of Physics and Center for Cosmology and Astro-Particle Physics, Ohio State University, Columbus, Ohio 43210, USA*
[18] *Department of Astronomy, Ohio State University, Columbus, Ohio 43210, USA*
[19] *Department of Physics, TU Dortmund University, D-44221 Dortmund, Germany*
[20] *Department of Physics, University of Alberta, Edmonton, Alberta, Canada T6G 2E1*
[21] *Département de physique nucléaire et corpusculaire, Université de Genève, CH-1211 Genève, Switzerland*
[22] *Department of Physics and Astronomy, University of Gent, B-9000 Gent, Belgium*
[23] *Department of Physics and Astronomy, University of California, Irvine, California 92697, USA*
[24] *Laboratory for High Energy Physics, École Polytechnique Fédérale, CH-1015 Lausanne, Switzerland*
[25] *Department of Physics and Astronomy, University of Kansas, Lawrence, Kansas 66045, USA*
[26] *Department of Astronomy, University of Wisconsin, Madison, Wisconsin 53706, USA*
[27] *Department of Physics and Wisconsin IceCube Particle Astrophysics Center, University of Wisconsin, Madison, Wisconsin 53706, USA*
[28] *Institute of Physics, University of Mainz, Staudinger Weg 7, D-55099 Mainz, Germany*
[29] *Université de Mons, 7000 Mons, Belgium*
[30] *Technical University of Munich, D-85748 Garching, Germany*
[31] *Bartol Research Institute and Department of Physics and Astronomy, University of Delaware, Newark, Delaware 19716, USA*
[32] *Department of Physics, University of Oxford, 1 Keble Road, Oxford OX1 3NP, United Kingdom*
[33] *Department of Physics, University of Wisconsin, River Falls, Wisconsin 54022, USA*
[34] *Oskar Klein Centre and Department of Physics, Stockholm University, SE-10691 Stockholm, Sweden*
[35] *Department of Physics and Astronomy, Stony Brook University, Stony Brook, New York 11794-3800, USA*
[36] *Department of Physics and Astronomy, University of Alabama, Tuscaloosa, Alabama 35487, USA*
[37] *Department of Astronomy and Astrophysics, Pennsylvania State University, University Park, Pennsylvania 16802, USA*
[38] *Department of Physics, Pennsylvania State University, University Park, Pennsylvania 16802, USA*
[39] *Department of Physics and Astronomy, Uppsala University, Box 516, S-75120 Uppsala, Sweden*
[40] *Department of Physics, University of Wuppertal, D-42119 Wuppertal, Germany*
[41] *DESY, D-15735 Zeuthen, Germany*
(Received 19 April 2013; published 8 July 2013)

We report on the observation of two neutrino-induced events which have an estimated deposited energy in the IceCube detector of 1.04 ± 0.16 and 1.14 ± 0.17 PeV, respectively, the highest neutrino energies observed so far. These events are consistent with fully contained particle showers induced by neutral-current $\nu_{e,\mu,\tau}$ ($\bar{\nu}_{e,\mu,\tau}$) or charged-current ν_e ($\bar{\nu}_e$) interactions within the IceCube detector. The events were discovered in a search for ultrahigh energy neutrinos using data corresponding to 615.9 days effective live time. The expected number of atmospheric background is $0.082 \pm 0.004(\text{stat})^{+0.041}_{-0.057}(\text{syst})$. The probability of observing two or more candidate events under the atmospheric background-only hypothesis is 2.9×10^{-3} (2.8σ) taking into account the uncertainty on the expected number of background events. These two events could be a first indication of an astrophysical neutrino flux; the moderate significance, however, does not permit a definitive conclusion at this time.

DOI: 10.1103/PhysRevLett.111.021103 PACS numbers: 95.85.Ry, 95.55.Vj, 98.70.Sa

Astrophysical neutrinos are key probes of the high-energy universe. Because of their unique properties, neutrinos escape even dense regions, are undeflected in galactic or extragalactic magnetic fields, and traverse the photon-filled universe unhindered. Thus, neutrinos provide direct information about the dynamics and interiors of cosmological objects of the high redshift universe like gamma-ray bursts and active galactic nuclei. Neutrinos at energies above several hundred TeV are particularly interesting as the atmospheric background in this region is very low and a few astrophysical neutrinos can be significant. This Letter reports on the observation of two high-energy particle shower events discovered in a search for ultrahigh energy neutrinos above about 1 PeV using the IceCube detector.

IceCube [1] detects and reconstructs neutrinos by recording Cherenkov photons emitted from secondary charged particles produced in neutral-current (NC) or charged-current (CC) interactions of the neutrinos in the 2800 m thick glacial ice at the geographic South Pole. IceCube was built between 2005 and 2010. It consists of an array of 5160 optical sensors [digital optical modules, (DOMs)] on 86 strings at depths between 1450 and 2450 m that instrument a volume of 1 km^3 of ice. Eight of the 86 strings belong to the DeepCore subarray [2], a more densely instrumented volume in the bottom center of the

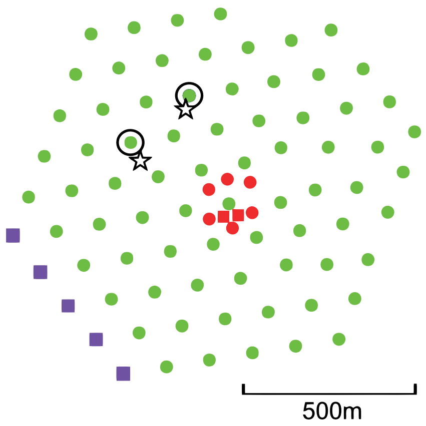

FIG. 1 (color online). Surface view of the full IceCube detector layout. Filled marks represent the positions of the IceCube strings. Red marks in the central region are the DeepCore strings. Squares represent the strings that did not exist in the IC79 configuration. Open circles are the positions of the closest strings to the observed two cascade events. Stars are their reconstructed vertex positions.

detector. Each DOM consists of a 10'' photomultiplier tube [3] in a spherical glass pressure vessel. Events are recorded as a series of pulses (waveform) in each DOM [4] where two basic neutrino event signatures are distinguished: a tracklike light pattern originating from neutrino-induced muons (tracks) and a spherical light pattern produced by hadronic or electromagnetic particle showers (cascades).

The analysis selects neutrino candidates calorimetrically using the total number of observed photoelectrons in each event (NPE) [4] as a proxy of the deposited energy [5], thus, retaining both bright tracks and cascades. Backgrounds come from muons and neutrinos generated in interactions of cosmic rays in the atmosphere. Because of their steeply falling energy spectra, little background is expected in the signal region above 1 PeV. The zenith angle distribution of atmospheric muons peaks in the downward-going direction and sharply decreases towards the horizon with a cutoff at a zenith angle θ of $\cos\theta \approx 0.15$ due to absorption in Earth. The atmospheric neutrino distributions have a weaker zenith-angle dependence. The analysis rejects downward-going atmospheric muons by employing event reconstructions based on a track hypothesis in combination with a higher NPE selection criterion in the downward-going region. All remaining events above the combined NPE threshold are considered to be signal candidates independent of their topological properties.

Data were collected between May 2010 and May 2012, an effective live time of 615.9 days excluding 54.2 days used for the optimization of the analysis. From May 2010 to May 2011, DOMs on 79 strings (IC79) were operational (285.8 days live time with 33.4 days excluded). This period was immediately followed by the first year data taking with the full 86-string (IC86) detector that lasted until May 2012 (330.1 days live time with 20.8 days excluded). The IC86 configuration is shown in Fig. 1. Events are triggered when eight or more DOMs record signals in local coincidences which occur when a nearest or next-to-nearest DOM on the same string triggers within ± 1 μs [4].

The data are filtered at the South Pole with a condition NPE $\geq$ 1000, and then sent to a northern computer farm via satellite. In order to avoid biases, we performed a blind analysis and only $\sim$10% of the data were used to develop the analysis. Photon arrival times are extracted from each waveform and stored as "hits." To remove hits from coincident noise, a two-staged cleaning based on the spatial separation and the time interval between hits is applied. Data from the DeepCore strings are discarded to maintain uniformity across the detector volume. To reject downward-going atmospheric muon background, only events with at least 300 hits and NPE $\geq$ 3200 are retained. To further reduce this background, the directions of the remaining events are reconstructed with a track hypothesis, and a stricter NPE criterion for downward-going tracks is applied [see Fig. 2 and Eq. (1)]: for IC79, a log-likelihood fit is performed [6] and an event selection based on a fit quality parameter is applied to remove events which contain muons from independent air showers. For IC86, a robust regression technique [7,8] is utilized to remove hits that have a timing significantly different from what is expected from the bulk of the photons from a muon track. Afterwards, the direction of the particle is

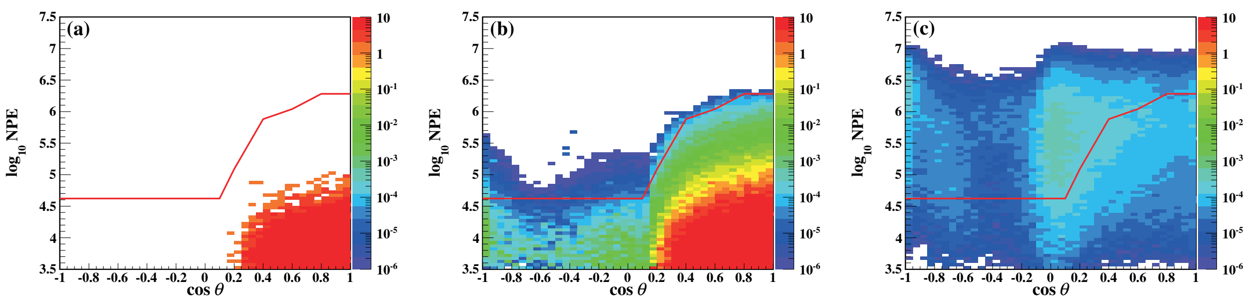

FIG. 2 (color online). Distribution of NPE and reconstructed zenith angle for (a) the IC79 experimental test sample, (b) the total background, and (c) cosmogenic signal neutrino [11]. The colors show event numbers per live time of 33.4 days. The solid lines represent the final selection criteria for IC79.

reconstructed with a basic algorithm that assumes a plane wave of photons traveling along the direction of the muon, "LineFit" [5]. Both algorithms reconstruct muon tracks with a zenith angle resolution of 1° or better.

Cascade events which pass the initial hit and NPE selection criteria are considered signal events and, therefore, should be affected as little as possible by the event rejections just described. As they resemble pointlike light sources, the reconstruction behavior of the two algorithms is indeed quite different finding nearly arbitrary zenith angles, albeit with a tendency toward upward-going and horizontal directions for the log-likelihood fit and LineFit, respectively. Since, for these directions, the NPE threshold value is lower than for downward-going events [see Fig. 2 and Eq. (1)], such events are retained in the final sample even if they would be rejected on account of their true direction.

The NPE threshold values for the two samples were separately optimized based on the simulations to maximize the signal [9,10] from the cosmogenic neutrino model [11]. Figure 2 shows the event distributions for the simulations and the experimental IC79 test sample (a live time of 33.4 days). The solid lines in Fig. 2 represent the final selection criteria for IC79 where events above the lines constitute the final sample. The final selection criteria for the IC86 sample are

$$\log_{10}\mathrm{NPE} \geq \begin{cases} 4.8 & \cos\theta < 0.075 \\ 4.8 + 1.6\sqrt{1 - \left(\frac{1.0-\cos\theta}{0.925}\right)^2} & \cos\theta \geq 0.075. \end{cases} \tag{1}$$

The resulting neutrino effective areas, the equivalent area at Earth's surface in which neutrinos are detected with 100% efficiency, averaged over the two-year period from May 2010 to May 2012 taking into account the different detector configurations, is shown in Fig. 3. The analysis starts to be sensitive in the energy region around 1 PeV with its sensitivity rapidly increasing with energy. The effective area is larger for ν_e than ν_μ or ν_τ below 10 PeV showing the sensitivity of the present analysis to cascade events in this energy region.

The expected numbers of background events in the final sample for the 615.9 day live time from atmospheric muons and neutrinos from decays of pions and kaons are $0.038 \pm 0.004(\mathrm{stat})^{+0.021}_{-0.038}(\mathrm{syst})$ and $0.012 \pm 0.001(\mathrm{stat})^{+0.010}_{-0.007}(\mathrm{syst})$, respectively. Compared to previous analyses, the utilized atmospheric neutrino flux models [12] accommodate an improved parametrization of the primary cosmic ray spectrum and composition which accounts now for the "knee" in the cosmic ray spectrum. Adding prompt atmospheric neutrinos from decays of charmed mesons assuming the model in [13] with the improved cosmic ray spectrum modeling, the total number of background events increases to $0.082 \pm 0.004(\mathrm{stat})^{+0.041}_{-0.057}(\mathrm{syst})$. Theoretical

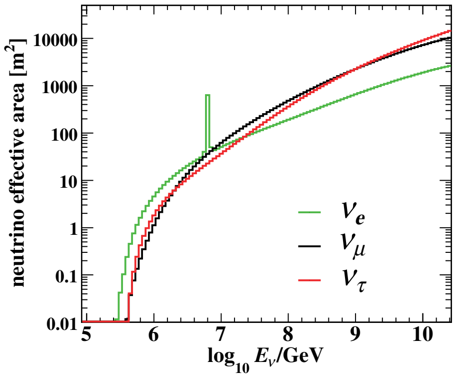

FIG. 3 (color online). The average neutrino effective area for a 4π isotropic flux, 615.9 days live time, and the IC79 and IC86 string configurations. Exposure of the sample used in this analysis is obtained by multiplying the effective area with the live time and 4π solid angle. The sharp peak for $\bar{\nu}_e$ is the Glashow resonance [24].

uncertainties in our baseline charmed-meson model [13] which uses perturbative-QCD calculations are included in the background estimation. Potential nonperturbative contributions, such as intrinsic charm in nuclei [14] or from the gluon density at small x, could lead to significantly larger cross sections and, hence, higher prompt neutrino fluxes. Preliminary IceCube limits on the prompt flux at 90% C.L. are a factor of 3.8 higher than the baseline model [15].

The main systematic uncertainties on the backgrounds are from the measurement of NPE and from uncertainties in the cosmic ray flux. They are estimated by varying the associated parameters in the simulation. The two dominant sources of experimental uncertainties are the absolute DOM sensitivity and the optical properties of the ice which contribute with (+ 43%, −26%) and (+ 0%, −42%), respectively. Uncertainties in the cosmic ray flux models are dominated by the primary composition (+ 0%, −37%) and the flux normalization (+ 19%, −26%). The theoretical uncertainty in the neutrino production from charm decay [13] relative to the total background is (+ 13%, −16%). The systematic uncertainties are assumed to be evenly distributed in the estimated allowed range and are summed in quadrature.

The atmospheric muon and neutrino background events are simulated independently. However, at higher energies, events induced by downward-going atmospheric neutrinos should also contain a significant amount of atmospheric muons produced in the same air shower as the neutrino [16]. Since these events are reconstructed as downward-going, they are more likely to be rejected with the higher NPE threshold in this region. Thus, the number of simulated atmospheric neutrino background events is likely overestimated here.

After unblinding 615.9 days of data, we observe two events that pass all the selection criteria. The hypothesis that the two events are fully explained by atmospheric

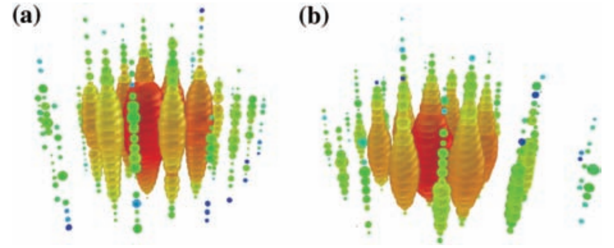

FIG. 4 (color online). The two observed events from (a) August 2011 and (b) January 2012. Each sphere represents a DOM. Colors represent the arrival times of the photons where red indicates early and blue late times. The size of the spheres is a measure for the recorded number of photoelectrons.

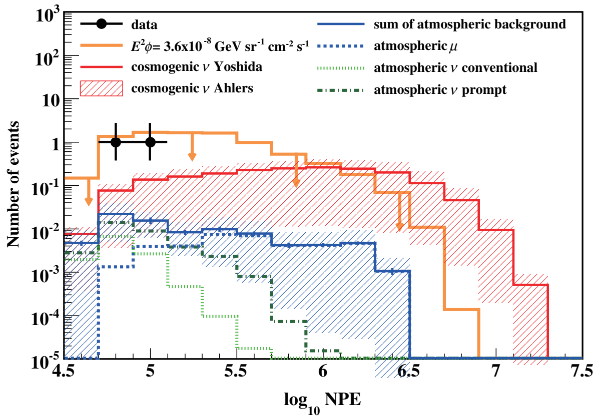

FIG. 5 (color online). NPE distributions for 615.9 days of live time at final selection level. The black points are the experimental data. The error bars on the data show the Feldman-Cousins 68% confidence interval [25]. The solid blue line marks the sum of the atmospheric muon (dashed blue), conventional atmospheric neutrino (dotted light green) and the baseline prompt atmospheric neutrino (dotted-dashed green) background. The error bars on the line and the shaded blue region are the statistical and systematic uncertainties, respectively. The red line represents the cosmogenic neutrino model [11]. The shaded region is the allowed level of the cosmogenic ν flux by Ahlers *et al.* [26]. The orange line represents an E^{-2} power-law flux up to an energy of 10^9 GeV with an all-flavor normalization of $E^2\phi_{\nu_e+\nu_\mu+\nu_\tau} = 3.6\times10^{-8}$ GeV sr^{-1} s^{-1} cm^{-2}, which is the integral upper limit obtained in a previous search in a similar energy range [9]. The signal fluxes are summed over all neutrino flavors, assuming a flavor ratio of ν_e:ν_μ:ν_τ = 1:1:1.

background including the baseline prompt atmospheric neutrino flux [13] has a p value of 2.9×10^{-3} (2.8σ). This value includes the uncertainties on the expected number of background events by marginalizing over a flat error distribution. While the prompt component has large theoretical uncertainties, obtaining two or more events with a probability of 10% would require a prompt flux that is about 15 times higher than the central value of our perturbative-QCD model. This contradicts our preliminary upper limit on the prompt flux [15]. Using an extreme prompt flux at the level of this upper limit, which covers a potential unknown contribution from intrinsic charm [17], yields a significance of 2.3σ.

The two events are shown in Fig. 4. They are from the IC86 sample, but would have also passed the selection criteria of the IC79 sample. Their spherical photon distributions are consistent with the pattern of Cherenkov photons from particle cascades induced by neutrino interactions within the IceCube detector. There are no indications for photons from incoming or outgoing muon or tau tracks. Hence, these events are most likely induced by either CC interactions of ν_e or NC interactions of ν_e, ν_μ, or ν_τ. CC interactions of ν_τ induce tau leptons with mean decay lengths of about 50 m at these energies [18]. The primary neutrino interaction and the secondary tau decay initiate separate cascades which, in a fraction of such events, lead to an observable double-peak structure in the recorded waveforms. The two events do not show a significant indication of such a signature. Figure 5 shows the final-selection NPE distributions for the experimental data, signal models, and background simulations. The two events are near the NPE threshold of the analysis and are consistent with a previous upper limit by IceCube [9] on an unbroken E^{-2} flux, while a flux corresponding to this upper limit predicts about 10 events above the NPE cut. The cosmogenic neutrino model [11] predicts an event rate of about 2 events in the corresponding live time but at significantly higher energies.

Maximum-likelihood methods are used to reconstruct the two events. The likelihood is the product of the Poisson probabilities to observe the recorded number of photoelectrons in a given time interval and DOM for a cascade hypothesis which depends on the interaction vertex, deposited energy and direction. Here, the time of the first hit mainly determines the vertex position and the recorded NPE plays a dominant role in estimating the deposited energy. The hit information used in the reconstruction is extracted from an unfolding procedure of the waveforms. The open circles in Fig. 1 indicate the strings closest to the reconstructed vertex positions. The reconstructed deposited energies of the two cascades are 1.04 and 1.14 PeV, respectively, with combined statistical and systematic uncertainties of $\pm15\%$ each. The errors on the deposited energies are obtained by simulating cascade events in the vicinity of the reconstructed energies and vertices. The study is specifically performed on each event and the larger of the two event uncertainties is cited for both events. Thus, the error associated with the two events differs from that of other cascade events observed in IceCube [19]. Since there is no absolute energy standard with adequate precision at these energies, the energy scale is derived from simulations based on measured ice properties and photomultiplier tube efficiencies which are assured by measurements of atmospheric muons. The main sources of systematic uncertainty on the

TABLE I. Characteristics of the two observed events. The depths of the reconstructed vertex positions "z" are with respect to the center of the IceCube detector at a depth of 1948 m.

Date (GMT)	August 8, 2011	January 3, 2012
NPE	7.0×10^4	9.6×10^4
Number of recorded DOMs	354	312
Reconstructed deposited energy (PeV)	1.04 ± 0.16	1.14 ± 0.17
Reconstructed z vertex (m)	122 ± 5	25 ± 5

reconstructed deposited energies are the absolute DOM sensitivity and the optical properties of the ice [20]. The effect of the latter is estimated to be +9% and −5% and is obtained by varying the scattering and absorption coefficients for the photon propagation by 10%. The reconstruction algorithm includes variations of the scattering and absorption coefficients with depth (ice layers) [21]. The effect of a possible azimuthal anisotropy of the ice parameters and a tilt of the ice layers on the reconstructed energies is estimated to be ±5%. The reconstructed energy depends linearly on the DOM efficiency, which has a 10% systematic uncertainty. The suppression of bremsstrahlung and pair production due to the Landau-Pomeranchuk-Migdal effect [22] is negligible in this energy range. The properties of the two observed events are summarized in Table I.

The reconstructed deposited energy is the energy of the incoming neutrino if the observed cascade is the result of a CC interaction of the ν_e neutrino, as in this case the total neutrino energy is deposited near the interaction vertex [23]. On the other hand, NC interactions of neutrinos of any flavor or interactions of $\bar{\nu}_e$ via the Glashow resonance at 6.3 PeV [24] with outgoing leptons induce cascades which carry only a fraction of the neutrino energy. The observed cascades are unlikely to originate from the Glashow resonance as only about 10% of these interactions will deposit 1.2 PeV or less in the detector in cascadelike signatures.

The two PeV neutrino events observed in two years of data taken with the IceCube neutrino telescope may be a first hint of an astrophysical high-energy neutrino flux. Given the yet rather moderate significance of 2.8σ with respect to the expected atmospheric background and the large uncertainties on its prompt component, a firm astrophysical interpretation requires more data in combination with analyses in other detection channels and energy ranges.

We acknowledge the support from the following agencies: U.S. National Science Foundation-Office of Polar Programs, U.S. National Science Foundation-Physics Division, University of Wisconsin Alumni Research Foundation, the Grid Laboratory Of Wisconsin (GLOW) grid infrastructure at the University of Wisconsin—Madison, the Open Science Grid (OSG) grid infrastructure; U.S. Department of Energy, and National Energy Research Scientific Computing Center, the Louisiana Optical Network Initiative (LONI) grid computing resources; Natural Sciences and Engineering Research Council of Canada, Compute Canada, and Compute West High Performance Computing; Swedish Research Council, Swedish Polar Research Secretariat, Swedish National Infrastructure for Computing (SNIC), and Knut and Alice Wallenberg Foundation, Sweden; German Ministry for Education and Research (BMBF), Deutsche Forschungsgemeinschaft (DFG), Helmholtz Alliance for Astroparticle Physics (HAP), Research Department of Plasmas with Complex Interactions (Bochum), Germany; Fund for Scientific Research (FNRS-FWO), FWO Odysseus programme, Flanders Institute to encourage scientific and technological research in industry (IWT), Belgian Federal Science Policy Office (Belspo); University of Oxford, United Kingdom; Marsden Fund, New Zealand; Australian Research Council; Japan Society for Promotion of Science (JSPS); the Swiss National Science Foundation (SNSF), Switzerland.

*Also at Physics Department, South Dakota School of Mines and Technology, Rapid City, South Dakota 57701, USA.

†Also at Los Alamos National Laboratory, Los Alamos, New Mexico 87545, USA.

‡Corresponding author.
aya@hepburn.s.chiba-u.ac.jp

§Also at Sezione INFN, Dipartimento di Fisica, I-70126 Bari, Italy.

‖Also at Department of Physics, Sungkyunkwan University, Suwon 440-746, Korea.

¶Also at NASA Goddard Space Flight Center, Greenbelt, Maryland 20771, USA.

[1] A. Achterberg *et al.* (IceCube Collaboration), Astropart. Phys. **26**, 155 (2006).

[2] R. Abbasi *et al.* (IceCube Collaboration), Astropart. Phys. **35**, 615 (2012).

[3] R. Abbasi *et al.* (IceCube collaboration), Nucl. Instrum. Methods Phys. Res., Sect. A **618**, 139 (2010).

[4] R. Abbasi *et al.* (IceCube collaboration), Nucl. Instrum. Methods Phys. Res., Sect. A **601**, 294 (2009).

[5] R. Abbasi *et al.* (IceCube Collaboration), Phys. Rev. D **82**, 072003 (2010).

[6] J. Ahrens *et al.*, Nucl. Instrum. Methods Phys. Res., Sect. B **524**, 169 (2004).

[7] P. Huber, *Robust Statistics* (Wiley, New York, 1981).

[8] M. Wellons *et al.*, Proceedings of the 33rd International Cosmic Ray Conference (ICRC2013) (2013) (to be published).
[9] R. Abbasi *et al.* (IceCube Collaboration), Phys. Rev. D **83**, 092003 (2011).
[10] G. Hill and K. Rawlins, Astropart. Phys. **19**, 393 (2003).
[11] S. Yoshida and M. Teshima, Prog. Theor. Phys. **89**, 833 (1993), the model with the source evolution $(z_{\max} + 1)^m$ with $m = 4$ extending to $z_{\max} = 4.0$.
[12] T. K. Gaisser, Astropart. Phys. **35**, 801 (2012).
[13] R. Enberg, M. H. Reno, and I. Sarcevic, Phys. Rev. D **78**, 043005 (2008).
[14] S. Brodsky, P. Hoyer, C. Peterson, and N. Sakai, Phys. Lett. **93B**, 451 (1980).
[15] A. Schukraft (IceCube Collaboration), arXiv:1302.0127.
[16] S. Schönert, T. K. Gaisser, E. Resconi, and O. Schulz, Phys. Rev. D **79**, 043009 (2009).
[17] M. Thunman, G. Ingelman, and P. Gondolo, Astropart. Phys. **5**, 309 (1996).
[18] D. Cowen (IceCube Collaboration), J. Phys. Conf. Ser. **60**, 227 (2007).
[19] R. Abbasi *et al.* (IceCube Collaboration), Phys. Rev. D **84**, 072001 (2011).
[20] M. Aartsen *et al.*, Nucl. Instrum. Methods Phys. Res., Sect. B **711**, 73 (2013).
[21] J. Lundberg, P. Miočinović, K. Woschnagg, T. Burgess, J. Adams, S. Hundertmark, P. Desiati, and P. Niessen, Nucl. Instrum. Methods Phys. Res., Sect. A **581**, 619 (2007).
[22] L. Gerhardt and S. R. Klein, Phys. Rev. D **82**, 074017 (2010).
[23] The energy reconstruction assumes that all light emission originates from an electromagnetic shower. A hadronic cascade with the same light yield as the observed events would, on average, have about 10% higher energy.
[24] S. L. Glashow, Phys. Rev. **118**, 316 (1960).
[25] G. J. Feldman and R. D. Cousins, Phys. Rev. D **57**, 3873 (1998).
[26] M. Ahlers, L. A. Anchordoqui, M. Gonzalez-Garcia, F. Halzen, and S. Sarkar, Astropart. Phys. **34**, 106 (2010).

Constraints on the origin of the ultrahigh energy cosmic rays using cosmic diffuse neutrino flux limits: An analytical approach

Shigeru Yoshida* and Aya Ishihara†

Department of Physics, Graduate School of Science, Chiba University, Chiba 263-8522, Japan

(Received 12 January 2012; published 15 March 2012)

Astrophysical neutrinos are expected to be produced in the interactions of ultrahigh energy cosmic rays with surrounding photons. The fluxes of the astrophysical neutrinos are highly dependent on the characteristics of the cosmic-ray sources, such as their cosmological distributions. We study possible constraints on the properties of cosmic-ray sources in a model-independent way using experimentally obtained diffuse neutrino flux above 100 PeV. The semianalytic formula is derived to estimate the cosmogenic neutrino fluxes as functions of source evolution parameter and source extension in redshift. The obtained formula converts the upper limits on the neutrino fluxes into the constraints on the cosmic-ray sources. It is found that the recently obtained upper limit on the cosmogenic neutrinos by IceCube constrains the scenarios with strongly evolving ultrahigh energy cosmic-ray sources, and the future limits from a 1 km^3 scale detector are able to further constrain the ultrahigh energy cosmic-rays sources with evolutions comparable to the cosmic star formation rate.

DOI: 10.1103/PhysRevD.85.063002 PACS numbers: 98.70.Sa, 95.75.Pq, 95.85.Ry

I. INTRODUCTION

The origin of the ultrahigh energy cosmic rays (UHECRs) has been a long-standing important question in astrophysics. While the observations by Auger [1,2] and HiRes [3] indicate that cosmic rays with energies above $\sim 10^{18.5}$ eV are of extragalactic origin, identification of astronomical objects responsible for the UHECR emission has not been achieved. Neutrinos, secondarily produced by UHECR nucleons, are expected to provide direct information on the UHECR origin, since a neutrino penetrates over cosmological distance without being deflected by the cosmic magnetic field nor absorbed by the photon field. The "cosmogenic" neutrinos [4] are produced by the collisions of UHECR nucleons with the cosmic microwave background (CMB) photon via photo-produced π meson decay as $\pi^\pm \to \mu^\pm \nu_\mu \to e^\pm \nu_e \nu_\mu$, known as the Greisen-Zatsepin-Kuzmin (GZK) mechanism [5]. The intensity of cosmogenic neutrinos indicates redshift distributions of the parent UHECR sources [6,7] in the Universe. The source distributions derived from the cosmogenic neutrino intensities can then be compared with distributions of known classes of the astronomical objects possibly responsible for the UHECR emissions. Therefore reliable extractions of the UHECR source distribution function (SDF) is one of the key issues in cosmogenic diffusive neutrino searches. Constraints on the sources of UHECRs derived from the measurements or upper limits of the ultrahigh energy neutrino flux are highly complimentary to the constraints from the diffuse photon flux [8,9], because the former does not rely on uncertain estimation of extragalactic background light (EBL).

*syoshida@hepburn.s.chiba-u.ac.jp
†aya@hepburn.s.chiba-u.ac.jp

In this work, we develop a method to bound the UHECR source evolution and its redshift dependence in a comprehensive way without introducing specific astronomical models. We derive an analytical formula to calculate intensities of the neutrinos produced by the GZK mechanism in the range between 100 PeV and 10 EeV. Using the formula, we extract the relation among the neutrino intensity and the UHECR SDF parameters. The use of the analytical formula allows us to calculate neutrino intensities in the full phase space of the source evolution parameters without an intensive computational task. The analytical formula can also be used as a practical tool to approximately calculate cosmogenic GZK neutrino intensity with given UHECR SDF, for example, for the performance studies of the future detectors such as KM3NET [10]. Finally we present model-independent constraints on the UHECR sources using the obtained formula with the upper limit [11] and the future sensitivity [12] on the cosmogenic neutrino detection by the IceCube neutrino observatory [13].

The standard cosmology with $H_0 \simeq 73.5\,\mathrm{km\,sec^{-1}\,Mpc^{-1}}$, $\Omega_M = 0.3$, and $\Omega_\Lambda = 0.7$ [14] is assumed throughout the paper.

II. ANALYTICAL FORMULA FOR ESTIMATING COSMOGENIC ν INTENSITY

The neutrino flux per unit energy, dJ_ν/dE_ν, is generally written as

$$\frac{dJ_\nu}{dE_\nu} = n_0 c \int_0^{z_{\max}} \psi(z_s) \left|\frac{dt}{dz}(z_s)\right| dz_s \int_0^{z_s} \left|\frac{dt}{dz}(z_\nu)\right| dz_\nu \times \int_{E_\nu}^{\infty} \frac{dN_{p\to\nu}}{dE_\nu^g dt^g}(z_\nu, z_s)\delta(E_\nu^g - (1+z_\nu)E_\nu)dE_\nu^g. \quad (1)$$

The first integral represents the total contribution of UHECR sources in the redshift up to $z_{\max}$, where $z_{\max}$ is the maximum redshift of the UHECR source distribution or, in other words, the time of the first UHECR emission in the Universe. $\psi(z_s)$ represents the cosmic evolution of the spectral emission rate per comoving volume and n_0 is the number density of UHECR sources at the present Universe. The relation between time and redshift is given as

$$|\frac{dt}{dz}(z_s)| \equiv |\frac{dt_s}{dz_s}| = [H_0(1+z_s)\sqrt{\Omega_M(1+z_s)^3+\Omega_\Lambda}]^{-1}.$$

The second integral calculates the total neutrino flux expected from a single UHECR source at redshift z_s generated via UHECR interactions at redshift $z_\nu(\leq z_s)$. $dN_{p\to\nu}/dE_\nu^g dt^g$ is the yield of generated neutrinos with energy of E_ν^g per unit time in the UHECR laboratory frame (the CMB rest frame). Suffixes s and g represent the quantities at the positions of UHECR sources and neutrino generation, respectively. The delta function indicates the neutrino energy loss due to the expansion of the Universe.

The neutrino yield, $dN_{p\to\nu}/dE_\nu^g dt^g$, at redshift z_ν by the GZK mechanism is expressed by a convolution of the UHECR intensity from a source at z_s, the CMB photon density, and the photo-pion interaction kinematics as

$$\frac{dN_{p\to\nu}}{dE_\nu^g dt^g} = \int dE_{\mathrm{CR}}\frac{dN_{\mathrm{CR}}}{dE_{\mathrm{CR}}}(z_s, z_\nu)c\int ds \times \int dE_\pi \frac{d\sigma_{\gamma p}}{dE_\pi}\frac{d\rho_{\pi\to\nu}}{dE_\nu^g}\frac{dn_\gamma}{ds}, \tag{2}$$

where $dN_{\mathrm{CR}}/dE_{\mathrm{CR}}$ is the number of UHECRs per unit time and energy at the redshift z_ν originating from a source at z_s, and s is the Lorentz-invariant Mandelstam variable, the square of invariant mass of the cosmic-ray nucleon and the target CMB photon. $\sigma_{\gamma p}$ is the photo-pion production cross section, $d\rho_{\pi\to\nu}/dE_\nu^g$ is the energy distribution of neutrinos from the photo-produced pion, and dn_γ/ds is the CMB photon number density in the UHECR frame per unit s.

We introduce the following approximations to simplify the calculations: (1) the contribution of UHECR colliding with infrared and optical universal photon (IR/O) backgrounds is negligible and only the contribution of photo-pion production cross section from Δ resonance is considered in collisions of UHECRs and CMB photons, and (2) the kinematics of the photo-pion production is represented by a single pion production. The first approximation allows the photon number density dn_γ/ds to be analytically obtained with the modification to the black-body distribution [6]. The contribution of neutrinos induced by UHECR interactions with IR/O becomes sizable only in the energy region below 100 PeV [15] while the effect is small in the higher energy region. Similarly the neutrinos from photo-produced pions outside the Δ resonance are mostly visible only in the lower energy range below 100 PeV [16], and the single pion production is the most dominant channel in the Δ resonance. The Δ-resonance approximation simplifies the integral on s in Eq. (2) to a multiplication of the integrand at $s = s_R(\simeq 1.5\ \mathrm{GeV}^2)$, where s_R is the Lorentz-invariant Mandelstam variable at the Δ resonance, and $\Delta s_R(\simeq 0.6\ \mathrm{GeV}^2)$, the width of the Δ resonance. The second approximation then gives [17]

$$\frac{d\rho_{\pi\to\nu}}{dE_\nu^g} \simeq \frac{1}{E_\pi}\frac{3}{1-r_\pi}, \tag{3}$$

where $r_\pi = m_\mu^2/m_\pi^2 \simeq 0.57$ is the muon-to-pion mass squared ratio. The factor three arises from the fact that three neutrinos are produced from the π meson and μ lepton decay chain. The allowed range of E_ν^g due to the kinematics is given by

$$0 \leq \frac{E_\nu^g}{E_\pi} \leq 1 - r_\pi, \tag{4}$$

where neutrino mass is neglected. With a good approximation that a single pion is isotropically emitted in the center-of-momentum frame, one obtains

$$\frac{d\sigma_{\gamma p}}{dE_\pi} = \frac{1}{E_{\mathrm{CR}}}\frac{d\sigma_{\gamma p}}{dx_\pi} \simeq \frac{1}{E_{\mathrm{CR}}}\frac{\sigma_{\gamma p}}{x^+ - x^-}, \tag{5}$$

where $x_\pi \equiv E_\pi/E_{\mathrm{CR}}$ is the relative energy of emitted pion normalized by the parent proton energy E_{CR}. $x^\pm$ are the maximal and minimal bound of x_π due to the kinematics and given by

$$x^\pm = \frac{s+m_\pi^2-m_p^2}{2s} \pm \frac{\sqrt{(s+m_\pi^2-m_p^2)^2-4sm_\pi^2}}{2s}, \tag{6}$$

where m_p is the proton mass.

Then we obtain the neutrino yield, Eq. (2), expressed as an analytical function with only a single energy integral,

$$\begin{aligned}\frac{dN_{p\to\nu}}{dE_\nu^g dt^d} \simeq & \frac{k_{\mathrm{B}}T(1+z_\nu)}{8\pi^2\hbar^3c^2}(s_R-m_p^2)\sigma_{\gamma p}^R \\ & \times \frac{s_R\Delta s_R}{\sqrt{(s_R+m_\pi^2-m_p^2)^2-4s_Rm_\pi^2}}\frac{3}{1-r_\pi} \\ & \times \int dE_{\mathrm{CR}}\frac{1}{E_{\mathrm{CR}}^3}\frac{dN_{\mathrm{CR}}}{dE_{\mathrm{CR}}} \\ & \times \ln\left(\frac{x_R^+}{\xi_R}\right)\{-\ln(1-e^{-(E_\Delta)/(1+z_\nu)E_{\mathrm{CR}}})\}.\end{aligned} \tag{7}$$

Here k_{B} is the Boltzmann constant, T is present temperature of the CMB. $E_\Delta \equiv (s_R - m_p^2)/4k_BT$ corresponds to the energy of UHECR protons colliding via Δ resonance at the present Universe. Suffix R denotes the values at the Δ resonance in the photo-pion reaction. For example, $\sigma_{\gamma p}^R = 2.1\times 10^{-28}\ \mathrm{cm}^2$ represents the photo-pion production cross section of channel $\gamma p \to n\pi^+$ at the Δ resonance and $x_R^\pm$ is given by Eq. (6) with $s = s_R$.

The parameter ξ_R reflects the kinematics bounds, Eqs. (4) and (6), and is defined by

$$\xi_R = \begin{cases} x_R^- & E_\nu^g \leq (1 - r_\pi) x_R^- E_{\rm CR}, \\ \frac{E_\nu^g}{(1-r_\pi)E_{\rm CR}} & \text{otherwise.} \end{cases} \tag{8}$$

$dN_{\rm CR}/dE_{\rm CR}$ is calculated by the energy loss formula with the continuous energy loss approximation [18] represented by

$$-\frac{dE_{\rm CR}}{cdt} = \frac{(1+z)^3}{\lambda_{\rm GZK}(E_{\rm CR}(1+z))} E_{\rm CR}, \tag{9}$$

where $\lambda_{\rm GZK}$ is the energy attenuation length governed by the GZK mechanism, mainly due to the photo-pion production of UHECRs and the CMB. The factor $(1+z)^3$ accounts for the increase of CMB photon number density with redshift z.

Here we introduce the final approximation that the energy attenuation length of UHECR by the GZK mechanism, $\lambda_{\rm GZK}$, is constant with energies above $E_{\rm GZK} \equiv 10^{20}$ eV. While $\lambda_{\rm GZK}$ rapidly decreases with cosmic-ray energy increase, it becomes a slight increase or constant above $\sim 3 \times 10^{20}$ eV for $z_\nu \sim 0$. Neutrinos from $z_\nu \gtrsim 1$ are the dominant contribution to the cosmogenic neutrino intensity at Earth and the turnover energy is shifted to lower energies $\lesssim E_{\rm GZK}$ due to the redshift effects for the Universe of $z_\nu \gtrsim 1$ [19]. Therefore this approximation reasonably describes the UHECR energy loss profile to calculate the neutrino yield. Assuming that the primary UHECR spectrum from a source at z_s follows the power law described by $dN_{\rm CR}(z_s, z_s)/dE_{\rm CR} = \kappa_{\rm CR}(E_{\rm CR}/E_{\rm GZK})^{-\alpha}$ up to $E_{\rm max}$, the maximal injected energy from a source, then the $dN_{\rm CR}(z_s, z_\nu)/dE_{\rm CR}$ is analytically obtained by

$$\frac{dN_{\rm CR}}{dE_{\rm CR}}(z_s, z_\nu) = \kappa_{\rm CR}\left(\frac{E_{\rm CR}}{E_{\rm GZK}}\right)^{-\alpha} \times e^{-(\alpha-1)(c/\lambda_{\rm GZK}H_0)(2/3\Omega_M)\{f(z_s)-f(z_\nu)\}}, \tag{10}$$

where $f(z) \equiv \sqrt{\Omega_M(1+z)^3 + \Omega_\Lambda}$ and $\kappa_{\rm CR}$ is a normalization constant. With Eq. (10), the energy integral on $E_{\rm CR}$ in Eq. (7) becomes an addition of integrals in the forms of $\int dy y^{-(\alpha+3)} \ln(1 - e^{-1/y})$ and $\int dy y^{-(\alpha+3)} \ln(1 - e^{-1/y}) \ln y$. An asymptotic approximation with numerical constants is found to provide approximate solutions of these integrals. The final formula of the neutrino yield is then obtained as

$$\begin{aligned} \frac{dN_{p\to\nu}}{dE_\nu^g dt^g} = {}& \kappa_{\rm CR} \frac{k_{\rm B}T}{8\pi^2\hbar^3c^2} \frac{(s_R - m_p^2)}{E_{\rm GZK}^2}\left(\frac{E_\Delta}{E_{\rm GZK}}\right)^{-(\alpha+2)} \sigma_{\gamma p}^R \\ & \times \frac{s_R \Delta s_R}{\sqrt{(s_R + m_\pi^2 - m_p^2)^2 - 4 s_R m_\pi^2}} \frac{3}{1 - r_\pi}(1+z_\nu)^{\alpha+3} \\ & \times e^{-(\alpha-1)(c/\lambda_{\rm GZK}H_0)(2/3\Omega_M)\{f(z_s)-f(z_\nu)\}} \\ & \times \left\{\epsilon_0 x_0^{-(\alpha+1)} e^{-2} \ln\left(\frac{x_R^+}{x_R^-}\right) + \epsilon_1 x_1^{-(\alpha+3)} e^{-1/x_1} \right. \\ & \left. \times e^{-2} \ln\left(x_1 \frac{E_\Delta}{E_\nu^g(1+z_\nu)} x_R^-(1 - r_\pi)\right)\right\}, \end{aligned} \tag{11}$$

where $x_0 = 0.275$, and $x_1 = 0.16$ are the empirically determined numerical constants. ϵ_0 and ϵ_1 are either unity or null, depending on neutrino energy. These are consequences of the kinematics bound for pions and neutrinos, Eq. (8), and given by

$$\epsilon_0 = \begin{cases} 1 & E_\nu^g(1+z_\nu) \leq x_1 E_\Delta x_R^+(1 - r_\pi), \\ 0 & \text{otherwise,} \end{cases} \tag{12}$$

and

$$\epsilon_1 = \begin{cases} 0 & E_\nu^g(1+z_\nu) \leq x_1 E_\Delta x_R^-(1-r_\pi), \\ 1 & x_1 E_\Delta x_R^-(1-r_\pi) \leq E_\nu^g(1+z_\nu) \leq x_1 E_\Delta x_R^+(1-r_\pi), \\ 0 & \text{otherwise.} \end{cases} \tag{13}$$

One can also find that $x_1 E_\Delta x_R^\pm(1 - r_\pi)$ in these equations represents the effective energy of neutrinos from decay of the pions with kinematically allowed maximum (x_R^+) and minimum (x_R^-) energies from Δ resonance in the γp collision. The $E_\nu^g(1+z_\nu) = E_\nu(1+z_\nu)^2$ factor reflects the redshift dependence of the CMB temperature and the redshift energy loss of neutrinos at z_ν.

Equation (1) with the Eq. (11) finally give the cosmogenic neutrino flux with double integrals of redshift z_s and z_ν. The z_ν integral is analytically solvable neglecting $O((\lambda_{\rm GZK}H_0/c)^2)$ or higher order terms because the energy attenuation length is much shorter than the cosmological time dimension. Then the final form of the cosmogenic neutrino intensity is obtained as

$$\begin{aligned} \frac{dJ_\nu}{dE_\nu} = {}& (\alpha - 1) F_{\rm CR} \frac{c}{H_0} \frac{k_{\rm B}T}{8\pi^2\hbar^3c^3} \frac{(s_R - m_p^2)}{E_{\rm GZK}^3}\left(\frac{E_\Delta}{E_{\rm GZK}}\right)^{-(\alpha+2)} \sigma_{\gamma p}^R \\ & \times \frac{s_R \Delta s_R}{\sqrt{(s_R + m_\pi^2 - m_p^2)^2 - 4 s_R m_\pi^2}} \frac{3}{1 - r_\pi} \zeta. \end{aligned} \tag{14}$$

Here $F_{\rm CR}$ represents the UHECR intensity above $E_{\rm GZK}$ and described by

$$\begin{aligned} F_{\rm CR} = {}& \int_{E_{\rm GZK}}^{E_{\rm max}} dE_{\rm CR} n_0 c \int_0^{z_{\rm max}} \psi(z_s) \left|\frac{dt}{dz}(z_s)\right| dz_s \frac{dN_{\rm CR}}{dE_{\rm CR}}(z_s, 0) \\ & \simeq n_0 \kappa_{\rm CR} E_{\rm GZK} \lambda_{\rm GZK}/(\alpha - 1)^2 \end{aligned} \tag{15}$$

assuming that $E_{\rm max} \gg E_{\rm GZK}$. $F_{\rm CR}$ gives the normalization of the neutrino flux in the present formulation in Eq. (14). It can be estimated by the observational data for actual calculation.

ζ in Eq. (14) is the term which accounts for the redshift dependence and is given by

$$\begin{aligned} \zeta = {}& \int_0^{z_{\rm max}} dz_s \frac{(1+z_s)^{(m+\alpha-1)}}{\sqrt{\Omega_M(1+z_s)^3 + \Omega_\Lambda}} \left\{\epsilon_0 x_0^{-(\alpha+1)} e^{-2} \ln\left(\frac{x_R^+}{x_R^-}\right)\right. \\ & \left. + \epsilon_1 x_1^{-(\alpha+3)} e^{-1/x_1} e^{-2} \ln\left(x_1 \frac{E_\Delta}{E_\nu(1+z_s)^2} x_R^-(1 - r_\pi)\right)\right\}, \end{aligned} \tag{16}$$

where ϵ_0 and ϵ_1 are obtained by Eqs. (12) and (13), respectively, replacing z_ν by z_s. The cosmic evolution function $\psi(z_s)$ is now parametrized as $(1+z_s)^m$ such that the parameter m represents the "scale" of the cosmic evolution often used in the literature [20]. The integral on z_s in Eq. (16) is analytically solvable when we use the fact that $\sqrt{\Omega_M(1+z_s)^3+\Omega_\Lambda} \gg \Omega_\Lambda$ in most of the integral range. Finally we obtain the final form of the redshift-dependent part of the analytical formula ζ as

$$\zeta = e^{-2}\frac{1}{\gamma_m}\Omega_M^{-((\alpha+m)/(3))}\Bigg\{(\Omega_M(1+z_{\rm up})^3+\Omega_\Lambda)^{\gamma_m/3}\Bigg(x_0^{-(\alpha+1)}\ln\Bigg(\frac{x_R^+}{x_R^-}\Bigg)+x_1^{-(\alpha+3)}e^{-(1/x_1)}\Bigg[\ln\Bigg(x_1\frac{E_\Delta}{E_\nu(1+z_{\rm up})^2}x_R^-(1-r_\pi)\Bigg)+\frac{2}{\gamma_m}\Bigg]\Bigg)$$
$$-(\Omega_M+\Omega_\Lambda)^{\gamma_m/3}x_0^{-(\alpha+1)}\ln\Bigg(\frac{x_R^+}{x_R^-}\Bigg)-(\Omega_M(1+z_{\rm down})^3+\Omega_\Lambda)^{\gamma_m/3}x_1^{-(\alpha+3)}e^{-(1/x_1)}\Bigg[\ln\Bigg(x_1\frac{E_\Delta}{E_\nu(1+z_{\rm down})^2}x_R^-(1-r_\pi)\Bigg)+\frac{2}{\gamma_m}\Bigg]\Bigg\} \tag{17}$$

where $\gamma_m \equiv (\alpha+m)-3/2$. $z_{\rm up}$ and $z_{\rm down}$ are the maximum and minimum bounds of the redshifts, respectively. These redshift bounds are associated with $z_{\rm max}$ in Eq. (1) but also depend on neutrino energies E_ν due to kinematics of π decay and the redshift energy loss. $z_{\rm up}$ is given by

$$1+z_{\rm up} = \begin{cases} 1 & x_1E_\Delta x_R^+(1-r_\pi) \le E_v, \\ \left(\frac{x_1E_\Delta}{E_v}x_R^+(1-r_\pi)\right)^{1/2} & \frac{x_1E_\Delta x_R^+(1-r_\pi)}{(1+z_{\rm max})^2} \le E_v \le x_1E_\Delta x_R^+(1-r_\pi), \\ 1+z_{\rm max} & E_v \le \frac{x_1E_\Delta x_R^+(1-r_\pi)}{(1+z_{\rm max})^2}. \end{cases} \tag{18}$$

$z_{\rm down}$ is also given by Eq. (18) replacing x_R^+ by x_R^-.

See Appendix B for the case of the astronomical objects of which cosmological evolution become constant above a certain redshift (see Ref. [21], for example).

III. VALIDITY OF THE ANALYTICAL FORMULA

The analytical formula for estimating cosmogenic neutrino fluxes [see Eqs. (14), (17), and (18)] is derived under several assumptions. Here we demonstrate the applicability of the formula in estimating neutrino flux in 100 PeV $\lesssim E_\nu \lesssim$ 10 EeV which is the main energy range of several cosmogenic neutrino searches [11,22]. In Table I, the cosmogenic neutrino integral flux above 1 EeV obtained by the analytical formula with $\alpha = 2.5$ is presented. We use the UHECR intensity $F_{\rm CR}(\ge E_{\rm GZK}) = 2.96 \times 10^{-21}\ {\rm cm^{-2}\,sec^{-1}\,sr^{-1}}$ in the present study, which is obtained from the measurement of the HiRes experiment [3]. The fluxes obtained by the full numerical calculations with the same or comparable source evolution parameters are also listed for comparison. The values in each parameter subset show an agreement within a factor of 2 for a comparable evolution scenario in the wide range of parameter numbers.

Figure 1 presents the neutrino fluxes obtained with the present analytical estimation and the full-blown numerical calculations. The fluxes calculated with the different techniques show the best agreement at ~1 EeV, the central energy in the cosmogenic neutrino search with IceCube [11]. The present formula provides a reasonable estimate of the neutrino flux from 100 PeV to 10 EeV with uncertainty of factor of ~2. Some deviations in the analytical formula from the full-blown numerical calculations arise mainly from the uncertainty in the intensity of the extragalactic UHECR component allowed by the observed UHECR spectrum, and the accuracy of the approximations used in derivation of the analytical formula. We discuss these issues in Sec. V.

TABLE I. Cosmogenic neutrino fluxes predicted by the model-dependent full numerical calculations and those given by the present analytical formula with the corresponding parameters on source evolution. The numbers by the full calculations were converted to be the sum over all three neutrino flavors from the original when appropriate.

ν flux model	Integral flux F ($E_\nu \ge 1$ EeV) [${\rm cm^{-2}\,sec^{-1}\,sr^{-1}}$]
Yoshida and Teshima [6]	
$m = 2.0$, $z_{\rm max} = 2.0$	5.39×10^{-18}
Ahlers *et al.* [9]	
$m = 2.0$, $z_{\rm max} = 2.0$	1.85×10^{-18}
("the minimal case")	
The analytical formula	
$m = 2.0$, $z_{\rm max} = 2.0$	4.91×10^{-18}
Kotera *et al.*[15]	
SFR1	1.07×10^{-17}
The analytical formula	
$m = 3.4 (z \le 1.0)$	
const. $(1 \le z \le 4)$	1.07×10^{-17}
Ahlers *et al.* [9]	
$m = 4.6$, $z_{\rm max} = 2.0$	3.39×10^{-17}
("the best fit")	
The analytical formula	
$m = 4.6$, $z_{\rm max} = 2.0$	4.09×10^{-17}
Kalashev *et al.* [23]	
$m = 5.0$, $z_{\rm max} = 3.0$	7.38×10^{-17}
The analytical formula	
$m = 5.0$, $z_{\rm max} = 3.0$	8.42×10^{-17}
Kotera *et al.* [15]	
Faranoff-Riley type II	6.74×10^{-17}
The analytical formula	
$m = 5.02 (z \le 1.5)$	
const $(1.5 \le z \le 2.5)$	5.21×10^{-17}

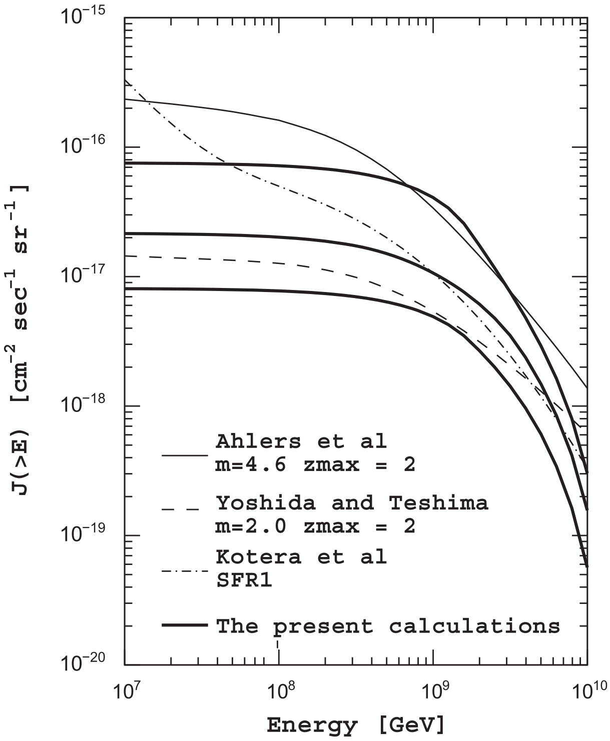

FIG. 1. Integral neutrino fluxes, J [cm^{-2} sec^{-1} sr^{-1}], as a function of neutrino energy. Bold lines represent the present analytical estimates and thin lines represent corresponding predictions by the full numerical calculations [9] or the Monte-Carlo simulations [6,15].

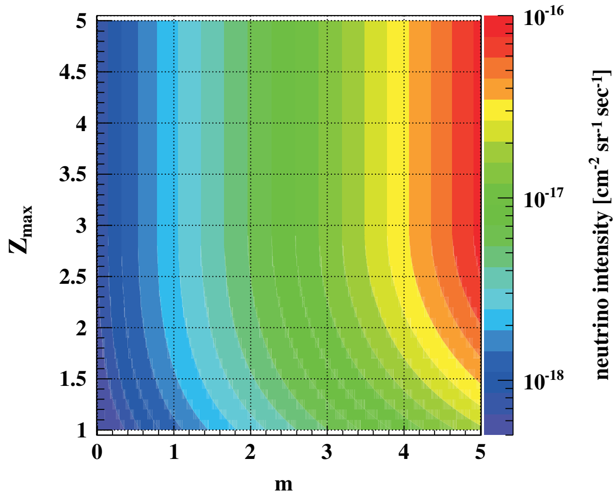

FIG. 2 (color online). Integral neutrino fluxes with energy above 1 EeV, J [cm^{-2} sec^{-1} sr^{-1}], on the plane of the source evolution parameters, m and $z_{\max}$.

IV. RESULTS

A. The relation between the ν flux and the cosmological evolution of the sources

Shown in Fig. 2 is the distribution of the cosmogenic neutrino integral fluxes with energies above 1 EeV in the parameter space of the evolution of UHECR sources (m, $z_{\max}$) calculated using the derived analytical formula. The fluxes vary by more than an order of magnitude with the evolution parameters. The distribution demonstrates that the neutrino intensity can indeed be an observable to imply the characteristics of the UHECR sources. The plot shows that cosmogenic neutrino flux around 1 EeV is mostly determined by source emissivity history up to redshift of $z_s \sim 3$. This is because the contributions of sources at $z_s \gtrsim 3$ represent only a small fraction of the total flux due to the redshift dilution [15].

B. Constraints on UHECR origin with the IceCube diffuse neutrino flux limit

Here we estimate the expected event rates with the IceCube neutrino observatory by using the derived analytical formula. The analytical function is valid in the IceCube cosmogenic neutrino detection energy range distributed around 1 EeV [11]. Convolution of Eq. (14) with the IceCube neutrino effective area [11,12] gives the event rate for the entire phase space of the evolution parameter m and the maximal redshift $z_{\max}$. Full mixing in the standard neutrino oscillation scenario is assumed and the intensity of neutrinos of each of three neutrino flavors corresponds to one third of the estimated neutrino intensity by the analytical function. The Feldman-Cousins upper bound [24] then defines the excluded region on the $m - z_{\max}$ plane at a given confidence level. Figure 3 displays the resultant constraints. The shaded region represents the factor of 2 uncertainty in the analytical estimation discussed in the previous section. The upper limit with the IceCube 2008–2009 data [11] has already started to constrain hypotheses of UHECR sources with strong evolution of $m \gtrsim 4.5$. While this bound may be still weaker than that by the Fermi diffuse γ-ray flux measurement [9], nevertheless the limit by neutrinos is important because the neutrino estimate does not involve the uncertainties of the assumptions of $E_{\max}$ nor the EBL intensity. The full IceCube five-year observation would certainly probe the most interesting region of the source evolution phase space where the strong candidates for the UHECR sources of the powerful astronomical objects such as radio galaxies and gamma-ray bursts are included.

V. DISCUSSION

The derived analytical formula to calculate intensities of the neutrinos produced by the GZK mechanism in the range between 100 PeV and 10 EeV is used to constrain the cosmological evolution of the UHECR sources.

The largest uncertainty in the present analytical formula at the lower energy range ($E_\nu \ll 1$ EeV) is due to the omission of the IR contribution to the cosmogenic neutrino production. Photo-produced pions from the UHECR

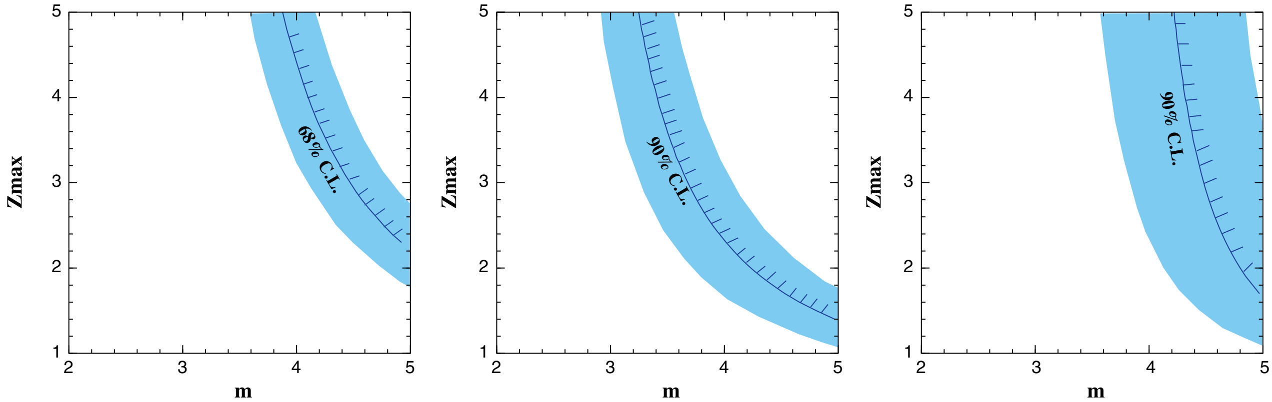

FIG. 3 (color online). Constraints on the UHECR source evolution m and $z_{\max}$ with the IceCube 2008–2009 flux limit [11] (left) and with the full IceCube five-year sensitivity [12] (middle). The areas above the solid lines are excluded by null detection of ν events. The shaded belts represent uncertainties in the present analytical estimation. The right panel shows the full IceCube five-year constraint when the emission rate per comoving volume becomes constant above z_s of 1.0. Excluded region at 68% confidence level (corresponding to $\simeq 1.1$ events assuming the same background rate of the IceCube 2008–2009 measurement [11]) and 90% confidence level ($\simeq 2.2$ events) is displayed.

interactions with the IR background are the major origin of neutrinos with energies below 10 PeV, however, the IR contribution is relatively minor in the higher energies where we mainly discuss the aspect of cosmogenic neutrino detection by IceCube. The amount of the IR contribution was studied, for example, in the calculations in Refs. [9,15]. The study in the latter reference exhibits much higher contribution of the IR background than in the former reference, where the effect is suppressed mainly due to the introduction of the minimal energy of extragalactic UHECR population. These differences can be seen in Fig. 1; the low energy component in Ref. [15] is substantially emphasized compared to the other calculations. These variations in the estimation of the IR contribution to the cosmogenic neutrino intensities are considered to be an additional uncertainty to the IR background yield itself, which is also not firmly understood [19,25]. Here we would like to emphasize that the omission of the IR background leads to a conservative constraint on the UHECR source evolution.

The second largest uncertainty is concerned with $F_{\rm CR}$, the UHECR intensity above $E_{\rm GZK} \simeq 10^{20}$ eV. The works in Refs. [9,26] allowed a sizable variation in the UHECR intensity within 99% confidence level of the statistical test against the observed data. This indicates that an extreme case of the UHECR intensity may lead to a large departure from the present estimate of the neutrino fluxes. For instance, the difference of their estimate for the scenario of $(m, z_{\max}) = (2, 2)$ found in Table I arises from their assumption of very steep UHECR spectrum leading to a minimal $F_{\rm CR}$ estimation. This uncertainty is, however, expected to be reduced in the future when the statistical uncertainties in the observations of UHECRs and/or the systematic uncertainty in the energy estimation are improved.

We would like to also emphasize that the neutrino intensity below 10 EeV is not largely affected by the detailed behavior of UHECR proton propagation in extragalactic space. This is because these neutrinos are mostly generated at cosmological distances which are substantially longer than the UHECR proton energy attenuation length in the CMB field. It is also suggested by no explicit dependence of $\lambda_{\rm GZK}$ in the final formula Eq. (14). This is related to the fact that the cosmogenic flux below 10 EeV is relatively insensitive to $E_{\max}$ and α, the maximal injection energy of UHECR protons from their sources and the spectral index of UHECR spectrum, respectively, while the flux above 10 EeV is sensitive to those parameters [6,19,23]. A scan of the parameter spaces of the cosmogenic neutrino sources for some known classes of astronomical objects with a numerical Monte-Carlo method was made in Refs. [15,19]. It was also shown that the intensity around 1 EeV is stable against $E_{\max}$ variation and the transition models between the Galactic and extragalactic cosmic-ray components. These observations are consistent with the fact that the neutrino intensities around 1 EeV by the relatively old works [6,16] assuming harder UHECR spectrum of $\alpha = 2.0$ and higher $E_{\max}$, and those by the recent works [9,15] with $\alpha \sim 2.5$ show an agreement also within a factor of 2. The difference between the present analytical formula and the full-blown simulation above $\sim$10 EeV in Fig. 1 is attributed to responses to $E_{\max}$. The present analytical estimates of neutrino fluxes for $100\ {\rm PeV} \lesssim E_\nu \lesssim 10$ EeV, the main energy range by the IceCube cosmogenic neutrino search, is robust against these parameters. We should note however that we use $F_{\rm CR}$ for the normalization constant assuming $E_{\max} \gg E_{\rm GZK}$. If $E_{\max}$ is comparable or lower than $E_{\rm GZK}$, the neutrino yield strongly depends on $E_{\max}$ and the present simple treatment is not capable of providing reasonable estimates of the cosmogenic neutrino fluxes.

The present analysis indicates that a five-year observation by the IceCube observatory will scan the source evolution parameter space of the most interest where many of the proposed UHECR astronomical sources are distributed. A null neutrino observation then would imply that either UHECR sources are only locally distributed ($z_{\max} \lesssim 1$), very weakly evolved ($m \lesssim 3$), or the mass composition of UHECRs is not dominated by proton primaries, but by heavier nuclei such as irons after all. The first two possibilities may lead to a speculation about the highest energy particle emission from an entirely different and probably dimmer class of objects than currently suggested. The last possibility has also been discussed with the measurement of the depth of maximum of air-showers by the Auger Collaboration [27]. A neutrino search in ultrahigh energies provides a complementary constraint on the proton fraction of UHECRs in this case [28].

VI. SUMMARY

We have derived the analytical formula to estimate the cosmogenic neutrino fluxes for a wide range of cosmological evolution parameters of UHECR emission sources. The analytical formula provides a practical tool for estimating the neutrino intensity at around the EeV energy region with a limited accuracy within a factor of ~ 2. The obtained analytical estimates have indicated that the present IceCube neutrino limit in 100 PeV–10 EeV energies disfavors the scenarios with the strongly evolved UHECR sources. The future IceCube observation will be able to scan most of the interesting parameter space of UHECR source evolution. Furthermore, while the deep and highly energetic part of Universe is inaccessible with photons or cosmic rays due to the CMB field, the current study implies that the neutrinos can be used as a rare tool to probe the far Universe.

With the greater statistics of ultrahigh energy neutrino detections by the future neutrino telescopes of ~ 100 km^2 areas, such as ARA [29] and ARIANNA [30], the analytical formula allows us to specify the astronomical classes of ultrahigh energy cosmic-ray sources. The pioneer prediction of the cosmogenic neutrinos in the 1960s [4] will finally lead to revealing the characteristics of an UHECR emission mechanism in the near future.

ACKNOWLEDGMENTS

We wish to acknowledge Kumiko Kotera for useful discussions in preparations for this work. The authors are also grateful to Markus Ahlers and Spencer Klein for valuable comments on the manuscript. A. Ishihara acknowledges support by the Research Fellowships of the Japan Society for the Promotion of Science for Young Scientist. This work was supported in part by the Grants-in-Aid in Scientific Research from the JSPS in Japan.

APPENDIX A: THE FLUX CALCULATION BASED ON ENERGETICS

Recently the possible upper limit on the cosmogenic neutrino flux has been discussed solely using the Fermi measurement on extragalactic diffuse γ-ray background [31]. In this work, the neutrino flux was approximately estimated by the energetics argument, calculating energy channeling into secondary neutrinos from a UHECR proton during its propagation in the CMB field. The neutrino flux is then calculated by

$$E_\nu \frac{dJ_\nu}{dE_\nu} = n_0 c \int_0^{z_{\max}} dz_s \psi(z_s) \left| \frac{dt}{dz}(z_s) \right| \times \int dE_{\rm CR} E_{\rm CR} \frac{dN_{\rm CR}}{dE_{\rm CR}} R_\nu(E_{\rm CR}) \frac{d\rho_\nu}{dE_\nu}. \quad \text{(A1)}$$

Here $dN_{\rm CR}/dE_{\rm CR}$ is the injected UHECR proton spectrum ($\sim E_p^{-\alpha}$) at the source redshift z_s, R_ν is a fraction of UHECR proton injection energy carried by the secondary neutrinos, and $d\rho_\nu/dE_\nu$ is a distribution of neutrino energy. R_ν was calculated in the earlier work [16] represented by a numerically fitted function as

$$R_\nu = \frac{0.45}{1 + \left(\frac{2\times 10^{11}\ \text{GeV}}{(1+z_s)E_{\rm CR}}\right)^2}. \quad \text{(A2)}$$

While the original work [31] represented $d\rho_\nu/dE_\nu$ as $\sim \delta(E_\nu - E_{\rm CR}/(20(1+z_s)))$ approximating each secondary neutrino receiving $1/20$ of the UHECR proton energy, we found that the single pion kinematics approximation would give a better agreement in the neutrino spectral shape with those obtained by the full-blown simulation. It is then written as

$$\frac{d\rho_\nu}{dE_\nu} \simeq (1+z_s)[E_{\rm CR}(x_R^+ - x_R^-)(1-r_\pi)]^{-1} \ln\left(\frac{x_R^+}{\xi_R}\right), \quad \text{(A3)}$$

where ξ_R is given by Eq. (8), replacing E_ν^g with $E_\nu(1+z_s)$.

This approach has an advantage in that it does not rely on the Δ-resonance approximation. Although we are not able to find out a complete analytical solution of the integrals in Eq. (A1), the numerical calculations indeed confirmed that Eq. (A1) reasonably reproduces the full simulation/numerical calculation results. It gives a better agreement than our formula at around 100 PeV, owing to inclusion of direct pion production yielding a pair of $\pi^+\pi^-$ by Eq. (A2) [16]. However, this energetics-based formulation significantly overestimates neutrino intensities with energy above 1 EeV. We suspect this is due to neglecting of the energy loss of UHECR protons. Energy of an UHECR proton is in many cases largely lower than its injected energy when it yields neutrinos, because of energy loss by the photo-pion production during the UHECR propagation. Without accounting for this effect, higher energy neutrino production is overweighted in the formulation. The overproduced high-energy neutrinos are then redshifted and accumulated even in the PeV regime when UHECR sources are strongly evolved. As a consequence, the estimated intensity departs from the calculation with the full-blown simulation in case of the strong evolution scenario. Since the GZK neutrino search by the IceCube detector is sensitive to the EeV range and to emission from strongly evolved sources, we concluded that the energetics-based formulation is not appropriate for our purpose.

APPENDIX B: THE ANALYTICAL FORMULA FOR THE PARTIALLY CONSTANT SOURCE EVOLUTION

Some classes of astronomical objects, like galaxy star formation, seem to exhibit evolution nearly constant above a certain redshift. For these cases, cosmological evolution of sources is written as $\psi(z_s) \sim (1+z_s)^m$ for $0 \le z_s \le \tilde{z}$ and $\psi(z_s) \sim (1+\tilde{z})^m$ for $\tilde{z} \le z_s \le z_{\max}$. The redshift-dependence term ζ (Eq. (16)) is then obtained with minor modifications on Eq. (17) and given as

$$\zeta = \zeta_{\tilde{z}} + \tilde{\zeta}, \tag{B1}$$

where $\zeta_{\tilde{z}}$ is given by Eq. (17) by replacing $z_{\max}$ with $\tilde{z}$, accounting for the evolution up to $z_s \le \tilde{z}$.

The additional term $\tilde{\zeta}$ is obtained in functions similar to Eq. (17) as

$$\begin{aligned}\tilde{\zeta} = {}& e^{-2}\frac{1}{\gamma_\alpha}\Omega_M^{-(\alpha/3)}(1+\tilde{z})^m\bigg\{(\Omega_M(1+\tilde{z}_{\mathrm{up}})^3+\Omega_\Lambda)^{\gamma_\alpha/3}\bigg(x_0^{-(\alpha+1)}\ln\bigg(\frac{x_R^+}{x_R^-}\bigg)\\ &+x_1^{-(\alpha+3)}e^{-(1/x_1)}\bigg[\ln\bigg(x_1\frac{E_\Delta}{E_\nu(1+\tilde{z}_{\mathrm{up}})^2}x_R^-(1-r_\pi)\bigg)+\frac{2}{\gamma_\alpha}\bigg]\bigg)-(\Omega_M(1+\tilde{z}_{\mathrm{down}})^3+\Omega_\Lambda)^{\gamma_\alpha/3}x_0^{-(\alpha+1)}\ln\bigg(\frac{x_R^+}{x_R^-}\bigg)\\ &-(\Omega_M(1+\tilde{z}_{\mathrm{down}})^3+\Omega_\Lambda)^{\gamma_\alpha/3}x_1^{-(\alpha+3)}e^{-(1/x_1)}\bigg[\ln\bigg(x_1\frac{E_\Delta}{E_\nu(1+\tilde{z}_{\mathrm{down}})^2}x_R^-(1-r_\pi)\bigg)+\frac{2}{\gamma_\alpha}\bigg]\bigg\},\end{aligned} \tag{B2}$$

where $\gamma_\alpha \equiv \alpha - \frac{3}{2}$ and the redshift bound $\tilde{z}_{\mathrm{up}}$ is given by

$$1+\tilde{z}_{\mathrm{up}} = \begin{cases} 1+\tilde{z} & \frac{x_1E_\Delta x_R^+(1-r_\pi)}{(1+\tilde{z})^2} \le E_\nu, \\ \left(\frac{x_1E_\Delta}{E_\nu}x_R^+(1-r_\pi)\right)^{1/2} & \frac{x_1E_\Delta x_R^+(1-r_\pi)}{(1+z_{\max})^2} \le E_\nu \le \frac{x_1E_\Delta x_R^+(1-r_\pi)}{(1+\tilde{z})^2}, \\ 1+z_{\max} & E_\nu \le \frac{x_1E_\Delta x_R^+(1-r_\pi)}{(1+z_{\max})^2}. \end{cases} \tag{B3}$$

$\tilde{z}_{\mathrm{down}}$ is written as the same equation (B3) by replacing x_R^+ with x_R^-.

[1] J. Abraham *et al.* (Pierre Auger Collaboration), Science **318**, 938 (2007).
[2] J. Abraham *et al.* (Pierre Auger Collaboration), Phys. Rev. Lett. **101**, 061101 (2008).
[3] R. U. Abbasi *et al.* (High Resolution Fly's Eye Collaboration), Phys. Rev. Lett. **92**, 151101 (2004).
[4] V. S. Berezinsky and G. T. Zatsepin, Phys. Lett. **28B**, 423 (1969).
[5] K. Greisen, Phys. Rev. Lett. **16**, 748 (1966); G. T. Zatsepin and V. A. Kuzmin, Pis'ma Zh. Eksp. Teor. Fiz. **4**, 114 (1966) [JETP Lett. **4**, 78 (1966)].
[6] S. Yoshida and M. Teshima, Prog. Theor. Phys. **89**, 833 (1993).
[7] S. Yoshida, H. Dai, C. H. Jui, and P. Sommers, Astrophys. J. **479**, 547 (1997).
[8] V. Berezinsky, A. Gazizov, M. Kachelriess, and S. Ostapchenko, Phys. Lett. B **695**, 13 (2011); G. B. Gelmini, O. Kalashev, and D. V. Semikoz, J. Cosmol. Astropart. Phys. 01 (2012) 044.
[9] M. Ahlers *et al.*, Astropart. Phys. **34**, 106 (2010).
[10] A Multi-Km3 Sized Neutrino Telescope, http://www.km3net.org/.
[11] R. Abbasi *et al.* (IceCube Collaboration), Phys. Rev. D **83**, 092003 (2011).
[12] A. Ishihara *et al.* (IceCube Collaboration), *Proceedings of 32nd ICRC, Beijing, China, 2011*, http://www.ihep.ac.cn/english/conference/icrc2011/paper/.
[13] A. Achterberg *et al.* (IceCube Collaboration), Astropart. Phys. **26**, 155 (2006).
[14] K. Nakamura *et al.* (Particle Data Group), J. Phys. G **37**, 075021 (2010).
[15] K. Kotera, D. Allard, and A. V. Olinto, J. Cosmol. Astropart. Phys. 10 (2010) 013.
[16] R. Engel, D. Seckel, and T. Stanev, Phys. Rev. D **64**, 093010 (2001).
[17] T. K. Gaisser, *Cosmic Rays and Particle Physics* (Cambridge University Press, Cambridge, England, 1990).
[18] P. Bhattacharjee and G. Sigl, Phys. Rep. **327**, 109 (2000).
[19] H. Takami, K. Murase, S. Nagataki, and K. Sato, Astropart. Phys. **31**, 201 (2009).
[20] See, for example, S. Yoshida, *Ultra-High Energy Particle Astrophysics* (Nova Science, New York, 2003).
[21] A. M. Hopkins and J. F. Beacom, Astrophys. J. **651**, 142 (2006).

[22] R. Abbasi *et al.* (IceCube Collaboration) Phys. Rev. D **82**, 072003 (2010).
[23] O. E. Kalashev, V. A. Kuzmin, D. V. Semikoz, and G. Sigl, Phys. Rev. D **66**, 063004 (2002).
[24] G. J. Feldman and R. D. Cousins, Phys. Rev. D **57**, 3873 (1998).
[25] D. S. Fixsen *et al.*, Astrophys. J. **508**, 123 (1998).
[26] M. Ahlers, M. C. Gonzalez-Garcia, and F. Halzen, Astropart. Phys. **35**, 87 (2011).
[27] J. Abraham *et al.* (Pierre Auger Collaboration) Phys. Rev. Lett. **104**, 091101 (2010).
[28] M. Ahlers, L. A. Anchordoqui, and S. Sarkar, Phys. Rev. D **79**, 083009 (2009).
[29] P. Allison *et al.*, Astropart. Phys. **35**, 457 (2012).
[30] L. Gerhardt *et al.*, Nucl. Instrum. Methods Phys. Res., Sect. A **624**, 85 (2010).
[31] X-Y. Wang, R-Y. Liu, and F. Aharonian, Astrophys. J. **736**, 112 (2011).

PHYSICAL REVIEW D **83,** 092003 (2011)

Constraints on the extremely-high energy cosmic neutrino flux with the IceCube 2008-2009 data

R. Abbasi,[28] Y. Abdou,[22] T. Abu-Zayyad,[33] J. Adams,[16] J. A. Aguilar,[28] M. Ahlers,[32] K. Andeen,[28] J. Auffenberg,[38] X. Bai,[31] M. Baker,[28] S. W. Barwick,[24] R. Bay,[7] J. L. Bazo Alba,[39] K. Beattie,[8] J. J. Beatty,[18,19] S. Bechet,[13] J. K. Becker,[10] K.-H. Becker,[38] M. L. Benabderrahmane,[39] S. BenZvi,[28] J. Berdermann,[39] P. Berghaus,[28] D. Berley,[17] E. Bernardini,[39] D. Bertrand,[13] D. Z. Besson,[26] D. Bindig,[38] M. Bissok,[1] E. Blaufuss,[17] J. Blumenthal,[1] D. J. Boersma,[1] C. Bohm,[34] D. Bose,[14] S. Böser,[11] O. Botner,[37] J. Braun,[28] A. M. Brown,[16] S. Buitink,[8] M. Carson,[22] D. Chirkin,[28] B. Christy,[17] J. Clem,[31] F. Clevermann,[20] S. Cohen,[25] C. Colnard,[23] D. F. Cowen,[36,35] M. V. D'Agostino,[7] M. Danninger,[34] J. Daughhetee,[5] J. C. Davis,[18] C. De Clercq,[14] L. Demirörs,[25] T. Denger,[11] O. Depaepe,[14] F. Descamps,[22] P. Desiati,[28] G. de Vries-Uiterweerd,[22] T. DeYoung,[36] J. C. Díaz-Vélez,[28] M. Dierckxsens,[13] J. Dreyer,[10] J. P. Dumm,[28] R. Ehrlich,[17] J. Eisch,[28] R. W. Ellsworth,[17] O. Engdegård,[37] S. Euler,[1] P. A. Evenson,[31] O. Fadiran,[4] A. R. Fazely,[6] A. Fedynitch,[10] T. Feusels,[22] K. Filimonov,[7] C. Finley,[34] T. Fischer-Wasels,[38] M. M. Foerster,[36] B. D. Fox,[36] A. Franckowiak,[11] R. Franke,[39] T. K. Gaisser,[31] J. Gallagher,[27] M. Geisler,[1] L. Gerhardt,[8,7] L. Gladstone,[28] T. Glüsenkamp,[1] A. Goldschmidt,[8] J. A. Goodman,[17] D. Gora,[39] D. Grant,[21] T. Griesel,[29] A. Groß,[16,23] S. Grullon,[28] M. Gurtner,[38] C. Ha,[36] A. Hallgren,[37] F. Halzen,[28] K. Han,[39] K. Hanson,[13,28] D. Heinen,[1] K. Helbing,[38] P. Herquet,[30] S. Hickford,[16] G. C. Hill,[28] K. D. Hoffman,[17] A. Homeier,[11] K. Hoshina,[28] D. Hubert,[14] W. Huelsnitz,[17] J.-P. Hülß,[1] P. O. Hulth,[34] K. Hultqvist,[34] S. Hussain,[31] A. Ishihara,[15,*] J. Jacobsen,[28] G. S. Japaridze,[4] H. Johansson,[34] J. M. Joseph,[8] K.-H. Kampert,[38] A. Kappes,[9] T. Karg,[38] A. Karle,[28] J. L. Kelley,[28] P. Kenny,[26] J. Kiryluk,[8,7] F. Kislat,[39] S. R. Klein,[8,7] J.-H. Köhne,[20] G. Kohnen,[30] H. Kolanoski,[9] L. Köpke,[29] S. Kopper,[38] D. J. Koskinen,[36] M. Kowalski,[11] T. Kowarik,[29] M. Krasberg,[28] T. Krings,[1] G. Kroll,[29] T. Kuwabara,[31] M. Labare,[14] S. Lafebre,[36] K. Laihem,[1] H. Landsman,[28] M. J. Larson,[36] R. Lauer,[39] J. Lünemann,[29] J. Madsen,[33] P. Majumdar,[39] A. Marotta,[13] R. Maruyama,[28] K. Mase,[15] H. S. Matis,[8] K. Meagher,[17] M. Merck,[28] P. Mészáros,[35,36] T. Meures,[1] E. Middell,[39] N. Milke,[20] J. Miller,[37] T. Montaruli,[28,†] R. Morse,[28] S. M. Movit,[35] R. Nahnhauer,[39] J. W. Nam,[24] U. Naumann,[38] P. Nießen,[31] D. R. Nygren,[8] S. Odrowski,[23] A. Olivas,[17] M. Olivo,[10] A. O'Murchadha,[28] M. Ono,[15] S. Panknin,[11] L. Paul,[1] C. Pérez de los Heros,[37] J. Petrovic,[13] A. Piegsa,[29] D. Pieloth,[20] R. Porrata,[7] J. Posselt,[38] P. B. Price,[7] G. T. Przybylski,[8] K. Rawlins,[3] P. Redl,[17] E. Resconi,[23] W. Rhode,[20] M. Ribordy,[25] A. Rizzo,[14] J. P. Rodrigues,[28] P. Roth,[17] F. Rothmaier,[29] C. Rott,[18] T. Ruhe,[20] D. Rutledge,[36] B. Ruzybayev,[31] D. Ryckbosch,[22] H.-G. Sander,[29] M. Santander,[28] S. Sarkar,[32] K. Schatto,[29] T. Schmidt,[17] A. Schönwald,[39] A. Schukraft,[1] A. Schultes,[38] O. Schulz,[23] M. Schunck,[1] D. Seckel,[31] B. Semburg,[38] S. H. Seo,[34] Y. Sestayo,[23] S. Seunarine,[12] A. Silvestri,[24] A. Slipak,[36] G. M. Spiczak,[33] C. Spiering,[39] M. Stamatikos,[18,‡] T. Stanev,[31] G. Stephens,[36] T. Stezelberger,[8] R. G. Stokstad,[8] A. Stössl,[39] S. Stoyanov,[31] E. A. Strahler,[14] T. Straszheim,[17] M. Stür,[11] G. W. Sullivan,[17] Q. Swillens,[13] H. Taavola,[37] I. Taboada,[5] A. Tamburro,[33] A. Tepe,[5] S. Ter-Antonyan,[6] S. Tilav,[31] P. A. Toale,[2] S. Toscano,[28] D. Tosi,[39] D. Turčan,[17] N. van Eijndhoven,[14] J. Vandenbroucke,[7] A. Van Overloop,[22] J. van Santen,[28] M. Vehring,[1] M. Voge,[11] C. Walck,[34] T. Waldenmaier,[9] M. Wallraff,[1] M. Walter,[39] Ch. Weaver,[28] C. Wendt,[28] S. Westerhoff,[28] N. Whitehorn,[28] K. Wiebe,[29] C. H. Wiebusch,[1] D. R. Williams,[2] R. Wischnewski,[39] H. Wissing,[17] M. Wolf,[23] T. R. Wood,[21] K. Woschnagg,[7] C. Xu,[31] X. W. Xu,[6] G. Yodh,[24] S. Yoshida,[15] and P. Zarzhitsky[2]

(IceCube Collaboration)

[1]*III. Physikalisches Institut, RWTH Aachen University, D-52056 Aachen, Germany*
[2]*Department of Physics and Astronomy, University of Alabama, Tuscaloosa, Alabama 35487, USA*
[3]*Department of Physics and Astronomy, University of Alaska Anchorage, 3211 Providence Dr., Anchorage, Alaska 99508, USA*
[4]*CTSPS, USAClark-Atlanta University, Atlanta, Georgia 30314, USA*
[5]*School of Physics and Center for Relativistic Astrophysics, Georgia Institute of Technology, Atlanta, Georgia 30332, USA*
[6]*Department of Physics, Southern University, Baton Rouge, Louisiana 70813, USA*
[7]*Department of Physics, University of California, Berkeley, California 94720, USA*
[8]*Lawrence Berkeley National Laboratory, Berkeley, California 94720, USA*
[9]*Institut für Physik, Humboldt-Universität zu Berlin, D-12489 Berlin, Germany*
[10]*Fakultät für Physik & Astronomie, Ruhr-Universität Bochum, D-44780 Bochum, Germany*
[11]*Physikalisches Institut, Universität Bonn, Nussallee 12, D-53115 Bonn, Germany*
[12]*Department of Physics, University of the West Indies, Cave Hill Campus, Bridgetown BB11000, Barbados*
[13]*Université Libre de Bruxelles, Science Faculty CP230, B-1050 Brussels, Belgium*
[14]*Vrije Universiteit Brussel, Dienst ELEM, B-1050 Brussels, Belgium*
[15]*Department of Physics, Chiba University, Chiba 263-8522, Japan*
[16]*Department of Physics and Astronomy, University of Canterbury, Private Bag 4800, Christchurch, New Zealand*

[17]Department of Physics, University of Maryland, College Park, Maryland 20742, USA
[18]Department of Physics and Center for Cosmology and Astro-Particle Physics, Ohio State University, Columbus, Ohio 43210, USA
[19]Department of Astronomy, Ohio State University, Columbus, Ohio 43210, USA
[20]Department of Physics, TU Dortmund University, D-44221 Dortmund, Germany
[21]Department of Physics, University of Alberta, Edmonton, Alberta, Canada T6G 2G7
[22]Department of Physics and Astronomy, University of Gent, B-9000 Gent, Belgium
[23]Max-Planck-Institut für Kernphysik, D-69177 Heidelberg, Germany
[24]Department of Physics and Astronomy, University of California, Irvine, California 92697, USA
[25]Laboratory for High Energy Physics, École Polytechnique Fédérale, CH-1015 Lausanne, Switzerland
[26]Department of Physics and Astronomy, University of Kansas, Lawrence, Kansas 66045, USA
[27]Department of Astronomy, University of Wisconsin, Madison, Wisconsin 53706, USA
[28]Department of Physics, University of Wisconsin, Madison, Wisconsin 53706, USA
[29]Institute of Physics, University of Mainz, Staudinger Weg 7, D-55099 Mainz, Germany
[30]Université de Mons, 7000 Mons, Belgium
[31]Bartol Research Institute and Department of Physics and Astronomy, University of Delaware, Newark, Delaware 19716, USA
[32]Department of Physics, University of Oxford, 1 Keble Road, Oxford OX1 3NP, UK
[33]Department of Physics, University of Wisconsin, River Falls, Wisconsin 54022, USA
[34]Oskar Klein center and Department of Physics, Stockholm University, SE-10691 Stockholm, Sweden
[35]Department of Astronomy and Astrophysics, Pennsylvania State University, University Park, Pennsylvania 16802, USA
[36]Department of Physics, Pennsylvania State University, University Park, Pennsylvania 16802, USA
[37]Department of Physics and Astronomy, Uppsala University, Box 516, S-75120 Uppsala, Sweden
[38]Department of Physics, University of Wuppertal, D-42119 Wuppertal, Germany
[39]DESY, D-15735 Zeuthen, Germany
(Received 22 March 2011; published 24 May 2011)

We report on a search for extremely-high energy neutrinos with energies greater than 10^6 GeV using the data taken with the IceCube detector at the South Pole. The data was collected between April 2008 and May 2009 with the half-completed IceCube array. The absence of signal candidate events in the sample of 333.5 days of live time significantly improves model-independent limits from previous searches and allows to place a limit on the diffuse flux of cosmic neutrinos with an E^{-2} spectrum in the energy range $2.0 \times 10^6 - 6.3 \times 10^9$ GeV to a level of $E^2\phi \leq 3.6 \times 10^{-8}$ GeV cm^{-2} sec^{-1} sr^{-1}.

DOI: 10.1103/PhysRevD.83.092003 PACS numbers: 98.70.Sa, 95.55.Vj

I. INTRODUCTION

Cosmogenic neutrinos, the daughter particles of the Greisen-Zatsepin-Kuzmin (GZK) process in which the highest energy cosmic rays interacting with the cosmic-microwave background [1,2], may give a unique picture of the Universe in the highest energy regime. Cosmogenic neutrinos carry information about the sources of the highest energy cosmic rays, such as their location, cosmological evolution, and cosmic-ray spectra at the sources. Various cosmogenic neutrino models [3–6] which assume primary cosmic ray protons predict neutrino fluxes $E_\nu^2\phi \geq 10^{-4}$ GeV^{-2} sec^{-1} sr^{-1} in the energy range 10^8 GeV $\leq E_\nu \leq 10^{10}$ GeV, which implies that the 4π solid angle averaged neutrino effective area divided by energy A_ν/E_ν must be larger than 10^{-5} m^2/GeV (e.g. $A_\nu \geq 10^3$ m^2 at 10^8 GeV and $A_\nu \geq 10^4$ m^2 at 10^9 GeV) to detect several cosmogenic neutrinos every year.

Several techniques have been used to realize such huge detection volumes for these extremely-high energy (EHE) neutrinos. Air-shower detectors search for neutrino-induced young inclined showers [7] or Earth-skimming events initiated by tau neutrinos [8]. Radio Cherenkov neutrino detectors search for radio Askar'yan pulses in a dielectric medium as the EHE neutrino signature [9–11]. Underground neutrino telescopes, such as IceCube, deployed in transparent naturally occurring media [12,13] can detect EHE neutrino interactions through the strong Cherenkov radiation emitted by the charged secondary particles. This technique is well established for observations of astrophysical neutrinos in the MeV to GeV energy region [14,15], and can also be utilized to search for cosmogenic EHE neutrinos with an appropriate background rejection method. In a neutrino telescope, an EHE neutrino interaction would be identified by the extremely-high number of Cherenkov photons deposited in the detector.

In this paper, we describe the search for neutrinos with energies above 10^6 GeV using data collected with the half-completed IceCube detector in 2008-2009. This analysis is sensitive to all three neutrino flavors. Compared to the previous EHE neutrino search described in Ref. [13], which used an earlier stage of the IceCube detector, the

*Corresponding author: aya@hepburn.s.chiba-u.ac.jp (A. Ishihara)
†also Università di Bari and Sezione INFN, Dipartimento di Fisica, I-70126, Bari, Italy
‡NASA Goddard Space Flight Center, Greenbelt, MD 20771, USA

current analysis benefits from the enlarged instrumented volume and from improved agreement between simulated and observed event distributions. This article presents the improved strategies implemented since the previous analysis [13].

II. DATA SETS

The analysis uses data collected from April 6, 2008 through May 20, 2009. At the time of data collection, the IceCube detector consisted of 2400 digital optical modules (DOMs) on 40 vertical strings. The volume of the detector was roughly 0.5 Km^3 with the detector center located at a depth of 1948 m below the ice surface. The DOMs consist of a 25 cm photomultiplier tube [16] with data acquisition and calibration electronics, data compression, communications, and control hardware [17]. The trigger setting was unchanged from the previous analysis [13].

The analysis was optimized on simulated data with most of the experimental data kept blind. A 10% subset of the experimental data was used for examinations of the Monte Carlo simulations and detector response. This subset comprised 35.8 days of detector live time distributed randomly throughout the data collection period, and was not used once the analysis was fully defined. The use of a statistically independent final sample conservatively ensures avoidance of possible analysis bias due to tuning a Monte Carlo simulation using an experimental subset. The selection criteria were then applied to the complementary 90% of the experimental data, comprising 333.5 days of live time.

The primary background in this analysis is muon bundles made up of large numbers of muons produced by high energy cosmic-ray interactions in the atmosphere. This background was simulated with the CORSIKA air-shower simulation package version 6.720 [18] with the SIBYLL 2.1 [19] and QGSJET-II [20] hadronic interaction models, without prompt muons from the heavy meson decays. Cosmic-ray interactions assuming pure proton and iron primary compositions in the energy region between 10^6 and 10^{10} GeV were simulated. Background contributions from primary cosmic-ray energies beyond 10^{10} GeV were estimated by extrapolation of the simulated sample up to the GZK cutoff energy of $\sim 5 \times 10^{10}$ GeV. EHE neutrino signal events in energies between 10^5 and 10^{11} GeV from several flux models [3–6,21,22] were simulated using the JULIET package [23].

III. EVENT SELECTION

The amount of energy deposited in the form of Cherenkov photons by the neutrino-induced charged particles in the detector is highly correlated with the energy of the particles [13]. An EHE neutrino interaction occurring inside or close to the IceCube detector would stand out against the background of cosmic-ray induced muons due to the much higher light deposition. The total number of photoelectrons (NPE) recorded in an event was used as the main distinctive feature to separate signal from background.

A. On-line sample

The number of photoelectrons (p.e.) recorded by an individual DOM was derived by integrating the pedestal subtracted waveforms. Each DOM has two waveform digitizers, that simultaneously capture p.e. signals with differing dynamic ranges and time windows [17]. The event total NPE was then obtained by summing the number of p.e. detected by each DOM. photomultiplier tube saturation effects and the sizes of the time windows limit the NPE estimation at high light levels. The initial NPE calculation was performed online at the South Pole. For this analysis we consider only events with $\mathrm{NPE}_{\mathrm{online}} \geq 630$. The event rate of this ‘‘online bright sample’’ was ~ 1.4 Hz. At this level, the background rate exceeded the expected signal rate by $\geq O(10^7)$.

B. Off-line sample

For the following data selection step, the NPE values were recalculated after eliminating photon signals from low energy muons accidentally coincident in a 20 μs time window of a large NPE event. These low energy muons leave a faint light, typically with an $\mathrm{NPE} < 9$. The light deposition of the coinciding low energy muon was, in most cases, spatially and temporally separated from the main bright p.e. cluster. While the few coincident photons have very a small impact on the NPE calculation, they can disturb the geometrical reconstruction of the particle tracks later on in the analysis. Contributions from coincident low energy muons were eliminated by removing p.e. signals that were temporally separated from the time of the highest light deposition associated with the main high NPE event. The recording time of a p.e. signal in the i_{th} DOM, $t_{10,i}$, was defined as the time at which 10% of the total charge had been captured. The time of the highest light deposition was defined as the time t_{LN} of the DOM which captured the largest p.e. signal in the event. This time, t_{LN}, was typically associated with the time of closest approach of the charged particle tracks to any DOM in the detector. For the offline NPE calculation and track reconstruction, those p.e. signals which occurred outside the time window $[-4.4\ \mu\mathrm{s}, 6.4\ \mu\mathrm{s}]$ around the t_{LN} were excluded. The ‘‘offline bright sample’’ selects events with $\mathrm{NPE} \geq 3.2 \times 10^3$ and the number of hit DOMs (NDOM) ≥ 200; here and below NPE and NDOM are obtained after the t_{LN} time window cleaning. These NPE and NDOM thresholds reduced the background rate by 2 orders of magnitude while keeping $\sim 70\%$ of the cosmogenic neutrino-induced events. The remaining backgrounds are bundles containing many hundreds of muons, with an estimated cosmic-ray energy above 10^7 GeV.

C. Quality cut

Apart from NPE, the particle direction and the depth distribution of the detected Cherenkov photons are distinctive event features that separate the EHE neutrino signal from the atmospheric muon background. Because of the energy dependence of the neutrino interaction cross section, most of the EHE neutrino signal is expected from directions close to the horizon. As a result of the depth dependence of the optical properties of the Polar ice, the largest photon signals are often detected in the deepest part of the detector, where the ice is most transparent [24]. On the other hand, the background atmospheric muons enter the detection volume from above and lose a substantial fraction of their energy during propagation through the detector. Therefore, the time and depth coordinates, z, of the detected Cherenkov photons, measured relative to the detector center, show negative correlation for background. The largest photon signals from these background muons are expected at shallow depths near the top of the detector. Exceptions are inclined atmospheric muon bundles that pass outside the instrumented volume with the point of closest approach in the deep, clear ice at the bottom of the detector, or individual muons that deposit most of their energy in an isolated catastrophic energy loss in the deep ice after having passed through the top part of the detector. Track reconstructions often fail to identify such atmospheric muon events as downward-going tracks, when most of the light deposition occurs in the deep part of the detector. Therefore, a track reconstruction is applied only to those events in which the DOM with the largest signal is located at $z > -300$ m ("shallow events"). The negative z value indicates the vertical distance below the center of the IceCube detector. For events with the largest photon signal at $z < -300$ m ("deep events"), further event selection criteria rely on timing instead of directional information.

For the shallow events, the particle directions are reconstructed with the LineFit algorithm [13]. Since the majority of the EHE neutrino-induced events is close to the horizon [23] while the directions of the background muon bundles are mostly vertical, it is important to minimize the number of background tracks that are misreconstructed as horizontal. In order to reject the misreconstructed background events, another simple one-dimensional reconstruction is introduced. The distribution of average depth of p.e. as a function of timing is fitted by a linear function, $\bar{z}(t_{10}) = C_0 + S_{zt} \cdot t_{10}$. The fit parameter, S_{zt}, is a measure for the speed at which the light signal propagates in z-direction, and hence for the inclination of the tracks. For vertically downward-going relativistic particles, the quantity S_{zt}/c takes values ~ -1, where c is the vacuum speed of light, whereas close to horizontal tracks yield values $S_{zt}/c \sim 0$. The shallow "quality bright sample" requires an additional condition of $(S_{zt}/c + \cos\theta) \geq -0.4$ where θ is the reconstructed zenith angle from the LineFit. This condition excludes events for which the one-dimensional fit suggests a significantly more vertical downward-going geometry than the LineFit. Both signal and background are reduced by less than $\sim$2% by this criterion. Figure 1 shows the distributions of NPE (panel (a)) and $\cos\theta$ (panel (b)) for experimental data, background and signal simulations in the quality bright sample. The distributions of CORSIKA-SIBYLL with an iron primary composition show a reasonable agreement with experimental data while the total event rates are 50% overestimated by simulation. The zenith angle reconstruction resolution of the shallow quality bright sample is $\sim 1.4°$ root mean square for muon bundle background and $\geq \sim 2.5°$ for ν_μ signal. This is because the ν_μ signal experiences more stochastic energy losses along with hadronic cascades at its interaction vertices.

The deep bright events ($Z_{\mathrm{LN}} \leq -300$ m) are mostly events that traverse the bottom edge of IceCube or are uncontained events that propagate or cascade below the detector. The inclination of these events tends to be reconstructed more horizontally than the true direction. The

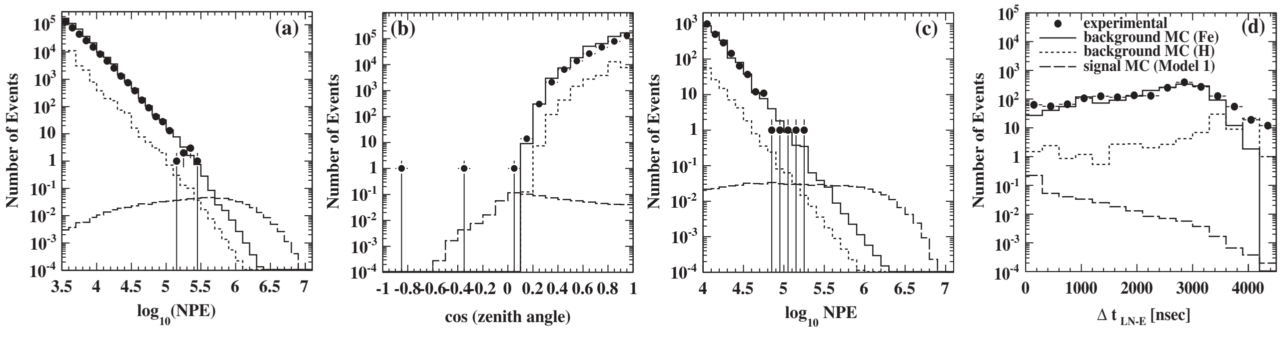

FIG. 1. Event observables in the quality bright sample that are used for the final selection criteria. Distributions of (a) NPE and (b) cosine of the reconstructed zenith angle for shallow events, and (c) NPE and (d) $\Delta t_{\mathrm{LN-E}}$ for deep events in a live time of 333.5 days. The black circles represent experimental data and the solid and dashed lines are CORSIKA-SIBYLL with iron and proton primaries, respectively. The expected signal distributions from simulations of the GZK 1 model (sum of all three neutrino flavors) are shown as long-dashed histograms. Systematic uncertainties are not included.

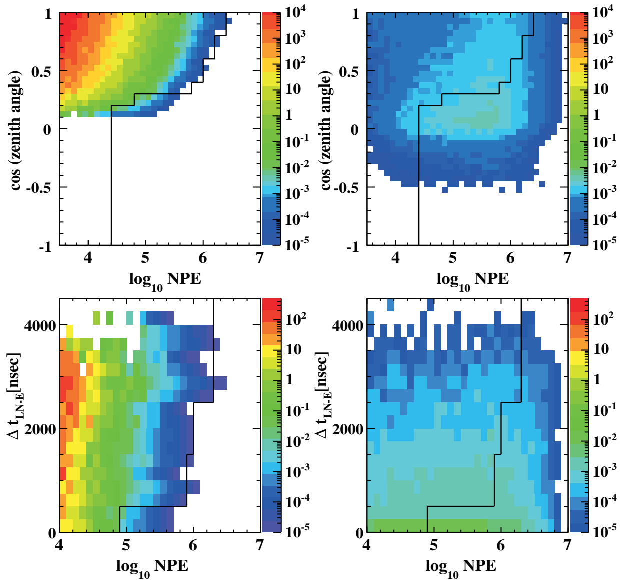

FIG. 2 (color online). Event number distributions of the shallow (upper panels) and deep (lower panels) quality bright sample in 333.5 days are shown for the background (left panels) and signal (right panels) simulations. The signal distributions are from GZK 1 model [3] adding all three flavors of neutrinos. The background distributions are from CORSIKA-SIBYLL with iron primaries. The series of thick lines in each panel indicate the final sample selection criteria.

agreement between the simulation and experimental distributions improves with increasing NPE threshold values for these events. Events with NPE $\leq 10^4$ are discarded from the deep quality bright sample in order to achieve a reasonable agreement between experimental data and simulations. Since the majority of the EHE neutrino-induced events have NPE $\geq 10^4$, the effect on the signal efficiency by this requirement is minimal. A fraction of 96% of background is rejected by the cut, while 91% of the signal is retained. Panel (c) in Fig. 1 shows the NPE distributions from the deep quality bright sample.

D. Final selection

The final event selection is chosen in order to minimize the model discovery factor (MDF $= \mu_{\mathrm{lds}}/N_{\mathrm{signal}}$) [25] in the region of the phase space where a better signal to background ratio (S/B) is expected, where μ_{lds} is the least number of events to claim signal discovery at 5σ significance and N_{signal} is the number of neutrinos expected from the GZK 1 [3] model flux. For the shallow events, high S/B is obtained in the region near the horizontal reconstructed direction as shown in Fig. 1(b). For the deep events, instead of reconstructing the inclination of events, we utilize the time interval, $\Delta t_{\mathrm{LN-E}}$, between the earliest detected photon in an event and t_{LN} to obtain the best S/B subsample. The vertical atmospheric muon bundle events with the largest number of p.e. near the bottom of IceCube are often associated with a small number of p.e. in the shallow detector region much earlier than t_{LN}. This contrasts to the EHE neutrino signal events. The main contributions to a detectable EHE signal in IceCube come from neutrino-induced horizontal muons and taus [23]. These produce the largest number of p.e. signals shortly after the first recorded photoelectrons. Contained cascadelike events induced by neutrino interactions [26] inside the IceCube detector volume also exhibit a similar trend. Figure 1(d) shows the distributions in the deep quality bright sample. The best S/B is achieved in the bin $\Delta t_{\mathrm{LN-E}} \sim 0$ ns. The high rate in the experimental data for $\Delta t_{\mathrm{LN-E}} \geq 3600$ is due to random noise in the DOMs and remaining coincident muons that were underestimated by the simulations. The slightly higher rate for the data in the bin $\Delta t_{\mathrm{LN-E}} \sim 0$ ns may reflect the fact that the ice is cleaner than what was simulated in the deep region. Figure 2 presents the event distributions in the planes of cosθ vs NPE for the shallow events and $\Delta t_{\mathrm{LN-E}}$ vs NPE for the deep events. Optimization is performed by differentiating the NPE threshold numbers in the region cos$\theta \leq 0.3$ or $\Delta t_{\mathrm{LN-E}} \leq 0.5\ \mu$s for the shallow and deep quality bright sample, respectively. The NPE threshold of the other region (cos$\theta \geq 0.3$ or $\Delta t_{\mathrm{LN-E}} \geq 0.5\ \mu$s) is conservatively determined such that the number of background events above the threshold is less than 10^{-4} of the full live time for each bin of cosθ with width 0.2 or 1 μs for $\Delta t_{\mathrm{LN-E}}$. This improves the detection sensitivity without sacrificing discovery potential. The solid lines in Fig. 2 are the final level selection criteria determined from the background (CORSIKA-SIBYLL, iron) and signal (GZK 1 [3]) Monte Carlo simulations following a blind analysis strategy. The minimum NPE

TABLE I. Number of events passing cuts at various selection levels with 333.5 days detector live time. The signal rates correspond to simulations of the GZK 1 model [3]. The errors of the online, offline and quality bright samples are statistical only. Systematic uncertainties in the expected event rates at the final selection level are given as asymmetric error intervals after the statistical error.

Samples	Experimental		Background MC (SIBYLL, iron)		Signal MC (GZK 1)	
On-line	3.7×10^7		$(3.8 \pm 0.1) \times 10^7$		1.8 ± 0.007	
Off-line	3.3×10^5		$(4.8 \pm 0.2) \times 10^5$		1.2 ± 0.006	
	Shallow	Deep	Shallow	Deep	Shallow	Deep
Quality	2.9×10^5	1.9×10^3	$(4.4 \pm 0.2) \times 10^5$	$(1.7 \pm 0.2) \times 10^3$	0.76 ± 0.005	0.43 ± 0.004
Final	0	0	$0.076 \pm 0.012^{+0.051}_{-0.075}$	$0.032 \pm 0.010^{+0.022}_{-0.032}$	$0.39 \pm 0.004^{+0.054}_{-0.043}$	$0.18 \pm 0.002^{+0.025}_{-0.020}$

threshold value is 2.5×10^4. Events with NPE above the threshold value in each bin are considered to be signal event candidates. No events above the threshold are found in the 10% subset of the experimental sample. Monte Carlo simulations indicate that a cosmic-ray primary energy of at least $\sim 2 \times 10^9$ GeV is required for a muon bundle to be selected as the final sample. Table I summarizes the number of events retained in each level of analysis.

IV. THE SYSTEMATICS

Table II summarizes the sources of statistical and systematic errors in signal and background. The systematic uncertainties are assumed to have a flat distribution and are summed in quadrature separately for background and signal.

The dominant source of systematic uncertainty in the signal event rate is the relationship between the measured NPE and the energy of the charged particles. The uncertainty is estimated by calibrating the absolute sensitivity of the DOMs in the laboratory and by calibrating the *in-situ* sensitivity using light sources codeployed with the DOMs in the ice. The estimation by the latter method involves systematic errors in the simulation of the photon propagation in the ice. The uncertainty associated with possible underestimation in the DOM's random noise is estimated by adding artificial random photoelectrons into 10% of the simulated events. The other uncertainties attributed to the neutrino interactions [27] and their daughters' interactions in the ice are similarly estimated as in the previous analysis [13].

TABLE II. List of the statistical and systematic errors for signal (top) and background (bottom) simulations. The uncertainties for the signal are listed relative to the rate estimated for GZK 1 [3]. The uncertainties in the signal rates vary with assumed signal spectra. The uncertainties in the background rate are estimated with CORSIKA-SIBYLL assuming iron composition.

Sources	Signal rate (%)
Statistical error	± 0.8
NPE	$+3.9/-7.2$
Noise	-1.8
Neutrino cross section	± 9.0
Photo-nuclear interaction	$+10.0$
Landau-Pomeranchuk-Migdal effect	± 1.0
Total:	$\pm 0.8(\text{stat}) + 14.0 - 11.7(\text{sys})$

Sources	Background rate (%)
Statistical error	± 17.0
NPE	$+37.1/-46.7$
Noise	-2.2
Cosmic ray composition	-83.9
Hadronic interaction model	$+36.1$
Coincident events	$+31.2$
Total:	$\pm 17.0(\text{stat}) + 60.4 - 96.0(\text{sys})$

The dominant source of systematic uncertainty in the background event rates arises from the uncertainty in the primary cosmic-ray composition at the relevant energies ($> 10^7$ GeV) and the hadronic interaction model used in the simulation of the air showers. The systematic uncertainty associated with the cosmic-ray composition is evaluated by considering two extreme cases of atmospheric muon simulations with either pure iron or pure proton primary compositions. Similarly, the uncertainty due to the hadronic interaction model is evaluated using atmospheric muon simulations with two different high energy hadronic interaction models: SIBYLL 2.1 and QGSJET-II. Systematic uncertainties associated with the NPE measurement and the possible DOM noise rate underestimation are determined in the same manner as for signal events. The background contribution from possible prompt muons created in decays of charmed mesons is negligible. There is also uncertainty due to statistical limitations of the simulated coincident muon sample at NPE $\geq 10^4$. This error is estimated by extrapolating distributions of statistically richer lower NPE coincident simulation events to the final selection region. Possible coincident events in the final sample are also estimated by the temporally and geometrically separated p.e. signals from the main p.e. cluster in each event. This coincident event check suggested that one of the two upward-going reconstructed events in Fig. 1(b) at $\cos\theta = -0.38$ was due to coincident muons. The other upward-going event ($\cos\theta = -0.83$) was possibly neutrino-induced, while the NPE values of both events were approximately 4300 p.e., a factor of 6 less than the final threshold value.

V. RESULTS

No events in the blinded 90% experimental data pass all the selection criteria. This is consistent with the expected background level of $0.11 \pm 0.02^{+0.06}_{-0.10}$ events in a live time of 333.5 days. The passing rates for experimental and simulated events at each selection level are listed in Table I.

The quasidifferential model-independent 90% CL limit on neutrino fluxes [28] normalized by energy decade is shown in Fig. 3 assuming full mixing in the standard neutrino flavor oscillation scenario. In the limit calculation, the energy decade averaged effective area is used and the contribution from the Glashow resonance [29] is neglected. Incorporating the statistical and systematic uncertainties, the background is expected to be found with a uniform prior probability between 0 and 0.19. These uncertainties are included in the final limit using a method outlined in [30]. This estimation together with the null result in the experimental sample gives the Feldman-Cousins 90% CL event upper limit [31] of 2.35 events. For cosmic neutrinos with an E^{-2} energy spectrum, this implies an integral flux limit of $E^2\phi \leq 3.6 \times 10^{-8}$ GeV cm^{-2} sec^{-1} sr^{-1} with the central 90% of the E^{-2} signal found in the energy interval

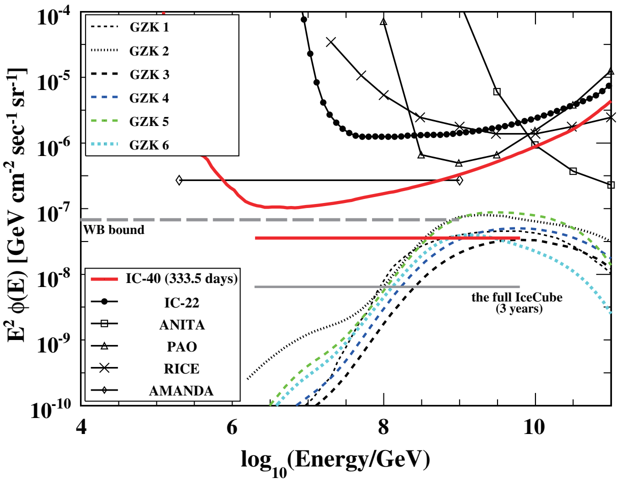

FIG. 3 (color online). All flavor neutrino flux differential limit and E^{-2} spectrum integrated limit from the 2008-2009 IceCube EHE analysis (bold solid lines). The systematic errors are included. Various model predictions (assuming primary protons) are shown for comparison: GZK 1 ($(m, Z_{\max}) = (4, 4)$) [3], GZK 2 [4], GZK 3 ($\Omega_\Lambda = 0.0$), GZK 4 ($\Omega_\Lambda = 0.7$) [5], GZK 5 (maximal) and GZK 6 (the best fit, incorporating the Fermi-LAT bound) [6]. The gray dashed horizontal line indicates the Waxman-Bahcall flux bound with cosmological evolution [32]. Model fluxes are summed over all neutrino flavors, assuming standard neutrino oscillations. The model-independent differential upper limits by other experiments are also shown for Auger (PAO) [8], RICE [9], ANITA [11], and the previous IceCube result (IC22) [13]. Limits from other experiments are converted to the all flavor limit assuming standard neutrino oscillation and a 90% quasidifferential limit when necessary. The integral flux limit on a pure E^{-2} spectrum is shown for AMANDA-II [12]. For reference, the estimated integrated limit for three years of observation with the full IceCube detector with the same analysis strategy is denoted as a gray solid line.

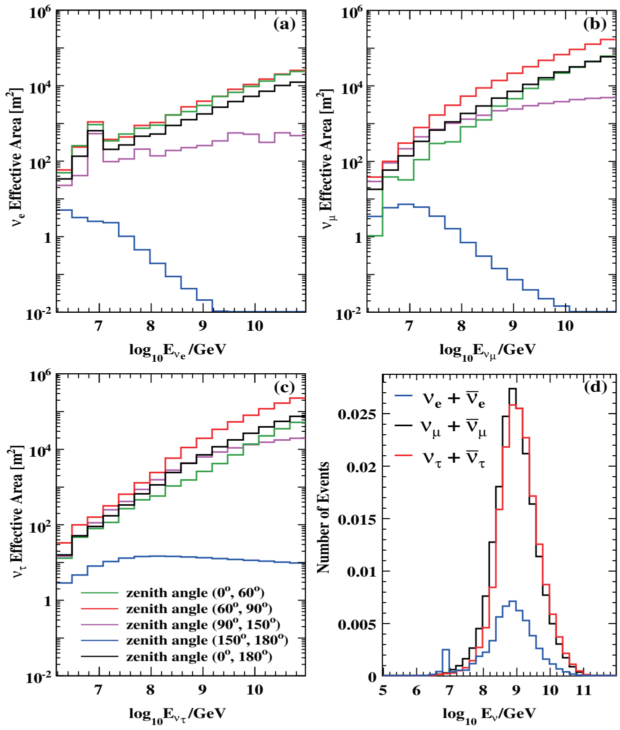

FIG. 4 (color online). Solid angle averaged neutrino effective area for four declination bands as well as that of the full solid angle average for (a) $\nu_e + \bar{\nu}_e$ (b) $\nu_\mu + \bar{\nu}_\mu$ and (c) $\nu_\tau + \bar{\nu}_\tau$, assuming equal flux of neutrinos and antineutrinos. The lower right plot shows the final level signal event distributions for 333.5 days with the GZK 6 model spectra [6] for each neutrino flavor.

$2.0 \times 10^6 - 6.3 \times 10^9$ GeV. This result is the first constraint of neutrino fluxes below the Waxman-Bahcall (WB) flux bound [32] in this energy region.

VI. DISCUSSIONS AND SUMMARY

We analyzed the 2008-09 data sample collected by the 40-string IceCube detector to search for extremely-high energy neutrinos with energies exceeding 10^6 GeV. The differential and integral limits obtained are significantly improved relative to our previous result [13]. This is due to both the increased instrumented volume and improvements of the Monte Carlo simulations. The improved agreement between experimental and simulated data allowed a loosening of the NPE threshold in the data selection, thereby lowering the energy threshold of the analysis and improving the selection efficiency for high energy signal events that occurred outside the instrumented volume. This can also be seen in the corresponding neutrino effective area at the final selection shown in Fig. 4. Compared to the previous search [13], the effective area is a factor of 6 and 3.3 increased at 3×10^7 GeV and 10^9 GeV, respectively. The full solid angle averaged 3 flavor (assuming ν_e:ν_μ:ν_τ: = 1:1:1) neutrino effective area reaches 300 m^2 at 10^8 GeV and 2100 m^2 at 10^9 GeV. The 90% CL differential limit at 10^9 GeV is a factor of ~4 higher than the fluxes predicted by the models GZK 2 and 5, and a factor of ~8 higher than the flux predicted by the models GZK 1, 4, 6, all of which assume primary protons. This suggests that the IceCube EHE neutrino search will reach these flux levels in the near future since the event rate is roughly proportional to the fiducial volume (see Fig. 3), and the current analysis used only the half-instrumented IceCube detector configuration. Further improvements in sensitivity would enable IceCube to act as a probe of the primary cosmic ray composition at GZK energies [33].

Figure 4 indicates that a large part of the EHE neutrino signal is expected from the zenith angle region between 60° and 90°. Upward-going EHE neutrinos are absorbed in the Earth. The propagation length of secondary muons and taus is greater than the distance between the surface and the IceCube fiducial volume. Thus, the inclined particles that reach the IceCube detector are created in the Earth. For ν_e,

TABLE III. Expected number of events in 333.5 days from several cosmogenic neutrino models and top-down models. The confidence interval for exclusion by this observations is also listed where appropriate. The cosmogenic neutrino models (GZK 1-6) assume the cosmic-ray primaries to be protons and different spectral indices/cutoff energies at sources as well as different cosmological evolution parameters and extension in redshift for the sources. Representative models with moderate (GZK 3, 4, 6), moderately strong (GZK 1) and strong (GZK 2, 5) source evolution parameters are listed here.

Models	Event rate	C.L. %
GZK 1 [3]	0.57	...
GZK 2 [4]	0.91	53.4
GZK 3 ($\Omega_\Lambda = 0.0$) [5]	0.29	...
GZK 4 ($\Omega_\Lambda = 0.7$) [5]	0.47	...
GZK 5 (maximal) [6]	0.89	52.8
GZK 6 (the best fit) [6]	0.43	...
Top-down 1 (SUSY) [22]	1.0	55.7
Top-down 2 (no-SUSY) [22]	5.7	99.6
Z-burst [21]	1.2	66.4
WB bound (with evolution) [32]	4.5	...
WB bound (without evolution) [32]	1.0	...

the event signatures are produced nearly at the neutrino interaction points and the current analysis is sensitive to all downward-going geometries. The peaked features in Fig. 4 (a) and 4(d) at $E_{\nu_e} \sim 6.3$ PeV are due to the Glashow resonance [29]. Expected signal energy distributions of GZK 6 at the final selection level are shown in the lower right panel in Fig. 4. The peak energy of the expected signal after all selection criteria is at $\sim 7.0 \times 10^8$ GeV. Significant contributions from all neutrino flavors are observed. In the GZK 6 model, 13% of the signal are from ν_e, 45% are from ν_μ and 42% are from ν_τ. Through-going tracks (muons and taus) constitute 60% of the signal rate and the rest are neutrino interactions that create cascadelike events near and inside the detector volume. Table III gives the event rates for several model fluxes of cosmogenic neutrinos, top-down scenarios, and a pure E^{-2} power-law neutrino spectrum normalized to the Waxman-Bahcall flux bounds for reference. We expect 0.3 to 0.9 cosmogenic neutrino events in 333.5 days, assuming moderate to strong cosmological source evolution models. The half-instrumented IceCube detector is already capable of constraining those models with relatively high neutrino fluxes. The IceCube sensitivity to cosmological EHE neutrinos continues to grow.

ACKNOWLEDGMENTS

We acknowledge the support from the following agencies: U.S. National Science Foundation-Office of Polar Programs, U.S. National Science Foundation-Physics Division, University of Wisconsin Almni Research Foundation, the Grid Laboratory Of Wisconsin (GLOW) grid infrastructure at the University of Wisconsin - Madison, the Open Science Grid (OSG) grid infrastructure; U.S. Department of Energy, and National Energy Research Scientific Computing Center, the Louisiana Optical Network Initiative (LONI) grid computing resources; National Science and Engineering Research Council of Canada; Swedish Research Council, Swedish Polar Research Secretariat, Swedish National Infrastructure for Computing (SNIC), and Knut and Alice Wallenberg Foundation, Sweden; German Ministry for Education and Research (BMBF), Deutsche Forschungsgemeinschaft (DFG), Research Department of Plasmas with Complex Interactions (Bochum), Germany; Fund for Scientific Research (FNRS-FWO), FWO Odysseus programme, Flanders Institute to encourage scientific and technological research in industry (IWT), Belgian Federal Science Policy Office (Belspo); University of Oxford, United Kingdom; Marsden Fund, New Zealand; Japan Society for Promotion of Science (JSPS); the Swiss National Science Foundation (SNSF), Switzerland; A. Groß acknowledges support by the EU Marie Curie OIF Program; J. P. Rodrigues acknowledges support by the Capes Foundation, Ministry of Education of Brazil.

[1] K. Greisen, Phys. Rev. Lett. **16**, 748 (1966); G. T. Zatsepin and V. A. Kuzmin, Pis'ma Zh. Eksp. Teor. Fiz. **4**, 114 (1966); [JETP Lett. **4**, 78 (1966)].
[2] V. S. Berezinsky and G. T. Zatsepin, Phys. Lett. B **28**, 423 (1969).
[3] S. Yoshida and M. Teshima, Prog. Theor. Phys. **89**, 833 (1993); The model with the source evolution $(z_{\max} + 1)^m$ with $m = 4$ extending to $z_{\max} = 4.0$.
[4] O. E. Kalashev, V. A. Kuzmin, D. V. Semikoz, and G. Sigl, Phys. Rev. D **66**, 063004 (2002).
[5] R. Engel, D. Seckel, and T. Stanev, Phys. Rev. D **64**, 093010 (2001).
[6] M. Ahlers *et al.*, Astropart. Phys. **34**, 106 (2010).
[7] R. U. Abassi *et al.* (HiRes Collaboration), Astrophys. J. **684**, 790 (2008).
[8] J. Abraham *et al.* (Pierre Auger Collaboration), Phys. Rev. D **79**, 102001 (2009); (Private communications).
[9] I. Kravchenko *et al.* (Rice Collaboration), Phys. Rev. D **73**, 082002 (2006).
[10] P. W. Gorham *et al.* (GLUE Collaboration), Phys. Rev. Lett. **93**, 041101 (2004).
[11] P. W. Gorham *et al.* (ANITA Collaboration), Phys. Rev. D **82**, 022004 (2010); arXiv:1011.5004 (erratum).

[12] M. Ackermann *et al.* (IceCube Collaboration), Astrophys. J. **675**, 1014 (2008).
[13] R. Abbasi *et al.* (IceCube Collaboration), Phys. Rev. D **82**, 072003 (2010).
[14] K. Hirata *et al.*, Phys. Rev. Lett. **58**, 1490 (1987); Y. Fukuda *et al.* (Kamiokande Collaboration), Phys. Rev. Lett. **77**, 1683 (1996); Y. Fukuda *et al.* (Super-Kamiokande Collaboration), Phys. Rev. Lett. **81**, 1158 (1998).
[15] Q. R. Ahmad *et al.* (SNO collaboration), Phys. Rev. Lett. **87**, 071301 (2001).
[16] R. Abbasi *et al.* (IceCube Collaboration), Nucl. Instrum. Methods Phys. Res., Sect. A **618**, 139 (2010).
[17] R. Abbasi *et al.* (IceCube Collaboration), Nucl. Instrum. Methods Phys. Res., Sect. A **601**, 294 (2009).
[18] D. Heck *et al.*, Forschungszentrum Karlsruhe Report FZKA 6019, 1998.
[19] E. J. Ahn, R. Engel, T. K. Gaisser, P. Lipari, and T. Stanev, Phys. Rev. D **80**, 094003 (2009).
[20] S. Ostapchenko, Phys. Rev. D **74**, 014026 (2006); Nucl. Phys. B, Proc. Suppl. **151**, 143 (2006).
[21] S. Yoshida, G. Sigl, and S. Lee, Phys. Rev. Lett. **81**, 5505 (1998).
[22] G. Sigl *et al.*, Phys. Rev. D **59**, 043504 (1998).
[23] S. Yoshida *et al.*, Phys. Rev. D **69**, 103004 (2004).
[24] M. Ackermann *et al.*, J. Geophys. Res. **111**, D13203 (2006).
[25] G. C. Hill *et al.*, in *the Proceedings of PHYSTAT2005, Oxford, England, 2005* (Imperial College Press, London, 2006), pp 108–111.
[26] R. Abbasi *et al.* (IceCube Collaboration), arXiv:1101.1692 [Phys. Rev. D. (to be published)].
[27] A. Cooper-Sarkar and S. Sarkar, J. High Energy Phys. 01 (2008) 075.
[28] L. A. Anchordoqui *et al.*, Phys. Rev. D **66**, 103002 (2002).
[29] S. L. Glashow, Phys. Rev. **118**, 316 (1960).
[30] F. Tegenfeldt and J. Conrad, Nucl. Instrum. Methods Phys. Res., Sect. A **539**, 407 (2005).
[31] G. J. Feldman and R. D. Cousins, Phys. Rev. D **57**, 3873 (1998).
[32] E. Waxman and J. Bahcall, Phys. Rev. D **59**, 023002 (1998); S. Razzaque, P. Meszaros, and E. Waxman, Phys. Rev. D **68**, 083001 (2003).
[33] L. A. Anchordoqui, H. Goldberg, D. Hooper, S. Sarkar, and A. M. Taylor, Phys. Rev. D **76**, 123008 (2007).

PHYSICAL REVIEW D **82,** 103012 (2010)

Constraints on neutrino-nucleon interactions at energies of 1 EeV with the IceCube Neutrino Observatory

Shigeru Yoshida*

Department of Physics, Graduate School of Science, Chiba University, Chiba 263-8522, Japan

(Received 8 September 2010; published 22 November 2010)

A search for extremely high energy cosmic neutrinos has been carried out with the IceCube Neutrino Observatory. The main signals in the search are neutrino-induced energetic charged leptons and their rate depends on the neutrino-nucleon cross section. The upper limit on the neutrino flux has implications for possible new physics beyond the standard model such as the extra space-time dimension scenarios which lead to a cross section much higher than the standard particle physics prediction. In this study we constrain the neutrino-nucleon cross section at energies beyond 10^9 GeV with the IceCube observation. The constraints are obtained as a function of the extraterrestrial neutrino flux in the relevant energy range, which accounts for the astrophysical uncertainty of neutrino production models.

DOI: 10.1103/PhysRevD.82.103012 PACS numbers: 98.70.Sa, 13.15.+g, 95.85.Ry

I. INTRODUCTION

High energy cosmic neutrino observations provide a rare opportunity to explore the neutrino-nucleon (νN) interaction behavior beyond energies accessible by the present accelerators. These neutrinos interact during their propagation in the Earth and produce energetic muons and taus. These secondary leptons reach underground neutrino detectors and leave detectable signals. The detection rate is, therefore, sensitive to neutrino-nucleon interaction probability. The center-of-mass energy of the collision, $\sqrt{s}$, is well above $\sim$10 TeV for cosmic neutrino energies on the order of 1 EeV ($= 10^9$ GeV). This is a representative energy range for the bulk of the GZK (Greisen-Zatsepin-Kuzmin) cosmogenic neutrinos, generated by the interactions between the highest energy cosmic ray nucleons and the cosmic microwave background photons [1].

The νN collision cross section can vary greatly if nonstandard particle physics beyond the standard model (SM) is considered in the high energy regime of $\sqrt{s} \gg$ TeV. The extra-dimension scenarios, for example, have predicted such effects [2,3]. In these scenarios, the virtual exchange of the Kaluza-Klein graviton [2] or microscopic black hole production [4] leads to a substantial increase of the neutrino-nucleon cross section by more than 2 orders of magnitude above the SM prediction. The effect would be sizable enough to affect the expected annual event rate [$O(0.1 - 1)$] of the GZK neutrinos in the $\sim$km^3 instrumentation volume of an underground neutrino telescope such as the IceCube observatory. Thereby, the search for extremely high energy (EHE) cosmic neutrinos leads to constraints on nonstandard particle physics [5].

The IceCube neutrino observatory has already begun EHE neutrino hunting with the partially deployed underground optical sensor array [6]. The 2007 partial IceCube detector realized a $\sim$0.7 km^2 effective area for muons with 10^9 GeV and recently placed a limit on the flux of EHE neutrinos approximately an order of magnitude higher than the expected GZK cosmogenic neutrino intensities with 242 days of observation [7]. Since new particle physics may vary the cross section by more than an order of magnitude as we noted above, this result should already imply a meaningful bound on the νN cross section. In this paper, we study the constraint on the νN cross section ($\sigma_{\nu N}$) by the null detection of EHE neutrinos with the 2007 IceCube observation. A model-independent bound is derived by estimating the lepton intensity at the IceCube depth with the SM cross section scaled by a constant. The constraint is displayed in the form of the excluded region on the plane of the cosmic neutrino flux and $\sigma_{\nu N}$. It is equivalent to an upper bound on $\sigma_{\nu N}$ for a given flux of astrophysical EHE neutrinos. We also study the model-dependent constraint on the microscopic black hole creation by neutrino-nucleon collision predicted in the extra-dimension scenario [5]. We calculate the fluxes of leptons propagating in the Earth including the black hole cross section and the final states to estimate expected event rate in an equivalent IceCube 2007 measurement as a function of extraterrestrial neutrino intensity. The null detection of signal candidates leads to a constraint on this particular scenario.

There are several works on model-independent upper bounds of $\sigma_{\nu N}$ using the observational limit of EHE neutrino flux in the literature. References [3,4,8] derived the bound using the results of horizontal air shower search by AGASA [9] and Fly's Eye [10]. References [8,11] set the limit based upon the flux bound by the RICE experiment [12]. Our approach in the present study is different mainly in two respects. The previous works assumed the GZK cosmogenic neutrino bulk as the *guaranteed* beam and deduced the cross section limit using the GZK neutrino intensity. Here extraterrestrial neutrino intensity is considered a free parameter. This method is an application of the

*syoshida@hepburn.s.chiba-u.ac.jp
URL: http://www.ppl.phys.chiba-u.jp/~syoshida

technique to derive the flux limit based upon the quasidifferential event rate [7,12,13], which is independent of specific neutrino flux models. It is valid when the cosmic neutrino flux and the cross section $\sigma_{\nu N}$ do not rapidly change over a decade of a given neutrino energy. As EHE cosmic ray composition and their origin are still quite uncertain, this approach provides more appropriate conservative limits on $\sigma_{\nu N}$. It also allows estimation of the minimum intensity of neutrino flux required to constrain the cross section. Another difference is that the previous works introduced the simplification that event rate solely depends on rates of electromagnetic or hadronic cascades directly initiated by neutrinos inside the effective volume of the detector. This is in fact a good approximation for the RICE experiment which is sensitive to radio emission from shower events. However, underground neutrino telescopes such as IceCube have larger effective areas for through-going muons and taus in EHE neutrino search [14–16]. This study of the model-independent limit includes calculation of not just intensities of neutrinos but also the secondary muon and tau fluxes reaching the detection volume for a given $\sigma_{\nu N}$ and includes their contributions in the overall event rate.

The paper is outlined as follows: First we discuss the model-independent constraint in Sec. II. The method to calculate the neutrino and the secondary lepton propagation from the Earth's surface to the IceCube detector depth is described. The fluxes for different strengths of $\sigma_{\nu N}$ are calculated and the resultant constraint is shown for both $\sigma_{\nu N}$ and the cosmic neutrino flux at neutrino energies of 1 and 10 EeV, respectively. Section III describes the constraint on the microscopic black hole production by neutrino-nucleon interaction as an example of the model-dependent bound on $\sigma_{\nu N}$. Fluxes of muons and taus from evaporation of black holes produced in the neutrino-nucleon collision in the Earth are calculated. Their contributions, as well as those from contained hadronic showers induced directly by the evaporation, would give an observable event rate in the IceCube 2007 measurement, and thereby put constraints on the black hole scenario. We summarize our conclusions in Sec. IV.

II. MODEL-INDEPENDENT CONSTRAINT ON THE NEUTRINO-NUCLEON CROSS SECTION

The flux limit obtained by the present IceCube observations allows us to place an upper bound on the neutrino-nucleon cross section in a model-independent manner; new physics cannot increase $\sigma_{\nu N}$ too much, otherwise EHE neutrinos would have produced observable events. As an underground neutrino telescope is sensitive to not just shower events induced from neutrinos, but also to through-going muons and taus generated by the neutrino-nucleon scattering, one must understand how much fluxes of these leptons reaching an underground detection volume is increased with $\sigma_{\nu N}$. In this section, we first discuss our method to calculate intensities of neutrinos, muons, and taus at the underground depth of the IceCube observatory for a wide range of $\sigma_{\nu N}$ strength, followed by a description of how they would contribute to the event rate. Finally the constraint on both $\sigma_{\nu N}$ and cosmic neutrino flux is described together with the relevant discussions.

A. The method

Given a neutrino flux at the surface of the Earth, the neutrino and charged lepton fluxes at the IceCube depth are calculated by the coupled transportation equations [16]:

$$\begin{aligned}\frac{dJ_\nu}{dX} = & -N_A\sigma_{\nu N,\mathrm{CC+NC}}J_\nu + \frac{m_l}{c\rho\tau_l^d}\int dE_l\frac{1}{E_l}\frac{dn_l^d}{dE_\nu}J_l(E_l)\\ & + N_A\int dE'_\nu\frac{d\sigma_{\nu N,\mathrm{NC}}}{dE_\nu}J_\nu(E'_\nu)\\ & + N_A\int dE'_l\frac{d\sigma_{lN,\mathrm{CC}}}{dE_\nu}J_l(E'_l),\end{aligned} \tag{1}$$

$$\begin{aligned}\frac{dJ_l}{dX} = & -N_A\sigma_{lN}J_l - \frac{m_l}{c\rho\tau_l^d E_l}J_l\\ & + N_A\int dE'_\nu\frac{d\sigma_{\nu N,\mathrm{CC}}}{dE_l}J_\nu(E'_\nu) + N_A\int dE'_l\frac{d\sigma_{lN}}{dE_l}J_l(E'_l)\\ & + \frac{m_l}{c\rho\tau_l^d}\int dE'_l\frac{1}{E'_l}\frac{dn_l^d}{dE_l}J_l(E'_l),\end{aligned} \tag{2}$$

where $J_l = dN_l/dE_l$ and $J_\nu = dN_\nu/dE_\nu$ are differential fluxes of charged leptons (muons and taus) and neutrinos, respectively. X is the column density, N_A is the Avogadro's number, ρ is the local density of the medium (rock/ice) in the propagation path, σ is the relevant interaction cross section, dn_l^d/dE is the energy distribution of the decay products which is derived from the decay rate per unit energy, c is the speed of light, and m_l and τ_l^d are the mass and the decay life time of the lepton l, respectively. CC(NC) denotes the charged (neutral) current interaction. In this study we scale $\sigma_{\nu N}$ to that of the SM prediction with the factor N_{scale}, i.e., $\sigma_{\nu N} \equiv N_{\mathrm{scale}}\sigma_{\nu N}^{\mathrm{SM}}$. It is an extremely intensive computational task to resolve the coupled questions above for every possible value of $\sigma_{\nu N}$. To avoid this difficulty, we introduce two assumptions to decouple the calculation of J_ν from the charged lepton transportation equation. The first is that distortion of the neutrino spectrum by the neutral current reaction is small and the other is that regeneration of neutrinos due to muon and tau decay and their weak interactions is negligible. These are very good approximations in the energy region above 10^8 GeV where even tau is unlikely to decay before reaching the IceCube instrumentation volume. Then the neutrino flux is simply given by the beam dumping factor as

$$J_\nu(E_\nu, X_{\mathrm{IC}}) = J_\nu(E_\nu, 0)e^{-N_{\mathrm{scale}}\sigma_{\nu N}^{\mathrm{SM,CC}}X_{\mathrm{IC}}}, \tag{3}$$

where $X_{\rm IC}$ is column density of the propagation path from the Earth's surface to the IceCube depth. The charged lepton fluxes, $J_{l=\mu,\tau}(E_l, X_{\rm IC})$, are obtained as

$$J_{\mu,\tau}(E_{\mu,\tau}, X_{\rm IC}) = N_A \int_0^{X_{\rm IC}} dX \int dE'_{\mu,\tau} \frac{dN_{\mu,\tau}}{dE_{\mu,\tau}}(E'_{\mu,\tau} \to E_{\mu,\tau}) \times \int dE_\nu N_{\rm scale} \frac{d\sigma_{\nu N}^{\rm SM,CC}}{dE'_{\mu,\tau}} \times J_\nu(E_\nu, 0) e^{-N_{\rm scale}\sigma_{\nu N}^{\rm SM,CC} X}. \quad (4)$$

Here $dN_{\mu,\tau}/dE_{\mu,\tau}(E'_{\mu,\tau} \to E_{\mu,\tau})$ represents distributions of muons and taus with energy of $E_{\mu,\tau}$ at $X_{\rm IC}$ created by νN collisions at depth X with an energy $E'_{\mu,\tau}$. This is calculated in the transportation equation, Eq. (2), with a replacement of $J_\nu(E'_\nu)$ by Eq. (3).

Calculation of the neutrino and the charged lepton fluxes with this method is feasible for a wide range of $N_{\rm scale}$ without any intensive computation. A comparison of the calculated fluxes with those obtained without the introduced simplification for a limited range of $N_{\rm scale}$ indicates that the relative difference we found in the resultant $J_{\nu,\mu,\tau}(X_{\rm IC})$ is within 40%. Since this analysis involves an *order* of magnitude of increase in $\sigma_{\nu N}$, the introduced approximations provide sufficient accuracy for the present study.

Figure 1 shows the calculated intensities of the secondary muons and taus for various $N_{\rm scale}$ factors. Here the primary neutrino spectrum is assumed to follow the GZK cosmogenic spectrum and flux calculated in Ref. [17] assuming an all-proton cosmic ray composition with a moderately strong source evolution, $(1+z)^m$ with $m = 4$ extending to $z = 4$. One can see that the intensity is nearly proportional to $N_{\rm scale}$ as expected since the interaction probability to generate muons and taus linearly depends on $\sigma_{\nu N}$. It should be pointed out, however, that the dependence starts to deviate from the complete linearity when the propagation distance is comparable to the mean free path of neutrinos, as one can find in the case of $N_{\rm scale} = 10$ in the figure. This is because the neutrino beam dumping factor in Eq. (3) becomes significant under these circumstances.

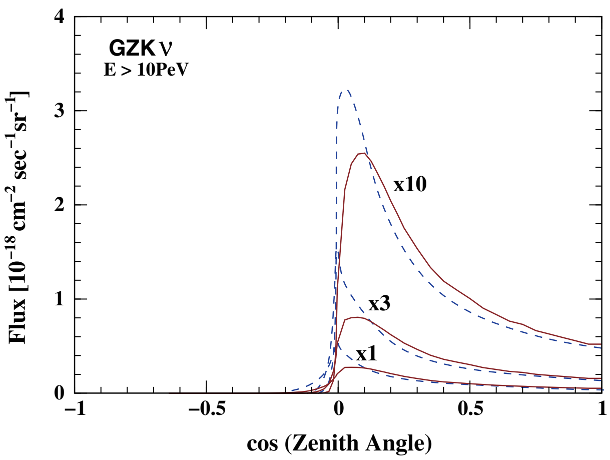

FIG. 1 (color online). Integral fluxes of the muon and taus above 10 PeV ($= 10^7$ GeV) at IceCube depth (~ 1450 m) for GZK cosmogenic neutrinos [17]. The solid lines represent muons while the dashed lines represent taus. Numbers on each of the curves are the multiplication factors ($N_{\rm scale}$) that enhance the standard νN cross section [19] in the relevant calculations.

The flux yield of leptons at the IceCube depth, Y^l_ν ($l = \nu$'s, μ, τ), originating from neutrinos with a given energy at the Earth's surface, E^s_ν, is given by Eq. (4) for muons and taus and by Eq. (3) for neutrinos, with an insertion of $J_\nu(E_\nu, 0) = \delta(E_\nu - E^s_\nu)$. Here E^s_ν denotes a given incoming neutrino energy at the Earth's surface. The resultant event rate per neutrino energy decade is then obtained by [7,12,13],

$$N_\nu(E^s_\nu) = \sum_{\nu=\nu_e,\nu_\mu,\nu_\tau} \frac{1}{3} \frac{dJ_{\nu_e+\nu_\mu+\nu_\tau}}{d\log E_\nu}(E^s_\nu) \int d\Omega \sum_{l=\nu_e,\nu_\mu,\nu_\tau,\mu,\tau} \times \int dE_l A_l(E_l) Y^l_\nu(E^s_\nu, E_l, X_{\rm IC}(\Omega), N_{\rm scale}), \quad (5)$$

where A_l is the effective area of the IceCube to detect the lepton l. In the equation above, the $l = \mu$, τ terms represent the through-going track events while the contribution of events directly induced by neutrinos inside the detection volume is represented by the terms $l = \nu_e$, ν_μ, ν_τ. The effective area for ν's, A_ν, is proportional to $\sigma_{\nu N}$ i.e., $N_{\rm scale}$ so the rate of contained shower events is linearly dependent on the neutrino-nucleon scattering probability. Note that the differential limit of the neutrino flux is given by Eq. (5) for $N_{\rm scale} = 1$ with $N_\nu = \bar{\mu}_{90}$ which corresponds to the 90% confidence level average upper limit. It calculates an upper bound of the number of events observed with bin width of a decade of energy with the condition that energy dependence of neutrino flux multiplied by the effective area behaves as $\sim 1/E$ [4,12]. Limiting $\sigma_{\nu N}$ in the present analysis corresponds to an extraction of the relation between $N_{\rm scale}$ and the (unknown) cosmic neutrino flux $J_{\nu_e+\nu_\mu+\nu_\tau}$ yielding $N_\nu = \bar{\mu}_{90}$. The obtained constraints on $\sigma_{\nu N}$ is represented as a function of $J_{\nu_e+\nu_\mu+\nu_\tau}$ for a given energy of E^s_ν. It consequently accounts for astrophysical uncertainties on the cosmic neutrino flux.

In scenarios with extra dimensions and strong gravity, Kaluza-Klein gravitons can change only the neutral current (NC) cross section because gravitons are electrically neutral. Any scenarios belonging to this category can be investigated by scaling only $\sigma_{\nu N}^{\rm NC}$ in the present analysis. The event rate calculation by Eq. (5) is then performed for $Y^l_\nu(N_{\rm scale} = 1)$ with the effective area for ν's, A_ν, enhanced by $(\sigma_{\nu N}^{\rm SM,CC} + N_{\rm scale}\sigma_{\nu N}^{\rm SM,NC})/(\sigma_{\nu N}^{\rm SM,CC} + \sigma_{\nu N}^{\rm SM,NC})$ since the rate of detectable events via the NC reaction by IceCube is proportional to $\sigma_{\nu N}^{\rm NC}$. We also show the constraint in this case.

B. Results

In this analysis we use the IceCube observation results with 242 days data in 2007 to limit $\sigma_{\nu N}$ using Eq. (5). No detection of signal candidates in the measurement has led to an upper limit of the neutrino flux of $1.4 \times 10^{-6}\ \mathrm{GeV\,cm^{-2}\,sec^{-1}\,sr^{-1}}$ [7] in the energy range from 3×10^7 to 3×10^9 GeV. The effective area A_l is $\sim 0.7\ \mathrm{km}^2$ for μ, $\sim 0.4\ \mathrm{km}^2$ for τ, and $3 \times 10^{-4}\ \mathrm{km}^2$ for ν's [7]. Constraints on $\sigma_{\nu N}$ are then derived with Eq. (5). The results for $E_\nu^s = 10^9$ and 10^{10} GeV are shown in Fig. 2. Enhancing the charged current cross section by more than a factor of 30 for $E_\nu = 1$ EeV (10^9 GeV) is disfavored if the astrophysical neutrino intensities are around $\sim 10^{-7}\ \mathrm{GeV\,cm^{-2}\,sec^{-1}\,sr^{-1}}$, near the upper bound of the GZK cosmogenic neutrino bulk. Note that neutrino-nucleon collision with $E_\nu = 1$ EeV corresponds to $\sqrt{s} \sim 40$ TeV and the present limit on $\sigma_{\nu N}$ would place a rather strong constraint on scenarios with extra dimensions and strong gravity, although more accurate estimation requires studies with a model-dependent approach which implements the cross section and the final-state particles from the collision predicted by a given particle physics model. Taking into account uncertainty on the astrophysical neutrino fluxes, any model that increases

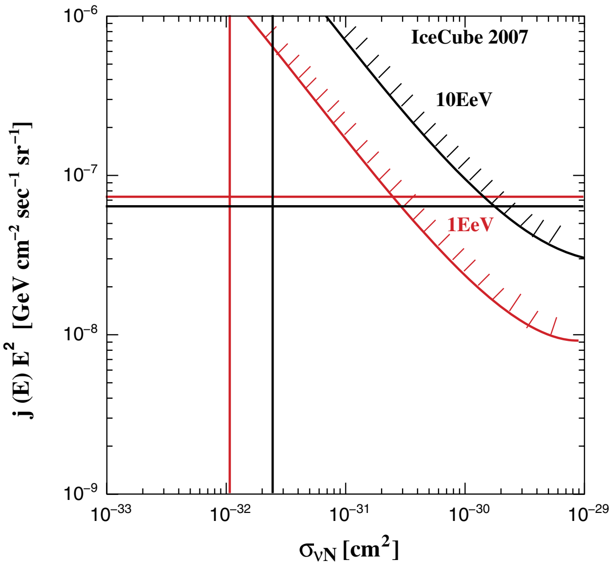

FIG. 2 (color online). Constraints on the all-flavor sum of cosmic neutrino flux and the charged current νN cross section based on the null detection of neutrino signals by the IceCube 2007 observation. The right upper region is excluded by the present analysis. The horizontal lines provide references of the expected GZK cosmogenic neutrino fluxes [20] and the vertical lines correspond to the SM cross section [19].

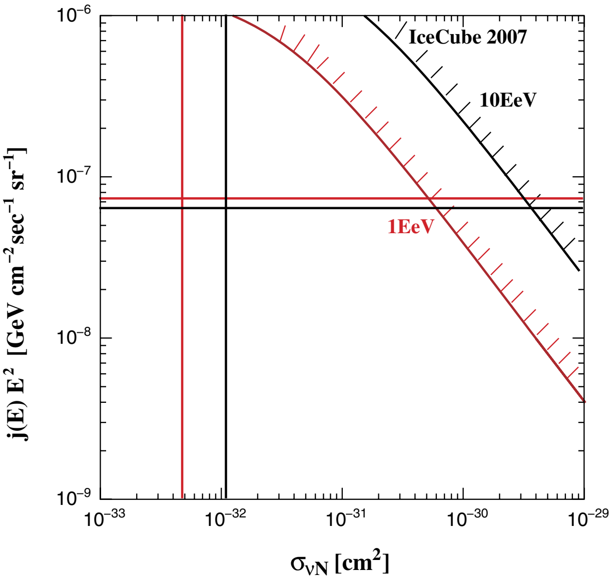

FIG. 3 (color online). Constraints on the all-flavor sum of cosmic neutrino flux and the neutral current νN cross section for the scenario that only the neutral current reaction is enhanced by a new physics beyond the standard model. The right upper region is excluded by the present analysis. The horizontal lines provide references of the expected GZK cosmogenic neutrino fluxes [20] and the vertical lines correspond to the SM cross section [19].

the neutrino-nucleon cross section to produce charged leptons by more than 2 orders of magnitude at $\sqrt{s} \sim 40$ TeV is disfavored by the IceCube observation. However, we should point out that the IceCube 2007 data could not constrain the charged current cross section if the intensity of cosmic neutrinos in the relevant energy region is fewer than $\sim 10^{-8}\ \mathrm{GeV\,cm^{-2}\,sec^{-1}\,sr^{-1}}$, within the lower range of prediction for the cosmogenic neutrino fluxes [18]. Absorption effects in the Earth becomes sizable in this case, resulting in less sensitivity to the cross section. This limitation will be improved for larger detection areas of the full IceCube detector.

Figure 3 shows the constraints when only the NC cross section is varied. Enhancement of $\sigma_{\nu N}^{\rm NC}$ by a factor beyond 100 at $\sqrt{s} \sim 40$ TeV is disfavored, but this strongly depends on the cosmic neutrino flux one assumes. Because the NC interaction does not absorb neutrinos during their propagation though the Earth, the cross section could be bounded even in the case when the neutrino flux is small, but the limit becomes rather weak; the allowed maximum enhancement factor is on the order of $\sim 10^3$.

III. CONSTRAINT ON THE MICROSCOPIC BLACK HOLE PRODUCTION

A constraint on a specific physics model that enhances the neutrino-nucleon cross section is obtained by the same

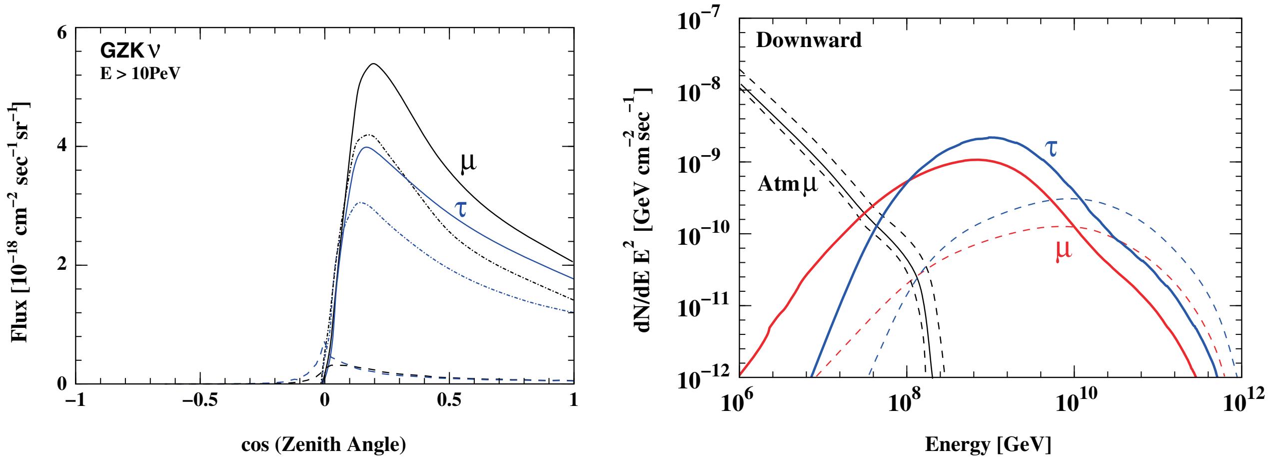

FIG. 4 (color online). (Left) integral fluxes of the muon and taus above 10 PeV ($= 10^7$ GeV) at IceCube depth (~ 1450 m) of the GZK cosmogenic neutrinos [17] in case of the microscopic black hole creation scenario [5] for $(M_D, x_{\min}) = (1\text{ TeV}, 1)$ (solid line), (1 TeV,3) (dotted-dashed line). The dashed line corresponds to the intensities obtained by the SM νN cross section [19]. (Right) energy spectra of the GZK ν induced muons and taus at IceCube depth with downgoing [i.e. cos(zenith) ≥ 0] geometry expected by the black hole model for $(M_D, x_{\min}) = (1\text{ TeV}, 1)$. The spectra produced by the SM cross section are also shown as dashed lines for comparison. The curve labeled "Atm μ" represents the atmospheric muon intensity estimated by the IceCube observation with its uncertainty expressed by the two dashed lines [21].

procedure for the model-independent bound, except the transport equations, Eqs. (1) and (2), would have total and differential neutrino cross section provided by both SM and the new model. Here we study the model of black hole creation as a possible consequence of low-scale gravity that may occur if space-time has more than four dimensions. We use the predicted cross section of lack hole production via the neutrino-nucleon scattering described by Ref. [5], parametrized by the Planck scale M_D, the ratio of the minimal black hole mass to the Planck scale $x_{\min}$, and the space-time dimension $D = 4 + n$. In this paper $n = 6$ and $M_D = 1$ TeV are assumed as representative numbers. The resultant cross section may exceed SM interaction rates by 2 orders of magnitude or even greater. Therefore, the model-independent bound shown in the previous section indicated that the 2007 IceCube observation should be already sensitive to some of the parameter space in the black hole creation model.

The final states in the neutrino-nucleon scattering in this model are quite different from the SM case. Black holes evaporate and generate multiple particles of all kinds, like leptons, quarks, gluons, and bosons. These products are distributed according to the number of degrees of freedom. Consequently, the average number of muons and taus, $N_{\mu+\tau}$, are $1/30$ of all particle average multiplicity $\bar{N}$, which is also determined by the specific model. As $\bar{N} \sim 10$ at neutrino energy of $E_\nu = 1$ EeV, multiple muon or tau production would very rarely occur. Then the *effective* differential cross section $d\sigma_{\nu N}/dE_{\mu,\tau}$ in the transport equations (1) and (2) in the black hole model is represented by

$$\frac{d\sigma_{\nu N}}{dE_{\mu,\tau}} = \frac{N_{\mu+\tau}(E_\nu)}{2}\sigma_{\nu N}(E_\nu)\frac{\bar{N}(E_\nu)}{2E_\nu} \tag{6}$$

with $0 \leq E_{\mu,\tau} \leq 2E_\nu/\bar{N}$. We take $\bar{N}$ from Ref. [5] in the present calculation. In this specific scenario, a muon or a tau carries a small fraction ($1/\bar{N} \sim 0.1$) of incoming neutrino energy E_ν in average, in contrast to the SM collision that takes away $1 - y \sim 0.8$ of neutrino energy by a generated charged lepton.

Solving the transport equations gives the intensities of secondary muons and taus, which are shown in Fig. 4. One can find in the zenith angle distribution (the left panel) that the intensities are increased by more than 2 orders of magnitude above the SM case. The large increase of $\sigma_{\nu N}$ enhances downgoing event rates while the upgoing muon and tau rates are more suppressed. The zenith angle distribution is consistent with the original work in Ref. [5]. It should also be noted that the energy spectra is substantially modified from those in the SM case (the right panel). The peak energy is around 1 EeV, an order of magnitude lower than the SM spectrum, reflecting the fact that a smaller fraction of neutrino energy is channeled into muons and taus via the black hole evaporation. The peak happens to match the most sensitive energy region in the IceCube EHE neutrino search [7].

Because $\sigma_{\nu N}$ is solely predicted by the specific model, the model-dependent constraints on νN interactions is represented in the plane of extraterrestrial neutrino flux and the number of events the IceCube 2007 run would have detected. Figure 5 shows the number of events as a function of the neutrino intensity at energy of 1 EeV, if the

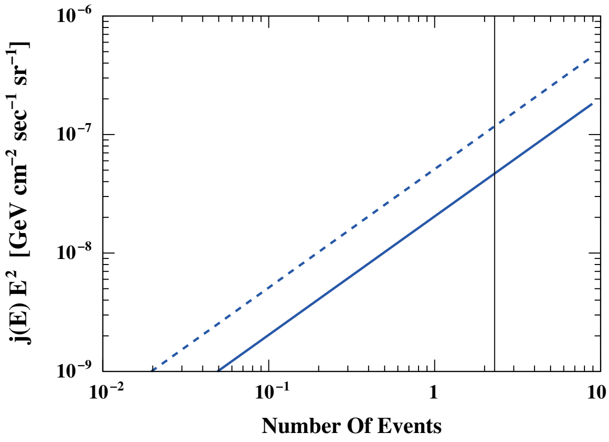

FIG. 5 (color online). Number of events as a function of extraterrestrial neutrino flux at 1 EeV for $(M_D, x_{\min}) = (1\ \text{TeV}, 1)$ (solid line), (1 TeV,3) (dashed line). The 90% C.L. line determined by the Poisson statistics is also shown as a vertical line for reference.

microscopic black hole evaporation occurs as in Ref. [5]. The Poisson statistics then determine the upper limit of neutrino flux that can be still consistent with the null observation by IceCube. It is indicated that the neutrino intensity of 10^{-7} GeV cm^{-2} sec^{-1} sr^{-1} is disfavored in this scenario. More parameter space of M_D and $x_{\min}$ will be further constrained by near future observation with IceCube whose detection volume is rapidly growing with an increase of the number of detectors in operation.

IV. CONCLUSIONS

The IceCube 2007 observation indicated that any scenario to enhance either the NC or both the NC and CC equivalent cross section by more than 100 at $\sqrt{s} \sim 40$ TeV is unlikely if the sum of the all three flavors of astrophysical neutrino fluxes are greater than $\sim 3 \times 10^{-8}$ GeV cm^{-2} sec^{-1} sr^{-1} in the EeV region. Many models of the GZK cosmogenic neutrinos exist to predict this flux range, thus the present constraints limit new particle physics beyond the SM, unless the extraterrestrial neutrino intensity is smaller than the expectation. The example of the model-dependent bound on $\sigma_{\nu N}$ has been also shown for the microscopic black hole evaporation scenario. A high cosmic neutrino intensity constrains the parameter space of the black hole creation. Future observation by the rapidly growing IceCube detectors will strongly limit particle physics models which predict an increase of neutrino-nucleon interaction probability.

ACKNOWLEDGMENTS

We wish to acknowledge the IceCube Collaboration for useful discussions and suggestions. We thank Jonathan Feng for helpful discussions on the physics models beyond the standard model and providing numerical data of the cross section and multiplicity distribution predicted by the micro black hole creation scenario. We also wish to thank Lisa Gerhardt for helpful comments on the manuscript. This work was supported in part by the Grants-in-Aid in Scientific Research from the JSPS (Japan Society for the Promotion of Science) in Japan.

[1] V. S. Beresinsky and G. T. Zatsepin, Phys. Lett. **28B**, 423 (1969).
[2] P. Jain, D. W. McKay, S. Panda, and J. P. Ralston, Phys. Lett. B **484**, 267 (2000).
[3] C. Tyler, A. V. Olinto, and G. Sigl, Phys. Rev. D **63**, 055001 (2001).
[4] L. A. Anchordoqui, J. L. Feng, H. Goldberg, and A. D. Shapere, Phys. Rev. D **66**, 103002 (2002).
[5] J. Alvarez-Muñiz, J. L. Feng, F. Halzen, T. Han, and D. Hooper, Phys. Rev. D **65**, 124015 (2002).
[6] A. Achterberg *et al.* (IceCube Collaboration), Astropart. Phys. **26**, 155 (2006).
[7] R. Abbasi *et al.* (IceCube Collaboration), Phys. Rev. D **82**, 072003 (2010).
[8] L. A. Anchordoqui, Z. Fodor, S. D. Katz, A. Ringwald, and H. Tu, J. Cosmol. Astropart. Phys. 06 (2005) 013.
[9] S. Yoshida *et al.* (AGASA Collaboration), in *Proceedings of the 27th International Cosmic Ray Conference* (Copernics Gesellschaft, Hamburg, Germany, 2001), Vol. 3, p. 1142.
[10] R. M. Baltrusaitis *et al.*, Phys. Rev. D **31**, 2192 (1985).
[11] V. Barger, P. Huber, and D. Marfatia, Phys. Lett. B **642**, 333 (2006).
[12] I. Kravchenko *et al.*, Phys. Rev. D **73**, 082002 (2006).
[13] X. Bertou *et al.*, Astropart. Phys. **17**, 183 (2002).
[14] J. Alvarez-Muñiz and F. Halzen, Phys. Rev. D **63**, 037302 (2001).
[15] J. Jones, I. Mocioiu, M. H. Reno, and I. Sarcevic, Phys. Rev. D **69**, 033004 (2004).
[16] S. Yoshida, R. Ishibashi, and H. Miyamoto, Phys. Rev. D **69**, 103004 (2004).
[17] S. Yoshida, H. Dai, C. C. H. Jui, and P. Sommers, Astrophys. J. **479**, 547 (1997).
[18] M. Ahlers *et al.*, Astropart. Phys. **34**, 106 (2010).
[19] R. Gandhi, C. Quigg, M. H. Reno, and I. Sarcevic, Astropart. Phys. **5**, 81 (1996); Phys. Rev. D **58**, 093009 (1998).
[20] O. E. Kalashev, V. A. Kuzmin, D. V. Semikoz, and G. Sigl, Phys. Rev. D **66**, 063004 (2002).
[21] A. Ishihara (IceCube Collaboration), arXiv:0711.0353.

PHYSICAL REVIEW D **82,** 072003 (2010)

First search for extremely high energy cosmogenic neutrinos with the IceCube Neutrino Observatory

R. Abbasi,[28] Y. Abdou,[22] T. Abu-Zayyad,[33] J. Adams,[16] J. A. Aguilar,[28] M. Ahlers,[32] K. Andeen,[28] J. Auffenberg,[39] X. Bai,[31] M. Baker,[28] S. W. Barwick,[24] R. Bay,[7] J. L. Bazo Alba,[40] K. Beattie,[8] J. J. Beatty,[18,19] S. Bechet,[13] J. K. Becker,[10] K.-H. Becker,[39] M. L. Benabderrahmane,[40] J. Berdermann,[40] P. Berghaus,[28] D. Berley,[17] E. Bernardini,[40] D. Bertrand,[13] D. Z. Besson,[26] M. Bissok,[1] E. Blaufuss,[17] D. J. Boersma,[1] C. Bohm,[34] S. Böser,[11] O. Botner,[37] L. Bradley,[36] J. Braun,[28] S. Buitink,[8] M. Carson,[22] D. Chirkin,[28] B. Christy,[17] J. Clem,[31] F. Clevermann,[20] S. Cohen,[25] C. Colnard,[23] D. F. Cowen,[36,35] M. V. D'Agostino,[7] M. Danninger,[34] J. C. Davis,[18] C. De Clercq,[14] L. Demirörs,[25] O. Depaepe,[14] F. Descamps,[22] P. Desiati,[28] G. de Vries-Uiterweerd,[22] T. DeYoung,[36] J. C. Díaz-Vélez,[28] J. Dreyer,[10] J. P. Dumm,[28] M. R. Duvoort,[38] R. Ehrlich,[17] J. Eisch,[28] R. W. Ellsworth,[17] O. Engdegård,[37] S. Euler,[1] P. A. Evenson,[31] O. Fadiran,[4] A. R. Fazely,[6] T. Feusels,[22] K. Filimonov,[7] C. Finley,[34] M. M. Foerster,[36] B. D. Fox,[36] A. Franckowiak,[11] R. Franke,[40] T. K. Gaisser,[31] J. Gallagher,[27] R. Ganugapati,[28] M. Geisler,[1] L. Gerhardt,[8,7] L. Gladstone,[28] T. Glüsenkamp,[1] A. Goldschmidt,[8] J. A. Goodman,[17] D. Grant,[21] T. Griesel,[29] A. Groß,[16,23] S. Grullon,[28] M. Gurtner,[39] C. Ha,[36] A. Hallgren,[37] F. Halzen,[28] K. Han,[16] K. Hanson,[28] K. Helbing,[39] P. Herquet,[30] S. Hickford,[16] G. C. Hill,[28] K. D. Hoffman,[17] A. Homeier,[11] K. Hoshina,[28] D. Hubert,[14] W. Huelsnitz,[17] J.-P. Hülß,[1] P. O. Hulth,[34] K. Hultqvist,[34] S. Hussain,[31] R. L. Imlay,[6] A. Ishihara,[15,*] J. Jacobsen,[28] G. S. Japaridze,[4] H. Johansson,[34] J. M. Joseph,[8] K.-H. Kampert,[39] A. Kappes,[28,†] T. Karg,[39] A. Karle,[28] J. L. Kelley,[28] N. Kemming,[9] P. Kenny,[26] J. Kiryluk,[8,7] F. Kislat,[40] S. R. Klein,[8,7] S. Knops,[1] J.-H. Köhne,[20] G. Kohnen,[30] H. Kolanoski,[9] L. Köpke,[29] D. J. Koskinen,[36] M. Kowalski,[11] T. Kowarik,[29] M. Krasberg,[28] T. Krings,[1] G. Kroll,[29] K. Kuehn,[18] T. Kuwabara,[31] M. Labare,[13] S. Lafebre,[36] K. Laihem,[1] H. Landsman,[28] R. Lauer,[40] R. Lehmann,[9] D. Lennarz,[1] J. Lünemann,[29] J. Madsen,[33] P. Majumdar,[40] R. Maruyama,[28] K. Mase,[15,‡] H. S. Matis,[8] M. Matusik,[39] K. Meagher,[17] M. Merck,[28] P. Mészáros,[35,36] T. Meures,[1] E. Middell,[40] N. Milke,[20] J. Miller,[37] T. Montaruli,[28,§] R. Morse,[28] S. M. Movit,[35] R. Nahnhauer,[40] J. W. Nam,[24] U. Naumann,[39] P. Nießen,[31] D. R. Nygren,[8] S. Odrowski,[23] A. Olivas,[17] M. Olivo,[37,10] M. Ono,[15] S. Panknin,[11] L. Paul,[1] C. Pérez de los Heros,[37] J. Petrovic,[13] A. Piegsa,[29] D. Pieloth,[20] R. Porrata,[7] J. Posselt,[39] P. B. Price,[7] M. Prikockis,[36] G. T. Przybylski,[8] K. Rawlins,[3] P. Redl,[17] E. Resconi,[23] W. Rhode,[20] M. Ribordy,[25] A. Rizzo,[14] J. P. Rodrigues,[28] P. Roth,[17] F. Rothmaier,[29] C. Rott,[18] C. Roucelle,[23] T. Ruhe,[20] D. Rutledge,[36] B. Ruzybayev,[31] D. Ryckbosch,[22] H.-G. Sander,[29] S. Sarkar,[32] K. Schatto,[29] S. Schlenstedt,[40] T. Schmidt,[17] D. Schneider,[28] A. Schukraft,[1] A. Schultes,[39] O. Schulz,[23] M. Schunck,[1] D. Seckel,[31] B. Semburg,[39] S. H. Seo,[34] Y. Sestayo,[23] S. Seunarine,[12] A. Silvestri,[24] A. Slipak,[36] G. M. Spiczak,[33] C. Spiering,[40] M. Stamatikos,[18,‖] T. Stanev,[31] G. Stephens,[36] T. Stezelberger,[8] R. G. Stokstad,[8] S. Stoyanov,[31] E. A. Strahler,[14] T. Straszheim,[17] G. W. Sullivan,[17] Q. Swillens,[13] I. Taboada,[5] A. Tamburro,[33] O. Tarasova,[40] A. Tepe,[5] S. Ter-Antonyan,[6] S. Tilav,[31] P. A. Toale,[36] D. Tosi,[40] D. Turčan,[17] N. van Eijndhoven,[14] J. Vandenbroucke,[7] A. Van Overloop,[22] J. van Santen,[9] B. Voigt,[40] C. Walck,[34] T. Waldenmaier,[9] M. Wallraff,[1] M. Walter,[40] C. Wendt,[28] S. Westerhoff,[28] N. Whitehorn,[28] K. Wiebe,[29] C. H. Wiebusch,[1] G. Wikström,[34] D. R. Williams,[2] R. Wischnewski,[40] H. Wissing,[17] K. Woschnagg,[7] C. Xu,[31] X. W. Xu,[6] G. Yodh,[24] S. Yoshida,[15,¶] and P. Zarzhitsky[2]

(IceCube Collaboration)

[1]*III. Physikalisches Institut, RWTH Aachen University, D-52056 Aachen, Germany*
[2]*Department of Physics and Astronomy, University of Alabama, Tuscaloosa, Alabama 35487, USA*
[3]*Department of Physics and Astronomy, University of Alaska Anchorage, 3211 Providence Dr., Anchorage, Alaska 99508, USA*
[4]*CTSPS, Clark-Atlanta University, Atlanta, Georgia 30314, USA*
[5]*School of Physics and Center for Relativistic Astrophysics, Georgia Institute of Technology, Atlanta, Georgia 30332, USA*
[6]*Department of Physics, Southern University, Baton Rouge, Louisiana 70813, USA*
[7]*Department of Physics, University of California, Berkeley, California 94720, USA*
[8]*Lawrence Berkeley National Laboratory, Berkeley, California 94720, USA*
[9]*Institut für Physik, Humboldt-Universität zu Berlin, D-12489 Berlin, Germany*
[10]*Fakultät für Physik and Astronomie, Ruhr-Universität Bochum, D-44780 Bochum, Germany*
[11]*Physikalisches Institut, Universität Bonn, Nussallee 12, D-53115 Bonn, Germany*
[12]*Department of Physics, University of the West Indies, Cave Hill Campus, Bridgetown BB11000, Barbados*
[13]*Université Libre de Bruxelles, Science Faculty CP230, B-1050 Brussels, Belgium*
[14]*Vrije Universiteit Brussel, Dienst ELEM, B-1050 Brussels, Belgium*
[15]*Department of Physics, Chiba University, Chiba 263-8522, Japan*
[16]*Department of Physics and Astronomy, University of Canterbury, Private Bag 4800, Christchurch, New Zealand*

[17]Department of Physics, University of Maryland, College Park, Maryland 20742, USA
[18]Department of Physics and Center for Cosmology and Astro-Particle Physics, Ohio State University, Columbus, Ohio 43210, USA
[19]Department of Astronomy, Ohio State University, Columbus, Ohio 43210, USA
[20]Department of Physics, TU Dortmund University, D-44221 Dortmund, Germany
[21]Department of Physics, University of Alberta, Edmonton, Alberta, Canada T6G 2G7
[22]Department of Subatomic and Radiation Physics, University of Gent, B-9000 Gent, Belgium
[23]Max-Planck-Institut für Kernphysik, D-69177 Heidelberg, Germany
[24]Department of Physics and Astronomy, University of California, Irvine, California 92697, USA
[25]Laboratory for High Energy Physics, École Polytechnique Fédérale, CH-1015 Lausanne, Switzerland
[26]Department of Physics and Astronomy, University of Kansas, Lawrence, Kansas 66045, USA
[27]Department of Astronomy, University of Wisconsin, Madison, Wisconsin 53706, USA
[28]Department of Physics, University of Wisconsin, Madison, Wisconsin 53706, USA
[29]Institute of Physics, University of Mainz, Staudinger Weg 7, D-55099 Mainz, Germany
[30]Université de Mons, 7000 Mons, Belgium
[31]Bartol Research Institute and Department of Physics and Astronomy, University of Delaware, Newark, Delaware 19716, USA
[32]Department of Physics, University of Oxford, 1 Keble Road, Oxford OX1 3NP, United Kingdom
[33]Department of Physics, University of Wisconsin, River Falls, Wisconsin 54022, USA
[34]Oskar Klein Centre and Department of Physics, Stockholm University, SE-10691 Stockholm, Sweden
[35]Department of Astronomy and Astrophysics, Pennsylvania State University, University Park, Pennsylvania 16802, USA
[36]Department of Physics, Pennsylvania State University, University Park, Pennsylvania 16802, USA
[37]Department of Physics and Astronomy, Uppsala University, Box 516, S-75120 Uppsala, Sweden
[38]Department of Physics and Astronomy, Utrecht University/SRON, NL-3584 CC Utrecht, The Netherlands
[39]Department of Physics, University of Wuppertal, D-42119 Wuppertal, Germany
[40]DESY, D-15735 Zeuthen, Germany

(Received 7 July 2010; published 7 October 2010)

We report on the results of the search for extremely-high energy neutrinos with energies above 10^7 GeV obtained with the partially ($\sim 30\%$) constructed IceCube in 2007. From the absence of signal events in the sample of 242.1 days of effective live time, we derive a 90% C.L. model independent differential upper limit based on the number of signal events per energy decade at $E^2\phi_{\nu_e+\nu_\mu+\nu_\tau} \simeq 1.4 \times 10^{-6}$ GeV cm^{-2} sec^{-1} sr^{-1} for neutrinos in the energy range from 3×10^7 to 3×10^9 GeV.

DOI: 10.1103/PhysRevD.82.072003 PACS numbers: 98.70.Sa, 95.85.Ry

I. INTRODUCTION

Detection of extremely-high energy (EHE) neutrinos with energies greater than 10^7 GeV may shed light on the long standing puzzle of the origin of EHE cosmic rays [1,2]. Several observational results have indicated that these EHE cosmic rays (EHECRs) are of extragalactic origin [3]. Further elucidation of their production mechanism by EHECR observation is, however, limited because the collisions of EHECR with the cosmic microwave background photons—known as the Greisen-Zatsepin-Kuzmin (GZK) mechanism [4]—prevent EHECRs from propagating over cosmological distances without losing a sizable fraction of their energy. On the other hand, cosmogenic neutrinos [5] produced by the GZK mechanism via photoproduced π meson decay as $\pi^\pm \rightarrow \mu^\pm \nu_\mu \rightarrow e^\pm \nu_e \nu_\mu$ carry information on the EHECR source evolution and the maximum energy of EHECRs at their production sites [6].

Detection of these EHE neutrinos is an experimental challenge because the very low EHE neutrino fluxes require a very large detector. The large size of the IceCube neutrino observatory [7], currently under construction at the geographic South Pole, will make it more effective than previous experiments in the search for these neutrinos [8,9]. Interactions of ν_μ, ν_e, and ν_τ and their antiparticles are observed through the Cherenkov radiation emitted by secondary particles. In the following, we do not distinguish between ν and $\bar{\nu}$; the simulations and sensitivity calculations assume an equal mixture of particles and antiparticles.

In this paper we will describe the first results of a search for signatures of cosmogenic neutrinos in the 2007 data acquired by the partially constructed IceCube neutrino observatory. This analysis selects events which produce a large amount of light in the detector. Based on simple criteria, such as the total number of observed Cherenkov

*Corresponding author.
aya@hepburn.s.chiba-u.ac.jp
†Also at Universität Erlangen-Nürnberg, Physikalisches Institut, D-91058, Erlangen, Germany.
‡Corresponding author.
mase@hepburn.s.chiba-u.ac.jp
§Also at Università di Bari and Sezione INFN, Dipartimento di Fisica, I-70126, Bari, Italy.
‖Also at NASA Goddard Space Flight Center, Greenbelt, MD 20771, USA.
¶Corresponding author.
syoshida@hepburn.s.chiba-u.ac.jp

photons and the results of reconstruction algorithms, it selects candidate neutrino events. Although ν_μ, ν_e, and ν_τ interactions look very different in IceCube, the selection criteria are sensitive to all three flavors.

II. THE ICECUBE DETECTOR

IceCube is a cubic-kilometer, high-energy cosmic neutrino telescope which is currently under construction. It uses the 2800 m thick glacial ice as a Cherenkov medium. Cherenkov photons emitted by relativistic charged particles, notably muons, electrons, and taus produced in charged current interactions and their secondaries, are detected by an array of photon sensors, known as digital optical modules (DOMs) [10]. The DOMs deep below the ice surface are deployed along electrical cable bundles that carry power and communication between the DOMs and surface electronics. The cable assemblies, often called strings, are lowered into holes drilled to a depth of 2450 m. The DOMs, spaced at intervals of 17 m, occupy the bottom 1000 m of each string. The strings are arranged in a hexagonal lattice pattern with a spacing of approximately 125 m. DOMs are also frozen into tanks located at the surface near the top of each hole. The tanks constitute an air shower array called IceTop [11].

The DOMs enclose a down-looking 25 cm photomultiplier tube (PMT) [12] with data acquisition and calibration electronics, light emitting diodes for calibration, and also data compression, communications, and control hardware [10] in a 35 cm diameter pressure sphere. Almost all of the PMTs are run at a gain of 10^7; PMT saturation effects become important at signal levels of about 5000 photoelectrons in a single DOM in 50 ns. When the DOM detects a photoelectron, it initiates an acquisition cycle, recording the PMT output with two waveform digitizer systems. The first system samples every 3.3 ns for 400 ns, with 14 bits of dynamic range. The second system samples every 25 ns for 6.4 μs, with 10 bits of dynamic range. The data acquisition system is designed such that the first system is sensitive to a bright photon source at close distance and the second system captures signal induced by photons emitted at large distance. This analysis uses the total number of photoelectrons detected by the PMTs as a measure of the event energy. For each DOM, the charge used is the one from whichever system recorded a larger number of photoelectrons. Because of the significant DOM-to-DOM differences in saturation behavior, the current analysis does not attempt to correct for PMT saturation. So, the signals from brightly illuminated DOMs are naturally truncated.

III. DATA AND SIMULATION

This analysis uses data collected from May 2007 through April 2008, when IceCube consisted of 22 strings (IC-22; 1320 DOMs) and 52 IceTop tanks. In order to greatly reduce random noise from radioactivity, in IC22 the DOMs only recorded signal waveforms when a local coincidence condition was satisfied, i.e. when an adjoining or next-to-nearest neighbor DOM was triggered within ± 1 μs. In 2007, the trigger selected time periods when 8 or more DOMs recorded local coincidence signals within 5 μs; when this happened, all hits within a 20 μs window were stored as an event. The average trigger rate was about 550 Hz. The high-multiplicity event sample used in this analysis imposes an additional condition requiring NDOM ≥ 80, where NDOM is the number of hit DOMs in an event. The average high-multiplicity event rate was approximately 1.5 Hz with a seasonal variation of 17%. A total of 3.2×10^7 events were tagged as high-multiplicity during the effective live time of 242.1 days (excluding the periods of unstable operation).

The high-multiplicity cut reduces the data by a factor of $\sim 3 \times 10^{-3}$ while preserving approximately 70% of the GZK neutrinos with projected trajectories that pass within 880 m of the center of IceCube. Here, and below, the GZK signal rates are based on the GZK spectra and flux calculated by Ref. [6] assuming an all-proton composition with a moderately strong source evolution, $(z+1)^m$ with $m = 4$ extending to $z = 4.0$. Neutrino oscillations modify the neutrino flavor ratio over the cosmological distances they travel and the fluxes at the Earth were calculated as in Ref. [13]. Note that the flavor ratio ν_e:ν_μ:ν_τ of cosmogenic neutrinos at the Earth is different from 1:1:1 as primary energy spectra of ν_e and ν_μ produced by the GZK mechanism are different because of a significant contribution of ν_e from neutron decay. This enhancement was included in the GZK neutrino flux calculations used here.

EHE neutrinos were simulated with the JULIET package [9] to generate and propagate the neutrinos through the Earth. All three flavors of neutrinos were simulated with energies between 10^5 and 10^{11} GeV. The resulting secondary muons and taus produced in the neutrino interactions are propagated through the rock and ice near the IceCube volume, also by JULIET. Hadronic and electromagnetic showers are also simulated; all of these showers are treated as point sources, without accounting for the LPM effect. The background muon bundles from cosmic rays in the energy range 10^6 to 10^{10} GeV were generated using CORSIKA [14] version 6.720 with the SIBYLL 2.1 hadronic interaction model or with QGSJET-II, without charm production [15]. The uncertain prompt muon component from charm decay may contribute to the background events [16]. The muons were propagated through the Earth using MMC [17]. Departures of observed data distributions from those of the CORSIKA based background events prompted us to also develop a phenomenological background model based on fits to data. Emission of Cherenkov photons and their propagation in the ice was simulated by the Photonics package [18]. Measurement of the absolute number of Cherenkov photons is important in the EHE neutrino search as it closely relates to the energy of the high-energy muons, taus, or electrons produced by EHE neutrinos. Therefore, the detection efficiency of the DOMs must be understood with good precision. The primary element, the PMT, is calibrated in the laboratory using a nitrogen laser to measure the photon detection efficiency [12]. This bare PMT data are used in a simulation package which propagates photons inside the glass sphere and the optical gel to the photocathode surface. The DOM simulation is followed by waveform calibration and the trigger condition is included in the simulation chain.

IV. ANALYSIS

A. Extremely-high energy event signatures and the initial event filter

The event signatures from ν_μ, ν_e, and ν_τ are very different. IceCube mainly detects cosmogenic neutrinos by the signals from the secondary muons and taus generated in the neutrino interaction in the rock or ice. At high energies, these particles are seen in the detector as series of energetic cascades from radiative energy loss processes such as pair creation, bremsstrahlung, and photonuclear interactions, rather than minimum-ionizing tracks. The radiative energy losses are approximately proportional to the energy of the muon or the tau, and so is the Cherenkov light yield. Electron neutrinos produce electromagnetic and hadronic showers, which are relatively compact sources of Cherenkov light. Muon and tau neutrinos within IceCube will also produce a hadronic shower from the struck nucleon, in addition to the muon or tau secondary.

Shown in Fig. 1 is the simulated distribution of the total number of photoelectrons per event (NPE) recorded by the the IC-22 detector as a function of the simulated true muon energy. A clear correlation between NPE and the energy of particles measured near IceCube is observed. The energies are sampled at a radius of 880 m from the IceCube center. This definition of energy is labeled ‘‘in-ice energy’’ and used throughout this paper. The visible departure from linearity for large NPE stems from the saturation of the detector during signal capture. Approximately 30% of EHE signal events are due to neutrino interactions inside the IceCube detector volume initiating a hadronic or electromagnetic cascade. The correlation between NPE and incoming neutrino energy also holds for these events. Electron neutrinos are detectable via this channel.

Because the energy spectrum of background atmospheric muons (both single muons and bundles) falls steeply with energy, the GZK neutrino flux should dominate over background in the high NPE region. Since the through-going muons and taus induced by EHE neutrinos enter into the IceCube volume mainly horizontally [8,9], the signal search criteria are chosen to favor roughly horizontal high NPE events.

The high-multiplicity NDOM $\geq$ 80 sample is dominated by atmospheric background muons. The next step of the

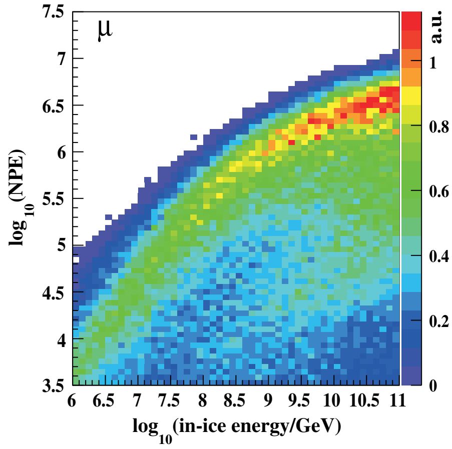

FIG. 1 (color online). Event distribution from Monte Carlo simulations of single muons with the IC-22 detector configurations in a plane of NPE and simulated true energy. The muon energy is given when the muon is 880 meters from the IceCube center (in-ice energy). The 80 DOM multiplicity cut (level-1 cut) is applied. The charged lepton energy distribution is assumed to follow E^{-1} in this plot for illustrative purposes. Only particles with trajectories intersecting within 880 m from the center of IceCube array are considered in the plots. More distant events do not contribute to the data sample.

analysis selects events with NPE $> 10^4$. This reduces the background by 3 orders of magnitude, leaving 6528 events, still dominated by background, while the GZK signal reduction is $\sim$24%.

Table I summarizes the number of events remaining at each level of the initial filtering. In order to estimate the background in the very high-energy region, the simulated data are compared to the experimental data in the region $10^4 <$ NPE $< 10^5$. The present analysis follows the blind analysis technique. In keeping with the IceCube blindness policy, events with NPE $\geq 10^5$ were not used for determining the background or setting cuts. This NPE threshold was chosen so that the possible contribution from signal events in the studied sample was negligible.

B. High-energy muon background

Bundles of muons generated in cosmic-ray air showers are the major background for the EHE neutrino signal search, because multiple muon tracks with a small geometrical separation resemble a single high-energy muon in the IceCube detector. The multiplicity, energy distribution, and separation distances for these muon bundles are not fully understood. Two independent Monte Carlo simulations are carried out to estimate the muon-bundle background in this EHE neutrino signal search.

The first is the full cosmic-ray air shower simulation with light and heavy ion primaries using the CORSIKA (SIBYLL) package [14]. Two extreme cases of composition are used to address the event rate variation due to the

TABLE I. Number of events at different filter levels for 242.1 days in 2007. The simulation predictions for the atmospheric muon background using the CORSIKA-SIBYLL package, the empirical model, and that for the GZK cosmogenic neutrino model are also listed for comparison. Errors shown here are statistical only. Refer to Sec. IVA for the definitions.

Filter levels	Observational data	Empirical model	CORSIKA (iron)	CORSIKA (proton)	Signal (GZK1 [6])
Level 1 (NDOM ≥ 80)	3.195×10^7	$\cdots$	$(1.84 \pm 0.08) \times 10^7$	$(7.71 \pm 0.45) \times 10^6$	$(886 \pm 8.9) \times 10^{-3}$
Level 2 (NPE $> 10^4$)	6528	$(6.82 \pm 0.42) \times 10^3$	$(1.09 \pm 0.09) \times 10^4$	$(1.63 \pm 0.17) \times 10^3$	$(670 \pm 7.5) \times 10^{-3}$

uncertainty in the primary cosmic-ray mass population. While the full air shower simulation includes a calculation of the production spectra of the multiple muons from meson decay, the simulation still introduces a large uncertainty because both the primary composition at relevant cosmic-ray energies ($> 10^7$ GeV) and the hadronic interaction model are highly uncertain.

The second simulation uses a model relying on a phenomenological fit to part of the experimental high-energy data. This empirical model approximates multiple muon tracks in an event by a single high-energy muon which is adequate at very high energies for the variables used in this analysis. The single muon approximation predicts larger fluctuations in NPE due to radiative energy losses of energetic muons, giving a rather conservative estimate of the background passing rate. The two independent sets of simulations with top-down and bottom-up approaches to describe the observational data complement each other improving the reliability of the background estimation.

1. Background estimation with CORSIKA

Figure 2 shows distributions for data and simulations at level-2 for NPE, the reconstructed zenith angle (θ), and the center-of-gravity depth of the events ($z_{\rm COG}$). The CORSIKA NPE distribution is extrapolated to the higher NPE region. Extrapolation was necessary mainly because of a lack of simulated CORSIKA events at primary cosmic-ray energies above 10^{10} GeV. The extrapolation accounts for the observed GZK cutoff at an energy around 5×10^{19} eV. The NPE-weighted LineFit algorithm was used to reconstruct zenith angle in this initial study. The NPE-weighted LineFit is a simple minimization of $\chi^2 = \Sigma_i NPE_i(\vec{r}_i - \vec{r}_{\rm COG} - t_i\vec{v})^2$, where t_i and NPE$_i$ represent, respectively, the time of the first photoelectron and the number of photoelectrons recorded by the ith DOM at the position $\vec{r}_i$ and $\vec{r}_{\rm COG} \equiv (\frac{\Sigma_i {\rm NPE}_i x_i}{\Sigma_i {\rm NPE}_i}, \frac{\Sigma_i {\rm NPE}_i y_i}{\Sigma_i {\rm NPE}_i}, \frac{\Sigma_i {\rm NPE}_i z_i}{\Sigma_i {\rm NPE}_i})$ is the NPE-weighted position of the center of gravity of the hits. The fit ignores the geometry of the Cherenkov cone and the optical properties of the medium and assumes light traveling with a velocity $\vec{v}$ along a one-dimensional path through the detector, passing through the center of gravity.

The measured event rates are close to the simulated rates based on CORSIKA-SIBYLL with iron primaries and above those based on CORSIKA-SIBYLL proton data in most regions. A significant discrepancy can be found in the rate of events with $\cos\theta \leq 0.3$, i.e. events reconstructed as horizontal or up-going, which is largely underestimated. Replacing SIBYLL with other hadronization models (e.g. QGSJET-II) does not change this behavior. The discrepancy may be due to a combination of uncertainties in the hadronic interaction models, cosmic-ray flux, and Cherenkov photon propagation in the glacial ice. Since the horizon is the key region for the EHE neutrino search, the background estimations were supplemented by an empirical model fit to a subsample of the data.

2. Construction of an empirical model

The empirical model is optimized to match the level-2 experimental data ($10^4 <$ NPE $< 10^5$). The possible signal

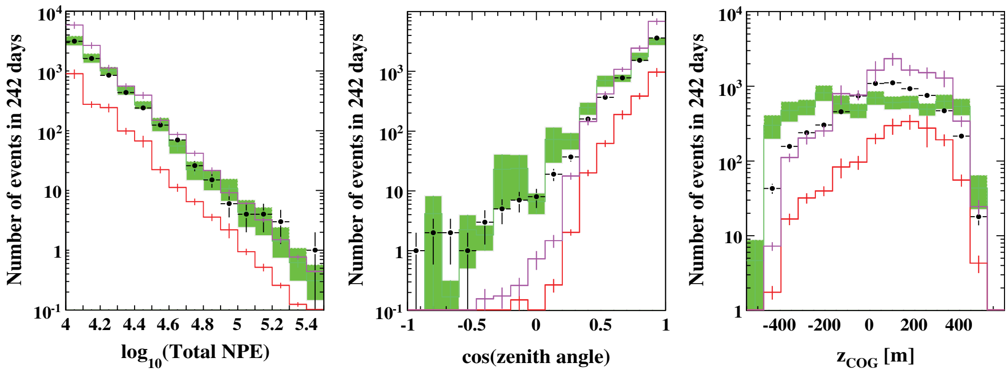

FIG. 2 (color online). Event distributions for NPE, cosine of reconstructed zenith angle, and the NPE-weighted mean depth of event ($z_{\rm COG}$) for observational and the background Monte Carlo simulation data. The black dots represent observational data after the NPE $> 10^4$ cut, red for CORSIKA proton (SIBYLL), magenta for CORSIKA iron (SIBYLL). Green shaded regions represent distributions obtained with the empirical model with the size of shade expressing the uncertainty of the model. See text for the details.

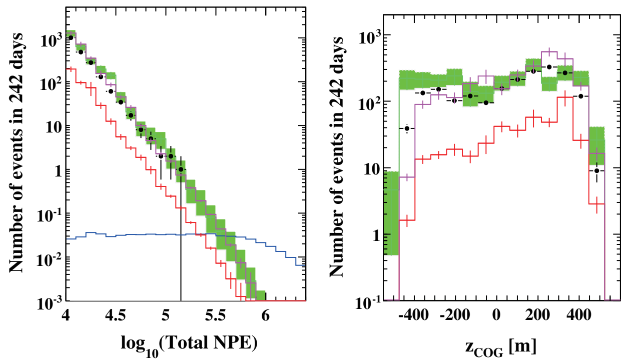

FIG. 3 (color online). Event distributions from the level-3 samples as functions of NPE (left) and $z_{\rm COG}$ (right). The black dots represent observational data, green boxes represent the empirical model including uncertainty. Red and magenta lines are CORSIKA samples with SIBYLL interaction model and proton and iron primaries, respectively. The left panel also includes the expected NPE distribution of events induced by the cosmogenic neutrinos [6] shown by the blue line for reference.

region (NPE $\geq 10^5$) is not used to avoid bias. The model provides a relation between the NPE of an event and the cosmic-ray primary energy. Its convolution with the cosmic-ray flux then gives the event rate with a given NPE. The cosmic-ray flux used in the present analysis is taken from the compilation in Ref. [2].

The model is based on the so-called Elbert formula [19] which parametrizes the mean multiplicity of muons with energies above a certain threshold E_μ:

$$N_\mu = \frac{E_T}{E_0}\frac{A^2}{\cos\theta'}\left(\frac{AE_\mu}{E_0}\right)^{-\alpha}\left(1-\frac{AE_\mu}{E_0}\right)^{\beta}, \qquad E_T = 14.5\ \mathrm{GeV}, \tag{1}$$

where A, E_0, and θ' are the mass number, the energy, and the zenith angle of the primary cosmic ray [20]. The energy weighted integration of the formula relates the total energy carried by a muon-bundle E_μ^B to the primary cosmic-ray energy E_0,

$$E_\mu^B \equiv \int_\epsilon^{E_0/A} \frac{dN_\mu}{dE_\mu} E_\mu dE_\mu \simeq E_T \frac{A}{\cos\theta'}\frac{\alpha}{\alpha-1}\left(\frac{A\epsilon}{E_0}\right)^{-\alpha+1}, \tag{2}$$

assuming $AE_\mu/E_0 \ll 1$. Here, ϵ is empirically determined by fit to the observed data. Assuming its corresponding energy at the IceCube depth, $\epsilon^{\textbf{in-ice}}$, is independent of zenith angle, ϵ (and thereby E_μ^B) can be calculated as a function of zenith angle by taking into account the energy loss during propagation through the Earth. The optimization of the two parameters α and $\epsilon^{\textbf{in-ice}}$ is performed by comparing the observed data to simulation of a single high-energy muon with energy of E_μ^B in the NPE and zenith angle space, independently. $A = 1$ is assumed in the optimization. The event distributions derived from the empirical model with optimized parameters ($\alpha = 1.97$ and $\epsilon^{\textbf{in-ice}} = 1500$ GeV) are given in Fig. 2. The green shaded region in the plot is obtained by allowing the model parameters to vary within $\pm 1\sigma$ from their optimized values. The discrepancies of $z_{\rm COG}$ at large depths for the empirical model and at small depths for CORSIKA/iron seem to be due to vertical, down-going events because a restriction of the zenith angle, $\cos\theta < 0.8$, improves the agreement in both cases. Since the majority of the EHE neutrino induced events is close to the horizon we can discard all events with $\cos\theta < 0.8$ without significant loss of signal efficiency (level-3 cut). The resulting distributions are shown in Fig. 3.

C. Search for EHE cosmogenic neutrino signal

The level-4 cut to eliminate the muon background is carried out in the NPE-$\cos\theta$ (NZ) plane. In accordance with the requirements of blindness, the cuts are finalized on simulated events alone without referring to real data. Because the optical properties of the glacial ice vary significantly with depth [21], and because the changing absorption and scattering lengths affect what IceCube observes, the final cuts are chosen to be depth dependent. The cuts are chosen based on the depth of the weighted center of gravity of the event, $z_{\rm COG}$. The distribution of events in the NZ plane depends on $z_{\rm COG}$. We divide the events into two groups according to their $z_{\rm COG}$ as follows:

$$\text{region A:} \quad -250 < z_{\rm COG} < -50\ \mathrm{m} \quad \text{and} \quad z_{\rm COG} > 50\ \mathrm{m},$$

$$\text{region B:} \quad z_{\rm COG} < -250\ \mathrm{m} \quad \text{and} \quad -50 < z_{\rm COG} < 50\ \mathrm{m}.$$

As seen in Fig. 4, region B contains a large number of horizontal and up-going mis-reconstructed background events, whereas the fraction of such events in region A is

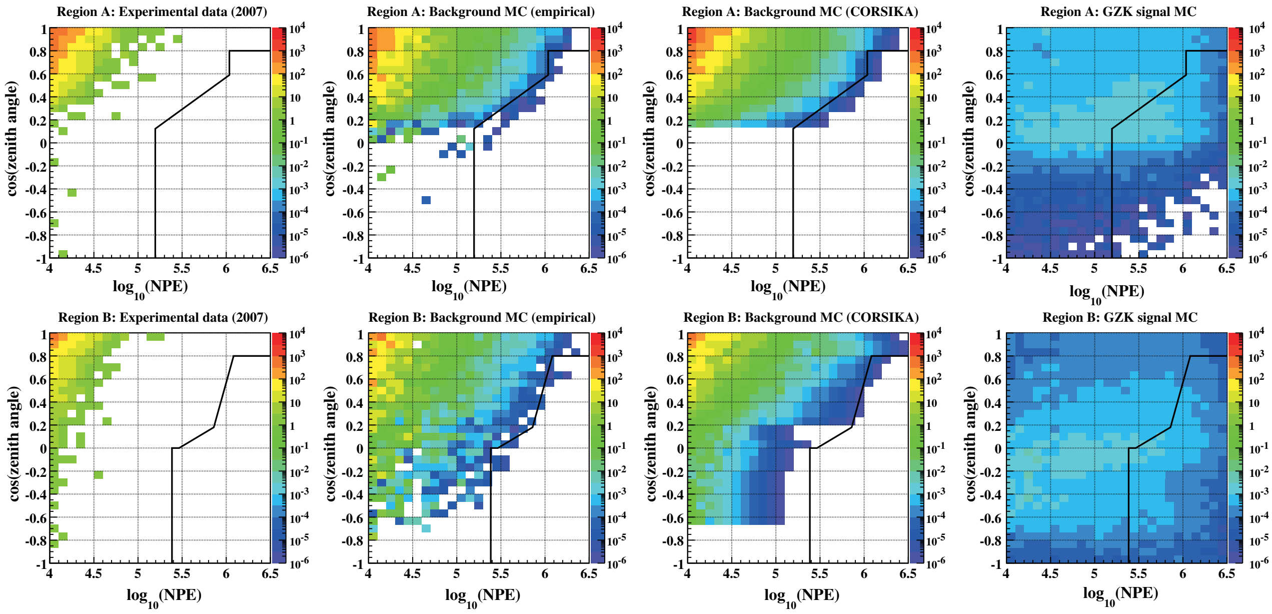

FIG. 4 (color online). Event number distributions passing the level-2 selection cut (NPE $> 10^4$) of the experimental data (left), the background from the empirical model (middle left), the background from CORSIKA-SIBYLL with iron primaries (middle right), and the signal (right) on the NZ plane at the IceCube depth. The upper (lower) panels show the distributions in the region A (B). The GZK neutrino flux [6] determines the event intensity in the signal Monte Carlo plot, adding all three flavors of neutrinos. The series of thick lines in each panel indicates the level-3 ($\cos(\theta) < 0.8$) and the final level-4 cuts.

very small. Figure 4 also shows the distributions of the experimental data and the simulated GZK neutrino induced signal events. The latter clearly accumulate near the horizontal direction regardless of the $z_{\rm COG}$ position and have on average larger NPE than the background sample. The selection criteria to separate signal from background are determined for region A and region B separately: For each bin of $\cos\theta$ (width 0.1), a threshold NPE is set such that the number of background events above the threshold is less than 10^{-4}. Tighter cuts to further reduce the background would also reduce the signal to an undesirable degree. The NPE thresholds in all the zenith angle bins are then connected to each other to form a series of lines on the NZ plane, defining the final level-4 cut, as drawn in Fig. 4. The cuts were optimized using the empirical model for background simulations, so we used extrapolated CORSIKA/iron data as a check of the final background level. Figure 4 also shows the distribution of background events in the NZ plane from the extrapolation. Table II summarizes the number of events remaining in the analysis after each of the cut levels.

The effective area as a function of energy at Earth's surface for each neutrino flavor is shown in the left panel of Fig. 5, averaged over all solid angles. The area increases with the energy owing to the increasing neutrino interaction cross sections and the increased probability of observing the interactions, which is different for each flavor.

At low energies, most of the ν_τ signal comes from events where the ν_τ interacts in the detector, or the τ decays in it. At higher energies, τ energy loss becomes large enough that through-going taus also pass the cuts. Contributions from ν_μ and ν_τ dominate over ν_e in the energy range above $\sim 10^8$ GeV, as the secondary produced muons and taus can travel long distances to reach the detection volume. This trend is reversed at lower energy where tau and muon energy losses are smaller, and ν_e's can deposit all of their energy into the detector volume. The effective area

TABLE II. Number of events at analysis filter levels for 242.1 days in 2007. The simulation predictions for the atmospheric muon background using the CORSIKA-SIBYLL package, the empirical model, and that for the GZK cosmogenic neutrino model are also listed for comparison. Errors shown here are statistical only. See Secs. IV B and IV C for details.

Analysis filter levels	Observational data	Empirical model	CORSIKA (iron)	CORSIKA (proton)	Signal (GZK1 [6])
Level 3 ($\cos(\theta) < 0.8$)	2014	$(2.65 \pm 0.21) \times 10^3$	$(2.68 \pm 0.19) \times 10^3$	$(4.16 \pm 0.40) \times 10^2$	$(620 \pm 7.3) \times 10^{-3}$
Level 4 (EHE ν search)	0	$(6.32 \pm 1.37) \times 10^{-4}$	$(4.18 \pm 1.29) \times 10^{-4}$	$(1.44 \pm 0.58) \times 10^{-4}$	$(155 \pm 1.4) \times 10^{-3}$

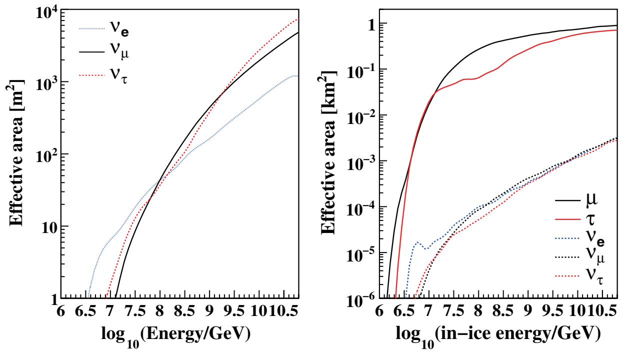

FIG. 5 (color online). The effective area of IC-22 for EHE neutrino search. The left panel shows the 4π solid angle averaged area as a function of neutrino energy at the Earth surface. The right panel shows the corresponding effective area for particles at 880 m from the IceCube center entering into the IC-22 fiducial volume. Muons and taus in this plot are secondary particles produced by neutrinos before reaching the neighborhood of the detector array. The energy here are defined as in-ice energy.

for ν_τ is larger than that for ν_μ at low energies, because of the events where taus decay inside the detector. At the highest energies, because of the larger mass of taus and increase of the tau decay time with energy, the tau range is longer than that of muons, leading to a larger effective area.

The right panel in Fig. 5 shows the effective area as a function of the in-ice energy (''in-ice area''). It represents the probability of detection of incoming particles with the present analysis. The area for incident muons and taus gradually increases with energy but is limited essentially by the physical cross section of the IC-22 array, $\sim$0.5 km^2. Because the Cherenkov yield of taus is smaller than muons with the same energy due to the smaller radiative energy loss, the detection probability of incident taus is lower, leading to the smaller in-ice area. Incoming neutrinos must interact to yield Cherenkov light to be detected. Therefore, the neutrino effective area becomes much smaller than that for muons or taus.

TABLE III. Expected event numbers passing the final level-4 selection criteria in the 2007 IC-22 observation. Models include the GZK models [6,22,23] and the Z-burst model [24]. The predictions are normalized to a live time of 242.1 days. Signal event numbers represent the sum over all three neutrino flavors. The first uncertainty is the statistical uncertainty determined by signal simulation statistics, and the second is the total systematic uncertainty from sources discussed in Sec. V.

Models	Number of Events per 242.1 days
GZK1 [6]	$(155 \pm 1.4^{+24}_{-40}) \times 10^{-3}$
GZK2 [22]	$(248 \pm 2.3^{+39}_{+65}) \times 10^{-3}$
GZK3 [23]	$(83 \pm 0.8 +^{+13}_{-21}) \times 10^{-3}$
Z-burst [24]	$(398 \pm 3.4^{+63}_{-95}) \times 10^{-3}$

The expected number of signal events for various neutrino production models after the level-4 cut are summarized in TABLE III. GZK1 [6] represents the case of a moderately strong source evolution, $(z+1)^m$ with $m = 4$ extending to $z = 4.0$, while GZK2 [22] assumes $m = 5$ up to $z = 2.0$, and GZK3 [23] uses $m = 3$ with a slightly different parametrization and a cutoff structure.

V. THE SYSTEMATICS

This search is based on the eventwise NPE and reconstructed zenith angle. The main systematic uncertainties derive from (1) the necessity to extrapolate the empirical fit to data by approximately an order of magnitude in NPE to estimate the background rate at the highest energies and from (2) the uncertainty of the absolute NPE scale. Table IV lists the sources of statistical and systematics errors.

A. Uncertainties in the background rate estimation

The largest uncertainty in the background rate estimate arises from the fact that the parameters of the empirical model were optimized for the observed events with $10^4 <$ NPE $< 10^5$ after level 2 selection. The limited statistics of this sample results in uncertainties on the parameters. The model was then extrapolated to a higher NPE region for the determination of the level-4 cut.

Allowing the parameters to vary within $\pm 1\sigma$ changes the background rate by between -59% (for the softest possible NPE spectrum after the level-4 cuts) and $+99\%$ (for the hardest possible NPE spectrum). Uncertainties in the detector sensitivity are incorporated by the parametrization. The difference in the background level estimated with the extrapolated CORSIKA/iron and the empirical model can be taken to indicate the level of systematic uncertainty due to model dependence. This uncertainty is approximately $\pm 15\%$ and can be assumed to include the possible contribution from charm decay. An uncertainty associated with the high-energy hadronic interaction model is evaluated using simulated muon-bundle intensity from SIBYLL and QGSJET-II with iron primaries and found to be $\pm 4\%$, which is negligible. An additional uncertainty of $\sim 17\%$ arises from the seasonal variation of the atmospheric muon rate as the signal selection criteria are based upon the season-averaged data.

B. Uncertainties of the signal rate estimate

The uncertainty in the relationship between measured NPE and the energies of charged particles is the largest systematic error affecting the signal event rate. It is the consequence of our limited understanding of the detector sensitivity, the photon propagation in ice, and the detector response to bright signals. It is evaluated using absolutely calibrated *in situ* light sources and amounts to a possible overestimation of NPE in simulation by 18.5%, which leads to decrease of the GZK signal rate by $\sim$21%.

TABLE IV. List of the statistical and systematic errors. The signal rate is estimated by assuming the high evolution flux $(m, Z_{max}) = (4, 4)$ in Ref [6].

Error source	Background rate	Signal (GZK) rate
Statistical error	±22%	±0.9%
Detector sensitivity	⋯	±8%
Yearly variation	±17%	⋯
Empirical model	+99/ − 59%	⋯
Background model dep.	±15%	⋯
NPE yield	⋯	+0/ − 21%
Neutrino cross section	⋯	±9%
Photonuclear interaction	⋯	+10%
LPM effect	⋯	±1%
Total	±22% (stat.)	±0.9% (stat.)
	+102/ − 63% (sys.)	+16/ − 26% (sys.)

Uncertainties of the relevant particle interactions in the EHE regime also add systematics in the signal rate estimation. The expected event rate scales nearly linearly with the neutrino-nucleon inelastic cross section in the EHE range. This scaling has been confirmed by numerical studies, artificially increasing the cross section. The cross section uncertainty has been recently reduced to be around ±9% with the inclusion of the most recent data from HERA and modern parton distribution functions [25]. Another systematic error arises from the photonuclear cross section of EHE muons and taus. The present calculation used the model by Bugaev and Shlepin [26], rewritten in Ref. [27], that includes a relatively reliable soft nonperturbative component and a less certain hard perturbative part. Ignoring the hard component in the simulation gives the most conservative estimate of the uncertainty and leads to a 10% event rate increase. The suppression of bremsstrahlung and pair production due to the LPM effect [28], for the relevant electron energies of 10^{9-10} GeV, increases the effective radiation length of the electromagnetic cascade to $O(30–100)$ m from ~36 cm [29]. Because the value is still comparable to the IceCube DOM separation, and the contribution from ν_e constitutes ≤ 20% of the total event rate in this energy range, the LPM effect has a negligible impact on the event rate. This has been confirmed by a special simulation study on ν_e including the LPM cascade elongation.

VI. RESULTS

No events are observed in the final data sample taken in 2007 with a live time of 242.1 days when applying the final level-4 selection criteria, which is consistent with the expected number of background events of 6.3×10^{-4}. We choose to present the resulting all flavor EHE neutrino upper limit in the quasi-differential form independent of the neutrino production model. Assuming full mixing due to oscillations, the experimental 90% confidence level upper limit is obtained by setting 2.44 events [30] for an upper bound of the number of events observed with bin width of a decade of energy with condition that energy dependence of neutrino flux multiplied by the effective area behaves as $\sim 1/E$ [31]. This limit is presented in Fig. 6 including the systematic errors. The plot indicates that the EHE neutrino search by the IceCube observatory is most sensitive to the neutrinos with energies on Earth's surface ranging between about 10^8 and 10^9 GeV. The absence of signal events in the sample of 242.1 days of effective live time results in a 90% C.L. differential upper limit on the neutrino flux of $E^2\phi_{\nu_e+\nu_\mu+\nu_\tau} \simeq 1.4 \times 10^{-6}$ GeV cm^{-2} sec^{-1} sr^{-1} on average for neutrinos with

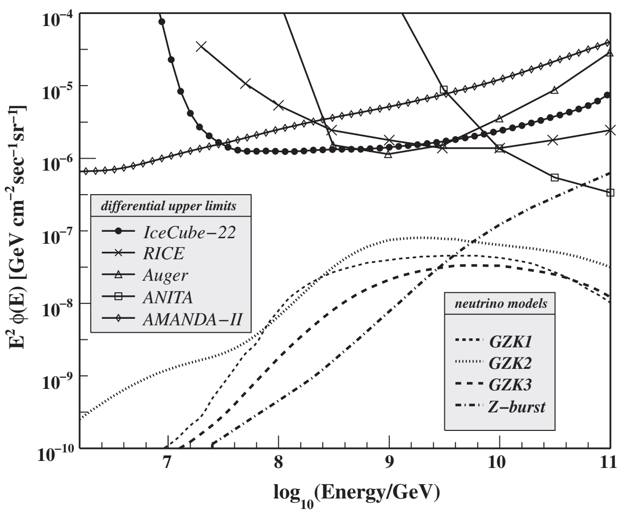

FIG. 6. The all flavor neutrino flux differential limit from the IC-22 EHE analysis (filled circles). The systematic errors are included. Also the various model predictions are shown for comparison: GZK model 1 [6] (short dashed line), GZK model 2 [22] (dotted line), GZK model 3 [23] (long dashed line), Z-burst model [24] (dashed dot line). The model independent differential upper limits by other experiments are also shown for Auger [32] (open triangles), RICE [31] (crosses), ANITA [34] (open squares), AMANDA [35] (rhombi). Limits from other experiments are converted to the all flavor limit assuming full mixing neutrino oscillations and 90% C.L when necessary.

an energy of $3 \times 10^7 \leq E \leq 3 \times 10^9$ GeV. Here $\phi_{\nu_e+\nu_\mu+\nu_\tau}$ denotes the differential flux of the sum over all three neutrino flavors, i.e. number of neutrinos per unit energy, area, time and solid angle.

The quasi-differential limit in Fig. 6 takes into account the systematic uncertainties. The background rate stays negligible $O(10^{-3})$ even including the systematic uncertainty and the resultant upper limit is unchanged. The signal rate uncertainty is strongly dominated by the uncertainty of the NPE yield which influences the number of expected signal events as a function of the neutrino energy. The upper limit is calculated by reducing NPE by 18.5% in the signal simulation to account for this factor. All the other sources of systematic error only slightly change the signal passing rate; they are independent of energy. They are included in the analysis by uniformly scaling the effective area in the limit calculation.

The present limit is approximately a factor of 20–30 higher than the intensity range expected in the GZK cosmogenic neutrino production models [6,22,23], as one can see in Fig. 6. The current limit for 242.1 days of observation is comparable to the Auger [32] and HiRes [33] bounds by their multiple year operation.

VII. CONCLUSIONS

The present work has demonstrated that the IceCube neutrino observatory is capable of searching for signatures of EHE cosmogenic neutrinos with relatively straightforward event selection methods. The model independent differential upper limit obtained with 242.1 days of observation in 2007, with approximately one quarter of the completed detector is $E^2\phi_{\nu_e+\nu_\mu+\nu_\tau} \simeq 1.4 \times 10^{-6}\,\mathrm{GeV\,cm^{-2}\,sec^{-1}\,sr^{-1}}$ for neutrinos with an energy of $3 \times 10^7 \leq E \leq 3 \times 10^9$ GeV. This is approximately a factor of 20 higher than the predicted GZK neutrino flux from relatively strongly evolved sources. In the future, data taken by IceCube with 40 to 86 strings operating should lead to a detection of cosmogenic neutrinos or a greatly improved limit.

ACKNOWLEDGMENTS

We acknowledge the support from the following agencies: U.S. National Science Foundation - Office of Polar Programs, U.S. National Science Foundation - Physics Division, University of Wisconsin Alumni Research Foundation, U.S. Department of Energy, and National Energy Research Scientific Computing Center, the Louisiana Optical Network Initiative (LONI) grid computing resources; Swedish Research Council, Swedish Polar Research Secretariat, Swedish National Infrastructure for Computing (SNIC), and Knut and Alice Wallenberg Foundation, Sweden; German Ministry for Education and Research (BMBF), Deutsche Forschungsgemeinschaft (DFG), Research Department of Plasmas with Complex Interactions (Bochum), Germany; Fund for Scientific Research (FNRS-FWO), FWO Odysseus programme, Flanders Institute to encourage scientific and technological research in industry (IWT), Belgian Federal Science Policy Office (Belspo); University of Oxford, United Kingdom; Marsden Fund, New Zealand; Japan Society for Promotion of Science (JSPS); the Swiss National Science Foundation (SNSF), Switzerland. A. Kappes and A. Groß acknowledge support by the EU Marie Curie OIF Program. J. P. Rodrigues acknowledges support by the Capes Foundation, Ministry of Education of Brazil. This analysis work has been particularly supported by the Japan-US Bilateral Joint Projects in the Japan Society for the Promotion of Science.

[1] For a review, see, e.g. J. W. Cronin, Rev. Mod. Phys. **71**, S165 (1999); S. Yoshida and H. Dai, J. Phys. G **24**, 905 (1998).
[2] M. Nagano and A. A. Watson, Rev. Mod. Phys. **72**, 689 (2000).
[3] N. Hayashida *et al.*, Phys. Rev. Lett. **77**, 1000 (1996); J. Abraham *et al.* (Pierre Auger Collaboration), Science **318**, 938 (2007).
[4] K. Greisen, Phys. Rev. Lett. **16**, 748 (1966); G. T. Zatsepin and V. A. Kuzmin, Pis'ma Zh. Eksp. Teor. Fiz. **4**, 114 (1966) [JETP Lett. **4**, 78 (1966)].
[5] V. S. Berezinsky and G. T. Zatsepin, Phys. Lett. **28B**, 423 (1969).
[6] S. Yoshida and M. Teshima, Prog. Theor. Phys. **89**, 833 (1993).
[7] A. Achterberg *et al.* (IceCube Collaboration), Astropart. Phys. **26**, 155 (2006).
[8] F. Halzen and D. Hooper, Phys. Rev. Lett. **97**, 071101 (2006).
[9] S. Yoshida *et al.*, Phys. Rev. D **69**, 103004 (2004).
[10] R. Abbasi *et al.* (IceCube Collaboration), Nucl. Instrum. Methods Phys. Res., Sect. A **601**, 294 (2009).
[11] R. Abbasi *et al.* (IceCube Collaboration), Astrophys. J. Lett. **689**, L65 (2008).
[12] R. Abbasi *et al.* (IceCube Collaboration), Nucl. Instrum. Methods Phys. Res., Sect. A **618**, 139 (2010).
[13] J. Jones, I. Mocioiu, M. H. Reno, and I. Sarcevic, Phys. Rev. D **69**, 033004 (2004).
[14] D. Heck *et al.*, Forschungszentrum Karlsruhe Report No. FZKA 6019 (1998).
[15] T. S. Sinegovskaya and S. I. Sinegovsky, Phys. Rev. D **63**, 096004 (2001).
[16] R. Enberg, M. H. Reno, and I. Sarcevic, Phys. Rev. D **78**, 043005 (2008).

[17] D. Chirkin and W. Rhode, arXiv:hep-ph/0407075v2.
[18] J. Lundberg *et al.*, Nucl. Instrum. Methods Phys. Res., Sect. A **581**, 619 (2007).
[19] T. K. Gaisser, *Cosmic Rays and Particle Physics* (Cambridge University Press, Cambridge, England, 1990), p. 206.
[20] J. W. Elbert, in *Proceedings of the DUMAND Summer Workshop, La Jolla, California, 1978*, edited by A. Roberts (Scripps Institution of Oceanography, La Jolla, CA, 1979) Vol. 2, p. 101.
[21] M. Ackermann *et al.*, J. Geophys. Res. **111**, D13203 (2006).
[22] O. E. Kalashev, V. A. Kuzmin, D. V. Semikoz, and G. Sigl, Phys. Rev. D **66**, 063004 (2002).
[23] R. Engel, D. Seckel, and T. Stanev, Phys. Rev. D **64**, 093010 (2001).
[24] S. Yoshida, G. Sigl, and S. Lee, Phys. Rev. Lett. **81**, 5505 (1998).
[25] A. Cooper-Sarkar and S. Sarkar, J. High Energy Phys. 01 (2008) 075.
[26] E. V. Bugaev and Yu. V. Shlepin, Phys. Rev. D **67**, 034027 (2003).
[27] E. Bugaev, T. Montaruli, Y. Shlepin, and I. Sokalski, Astropart. Phys. **21**, 491 (2004).
[28] L. Landau and I. Pomeranchuk, Dokl. Akad. Nauk SSSR **92**, 535 (1953); A. Migdal, JETP **5**, 527 (1953).
[29] S. Klein, Rev. Mod. Phys. **71**, 1501 (1999).
[30] G. J. Feldman and R. D. Cousins, Phys. Rev. D **57**, 3873 (1998).
[31] I. Kravchenko *et al.* (Rice Collaboration), Phys. Rev. D **73**, 082002 (2006).
[32] J. Abraham *et al.* (Pierre Auger Collaboration), Phys. Rev. D **79**, 102001 (2009).
[33] R. U. Abbasi *et al.* (HiRes Collaboration), Astrophys. J. **684**, 790 (2008).
[34] P. W. Gorham *et al.* (ANITA Collaboration), Phys. Rev. D **82**, 022004 (2010).
[35] M. Ackermann *et al.* (IceCube Collaboration), Astrophys. J. **675**, 1014 (2008).

Nuclear Instruments and Methods in Physics Research A 618 (2010) 139–152

Contents lists available at ScienceDirect

Nuclear Instruments and Methods in Physics Research A

journal homepage: www.elsevier.com/locate/nima

Calibration and characterization of the IceCube photomultiplier tube

R. Abbasi [z], Y. Abdou [t], T. Abu-Zayyad [af], J. Adams [o], J.A. Aguilar [z], M. Ahlers [ae], K. Andeen [z], J. Auffenberg [al], X. Bai [ad], M. Baker [z], S.W. Barwick [v], R. Bay [g], J.L. Bazo Alba [am], K. Beattie [h], J.J. Beatty [q,r], S. Bechet [l], J.K. Becker [j], K.-H. Becker [al], M.L. Benabderrahmane [am], J. Berdermann [am], P. Berghaus [z], D. Berley [p], E. Bernardini [am], D. Bertrand [l], D.Z. Besson [x], M. Bissok [a], E. Blaufuss [p], D.J. Boersma [a], C. Bohm [ag], O. Botner [aj], L. Bradley [ai], J. Braun [z], S. Buitink [h], M. Carson [t], D. Chirkin [z], B. Christy [p], J. Clem [ad], S. Cohen [w], C. Colnard [u], D.F. Cowen [ai,ah], M.V. D'Agostino [g], M. Danninger [ag], C. De Clercq [m], L. Demirörs [w], O. Depaepe [m], F. Descamps [t], P. Desiati [z], G. de Vries-Uiterweerd [t], T. DeYoung [ai], J.C. Díaz-Vélez [z], J. Dreyer [s,j], J.P. Dumm [z], M.R. Duvoort [ak], R. Ehrlich [p], J. Eisch [z], R.W. Ellsworth [p], O. Engdegård [aj], S. Euler [a], P.A. Evenson [ad], O. Fadiran [d], A.R. Fazely [f], T. Feusels [t], K. Filimonov [g], C. Finley [ag], M.M. Foerster [ai], B.D. Fox [ai], A. Franckowiak [i], R. Franke [am], T.K. Gaisser [ad], J. Gallagher [y], R. Ganugapati [z], M. Geisler [a], L. Gerhardt [h,g], L. Gladstone [z], A. Goldschmidt [h], J.A. Goodman [p], D. Grant [ai], T. Griesel [ab], A. Groß [o,u], S. Grullon [z], R.M. Gunasingha [f], M. Gurtner [al], C. Ha [ai], A. Hallgren [aj], F. Halzen [z], K. Han [o], K. Hanson [z], Y. Hasegawa [n], J. Haugen [z], K. Helbing [al], P. Herquet [ac], S. Hickford [o], G.C. Hill [z], K.D. Hoffman [p], A. Homeier [i], K. Hoshina [z], D. Hubert [m], W. Huelsnitz [p], J.-P. Hülß [a], P.O. Hulth [ag], K. Hultqvist [ag], S. Hussain [ad], R.L. Imlay [f], M. Inaba [n], A. Ishihara [n], J. Jacobsen [z], G.S. Japaridze [d], H. Johansson [ag], J.M. Joseph [h], K.-H. Kampert [al], A. Kappes [z,1], T. Karg [al], A. Karle [z], J.L. Kelley [z], N. Kemming [i], P. Kenny [x], J. Kiryluk [h,g], F. Kislat [am], N. Kitamura [z], S.R. Klein [h,g], S. Knops [a], G. Kohnen [ac], H. Kolanoski [i], L. Köpke [ab], D.J. Koskinen [ai], M. Kowalski [k], T. Kowarik [ab], M. Krasberg [z], T. Krings [a], G. Kroll [ab], K. Kuehn [q], T. Kuwabara [ad], M. Labare [l], S. Lafebre [ai], K. Laihem [a], H. Landsman [z], R. Lauer [am], A. Laundrie [z], R. Lehmann [i], D. Lennarz [a], J. Lünemann [ab], J. Madsen [af], P. Majumdar [am], R. Maruyama [z], K. Mase [n,*], H.S. Matis [h], M. Matusik [al], K. Meagher [p], M. Merck [z], P. Mészáros [ah,ai], T. Meures [a], E. Middell [am], N. Milke [s], H. Miyamoto [n], T. Montaruli [z,2], R. Morse [z], S.M. Movit [ah], R. Nahnhauer [am], J.W. Nam [v], U. Naumann [al], P. Nießen [ad], D.R. Nygren [h], S. Odrowski [u], A. Olivas [p], M. Olivo [aj,j], M. Ono [n], S. Panknin [i], L. Paul [a], C. Pérez de los Heros [aj], J. Petrovic [l], A. Piegsa [ab], D. Pieloth [s], A.C. Pohl [aj,3], R. Porrata [g], J. Posselt [al], P.B. Price [g], M. Prikockis [ai], G.T. Przybylski [h], K. Rawlins [c], P. Redl [p], E. Resconi [u], W. Rhode [s], M. Ribordy [w], A. Rizzo [m], P. Robl [aa], J.P. Rodrigues [z], P. Roth [p], F. Rothmaier [ab], C. Rott [q], C. Roucelle [u], D. Rutledge [ai], B. Ruzybayev [ad], D. Ryckbosch [t], H.-G. Sander [ab], P. Sandstrom [z], S. Sarkar [ae], K. Schatto [ab], S. Schlenstedt [am], T. Schmidt [p], D. Schneider [z], A. Schukraft [a], A. Schultes [al], O. Schulz [u], M. Schunck [a], D. Seckel [ad], B. Semburg [al], S.H. Seo [ag], Y. Sestayo [u], S. Seunarine [o], A. Silvestri [v], A. Slipak [ai], G.M. Spiczak [af], C. Spiering [am], M. Stamatikos [q,4], T. Stanev [ad], G. Stephens [ai], T. Stezelberger [h], R.G. Stokstad [h], S. Stoyanov [ad], E.A. Strahler [m], T. Straszheim [p], G.W. Sullivan [p], Q. Swillens [l], I. Taboada [e], A. Tamburro [af], O. Tarasova [am], A. Tepe [e], S. Ter-Antonyan [f], C. Terranova [w], S. Tilav [ad], P.A. Toale [ai], D. Tosi [am], D. Turčan [p], N. van Eijndhoven [m], J. Vandenbroucke [g], A. Van Overloop [t], J. van Santen [i], B. Voigt [am], D. Wahl [aa], C. Walck [ag], T. Waldenmaier [i], M. Wallraff [a], M. Walter [am], C. Wendt [z,*], S. Westerhoff [z], N. Whitehorn [z], K. Wiebe [ab], C.H. Wiebusch [a], G. Wikström [ag], D.R. Williams [b], R. Wischnewski [am], H. Wissing [p], K. Woschnagg [g], C. Xu [ad], X.W. Xu [f], G. Yodh [v], S. Yoshida [n,*], P. Zarzhitsky [b]

[a] III. Physikalisches Institut, RWTH Aachen University, D-52056 Aachen, Germany
[b] Department of Physics and Astronomy, University of Alabama, Tuscaloosa, AL 35487, USA
[c] Department of Physics and Astronomy, University of Alaska Anchorage, 3211 Providence Dr., Anchorage, AK 99508, USA
[d] CTSPS, Clark-Atlanta University, Atlanta, GA 30314, USA
[e] School of Physics and Center for Relativistic Astrophysics, Georgia Institute of Technology, Atlanta, GA 30332, USA
[f] Department of Physics, Southern University, Baton Rouge, LA 70813, USA
[g] Department of Physics, University of California, Berkeley, CA 94720, USA

0168-9002/$ - see front matter
doi:10.1016/j.nima.2010.03.102

[h] Lawrence Berkeley National Laboratory, Berkeley, CA 94720, USA
[i] Institut für Physik, Humboldt-Universität zu Berlin, D-12489 Berlin, Germany
[j] Fakultät für Physik & Astronomie, Ruhr-Universität Bochum, D-44780 Bochum, Germany
[k] Physikalisches Institut, Universität Bonn, Nussallee 12, D-53115 Bonn, Germany
[l] Université Libre de Bruxelles, Science Faculty CP230, B-1050 Brussels, Belgium
[m] Vrije Universiteit Brussel, Dienst ELEM, B-1050 Brussels, Belgium
[n] Department of Physics, Chiba University, Chiba 263-8522, Japan
[o] Department of Physics and Astronomy, University of Canterbury, Private Bag 4800, Christchurch, New Zealand
[p] Department of Physics, University of Maryland, College Park, MD 20742, USA
[q] Department of Physics and Center for Cosmology and Astro-Particle Physics, Ohio State University, Columbus, OH 43210, USA
[r] Department of Astronomy, Ohio State University, Columbus, OH 43210, USA
[s] Department of Physics, TU Dortmund University, D-44221 Dortmund, Germany
[t] Department of Subatomic and Radiation Physics, University of Gent, B-9000 Gent, Belgium
[u] Max-Planck-Institut für Kernphysik, D-69177 Heidelberg, Germany
[v] Department of Physics and Astronomy, University of California, Irvine, CA 92697, USA
[w] Laboratory for High Energy Physics, École Polytechnique Fédérale, CH-1015 Lausanne, Switzerland
[x] Department of Physics and Astronomy, University of Kansas, Lawrence, KS 66045, USA
[y] Department of Astronomy, University of Wisconsin, Madison, WI 53706, USA
[z] Department of Physics, University of Wisconsin, Madison, WI 53706, USA
[aa] Physical Sciences Laboratory, University of Wisconsin, Madison, WI 53706, USA
[ab] Institute of Physics, University of Mainz, Staudinger Weg 7, D-55099 Mainz, Germany
[ac] Université de Mons, 7000 Mons, Belgium
[ad] Bartol Research Institute and Department of Physics and Astronomy, University of Delaware, Newark, DE 19716, USA
[ae] Department of Physics, University of Oxford, 1 Keble Road, Oxford OX1 3NP, UK
[af] Department of Physics, University of Wisconsin, River Falls, WI 54022, USA
[ag] Oskar Klein Centre and Department of Physics, Stockholm University, SE-10691 Stockholm, Sweden
[ah] Department of Astronomy and Astrophysics, Pennsylvania State University, University Park, PA 16802, USA
[ai] Department of Physics, Pennsylvania State University, University Park, PA 16802, USA
[aj] Department of Physics and Astronomy, Uppsala University, Box 516, S-75120 Uppsala, Sweden
[ak] Department of Physics and Astronomy, Utrecht University/SRON, NL-3584 CC Utrecht, The Netherlands
[al] Department of Physics, University of Wuppertal, D-42119 Wuppertal, Germany
[am] DESY, D-15735 Zeuthen, Germany

ARTICLE INFO

Article history:
Received 4 March 2010
Accepted 6 March 2010
Available online 18 March 2010

Keywords:
PMT
Neutrino
Cosmic rays
Ice
Cherenkov

ABSTRACT

Over 5000 PMTs are being deployed at the South Pole to compose the IceCube neutrino observatory. Many are placed deep in the ice to detect Cherenkov light emitted by the products of high-energy neutrino interactions, and others are frozen into tanks on the surface to detect particles from atmospheric cosmic ray showers. IceCube is using the 10-in. diameter R7081-02 made by Hamamatsu Photonics. This paper describes the laboratory characterization and calibration of these PMTs before deployment. PMTs were illuminated with pulses ranging from single photons to saturation level. Parameterizations are given for the single photoelectron charge spectrum and the saturation behavior. Time resolution, late pulses and afterpulses are characterized. Because the PMTs are relatively large, the cathode sensitivity uniformity was measured. The absolute photon detection efficiency was calibrated using Rayleigh-scattered photons from a nitrogen laser. Measured characteristics are discussed in the context of their relevance to IceCube event reconstruction and simulation efforts.

1. Introduction

IceCube [1,2] is a kilometer-scale high energy neutrino telescope currently under construction at the geographic South Pole. A primary goal is to detect high energy neutrinos from astrophysical sources, helping to elucidate the mechanisms for production of high energy cosmic rays [3].

IceCube uses the 2800 m thick glacial ice sheet as a Cherenkov radiator for charged particles, for example those created when cosmic neutrinos collide with subatomic particles in the ice or nearby rock. Neutrino interactions can create high energy muons, electrons or tau particles, which must be distinguished from downgoing background muons based on the pattern of light emitted. The Cherenkov light from these particles is detected by an embedded array of Digital Optical Modules (DOMs), each of which incorporates a 10 in. diameter R7081-02 photomultiplier tube (PMT) made by Hamamatsu Photonics. The DOMs transmit time-stamped digitized PMT signal waveforms to computers at the surface.

The finished array will consist of 4800 DOMs at depths of 1450–2450 m, deployed at 17 m intervals along 80 vertical cables, which in turn are arranged in a triangular lattice with a horizontal spacing of approximately 125 m. An additional 320 DOMs will be frozen into 1.8 m diameter ice tanks located at the surface to form the IceTop array, which is designed for detection of cosmic ray air showers. The geometrical cross-sectional area will be $\sim 1\,\mathrm{km}^2$ and the volume of ice encompassed will be $\sim 1\,\mathrm{km}^3$. Another 360 DOMs will be deployed in a more compact geometry ("Deep Core" [4]) using PMTs almost identical to those described here but with a higher efficiency photocathode.

* Corresponding authors. Tel.: +608 890 0577.
E-mail addresses: mase@hepburn.s.chiba-u.ac.jp (K. Mase), chris.wendt@icecube.wisc.edu, chwendt@icecube.wisc.edu (C. Wendt), syoshida@hepburn.s.chiba-u.ac.jp (S. Yoshida).

[1] Affiliated with Universität Erlangen-Nürnberg, Physikalisches Institut, D-91058 Erlangen, Germany.
[2] On leave of absence from Università di Bari and Sezione INFN, Dipartimento di Fisica, I-70126 Bari, Italy.
[3] Affiliated with School of Pure and Applied Natural Sciences, Kalmar University, S-39182 Kalmar, Sweden.
[4] NASA Goddard Space Flight Center, Greenbelt, MD 20771, USA.

In this paper we describe measurements characterizing and calibrating IceCube PMTs, and discuss their relevance to detector performance and event reconstruction. First we describe the signals of interest in Section 2. Section 3 briefly describes the DOMs in which IceCube PMTs are deployed. Section 4 describes selection and basic features of the PMT, including the dark noise rate. Section 5 presents the design of the HV divider circuit. Sections 6–9 discuss characteristics of the PMT in the photon counting regime, starting with single photon waveforms and charge distributions. Time resolution is studied with a pulsed laser system. Uniformity of the photon detection response on the photocathode area is measured by scanning the entire cathode surface with a UV LED. Absolute efficiency calibration of the IceCube PMTs is carried out using Rayleigh-scattered light from a calibrated laser beam. Sections 10–11 describe response to bright pulses of light, including saturation behavior and afterpulse characteristics.

2. Characteristics of optical signals in IceCube

We begin by summarizing what the PMTs are supposed to detect, namely the optical signals generated by neutrinos in IceCube [1,2]. Of particular relevance are the amplitudes and widths of the pulses, requirements on time resolution, and how the pulses are used to reconstruct physics events or reject backgrounds.

In detection of a high energy ν_μ by IceCube, the neutrino interaction creates a muon that traverses kilometers of ice and generates Cherenkov light along its path. Above 1 TeV, the muon loses energy stochastically to produce multiple showers of secondary particles, resulting in an overall light yield proportional to the muon energy [5,6]. Most light is emitted near the Cherenkov angle, which is 41° away from the track direction. The arrival times of detected photons depend on the position of each DOM relative to the muon's path. For close DOMs, most photons arrive in a pulse less than 50 ns wide, in which the earliest photons have traveled straight from the muon track without scattering. Significant scattering accumulates along photon trajectories with a characteristic length scale of about 25 m [7], so light pulses lengthen with distance and reach 1 μs (FWHM) for DOMs 160 m away from a muon track. Depending on primary energy and distance from the track, each PMT can see single photons or pulses ranging up to thousands of photons.

Event reconstruction [1,2,8] builds on principles established for the predecessor array, AMANDA [9,10]. The observed PMT waveforms from individual DOMs are correlated and built into events, which are fitted to physics hypotheses using the maximum likelihood method. Each fit has access to the complete pattern of light amplitude and timing seen by the DOMs, and accounts for the DOMs' time response and optical sensitivity as well as time dispersion and optical attenuation introduced by the ice. The fit gives the direction and energy of the muon, which in turn characterizes its parent neutrino.

The observed light pattern is also used to distinguish the rare neutrino events from the large background of muons created in cosmic ray air showers, which are 10^6 times more numerous. For this the reconstructed direction is key, because neutrinos can come from any direction, even up from below, but the background muons are downgoing. A small fraction of background events can be misreconstructed in direction, thereby appearing to come from neutrinos, but the pattern of detected light will generally be a poor match compared to expectations for a properly reconstructed track. Misreconstruction can be aggravated by additional muons from the same shower or other coincident showers. This separation between signal and background is accomplished by evaluating relative probabilities on an event-by-event basis, and is aided by good time and amplitude resolution as well as by low PMT noise rates.

Similar principles apply to other types of high energy neutrino interaction. Instead of a muon, an electron can be created that loses its energy in a few-meter-long particle shower [11]; on the scale of IceCube, such a shower appears almost like a point source of Cherenkov light. For a sufficiently energetic neutrino, the light can be detected hundreds of meters away, and nearby DOMs can see enough light to drive their PMTs into the nonlinear saturation regime. Therefore proper modeling of saturation behavior is needed for good reconstruction and background rejection.

Design studies [2] for important physics goals have shown that sufficient reconstruction quality is achieved for a PMT timing resolution of 5 ns, low-temperature noise rate below 500 Hz, and effective dynamic range of 200 photoelectrons per 15 ns.

In the case of lower energy (MeV) neutrinos from supernovae, IceCube cannot resolve individual interactions. Instead, supernovae would be detected as a momentary increase in the collective photon counting rate for the whole array, corresponding to a large number of neutrino interactions within a few seconds. The dark noise rate of the PMTs is particularly important here, because it dictates the statistical significance of any excess count rate.

IceTop uses DOMs identical to those in the deep ice. Here the signals arise from muons, electrons and gamma rays in cosmic ray air showers [12]. These particles deposit energy in the ice tanks housing the DOMs, resulting in light pulses up to several hundred nanoseconds long. The arrival times and amplitudes in the surface array are then used to reconstruct the shower core position, direction, and energy. An overall timing resolution of 10 ns provides pointing accuracy of about 1°. The PMT pulses range from single photoelectrons at the periphery of showers to 10^5 photoelectrons for a 1 EeV shower that strikes within the array. To achieve the implied dynamic range, each tank contains two DOMs operating at gains differing by a factor 50.

3. The IceCube optical detector: DOM

The Digital Optical Module is the fundamental element for both optical detection and data acquisition in IceCube [2,13,14]. It contains a 10 in. diameter PMT supported by coupling gel, the PMT high voltage generator and divider circuits, an LED flasher board used for calibration of the array geometry and study of ice properties, and the DOM mainboard which contains the analog and digital signal processing electronics [14]. The PMT is surrounded by a μ−metal grid to shield it from the terrestrial magnetic field and improve the PMT performance. All systems are housed within a pressure sphere made of 0.5 in. thick glass, capable of withstanding pressures to 70 MPa. The glass and gel set the short wavelength cutoff of the DOM at about 350 nm, where the PMT by itself is still relatively efficient.

Strings of DOMs are deployed into water columns that have been melted by a hot-water drill. After refreezing, DOMs are optically well coupled to the surrounding glacial ice. Signal and power connections between the DOMs and the surface are provided by copper twisted-pair wires bundled together to form the main cables. PMT signals are digitized on the mainboard, buffered in memory, and sent to the surface upon command of surface readout processors.

4. PMT selection and dark noise rate

A number of large-area PMTs are commercially available and have been used successfully to instrument large volumes in other experiments. IceCube selected the R7081-02 made by Hamamatsu Photonics, emphasizing the criteria of low dark noise and good time and charge resolution for single photons. Some manufacturer's specifications are shown in Table 1, and more detailed measurements are described in the following.

The nominal gain of 10^7 was chosen to give single photon pulses around 8 mV, which is well above the digitizer precision and other electronic noise levels (both ~ 0.1 mV). Aging was not a concern for gain selection, since at the expected noise rates, the corresponding total charge delivered by each deep-ice PMT will be less than 1 C after 20 years (or 100 C for IceTop). Tubes with 10 and 12 stages were evaluated, with the 10 stage options showing a better peak-to-valley ratio at this gain. Lower gains of 5×10^6 and 10^5 were chosen for IceTop PMTs because air shower pulses generally comprise many photon detections.

The R7081-02 has 10 linear focused dynode stages and achieved the nominal gain of 10^7 at about 1300 V in our tests with the recommended divider ratios (observed range 1050–1600 V for 3744 PMTs). Its 10 in. diameter photocathode is composed of the standard bialkali material (Sb–Rb–Cs, Sb–K–Cs) with a peak quantum efficiency of approximately 25% at 390 nm. With a borosilicate glass envelope, the spectral response [16] is a good match to the spectrum of Cherenkov light after propagation through ice [7], especially considering the 350 nm cutoff of the housing.

In response to IceCube requirements, the supplied R7081-02 units were manufactured with a custom low radioactivity glass. The resulting dark count rate at low temperatures is close to 300 Hz in the -40 to $-20\,^{\circ}$C range of greatest interest for IceCube (Fig. 1). The higher room temperature rate can be attributed mostly to cathode thermionic emission, which is suppressed at low temperature. The low temperature rate is believed to be dominated by radioactive decays plus scintillation in the PMT glass envelope, and shows a rise with decreasing temperature similar to that reported in other studies [17]. The association of this rate with decays is supported by time correlations observed on scales up to 1 ms, as can result from delayed particle capture or de-excitation of states created by decays. It is also supported by the observed effect of taping: for these measurements, the entire outside surface of the PMT glass was covered in black vinyl tape, pulled tightly against the glass to avoid bubbles. The taping is observed to reduce the low-temperature noise rate by about half. The reduction is attributed to absorption of outward going decay photons, which can otherwise be channeled to the photocathode via internal reflection. The taped result is appropriate for PMTs installed in IceCube DOMs because they are optically coupled to gel (then glass and ice) where the refractive index matches better than it does for air.

The low dark rate allows IceCube to record all events that satisfy simple multiplicity conditions, and is particularly important for observation of any galactic supernova event. Such a supernova could yield about 10^6 excess photon counts in IceCube over a few seconds [18]. The single-PMT dark rate, multiplied by the number of PMTs, contributes a background rate of 1.5×10^6 Hz, with a similar contribution from decays in the DOMs' glass housing. The excess from a supernova would be easily observed above this background, even including the details of its time structure.

Table 1
Hamamatsu specifications for the R7081-02 PMT (typical) [15].

Spectral response	300–650 nm
Quantum efficiency at 390 nm	25%
Supply voltage for gain 10^7	1500 V
Dark rate at $-40\,^{\circ}$C	500 Hz
Transit time spread	3.2 ns
Peak to valley ratio for single photons	2.5
Pulse linearity at 2% deviation	70 mA

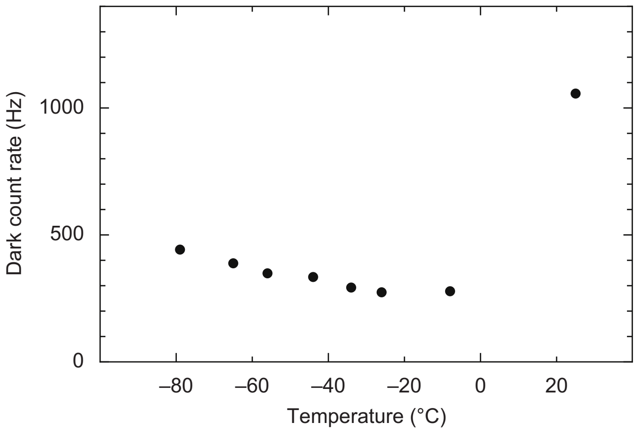

Fig. 1. Dark count rate versus temperature for a sample IceCube PMT covered with black tape (see text). Rates were recorded after a settling time of 12 h of dark operation at gain 10^7 and discriminator threshold 0.25 times the single photoelectron peak. An artificial deadtime circuit rejected additional hits within 6 μs of each count, including about half of all afterpulses (Section 11). The contribution from cosmic rays (<5 Hz) has not been subtracted.

On the other hand, a high energy neutrino event creates optical pulses distributed over 3 μs, with most information contained within a time window less than 300 ns wide in each DOM. Because this window is so short, the low PMT dark rate implies that only 1% of muons would be accompanied by a relevant noise count among the 100 DOMs closest to the track, and many of these DOMs detect multiple signal photons. Therefore the degradation of reconstruction and background rejection is very small. The dark noise rate has even less effect for IceTop DOMs, due to higher thresholds and coincidence requirements.

5. High voltage divider circuit

The relative dynode voltage ratios for R7081-02 have been optimized by Hamamatsu to achieve a maximum collection efficiency while achieving 10^7 gain between 1050 and 1600 V. Our high voltage subsystem design fulfills the additional requirements of low power consumption, long-term reliability, and sustained response to very bright pulses lasting up to a microsecond.

The dynode voltages are provided by a passive resistive divider with a total resistance of 130 MΩ (Fig. 2). The rather high total resistance is chosen to minimize power consumption, which is an important economic consideration for operations at the South Pole. A custom, compact, high voltage generator [19] that is both low power (<300 mW) and low noise (<1 mV ripple, peak-to-peak) is used in conjunction with the passive divider.

Capacitors are placed across the last six dynode intervals and between the last dynode and anode. These capacitors help sustain the PMT output for large pulses of up to 10^6 photoelectrons (p.e.). Even for illumination in the PMT saturation region (~ 200 p.e./ns, see Section 10), the transient gain loss after a 1 μs pulse (2×10^5 p.e.) is observed to be less than 1%. A detailed simulation [20] indicates that such a pulse could arise from a 50 PeV electron shower 100 m away from the PMT, which would then be faithfully recorded. Pulses up to five times this large (10^6 p.e.) still result in less than 20% transient gain loss, so while the primary pulse would be completely saturated, afterpulse amplitude could be used to estimate the total illumination (Section 11). Finally above

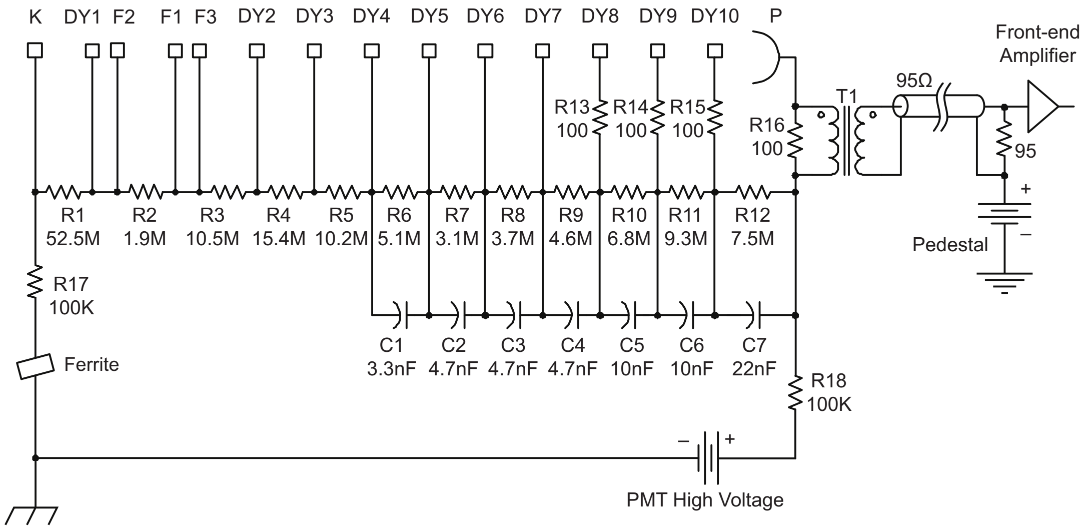

Fig. 2. Schematic of the passive HV divider circuit, shown with coupling to the front-end amplifier on the digitizer board.

2×10^7 p.e. the gain loss rises rapidly above 50%. For all these transient gain losses, recovery occurs within the RC time constants of order 1 s.

Low-inductance resistors (100 Ω, R13 through R15) are used to dampen ringing that arises from coupling of the larger dynode filter capacitors with parasitic inductance in the dynode leads and printed circuit traces. This ringing could otherwise be a nuisance when reconstructing a single PMT output waveform as a series of photon hits.

The IceCube PMTs are operated with their cathode at ground potential. Therefore the high voltage anode is AC coupled to the front-end amplifiers. For the AC coupling, we use a custom bifilar-wound 1:1 toroidal transformer rather than a DC blocking capacitor. High voltage reliability is achieved in the transformer winding using wire with insulation rated for over 5 kV DC. The resulting stray capacitance from anode to front-end amplifier is only 30 pF, which limits the stored energy which might damage the analog front-end if sparking should occur in the HV system. In contrast, a coupling capacitor large enough to meet the signal droop specification would be at least 1000 times larger than the stray capacitance of the transformer. The transformer topology also reduces noise by avoiding noisy high voltage ceramic signal coupling capacitors and by breaking a ground loop path involving the HV power supply. The ferrite and resistors in series with the HV supply further reduce coupling of high frequency noise to the front end input.

The transformer coupling delivers good signal fidelity for single-photoelectron (SPE) waveforms with risetimes of a few ns, while transmitting wide pulses exceeding 1 μs with less than 10% droop and undershoot. The custom design uses 18 bifilar turns on a ferrite (Magnetics Type H) toroid core, providing roughly flat coupling from 8 kHz to over 100 MHz at operating temperatures down to −40 °C. The self-resonant frequency is above 150 MHz. The low operation temperature presented a challenge because the permeability of the transformer core decreases rapidly with temperature, leading to a shorter droop time constant. Although most DOMs have a time constant around 15 μs at ambient temperatures near −30 °C, 1200 DOMs were built using an older transformer design yielding a time constant around 1.5 μs at −30 °C. The improved performance of the new design was achieved with a larger core and more turns, at the expense of a slightly wider SPE pulse shape (Fig. 3). The two designs are deployed intermixed.

The droop and undershoot are relevant for the μs long trains of photon pulses expected in DOMs over 100 m away from high energy events, such as 10 TeV electron showers or 500 TeV muon tracks. The small remaining effects are corrected by a software digital filter as a first step in event reconstruction, based on individual time constants for each DOM. The residual error is typically less than 1% of the pulse amplitude (except for pulses with peak or undershoot outside the ADC dynamic range, which is limited after 400 ns [14]).

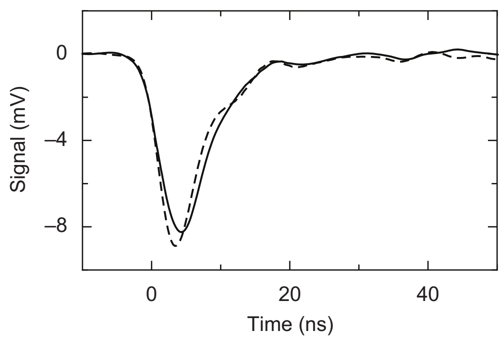

Fig. 3. Average of 10,000 SPE waveforms for one PMT at gain 1×10^7, as seen at the secondary of the AC coupling transformer. Results for other PMT samples are very similar. The solid and dashed curves correspond to new and old transformer designs discussed in Section 5.

The divider circuit is constructed on a 10 cm-diameter printed circuit board which is directly solder-mounted to the PMT. All components (except R13–R16) are through-hole mount type, selected with a voltage derating factor of two or greater (typically four) to ensure long-term reliability. Strict voltage and voltage gradient rules are applied to the board layout.

Coaxial cables are used for the connections to the high voltage generator and the front end amplifier on the digitizer board. The effective load for anode output pulses is 50Ω (43Ω for the older transformer design), which includes a back-termination resistor on the primary side of the transformer (R16), the transformer AC response, and the input impedance of the amplifier.

6. Single photoelectron waveform and charge

The SPE waveform shape and charge probability distribution are important for event reconstruction. The DOM waveform digitizers are triggered when the signal reaches about 0.25 times the typical SPE peak amplitude, after which the PMT output waveform is digitized for up to 6.4 μs. The detection efficiency for single photons depends directly on the fraction of the SPE charge distribution above trigger threshold. For high energy neutrino events, many waveforms show contributions from multiple photons, all of which could provide useful information during event reconstruction. The overall light yield provides an estimate of the neutrino energy, and the space and time distribution of light helps to reconstruct direction and reject backgrounds. The time distribution of photons can be extracted from each PMT waveform if the response to single photons is well understood. The response to each photon is approximately given by the average SPE waveform, scaled randomly according to the complete charge probability distribution.

In order to mimic the ambient temperature in the ice, PMTs were placed in a freezer box at $-32\,^{\circ}$C and illuminated by diffused light from a 375 nm UV LED. The light was generated in 10 ns pulses with intensity of about 0.1 photons per shot (~ 0.02 photoelectrons per shot), dim enough to initiate only SPE signals.

Fig. 3 shows the average SPE waveform, measured at the output of the AC coupling transformer with a digital storage oscilloscope (LeCroy LT374, 500 MHz bandwidth, 0.5 ns samples). Here the 95 Ω input impedance of the DOM's front end amplifier was replaced by the series combination of a 50 Ω resistor and the oscilloscope input.

Individual waveforms have different amplitudes but their shapes are similar to within a few percent. The waveform is dominated by a peak of Gaussian shape ($\sigma = 3.2$ ns) which accounts for 83% of the area. A tail on the late side of the peak accounts for the remaining area and exhibits a small amount of ringing. About 90% of the charge is collected before 10 ns after the peak. A substantial part of the observed pulse width is attributed to the damping resistors and the coupling transformer (Section 5).

To study the total charge in SPE events, a computer-controlled integrating ADC module (LeCroy 2249A) was used to integrate charge in a 70 ns window, triggered by the synchronization signal of the LED pulse generator. Fig. 4 shows a typical charge histogram, which exhibits a clear SPE peak to the right of the pedestal peak. The Gaussian part of the SPE peak corresponds to a charge resolution of approximately 30%.

The non-Gaussian component rising below 0.3 times the SPE charge in Fig. 4 has been studied to verify that such small pulses actually reflect in-time detection of photons, and not accidental coincidences of noise pulses such as from thermionic emission at the dynodes. The check for a noise contribution was done with the LED light output disabled (but not the synchronization signal that triggers acquisitions); all counts outside the narrow pedestal region were greatly suppressed compared to Fig. 4.

The low-charge component has been described in the past for many PMTs [21], and has been attributed to a sizable probability for backscattering of the primary photoelectron at the first dynode [22,23], leading to events where only a few secondaries are produced instead of the usual 10–20.

The shape of the low-charge component is important because even small pulses below the DOM's trigger threshold will be recorded in events with multiple photoelectrons. Therefore event reconstruction should account for the entire charge probability distribution down to zero charge, which we model as a Gaussian plus an exponential term [21]:

$$f(q) = \frac{P_e}{q_\tau}\exp\left[-\frac{q}{q_\tau}\right] + (1-P_e)\frac{1}{\sqrt{2\pi}\sigma_q}\exp\left[-\frac{(q-q_0)^2}{2\sigma_q^2}\right]. \qquad (1)$$

Here P_e is the fraction of events in the low-charge exponential part, q_0 is the charge at the SPE peak which defines the PMT gain, σ_q is the width of the Gaussian fit around the SPE peak, and q_τ is the decay constant in the exponential component. Fig. 4 shows that this is a good model for the shape of the charge histogram away from the pedestal.

Fig. 5 shows results of fitting equation (1) for a large sample of PMTs at different gains above 5×10^7, excluding the very low charge region $q<0.15q_0$ and the very high charge region more than 2σ past the peak. The value of q_τ/q_0 is substantially degenerate with P_e for describing observed spectra in the fitted range, so it has been fixed at the representative value of 0.20. The scaled quantities σ_q/q_0, q_τ/q_0, and P_e are found not to vary strongly with the PMT gain. The very small pulses with $q<0.15q_0$ were omitted to avoid confusion with the tail of the pedestal distribution; results were the same if the low-charge cut was moved to $0.25q_0$. The charge resolution σ_q/q_0 has been separately studied for gains between 10^7 and 10^8 and again no significant variations were seen.

Fig. 5 also shows the spread in parameters from PMT to PMT. The distribution in each parameter is approximately Gaussian,

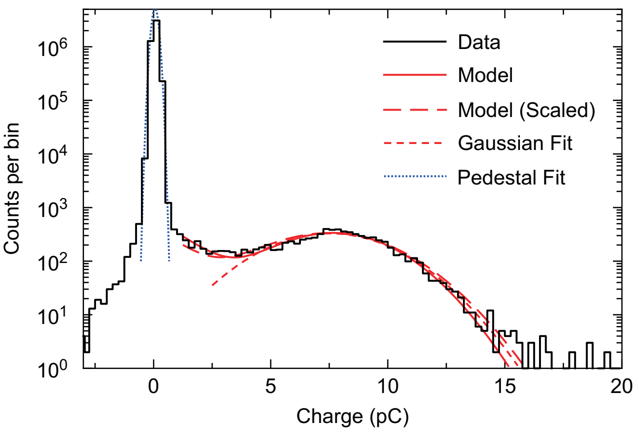

Fig. 4. Typical pedestal-subtracted SPE charge histogram at gain 5×10^7, including pedestal peak. Fits refer to Eq. (1), with the constraint $q_\tau/q_0 = 0.2$. The remaining parameters are optimized to fit this histogram for the curve labeled "Model", while "Model (Scaled)" optimizes only the scale parameter q_0 while holding σ_q/q_0 and P_e at values that describe the average of 120 PMTs.

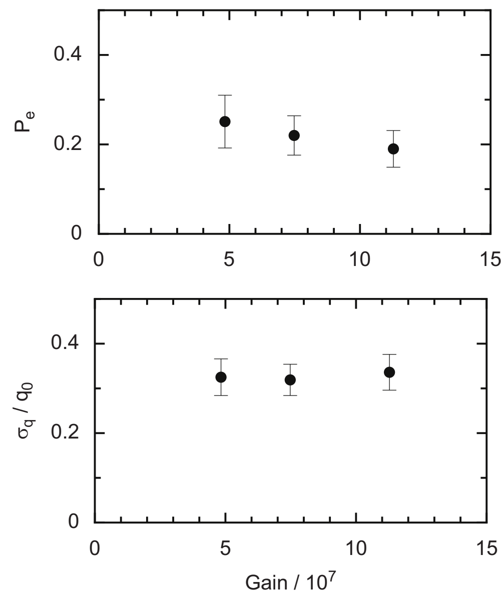

Fig. 5. Scaled parameters from Eq. (1) as a function of PMT gain. The error bars show the 1σ spread in parameters obtained for a sampling of 115 PMTs.

with the width shown by the error bars. The spread is substantial, but is not expected to have a large effect on data analysis, so the IceCube PMTs do not need to be parameterized individually. Instead, an average model is currently used in event simulation and reconstruction, without modeling the spread. The similarity among PMTs can also be gauged from Fig. 4, where data from one PMT is compared with a model curve scaled from the average fit results for 120 PMTs.

The above measurements were performed with diffuse light and represent an average over the photocathode surface. In a separate measurement at gain 10^7, substantial differences were observed as a function of position; for example, the peak-to-valley ratio decreased to near unity close to the edge of the photocathode, compounding the effects of gain variation (Section 8).

7. Time resolution

The timing of recorded SPE waveforms, relative to the photon arrival time, was studied at $-40\,^{\circ}$C using fast pulses (FWHM 50 ps) from a Hamamatsu PLP-10 diode laser. Pulses were optically attenuated and diffused over the PMT face, yielding an average of 0.04 photoelectrons per shot. The wavelength was 405 nm.

Each PMT was set for gain 10^7 based on its SPE charge spectrum. Hits greater than 0.4 times the SPE charge were recorded using the DOM digitization and readout electronics. Synchronization pulses from the laser were also digitized to indicate the true photon arrival times to within a fixed offset. Hit times were defined as the points where each waveform reached 50% of its maximum, resulting in the time resolution histogram of Fig. 6.

The main peak of the time histogram has width equivalent to a Gaussian of $\sigma = 2.0$ ns, although the rising and falling edges of the peak fit better to half-Gaussians with $\sigma = 1.2$ and 2.7 ns, respectively. Some of the width can be attributed to simultaneous illumination of the entire photocathode in our tests. When illuminated at the center only, the width decreased to 1.5 ns; conversely, the outer 3 cm of the photocathode exhibited additional delay of about 3 ns and additional broadening. The data acquisition system contributed a time smearing of less than 0.6 ns, which has not been subtracted.

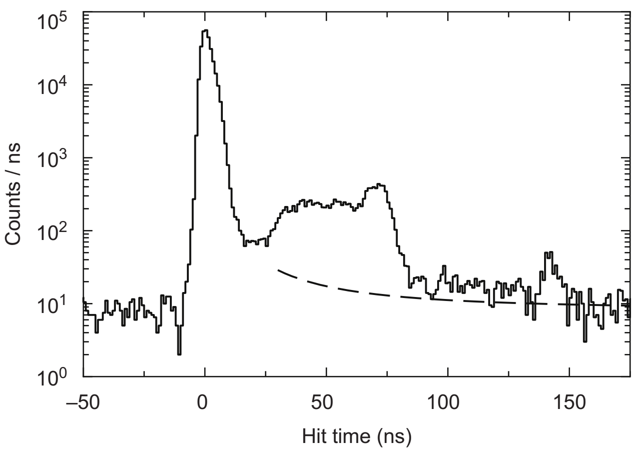

Fig. 6. Typical distribution of SPE hit times for an IceCube PMT, when illuminated by narrow pulses from a diode laser. Counts are shown for 1 ns time bins, referenced to a laser synchronization pulse. A small fraction of late pulses (dashed line) are due to laser afterglow plus the random background count rate; hit fractions described in the text are corrected accordingly. The random background also explains the counts before the synchronization pulse.

About 4% of hits are found in a shoulder (25–65 ns) and secondary peak at 71 ns, and 0.2% make up a corresponding tertiary structure (85–160 ns). The delayed hits are believed to arise when an electron trajectory is scattered back from the first dynode towards the photocathode, where it turns around and then eventually arrives back at the first dynode to initiate the pulse [23–25].

Because of strong photon scattering in the ice, the dispersion of hit times by the PMT at the 2 ns scale is not a limiting factor for reconstruction in IceCube; likewise for the tail at late times. Considering the spacing between DOMs, photons must typically travel tens of meters before detection, which is comparable to the scattering length of around 25 m [7]. A detailed simulation of photon scattering [26] showed that at 10 m distance, about 40% of photons are delayed by more than 5 ns, and 10% of photons are delayed between 20 and 80 ns. This is larger than the corresponding effects from the PMT itself. On the other hand, DOMs close to a high energy track can be expected to detect at least one photon with negligible delay, and then the very small 1.2 ns dispersion on the early side of the time resolution peak may be relevant when reconstructing arrival time of the earliest photon or the pulse rise time.

The time resolution study also reveals DOM-to-DOM differences in the nominal delay of SPE waveforms relative to photon arrival time. This delay includes PMT transit time plus signal delays between the PMT output and the digitizer. The PMT transit time is found to vary according to the square root of the applied voltage,

$$T_{transit}(V_{PMT}) = T_0 + 2\kappa V_0 \sqrt{V_0/V_{PMT}} \quad (2)$$

where $\kappa = 0.017$ ns/V is the slope at $V_0 = 1500$ V. The voltage applied to each PMT is set for a design gain 10^7, which is achieved between 1050 and 1600 V in 99.9% of PMTs. The resulting RMS spread of the overall time offset is 2.7 ns. We find 5% of DOMs more than 5 ns away from the mean, so the DOM-to-DOM corrections are currently included in reconstruction.

8. Two-dimensional photocathode scan

The number of photons arriving at the PMT is calculated from the observed photoelectron signals via the PMT optical efficiency. This is separated into an overall "absolute efficiency" and an angular dependence. The dominant factor in angular dependence is just the amount of photocathode area which can be seen from various directions. However, this has to be adjusted for the fact that the photocathode surface is very large and different portions do not all yield the same efficiency.

We have systematically analyzed the variation of efficiency with photocathode position at $25\,^{\circ}$C, using a two-dimensional scan system. A UV LED (370 nm) with collimator produced a 1 mm spot which was moved along the curved PMT surface, maintaining normal incidence of the light. The LED delivered approximately 125 photons per 80 ns pulse. The anode voltage was set for gain 10^7 at the center of the photocathode, as measured by the SPE charge peak (q_0 in Eq. (1)). The PMT pulse charge for each position was then measured by an integrating ADC triggered by the LED pulser.

Fig. 7 shows typical response maps on the cathode surface. The measured charge is proportional to the net photomultiplier efficiency and reflects the combined position dependence of photocathode quantum efficiency, collection efficiency, and dynode multiplication. PMT to PMT variation of the efficiency at a given spot on the photocathode may be as great as 40%, however, the spread in the area-integrated efficiency from PMT to PMT is much smaller, of order 10% (see Section 9). The average

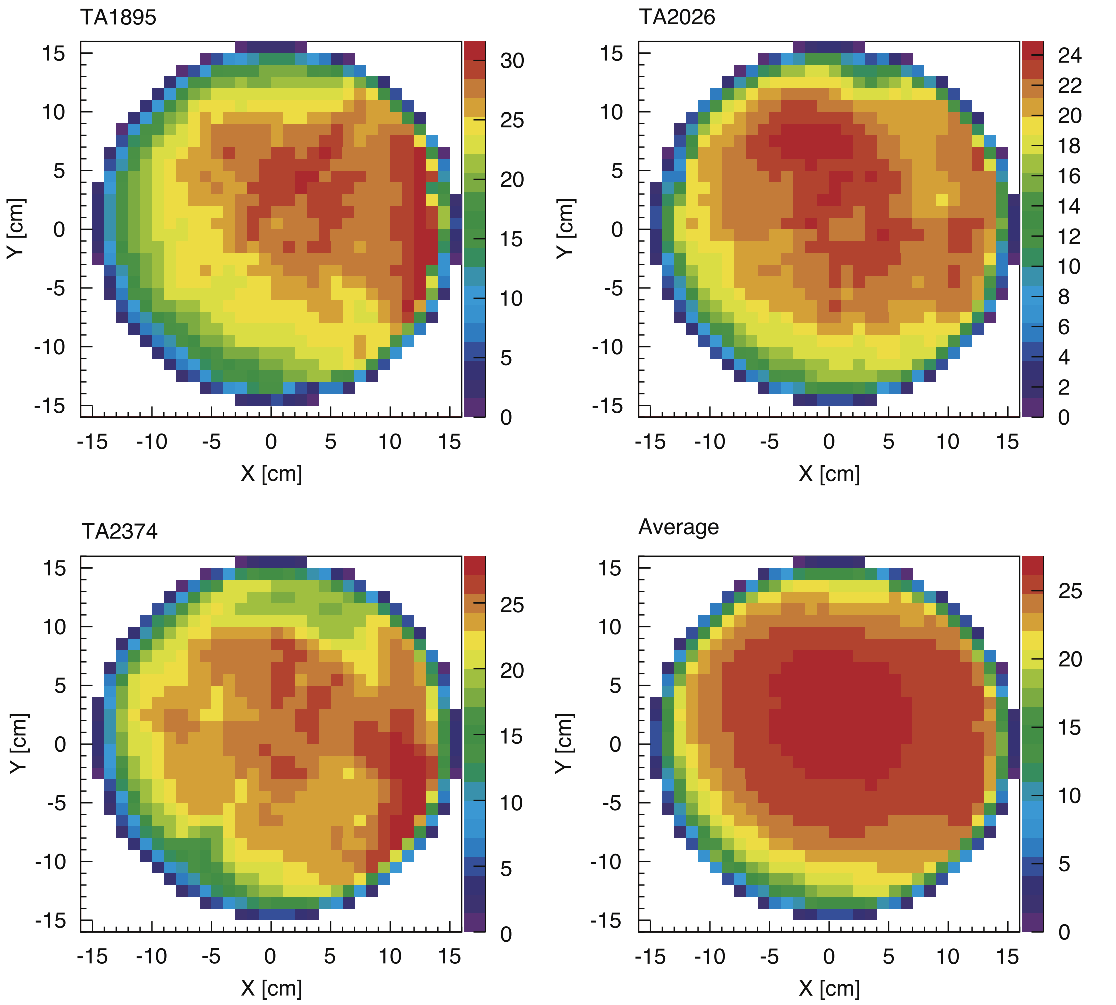

Fig. 7. Position dependence of the light pulse response for three example PMTs, and the average of 135 PMTs (lower right). The X–Y coordinates measure distance from the center of the photocathode along the curved PMT face. The value at each X–Y position indicates the PMT output pulse charge in units of the SPE charge, averaged over many pulses.

map shows a uniform falloff in the edge region, except for a small bias in the $+X$ direction. All PMTs were measured in the same orientation, so this bias could be associated to the first dynode position or the geomagnetic field.

A small part of the variation seen in the scans can be attributed to systematic errors, which arise mainly from the geomagnetic field and LED luminosity variance. The geomagnetic field of 462 mG is attenuated by about 50% with a shield made of μ- metal sheet and wire, as also used in IceCube DOMs. By comparing measurements with the PMT rotated from its standard orientation in various ways, we determined the field's effect on the efficiency variation is about 10%. Because the magnetic shield is the same, the overall results are representative of what is expected for deployed IceCube DOMs. (The field at the South Pole is 553 mG, and more vertical relative to the PMT axis.) The time dependence of LED luminosity affected the shape of each scan by less than 2%, as seen by reproducibility of the scan results.

By reducing the light intensity to give only SPE hits, a similar map has been constructed for gain variation. The gain can vary as a function of position because the corresponding photoelectron trajectories arrive differently at the first dynode, leading to different yields of secondary electrons. The observed gain (defined by q_0 in Eq. (1)) varies within $\pm 10\%$ over the active region when high voltage is set for gain 5×10^7 at the center. However, the low-charge contribution to the SPE charge spectrum (P_e in Eq. (1)) was found to also vary with position, so that the peak-to-valley ratio decreases close to unity near the edge of the photocathode. In this way, the average charge delivered per photoelectron was observed to decrease by up to 30% at nominal gain 10^7. Because of these effects, the detection efficiency map for single photons using a specific discriminator threshold can differ somewhat from the maps of Fig. 7.

The integrated sensitivity for a broad beam of photons incident from a particular direction follows from the cathode efficiency maps by averaging over the surface seen from that direction [27], with correction for non-normal incidence on surface elements as appropriate [28]. For this purpose the relative efficiency map is assumed not to vary with wavelength, i.e., each position is assumed to obey the spectral response curve given by the manufacturer [16]. The averaging substantially reduces the effect of variations over the surface so the sensitivity is not strongly dependent on direction at moderate polar angles. Only light that arrives at large polar angles relative to the PMT axis will primarily illuminate the equator region and therefore show strong azimuthal dependence. Likewise, the variation in charge spectrum from center to edge has little effect after averaging.

The scans were performed on a small fraction of the IceCube PMTs, so only the average variation with polar angle is used in simulation and reconstruction. For IceCube, the remaining PMT-to-PMT variation in directional sensitivity has very small consequences, because light is typically scattered after traveling about 25 m through the ice, and additional scattering takes place in the refrozen ice in the hole where the DOMs are deployed. The PMT-to-PMT variation, as well as the position dependence itself, could be more important for detectors deployed in water where scattering lengths are much longer [29].

9. Absolute efficiency calibration

The absolute calibration of PMT optical efficiency is important because IceCube uses the observed number of photons to estimate energy in reconstructed neutrino interactions. Showers initiated by electrons or tau leptons yield light in proportion to the energy, and so do muons above 1 TeV where energy loss is dominated by direct pair production, photonuclear interactions and bremsstrahlung [5,6].

Optical efficiency can be studied after deployment by using light from muons (produced in cosmic ray showers above IceCube) or from calibrated beacons deployed in the ice nearby. However, it is hard to isolate the PMT response from the effects of light scattering and attenuation in the ice, which have some uncertainties [7].

Here we describe the laboratory calibration of standard PMTs installed in 16 IceCube DOMs distributed throughout the array. The calibrated PMTs provide direct information for the energy calibration of IceCube, and will also help clarify the ice effects in other studies, which is an important subject on its own.

9.1. Technique

Our setup for measuring a PMT's UV photon detection efficiency is shown in Fig. 8. A pulsed 337 nm laser beam is passed through a chamber containing pure nitrogen gas, and the PMT to be calibrated is illuminated by the tiny amount of light that is Rayleigh scattered at about 90° from the beam. The PMT is rotated inside the dark box to probe different positions on the photocathode surface. The primary beam intensity is measured with a calibrated silicon photodiode "energy probe", and sets the fundamental scale for our efficiency measurement. A pressure gauge and temperature sensor provide the gas density. Beam intensity, geometry and gas density are then folded with the well-known Rayleigh scattering cross-section to obtain the absolute number of photons per pulse incident on the PMT. Individual photon detections are counted in each pulse and divided by the number incident to obtain the optical sensitivity at 337 nm. Additional corrections (Section 9.4) are needed to obtain DOM efficiency at wavelengths around 400 nm where IceCube is most sensitive.

The measurement combines effects of quantum efficiency and collection efficiency, and can be directly applied in IceCube analysis. It is different from the usual quantum efficiency measurement, which is based on cathode current response to a calibrated DC light source [16,30].

The laser (Spectra-Physics VSL-337ND-S) emits 4 ns pulses containing $\sim 10^{10}$ photons, as measured by the silicon photodiode probe (Laser Probe, Inc., RjP-465). After a warm-up delay, pulse energies are stable to within $\pm 2\%$.

The beam width is 1 mm, so the illuminated gas volume may be considered as a line source of Rayleigh scattered light. Apertures between the beam and the PMT define a source region with effective length of about 1 cm and a spot size on the PMT of about 1.5 cm. Photons can reach the PMT if they are scattered from the source region into a solid angle of about 7.6×10^{-4} sr around the 90° direction, while other scattered photons are eventually absorbed on baffles or other surfaces inside the chamber.

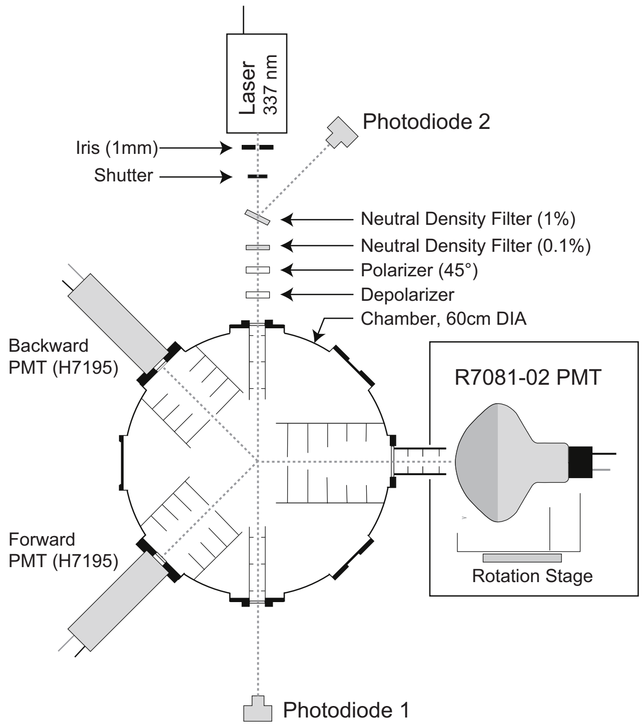

Fig. 8. Schematic view of the absolute calibration system. Photodiode 1 establishes the beam intensity, which is used to predict the amount of Rayleigh-scattered light reaching the R7081-02 PMT. The Hamamatsu H7195 PMTs and the other photodiode are for monitoring. Optical baffles define the scattering geometry, and chamber windows are anti-reflection coated UV quartz ($R < 0.1\%$ at 337 nm).

The Rayleigh scattering cross-section for a circularly polarized beam on nitrogen gas is taken as [31]

$$\frac{d\sigma_R}{d\Omega} = \frac{3}{16\pi}(1+\cos^2\theta) \times (3.50 \pm 0.02) \times 10^{-26}\,\mathrm{cm}^2 \tag{3}$$

with θ as the polar angle relative to the beam direction. The geometrical integration over the source region and corresponding solid angles is handled in a detailed ray-tracing calculation. After accounting for pressure and temperature, this yields the overall number of scattered photons reaching the PMT, typically 0.5 per pulse. With detection efficiency around 20%, this corresponds to ~ 0.1 SPE per pulse.

For counting photon detections, the PMT output charge is integrated for each laser pulse with a CAMAC ADC. The gating time is 184 ns which is long enough to include the late PMT pulses described in Section 7. The PMT gain is set close to 10^8 as defined by the SPE peak, q_0 in Eq. (1). We then count the number of events with charge q greater than a threshold $q_{th} = 0.5q_0$, which can be clearly discriminated in the charge histogram. A small correction for events with multiple photoelectrons yields the number of detected photons with $q > q_{th}$.

The PMT efficiency η for $q_{th} = 0.5q_0$ is then given by comparing the number of detected photons to the number reaching the PMT. The efficiency for other charge thresholds can be computed by extrapolation with the SPE charge response model, Eq. (1).

9.2. Results

Fig. 9 shows the measured detection efficiency as a function of distance from the cathode center. It also shows that the absolute

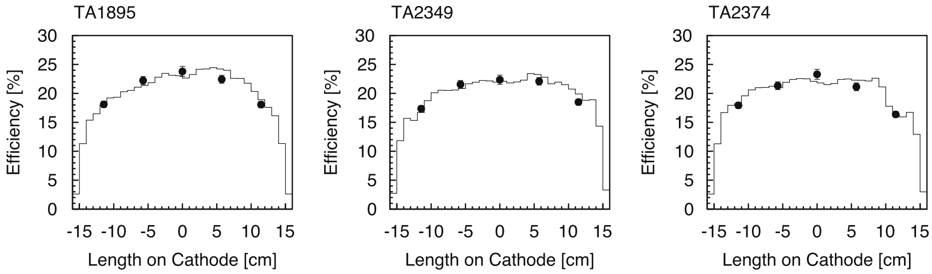

Fig. 9. Detection efficiency as a function of distance from the cathode center for three different PMTs. The points with error bars show absolute efficiency measurements extrapolated to $q_{th}=0$. The histogram curves show corresponding results from the 2D relative efficiency scans (Section 8) after normalization. Systematic uncertainties for the histograms are described in Section 8.

Table 2
Measured photon detection efficiency (η) and photon effective area (A_{eff}) at 25 °C for four different PMTs at wavelength 337 nm and gain 10^8.

PMT	η_{center} (%) ($q_{th}=0.5q_0$)	η_{whole} (%) ($q_{th}=0.5q_0$)	η_{whole} (%) ($q_{th}=0$)	A_{eff} (cm^2) ($q_{th}=0.5q_0$)	A_{eff} (cm^2) ($q_{th}=0$)
TA1895	16.4	13.2	18.6	84	119
TA2086	16.5	13.6	18.8	87	120
TA2349	15.1	12.1	17.6	77	112
TA2374	16.4	13.0	17.8	83	114

Values for $q_{th}=0$ were extrapolated using Eq. (1), where model parameters were fit independently for each PMT.

Table 3
Systematic error budget for the PMT efficiency calibration.

Source	$\Delta\eta/\eta$ (%)
Laser beam energy	5
Aperture	4
Ambient magnetic field	4
Pressure and temperature	1
Polarization	1
Rayleigh cross-section	0.5
Dark noise/cosmic rays	0.2
Overall	7.7

efficiency measurements follow closely the shape expected from the 2D relative efficiency scans (Section 8). Consequently, the relative efficiency scans can be normalized to the absolute measurements and used to estimate the absolute efficiency averaged over any given area of the photocathode surface.

Table 2 lists measured efficiencies at the center and averaged over the whole photocathode area. The latter is defined to include all points within 15 cm of the PMT axis, measured along the curved surface. Table 2 also includes the photon "effective area" which means the amount of ideal surface with 100% efficiency that corresponds to the actual convolution of area and efficiency. Here it is quoted for light uniformly spread over the PMT surface, with normal incidence. For use in IceCube analysis, a similar calculation is performed for unidirectional beams as a function of the beam angle, folding in the variation of cathode response and optical effects at material boundaries.

The detection efficiencies in the central area of the photocathode are close to 20% if extrapolated to $q_{th}=0$. These values have been compared on a PMT-by-PMT basis with measurements by Hamamatsu using cathode response to DC light sources. We find very good agreement, which implies that the collection efficiency is not much less than 100% at the cathode center.

IceCube PMTs operate at lower voltages than used in this measurement (gain 10^7 instead of 10^8), so collection efficiency is expected to be slightly lower. However, this effect is expected to be concentrated at the edges where the electron optics are less ideal, and the efficiency falloff near the edges is obtained from the 2D relative efficiency scans (Section 8). Since those scans were done at gain 10^7, no additional correction is necessary for the results in Table 2.

9.3. Uncertainties

The overall systematic uncertainty $\Delta\eta/\eta$ of the PMT detection efficiency measurement is 7.7%, as detailed in Table 3. In addition, the measurement of each position on the PMT face has a typical statistical uncertainty of about 5%, set by the number of SPE hits recorded. This is reduced to about 2% when calculating efficiency for the whole PMT by combining information from the individual face positions, but the extrapolation relies on the 2D map (Section 8) which has comparable uncertainties.

The dominant contributions to systematic error arise from the laser beam energy measurement, the geometry of the scattering chamber, and the geomagnetic field. The first two enter directly into the calculation of the number of photons reaching the PMT. The beam energy comes from the laser energy probe, which was factory calibrated to within 5% at 337 nm. The aperture uncertainty of 4% comes from geometrical survey of the chamber, which is used in the ray tracing program.

The ambient geomagnetic field is 462 mG and is unshielded in the current setup. By changing the orientation of the PMT, we showed that it affects the point-to-point response map at the 20% level but the average over the surface varies by only 4%.

The Rayleigh scattering angular distribution depends on the polarization of the laser beam [32], so care was required to limit any polarization effect. The effect can be strong because the PMT only sees a Rayleigh scattering signal from the vertical component of polarization: the horizontal component induces a dipole moment oscillating perpendicular to the beam in the horizontal plane, which cannot emit power to the PMT which is in the same direction. On the other hand the energy probe reads the total power regardless of polarization, so the fraction of power in the vertical direction must be under control. In our setup (Fig. 8), the laser beam is first linearly polarized at 45° and then passed through a quartz $\lambda/4$ waveplate to convert it to 100% circular polarization. By rotating a linear polarizer in the beam, we verified that the resulting horizontal and vertical components are equal to within better than 1%, which leads to a limit of 1% for the corresponding systematic effect on the efficiency measurement.

Several analyses were performed to show that the scattered photons are coming from Rayleigh scattering and not other sources such as residual suspended dust. We checked for expected scaling with gas density down to low pressure, symmetry of scattered light seen in forward and backward monitoring PMTs (see Fig. 8), and repeatability of measurements after long time intervals.

The main systematic uncertainties in our method could be reduced if desired, comparable to the current statistical precision of about 2%. To accomplish this, one would calibrate the silicon photodiode "energy meter" at the 1% level; measure the aperture geometry more precisely; and provide good shielding from the geomagnetic field.

9.4. Additional corrections

There are additional steps to obtain the detection efficiency of DOMs from the PMT efficiency measurements, and these will be reported separately along with other studies on assembled DOMs. Corrections include attenuation of light in the glass pressure housing and the gel used for optical and mechanical coupling, wavelength dependence in both the PMT sensitivity (quoted by the manufacturer [16]) and the attenuation factors, and the geometry of incident rays. These effects are included in a detailed optical simulation of the DOMs [27,33] which will be compared to laboratory measurements on assembled DOMs. A full detector simulation can be used to combine the absolute efficiencies at 337 nm, the wavelength dependences, and the spectrum of light received from neutrino interactions. Investigations of the combined effect show that IceCube detects signal photons in a broad range centered on about 400 nm. These studies will be presented elsewhere.

Our measurements were at 25 °C, and some temperature dependence can be expected. The manufacturer quotes a temperature coefficient of $-0.2\%/^\circ$C for cathode sensitivity [16]. This is being directly addressed by relative measurements of optical efficiency of assembled DOMs at −45, −20 °C and room temperature.

10. PMT linearity and saturation behavior

For most neutrino interactions expected in IceCube, any one PMT will not detect more than a handful of photons. For such events, and even when up to a few hundred are detected, the PMT output is proportional to the number of photons detected. However, some of the most interesting signal events would be expected to deposit large amounts of energy within tens of meters of individual PMTs, and then the PMT response can be less than proportional. Optimal reconstruction requires measuring the linearity limit and modeling the nonlinear saturation behavior.

To study saturation behavior, PMTs were illuminated with LED pulses of various durations and brightnesses. The duration of the light pulses was varied from 3 ns to 1 μs, as measured with a fast PIN photodiode (1 ns response time). A set of calibrated neutral density filters was used to control the light level. For a given LED brightness, illumination was first measured by the PMT signal, using a filter with sufficient attenuation to allow linear operation of the PMT. The observed signal was converted to a photoelectron rate and a total number of photoelectrons (p.e.) using the SPE charge q_0, determined in a separate step. Then the illumination level was increased by using different filters, with the new number of p.e. calculated from the ratio of filter attenuation coefficients.

Fig. 10(a) shows the observed peak anode current I as a function of the ideal peak current I_0, defined as the peak p.e. rate times the SPE charge. At gain 10^7, the PMT response is linear within 10% up to currents of about 50 mA (31 p.e./ns), but saturates completely at about 150 mA. Peak responses to different light pulse widths from 3 to 400 ns lie along a single curve. The 3 and 20 ns width pulses were approximately Gaussian in shape, so the observation of identical peak response supports a saturation model where the observed current is a direct function of the instantaneous illumination, with little cumulative effect from previous illumination. In particular the data are inconsistent with models expressed in terms of total pulse charge, which were used in some older versions of the IceCube simulation software. The 400 ns pulses were approximately rectangular in shape and the output current mirrored this shape well even in the saturation region, again as expected for an instantaneous current saturation model. Even long light pulses near saturation level show only about 5% decline from 100 mA after 1 μs of steady illumination. (Note this small history effect is independent of the transient gain loss due to discharge of the dynode capacitors, which remains below 1% for such a pulse.)

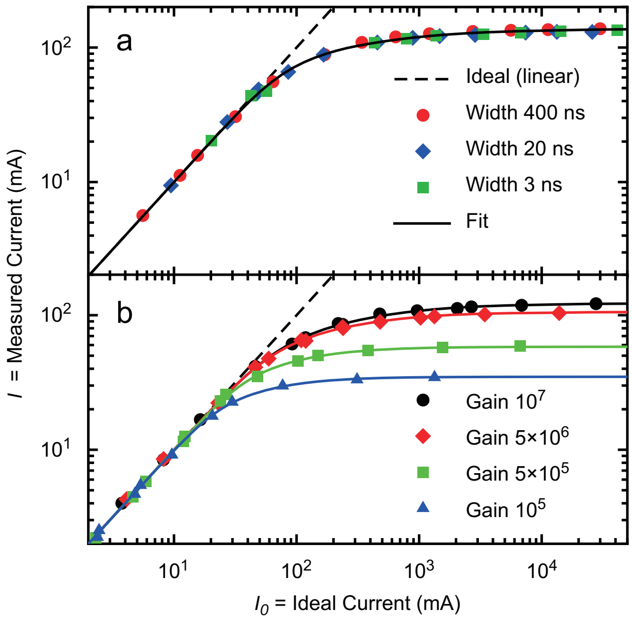

Fig. 10. (a) PMT saturation curve for gain 10^7. The measured current is plotted against the instantaneous light level, defined in terms of the current that would be expected for an ideal (linear) device. Data points correspond to peak currents for the indicated pulse widths. The fit curve is given by Eq. (4), with parameters chosen optimally for this PMT (serial number SA2747). (b) Effect of PMT gain on the saturation curve. Data points correspond to peak currents for 200 ns pulses for PMT serial number AA0020. The curves show the fitted parameterization, Eq. (5).

The same saturation behavior was found to apply regardless of what part of the cathode was illuminated, even at −30 °C, which indicates that photocathode surface resistance [16] is not important on the relevant time scales.

The instantaneous current response is well parameterized by the following:

$$\ln I_0 = \ln I + C\frac{(I/A)^B}{(1-I/A)^{1/4}}. \tag{4}$$

The parameters A, B and C differ substantially from one PMT to another (Table 4), so the model should not be used to invert observed saturated pulses unless each PMT is fully characterized.

Fig. 10(b) shows additional measurements at a range of lower gains down to 10^5, relevant for IceTop DOMs. The model of Eq. (4) continues to apply over the full range if the parameters are scaled approximately as powers of the gain, as shown by the curves which are scaled by $\gamma \equiv \mathrm{Gain}/10^6$:

$$A(\gamma) = 285\gamma^{0.52}/(1+\gamma^{1/4})^2$$

$$B(\gamma) = 13\gamma^{0.18}/(1+\gamma^{1/4})^2$$

$$C(\gamma) = 0.32\gamma^{-0.13}(1+\gamma^{1/4})^2. \tag{5}$$

The given parameters apply to a single measured PMT, but similar scaling behavior can be expected for other examples; as a first estimate one would adjust the leading coefficients in each parameter to match measurements at a particular gain, and retain the same scaling with gain. Note the good numerical behavior of the scaling equations allows them to be used also for estimates outside the given range of gain.

The instantaneous current model also helps understand how the response to narrow light pulses (3 ns FWHM) broadens as intensity increases (Fig. 11). With the light pulse strongly attenuated (220 p.e.), the PMT output pulse width is similar to the SPE response, about 10 ns. As more light is allowed to reach the PMT (3700 p.e.), first a gradual broadening occurs to about 20 ns width. This broadening follows from Eq. (4) because the peak current is more attenuated than the rising and trailing edges. At this point a tail is visible, along with a second peak delayed by about 60 ns relative to the main peak. These are consistent with the late photoelectron responses seen in SPE time resolution measurements (Section 7), except that the relative sizes of main peak and tail are altered by saturation in the main peak. At still higher light levels (210,000 p.e.), the second tail peak is comparable in size to the fully saturated main peak, and the total width is dominated by the combination of the two peaks.

The highest light level in Fig. 11 also exposes a small pre-pulse 30 ns before the main peak, as well as a substantial afterpulse starting several hundred ns later (see Section 11). The pre-pulse is ascribed to photoelectrons ejected from the first dynode, and is somewhat exaggerated in Fig. 11 because the light source was aimed at the center of the cathode with the dynode directly behind. The individual quanta comprising the pre-pulse were separately studied using SPE-level illumination, and were found to be between 1/10 and 1/20 of the SPE pulse size, occurring at less than 1% of the SPE rate. The ratio between sizes of SPE pulses and pre-pulse quanta is similar to the typical first dynode gain reported by the manufacturer [24]. Because individual pre-pulse quanta are below threshold for triggering DOMs, they have a small impact on event reconstruction. The combined pre-pulses from many photons would only be observable for a large, narrow light pulse ($\sim$5000 photons detected within 30 ns). Pulses originating more than $\sim$25 m from a DOM would generally be broader than this, due to scattering in the ice [7].

The saturation model (Eq. (4)) can be important for reconstruction of very high energy neutrinos that produce electromagnetic or hadronic showers. Ideally, reconstruction would rely most heavily on the PMTs closest to a shower, because the light pulse is broadened and attenuated as it travels through the ice [7]; however, these PMTs can be saturated for high energy events. The energy where saturation effects become important can be estimated by choosing a characteristic distance of 60 m, which is about half the inter-string spacing. At this distance, simulations [20] show that a 600 TeV shower yields peak intensity of 30 p.e./ns, equivalent to the linearity limit of 50 mA. Above this energy, signals in close PMTs require a correction for saturation. Above $\sim$10 PeV, many nearby PMTs are badly saturated and the shower energy measurement must rely mostly on far-away PMTs. However, even badly saturated PMTs measure the beginning and end of the pulse, which can be used to constrain the event geometry.

Table 4
Saturation curve parameters for three PMT samples, as defined for Eq. (4).

PMT serial no.	*A* (mA)	*B*	*C*
AA0020	126	2.02	2.98
SA2747	138	2.05	3.23
SA2749	138	1.82	2.67

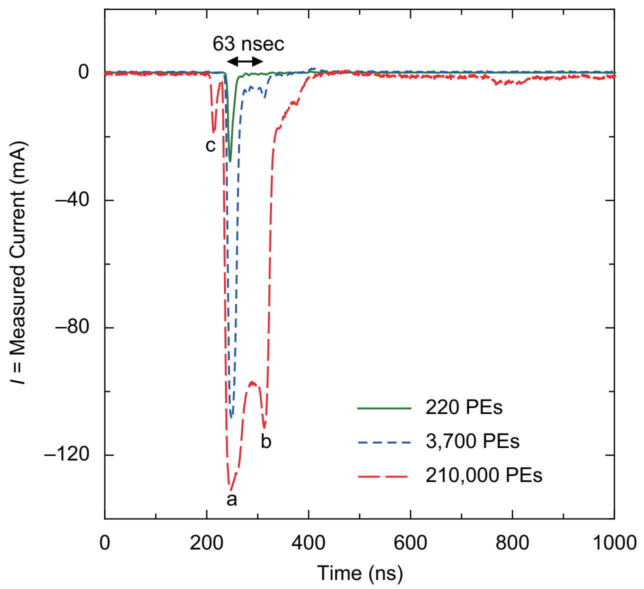

Fig. 11. Average waveforms observed in PMT serial number SA2747 for 3 ns (FWHM) light pulses with progressively higher intensity: (a) main peak; (b) secondary peak due to unusual electron trajectories and (c) pre-pulse.

11. Afterpulses

As shown in Figs. 6 and 11, the prompt response to a light pulse has a tail extending to about 100 ns. Afterpulses are seen in the range of 300 ns to 11 μs. Such afterpulses are a common feature of PMTs, and are attributed to ionization of residual gases by electrons accelerated in the space between dynodes [34]. Ions created in this way can be accelerated back to the photocathode, causing ejection of electrons which are subsequently amplified like the original photoelectrons. Some ions strike one of the dynodes instead, but the corresponding ejecta are amplified much less and could easily go undetected.

Afterpulse measurements were made at 25 °C with LED pulses of 40 ns width, using calibrated optical attenuators to control the intensity, as for the saturation measurements (Section 10). In a bright LED flash, many individual ions are created, and their responses add up to an afterpulse waveform with well defined peaks and valleys (Fig. 12). The various peaks are believed to correspond to ions of different masses, according to their individual flight times in the accelerating field [34]. Prominent afterpulse peaks for this PMT occur around 600 ns, 2 and 8 μs after the main response peak. The peaks are fairly wide and no period is entirely devoid of afterpulses until after 11 μs.

The average afterpulse waveform grows almost linearly with the flash brightness even up to the highest intensity studied (4.4×10^6 p.e. in 40 ns), where the primary response is completely saturated at $\sim$1000 p.e./ns (Fig. 10). This suggests that observed afterpulses arise primarily from ions generated in earlier stages of the multiplier, whose electron currents continue to rise even when later stages have saturated.

Up to primary pulses of 1×10^6 p.e., the integral from 300 ns to 11 μs corresponds to 0.06 SPE per primary photoelectron.

For dimmer flashes, individual events have a small number of afterpulse electrons. These appear as separate single afterpulses distributed in time, with probability that can be approximately

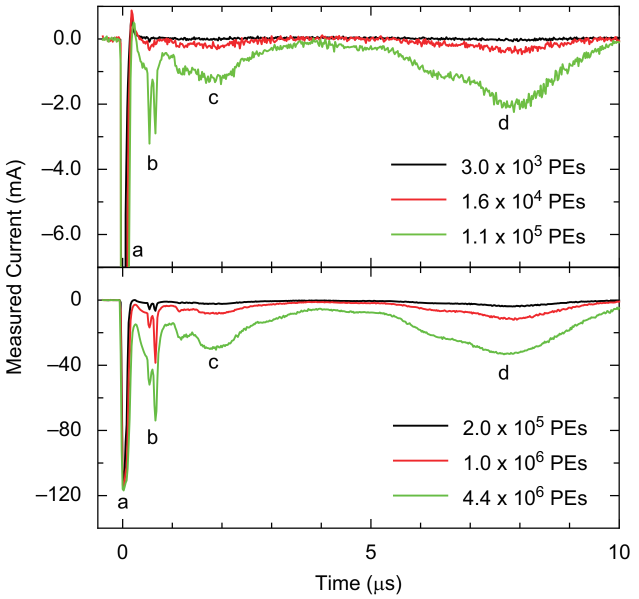

Fig. 12. PMT afterpulse waveforms for bright flashes lasting 40 ns. Each curve is averaged over many flashes. The primary response (a) is off-scale and saturated at most of these intensities. Brightness of flashes is determined by the method of Section 10, which is independent of PMT saturation effects. Prominent afterpulse peaks are seen around (b) 600 ns, (c) 2 μs and (d) 8 μs after the primary response. The afterpulse waveforms grow nearly linearly with flash intensity up to the maximum intensity measured. The PMT was operated at gain of 10^7, with the anode at 1326 V. Some variation in afterpulse waveforms is observed from one PMT to another of the same type. Measurement of tails at very late times is slightly affected by an AC coupling time constant of 80 μs.

predicted from the average waveforms of Fig. 12. Because different ions are associated with different time ranges, and because some ions eject multiple electrons from the photocathode, each afterpulse delay range will be characterized by a different fundamental charge distribution. We have observed corresponding peak charges from 1 SPE to 13 SPE, consistent with a recent more detailed study of individual ion afterpulses [35].

The above observations are from study of only a few PMT samples, and the numbers quoted pertain to only one (serial AA0020). Although quantitative differences are seen from one sample to another, the information allows one to assess whether afterpulses affect IceCube event reconstructions, and to limit small systematic errors. If a particular physics analysis then appears sensitive to afterpulses, a larger sample of PMTs would have to be studied quantitatively to provide the necessary corrections.

Given the small ratio of charge between afterpulse and primary pulse, it can be expected that most IceCube analyses will not be strongly sensitive to the details of afterpulses. Typical IceCube events yield hits in each PMT that are spread over times of a few hundred nanoseconds, well before the main part of the afterpulse distribution. For very high energy events (e.g. electron energy 1 PeV in the deep ice), signals are likely to be seen by PMTs 500 m away where arrival times are dispersed over 2 μs (FWHM), and then the afterpulse distribution becomes more relevant. However, the main effect is a minor distortion of the late part of the pulse, which already has an intrinsically long tail due to scattering. Generally one does not lose much information by disregarding details of the waveforms at late times.

However, some events can have multiple peaks in the photon time distributions, and then a characterization of afterpulses can be important for proper reconstruction. The most common case is an event with coincident arrival of one or more downgoing muons from cosmic ray showers above the detector, which calls for disentangling the hits originating from multiple tracks, and therefore also the afterpulses. Multiple muons can also arise from a single shower, and when the resulting tracks are well separated they can yield multiple hits. More intriguing is the possibility of ν_τ interactions which can create two showers of particles separated by hundreds of meters [36]. In such a case some PMTs can see pulses of light separated by a few microseconds, so effects of afterpulses should be considered carefully. The late pulses described in Section 7 should also be considered in these contexts.

12. Summary

The R7081-02 PMT has been characterized and key findings were discussed in the context of IceCube physics goals. We observe a single-photoelectron time resolution of 2.0 ns averaged over the face of the PMT. A small fraction of the pulses arrive much later, with about 4% between 25 and 65 ns late. We also observe prepulsing and afterpulsing, with afterpulsing occurring up to 11 μs late. The single photoelectron charge spectrum is well fit by a Gaussian corresponding to charge resolution near 30%, plus a contribution at low charge which is represented by an exponential. The dark rate was measured to be 300 Hz in the temperature range −40 to −20 °C. A new method for optical sensitivity calibration has been demonstrated, which uses Rayleigh scattering to scale from the intensity of a primary laser beam to the much smaller number of photons reaching a target PMT. Measurements of dark rate, single photon detection efficiency, single photoelectron waveform and charge, time resolution, large pulse response, and afterpulses will serve as input for detailed simulation of IceCube physics events.

Acknowledgements

We acknowledge support from the following agencies: U.S. National Science Foundation-Office of Polar Program, U.S. National Science Foundation-Physics Division, University of Wisconsin Alumni Research Foundation, U.S. Department of Energy, and National Energy Research Scientific Computing Center, the Louisiana Optical Network Initiative (LONI) grid computing resources; Swedish Research Council, Swedish Polar Research Secretariat, and Knut and Alice Wallenberg Foundation, Sweden; German Ministry for Education and Research (BMBF), Deutsche Forschungsgemeinschaft (DFG), Research Department of Plasmas with Complex Interactions (Bochum), Germany; Fund for Scientific Research (FNRS-FWO), FWO Odysseus programme, Flanders Institute to encourage scientific and technological research in industry (IWT), Belgian Federal Science Policy Office (Belspo); Marsden Fund, New Zealand; Japan Society for the Promotion of Science (JSPS); M. Ribordy acknowledges the support of the SNF (Switzerland); A. Kappes and A. Groß acknowledge support by the EU Marie Curie OIF Program; J.P. Rodrigues acknowledge support by the Capes Foundation, Ministry of Education of Brazil.

References

[1] J. Ahrens, et al.IceCube Collaboration, Astropart. Phys. 20 (2004) 507.
[2] J. Ahrens, et al., IceCube Collaboration, IceCube Preliminary Design Document, 2001 ⟨http://icecube.wisc.edu/⟩.
[3] T.K. Gaisser, F. Halzen, T. Stanev, Phys. Rep. 258 (1995) 173;
J.G. Learned, K. Mannheim, Annu. Rev. Nucl. Part. Sci. 50 (2000) 679;
F. Halzen, D. Hooper, Rep. Prog. Phys. 65 (2002) 1025.
[4] A. Karle for the IceCube Collaboration, IceCube, in: Proceedings of the 31st International Cosmic Ray Conference, 7–15 July 2009, Lodz, Poland.

[5] W. Lohmann, R. Kopp, R. Voss, Energy loss of muons in the energy range 1–10 000 GeV, CERN Report 85–03, 1985.
[6] D. Chirkin, W. Rhode, preprint arXiv:hep-ph/0407075v2, 2008.
[7] M. Ackermann, et al., J. Geophys. Res. 11 (2006) D13203.
[8] D. Chirkin for the IceCube Collaboration, in: Proceedings of the 30th International Cosmic Ray Conference, 3–11 July 2007, Merida, Yucatan, Mexico, session HE1.5; in arXiv:0711.0353 [astro-ph], pp. 151–154.
[9] E. Andres, et al.AMANDA Collaboration, Astropart. Phys. 13 (2000) 1.
[10] J. Ahrens, et al.AMANDA Collaboration, Phys. Rev. D 66 (2002) 12005.
[11] E. Middell, J. McCartin M. D'Agostino for the IceCube Collaboration, in: Proceedings of the 31st International Cosmic Ray Conference, 7–15 July 2009, Lodz, Poland.
[12] T. Gaiser et al., IceCube Collaboration, IceTop Preliminary Design Document, 2003 ⟨http://icecube.wisc.edu/⟩.
[13] A. Achterberg, et al.IceCube Collaboration, Astropart. Phys. 26 (2006) 155.
[14] R. Abbasi, et al.IceCube Collaboration, Nucl. Instr. and Meth. A 601 (2009) 294.
[15] Hamamatsu Corp., R7081-02 Photomultiplier Tube Data, 2003.
[16] Hamamatsu Corp., Photomultiplier Tubes: Basics and Applications, third ed., 2007.
[17] A. Ankowski, et al., Nucl. Instr. and Meth. A 556 (2006) 146;
J.A. Nikkel, W.H. Lippincott, D.N. McKinsey, J. Instrum. 2 (2007) 1004;
H.O. Meyer, preprint arXiv:0805:0771v1 [nucl-ex], 2008.
[18] A.S. Dighe, M.Th. Keil, G.G. Raffelt, J. Cosmol. Astropart. Phys. 0306 (2003) 005.
[19] EMCO High Voltage Corporation, Sutter Creek, CA.
[20] J. Lundberg, et al., Nucl. Instr. and Meth. A 581 (2007) 619.
[21] R. Dossi, et al., Nucl. Instr. and Meth. A 451 (2000) 623.
[22] P.B. Coates, J. Phys. D Appl. Phys. 6 (1973) 153.
[23] O.Ju. Smirnov, P. Lombardi, G. Ranucci, Instrum. Exp. Tech. 47 (2004) 69.
[24] Hamamatsu Corp., Personal communication.
[25] B.K. Lubsandorzhiev, P.G. Pokhil, R.V. Vasiljev, A.G. Wright, Nucl. Instr. and Meth. A 442 (2000) 452.
[26] A. Karle, Monte Carlo simulation of photon transport and detection in deep ice: muons and cascades, in: Proceedings of the Workshop on Simulation and Analysis Methods for Large Neutrino Telescopes, DESY 1998.
[27] K. Hoshina ⟨http://www.ppl.phys.chiba-u.jp/ROMEO/⟩.
[28] D. Motta, S. Schönert, Nucl. Instr. and Meth. A 539 (2005) 217.
[29] S. Fukuda, et al.The Super-Kamiokande Collaboration, Nucl. Instr. and Meth. A 501 (2003) 418;
A. Aguilar, et al., Astropart. Phys. 23 (2005) 131.
[30] R. Mirzoyan, et al., Nucl. Instr. and Meth. A 572 (2007) 449.
[31] H. Naus, W. Ubachs, Opt. Lett. 25 (2000) 347 and references therein..
[32] W. Reckers, Y. Gu, E.W. Rothe, H. Voges, Appl. Spectrosc. 51 (1997) 1012.
[33] S. Agostinelli, et al., Nucl. Instr. and Meth. A 506 (2003) 250.
[34] P.B. Coates, J. Phys. D 6 (1973) 1159.
[35] K. J. Ma, et al., preprint arXiv:0911.5336v1 [physics.ins-det], 2009.
[36] J.G. Learned, S. Pakvasa, Astropart. Phys. 3 (1995) 267.

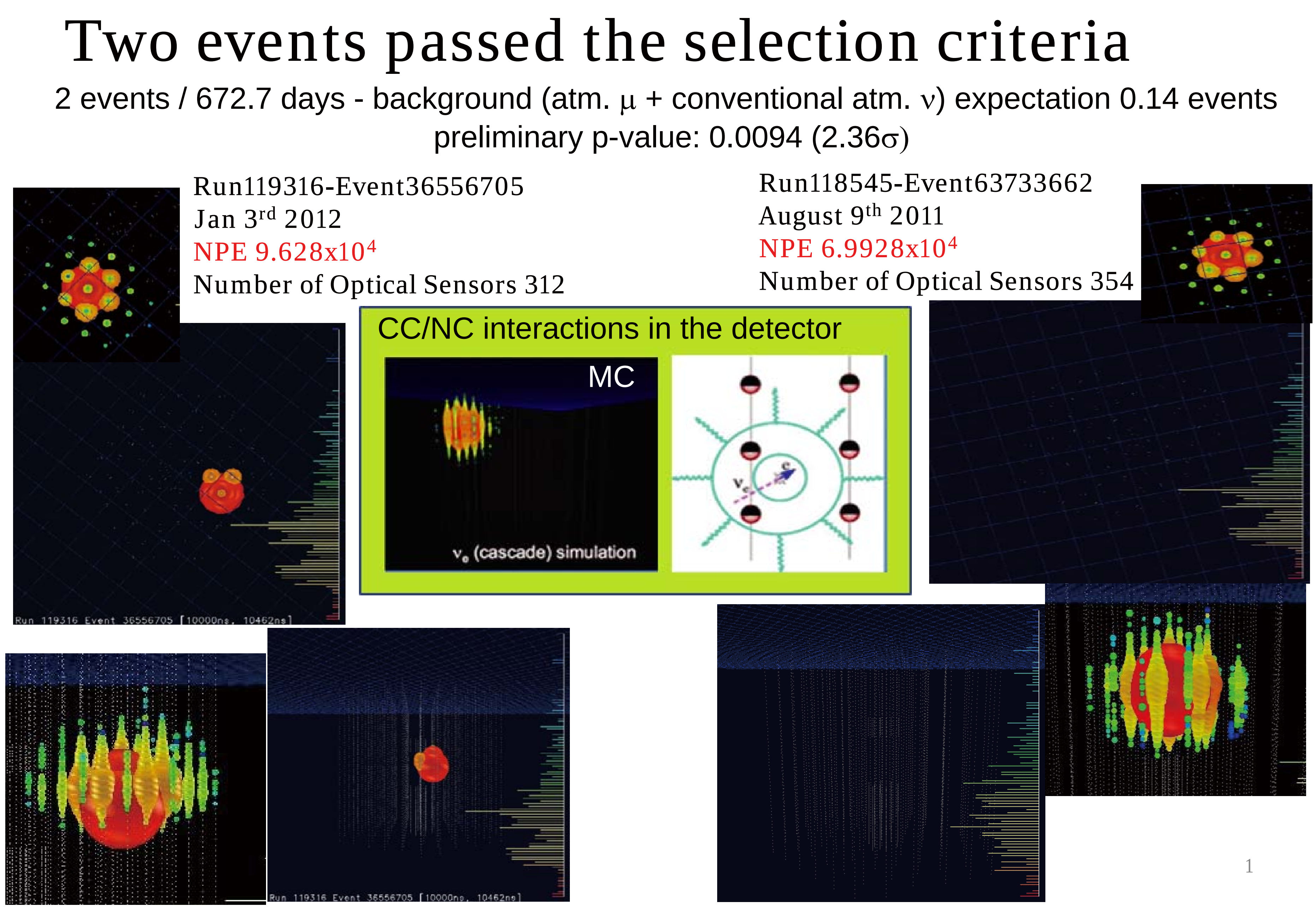

2012 年ニュートリノ物理・宇宙物理国際会議において、二つの宇宙ニュートリノ事象候補検出を初公表したときの発表スライド。石原氏が IceCube 国際共同実験グループを代表して発表した。

The slide of the first announcement on the detection of two PeV-Energy cosmic neutrino event candidates by IceCube at the Neutrino 2012 conference. Presented by Ishihara of Chiba University representing the IceCube Collaboration.

千葉大学研究室の冷凍庫の中に置かれた IceCube 実験用光電子増倍管。当時予算が限られていたため、支持台は大学構内のゴミ捨て場から拾ってきた材料で作った。この測定データから信号応答模型が作られ、IceCube実験検出器シミュレーターに実装されることになる (2004年)。

The IceCube PMT set in the freezer box in the laboratory of the Chiba IceCube group. The limited funding available at that time made us build the PMT supporters with the free materials found in the university garbage pit. The data from this measurement has built the signal response model implemented in the IceCube detector simulation (2004).

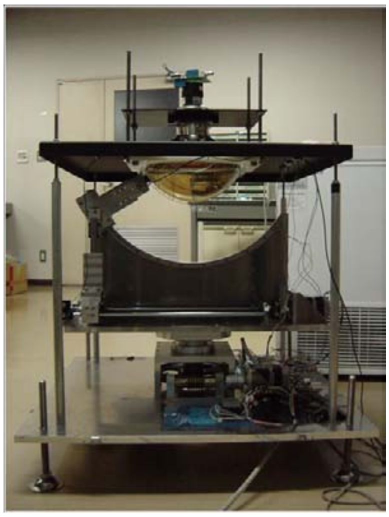

PMT光電面をスキャンし、場所毎の光電変換効率を調べた。この結果も検出器シミュレーターに実装され使われている (2004年)。

The device to scan the photo-cathode surface for measurement of the position-dependent photon detection efficiency. The knowledges from this measurement are included in the PMT simulation for the present IceCube MC data generation (2004).

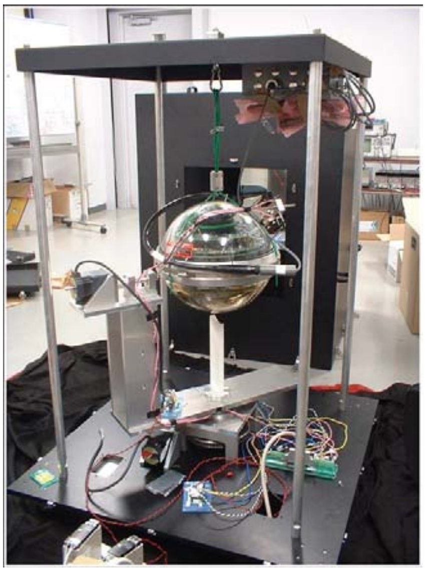

PMTを格納する耐圧ガラス球に被われたIceCube 光検出器モジュール(DOM)の検出効率の位置依存性を測定する装置 (2005年)。測定された角度依存性はIceCube モンテカルロシミュレーションの重要なパラメータのひとつである。

The scanning instrument for the IceCube optical detector modules (DOM) housing the PMT within a pressure sphere.The obtained angular acceptance of the photon conversion efficiency is among the key parameters in the IceCube detector simulation (2005).

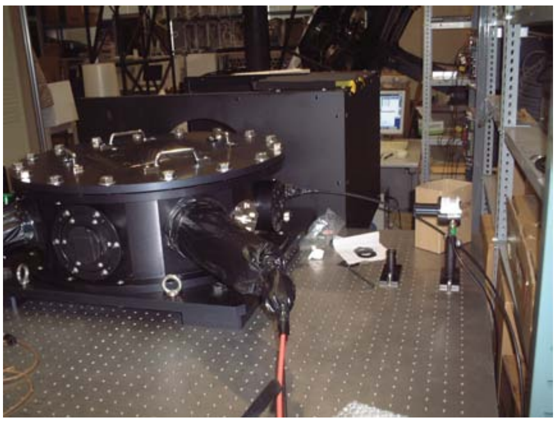

IceCube PMT/DOM の光子検出効率の絶対量を測定するためのセットアップ。窒素ガスを密封したチェンバーとモニター用のPMTが手前にある。奥に見えるのがIceCube PMT が格納されている暗箱である(2005年)。

Our setup for measuring the PMT/DOM photon detection efficiency. A pulsed 337nm laser beam is passed through a chamber containing pure nitrogen gas put on the optical bench. You can see a black dark box behind it housing the IceCube PMT/DOM to be calibrated (2005).

較正される IceCube PMT。位置決めのためのナトリウムレーザーの光が赤い点としてPMT表面に映っている(2005年)。

An IceCube PMT to be calibrated by the chamber. A red light spot from a natrium laser is seen in front of the PMT photo-cathode surface. This is the procedure for aligning the PMT and the beam axis in a straight line (2005).

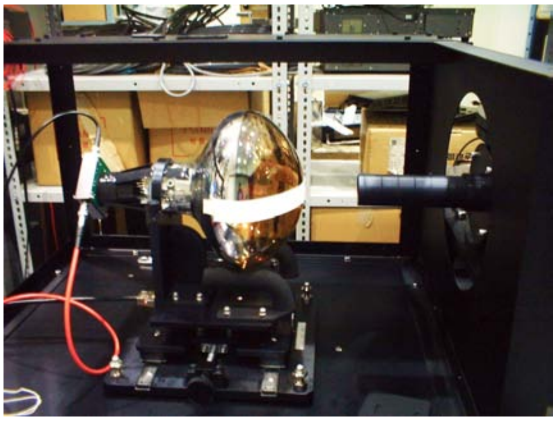

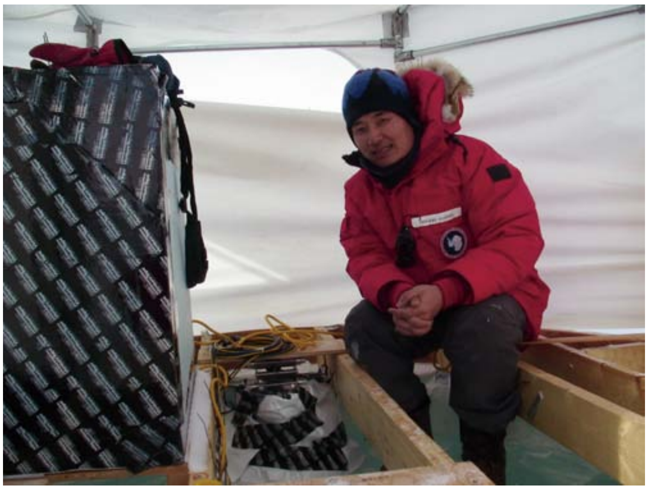

南極点で凍えている吉田氏。IceTop 用の水タンクの開発を手伝っていた(2003年)。

Yoshida freezing at the South Pole. He was helping the R&D of the water tank detector for the IceTop, the sub-component of IceCube for measuring air showers (2003).

氷河内の光散乱を測定するチェンバーを製作し、南極に送った(2009年)。

The "Bubble Search Light", a chamber to measure the photon scattering length in the polar ice, was built and shipped to the South Pole (2009).

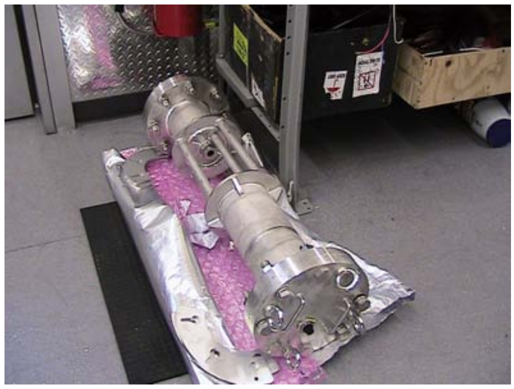

南極にてチェンバーを埋設する石原氏(右端)と埋設チームのメンバー(2009年)。

Ishihara (far right) together with the deployment team at the South Pole. Just before deploying the "Bubble Search Light" down to the glacier ice (2009).

ICRC（宇宙線国際会議）最終日に総括講演を行っている吉田氏（2005年）。ICRCにおける総括講演者としては1999年以来2回めとなる登板であった。

Yoshida giving his Rapporteur talk at the ICRC (International Cosmic Ray Conference) 2005. This was his 2nd appearance as a Rapporteur for the conference since he had first worked on the same task in 1999.

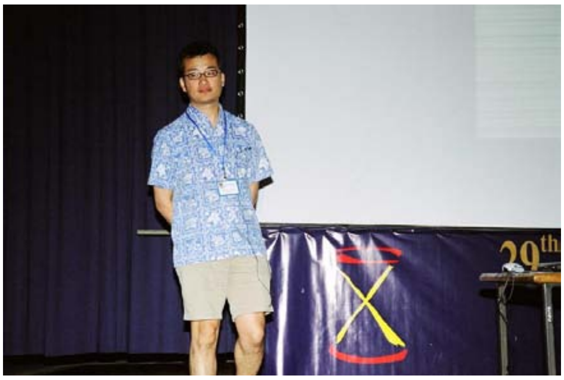

ニュートリノ物理・宇宙物理国際会議で、IceCube 実験による高エネルギー宇宙ニュートリノ事象候補の初検出を世界に公表する石原氏（2012年）。

Ishihara, at the Neutrino 2012, making the first announcement to the world on the IceCube's detection of two PeV-Energy neutrinos as the candidates of cosmic neutrinos.

IUPAP（国際純粋・応用物理学連合）若手賞を受賞し、ICRC（宇宙線国際会議）開会式にてメダルと賞状を手にする石原氏（2013年）。

Ishihara, who was awarded the IUPAP Young Scientist Prize, with the medal and the certificate at the opening ceremony of the ICRC 2013 (2013).

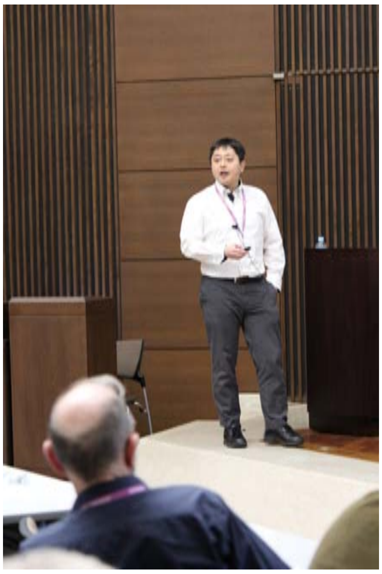

リングイメージングチェレンコフ検出器国際ワークショップ(RICH)にて国際共同実験グループを代表して、IceCube 実験の最新成果について報告する間瀬氏（2013年）。

Mase giving a talk on the latest results from IceCube, representing the collaboration at the International Workshop on Ring Imaging Cherenkov Detectors (RICH) 2013.

CHIBA
UNIVERSITY